

**MEASUREMENT OF THE TOP QUARK PAIR PRODUCTION CROSS  
SECTION IN  $p\bar{p}$  COLLISIONS AT  $\sqrt{s} = 1.96$  TeV**

BY

GUSTAVO J. OTERO Y GARZÓN  
B.S. (University of Buenos Aires, Argentina) 2001

THESIS

Submitted in partial fulfillment of the requirements  
for the degree of Doctor of Philosophy in Physics  
in the Graduate College of the  
University of Illinois at Chicago, 2006

Chicago, Illinois

*To my loving Julia.*

## ACKNOWLEDGMENTS

I am deeply grateful to my advisor Prof. Dr. Cecilia Gerber for giving me the opportunity to work within the DØ Collaboration, for your guidance and vast experience, for your trust and encouragement during the last four years, for being there whenever it was necessary, and for making this intense experience enjoyable.

I am highly thankful to Dr. Elizaveta Shabalina who has been guiding not only this but many analyses with your vast knowledge. I owe a debt of gratitude for your continuous and sagacious help. I would also like to thank the other members of the UIC group at DØ, Profs. Dr. Mark Adams and Dr. Nikos Varelas, for their assistance.

I would like to express my gratitude to Dr. Aurelio Juste for being such an inspiring physicist. It has been an honor working with you.

I thank all the people within the Top Group, those who helped pushing this analysis forward and shared their experience, in particular Dr. Christophe Clement, Dr. Flera Rizatdinova, Dr. Marc-André Pleier and Dr. Gregorio Bernardi.

I am also hugely indebted to Jonas Strandberg for sharing a lot of great work and for being enormously helpful. Thanks to Sara Lager, Nils Gollub and Jean-Roch Vlimant for being always a great help.

Working for the upgrade of the DØ Silicon Detector was an enriching experience and I will always remember the pleasure of working with Dr. Andrei Nomerotski. I also thank Bob Angstadt for your patience and your teaching.

## **ACKNOWLEDGMENTS (Continued)**

The analysis presented is one more of the many that were possible thanks to the dedicated work of the people, scientist and technicians at the Tevatron and the DØ experiment.

My friends at UIC made this years an unforgetable experience. Thanks Mario, Marc, James and Tim!

I thank my parents for giving me everything, and my family and friends for your unconditional support and love.

Finally, I thank you, Julia, your love has enriched every day of my life.

Gustavo

## TABLE OF CONTENTS

<u>CHAPTER</u>		<u>PAGE</u>
<b>1 INTRODUCTION . . . . .</b>		<b>1</b>
<b>2 THEORETICAL ASPECTS . . . . .</b>		<b>3</b>
2.1 The Standard Model of Elementary Particles . . . . .		4
2.2 The Physics of the Top Quark . . . . .		6
2.2.1 Properties of the Top Quark . . . . .		7
2.2.2 The Virtual Top Quark . . . . .		9
2.2.3 Top Quark Pair Production via the Strong Interaction . . . . .		14
2.2.4 Production of the Top Quark via the Weak Interaction . . . . .		24
2.2.5 Decay of the Top Quark . . . . .		26
2.2.6 Signature of $t\bar{t}$ Events . . . . .		27
2.3 The Physics of the Bottom Quark . . . . .		31
2.4 Signature for $t\bar{t}$ Events in the Lepton + Jets Final State . . . . .		32
2.5 Electroweak $W$ Boson Production in Association with Jets . . . . .		32
2.6 QCD Multijet Production . . . . .		36
2.7 Additional Background Processes . . . . .		37
2.7.1 Single Top Production . . . . .		37
2.7.2 Vector Boson Pair Production . . . . .		38
2.7.3 $Z/\gamma^* \rightarrow \tau\tau$ Production in Association with Jets . . . . .		39
2.8 Monte Carlo Simulation . . . . .		39
2.8.1 $t\bar{t}$ Signal Simulation . . . . .		43
2.8.2 $W$ -plus-jets Background Simulation . . . . .		44
2.8.2.1 Jet-Parton Matching . . . . .		46
2.8.3 Additional Backgrounds . . . . .		49
2.9 Measurement of the Luminosity . . . . .		50
2.9.1 The Total $p\bar{p}$ Cross Section and the Optical Theorem . . . . .		51
<b>3 EXPERIMENTAL APPARATUS . . . . .</b>		<b>55</b>
3.1 The FERMILAB Accelerators . . . . .		55
3.2 Interactions of Energetic Particles with Matter . . . . .		61
3.3 The DØ Detector . . . . .		66
3.3.1 Coordinate System . . . . .		66
3.3.2 Luminosity Monitor . . . . .		69
3.3.3 The Central Tracking System . . . . .		70
3.3.4 The Calorimeter System . . . . .		81
3.3.5 The Muon System . . . . .		93
3.3.6 The Forward Proton Detector . . . . .		99

## TABLE OF CONTENTS (Continued)

<u>CHAPTER</u>		<u>PAGE</u>
3.3.7	The Trigger System . . . . .	101
<b>4</b>	<b>EVENT RECONSTRUCTION AND OBJECT IDENTIFICATION . . . . .</b>	<b>106</b>
4.1	Charged Tracks . . . . .	107
4.2	Primary Vertex . . . . .	107
4.3	Muons . . . . .	111
4.3.1	Muon Identification Criteria . . . . .	112
4.3.2	Muon Momentum Correction . . . . .	113
4.3.3	Muon Momentum Scale and Resolution . . . . .	114
4.3.4	Muon Isolation Criteria . . . . .	117
4.4	Electrons . . . . .	118
4.4.1	Electron Reconstruction and Identification . . . . .	120
4.4.2	Electron Energy Scale . . . . .	125
4.4.3	Electron Energy Resolution . . . . .	127
4.5	Jets . . . . .	128
4.5.1	The Jet Reconstruction Algorithm . . . . .	129
4.5.2	The T42 Algorithm . . . . .	131
4.5.3	Jet Identification . . . . .	133
4.5.3.1	L1 Jet Confirmation . . . . .	134
4.5.4	Separation of Jets from Electromagnetic Objects . . . . .	136
4.5.5	Jet Energy Scale . . . . .	137
4.5.6	Jet Energy Resolution . . . . .	139
4.6	Missing $E_T$ . . . . .	146
4.6.1	$E_T$ Resolution . . . . .	147
4.7	$b$ Jets . . . . .	149
4.7.1	Secondary Vertex Tagger Algorithm . . . . .	150
4.7.1.1	Track-Jets . . . . .	152
4.7.1.2	Secondary Vertex Finding . . . . .	152
<b>5</b>	<b>EVENT TRIGGER AND DATA SAMPLE . . . . .</b>	<b>156</b>
5.1	Trigger Efficiency Measurement . . . . .	156
5.1.1	Muon Trigger . . . . .	162
5.1.2	Electron Trigger . . . . .	164
5.1.3	Jet Trigger . . . . .	165
5.1.4	Event Trigger Efficiency . . . . .	168
5.2	Data Sample . . . . .	170
5.2.1	Data Quality Selection . . . . .	171
5.2.2	Integrated Luminosity of the Data Samples . . . . .	174
<b>6</b>	<b>JET TAGGING EFFICIENCIES . . . . .</b>	<b>176</b>
6.1	Taggability . . . . .	176

## TABLE OF CONTENTS (Continued)

<u>CHAPTER</u>		<u>PAGE</u>
6.1.1	Jet Flavor Dependence of Taggability . . . . .	187
6.2	<i>b</i> -Tagging Efficiency . . . . .	191
6.2.1	System8 Method . . . . .	191
6.2.2	Inclusive <i>b</i> -Tagging Efficiency . . . . .	196
6.3	<i>c</i> -Tagging Efficiency . . . . .	197
6.4	Mis-Tagging Rate . . . . .	199
<b>7</b>	<b>THE <math>t\bar{t}</math> PRODUCTION CROSS-SECTION MEASUREMENT . . . . .</b>	<b>207</b>
7.1	$t\bar{t}$ Event Preselection . . . . .	208
7.1.1	Muon Channel Preselection . . . . .	209
7.1.2	Electron Channel Preselection . . . . .	214
7.1.3	Composition of the Preselected Samples - Matrix Method . . . . .	218
7.2	Composition of the Tagged Sample . . . . .	224
7.2.1	Evaluation of the QCD Background . . . . .	226
7.2.2	$t\bar{t}$ Signal . . . . .	230
7.2.3	$W$ -plus-jets Background . . . . .	233
7.2.4	Other Physics Backgrounds . . . . .	240
7.3	Systematic Uncertainties . . . . .	242
7.4	Cross-Section Extraction Procedure . . . . .	254
7.4.1	Treatment of systematic uncertainties . . . . .	257
7.5	Observed and Predicted Number of Tagged Events . . . . .	259
7.6	The $t\bar{t}$ Production Cross-Section . . . . .	268
<b>8</b>	<b>SUMMARY AND CONCLUSIONS . . . . .</b>	<b>276</b>
<b>APPENDICES . . . . .</b>		<b>279</b>
<b>Appendix A</b>		280
<b>Appendix B</b>		295
<b>Appendix C</b>		305
<b>Appendix D</b>		311
<b>CITED LITERATURE . . . . .</b>		<b>338</b>

## LIST OF TABLES

<u>TABLE</u>		<u>PAGE</u>
I	THE THREE GENERATIONS OF THE CONSTITUENTS OF MATTER AND THE GAUGE BOSONS. THE DATES OF DISCOVERY ARE GIVEN IN PARENTHESES. . . . .	4
II	RELATIVE CONTRIBUTIONS TO THE LEADING ORDER $T\bar{T}$ CROSS SECTION FOR THE TEVATRON RUN I AND RUN II AND THE LHC. THE HIGHER THE CENTER-OF-MASS, THE HIGHER THE CONTRIBUTION FROM THE GLUON FUSION PROCESS. THIS IS DUE TO THE INCREASED GLUON PROBABILITY DENSITY AT LOWER VALUES OF ACCESSIBLE $X$ . . . . .	24
III	LEADING ORDER AND BEST KNOWN BRANCHING FRACTIONS OF THE REAL $W^+$ BOSON DECAY, ASSUMING LEPTON UNIVERSALITY. IDENTICAL FOR THE CHARGE CONJUGATES OF THE MODES ABOVE ( $W^-$ ). . . . .	28
IV	BRANCHING FRACTIONS OF THE REAL $\tau^-$ LEPTON DECAY. IDENTICAL FOR THE CHARGE CONJUGATES OF THE MODES ABOVE ( $\tau^+$ ). . . . .	30
V	$T\bar{T}$ DECAY CHANNELS, BORN LEVEL AND BEST KNOWN BRANCHING FRACTIONS. THE CHARGE CONJUGATED FINAL STATES ARE IMPLIED. $\ell_{(\tau)}$ , WITH $\ell = (e, \mu)$ , INCLUDE BOTH THE DECAY MODES $W \rightarrow \ell\nu$ AND $W \rightarrow \tau\nu \rightarrow \ell + \nu\nu\nu$ . THE BRANCHING FRACTIONS CONSIDERED FOR THE DØ ANALYSES ARE DENOTED BY $E\ E$ , $\mu\mu$ AND $E\ \mu$ , $E + \text{JETS}$ AND $\mu + \text{JETS}$ , AND ALL-JETS. . . . .	30
VI	TOTAL NLO CROSS SECTION FOR THE GIVEN DI-BOSON PROCESSES FOR A $P\bar{P}$ CENTER-OF-MASS ENERGY OF 2 TEV. . . . .	39
VII	MAIN GENERATION PARAMETERS FOR $T\bar{T}$ AND $W$ -PLUS-JETS. . . . .	44
VIII	$W + \text{JETS}$ PROCESSES IN ALPGEN AND THEIR CROSS-SECTIONS FOR THE LEPTONIC $W$ BOSON DECAY, $\sigma \equiv \sigma_{P\bar{P} \rightarrow W + \text{JETS}} BR(W \rightarrow e\nu)$ , WHERE $J = U, D, S, G$ AND $J = U, D, S, G, C$ . . . . .	45

## LIST OF TABLES (Continued)

<u>TABLE</u>			<u>PAGE</u>
IX	CROSS SECTIONS FOR BACKGROUND PROCESSES AND THE CORRESPONDING NLO CORRECTION FACTORS (WHERE APPLICABLE) USED IN THE CURRENT ANALYSIS. . . . .		50
X	SPECIFICATIONS OF THE SILICON VERTEX DETECTOR. . .		75
XI	CALORIMETER ENERGY RESOLUTION PARAMETERS, MEASURED WITH ELECTRONS FOR THE ELECTROMAGNETIC SECTION ( $C$ FROM THE $Z \rightarrow E E$ MASS RESOLUTION, $S$ FROM THE TEST BEAM AND $N$ FROM $W \rightarrow E \nu$ ) AND WITH PIONS FROM THE TEST BEAM FOR THE HADRONIC SECTION.		91
XII	TRACK SELECTION OF THE TWO VERTEX ALGORITHMS AT THE SECOND PASS. . . . .		110
XIII	RESULT OF THE KOLMOGOROV-SMIRNOV GOODNESS-OF-FIT TESTS FOR MUONS IN THE CENTRAL REGION ( $ \eta_{DET}  < 1.62$ ) AND MUONS IN THE FORWARD REGION ( $1.62 \leq  \eta_{DET}  \leq 2.00$ ). $\alpha$ REPRESENTS THE TRANSVERSE MOMENTUM SCALE CORRECTION AND $\sigma_\xi$ IS THE WIDTH OF THE GAUSSIAN OVERSMEARING. . . . .		116
XIV	ADDITIONAL JET IDENTIFICATION CRITERION: CUT VALUES ON $\frac{L1SET}{E_T^{RECO} \times (1-CHF)}$ FOR THE THREE CALORIMETER REGIONS. . . . .		136
XV	JET ENERGY RESOLUTION COEFFICIENTS FOR DATA. . . .		143
XVI	JET ENERGY RESOLUTION COEFFICIENTS FOR MC. . . .		146
XVII	SUMMARY OF TRIGGERS USED IN TRIGGER LISTS V8 TO V13 IN THE MUON-PLUS-JETS CHANNEL. . . . .		157
XVIII	SUMMARY OF TRIGGERS USED IN TRIGGER LISTS V8 TO V13 IN THE ELECTRON-PLUS-JETS CHANNEL. . . . .		158
XIX	RUN QUALITY REQUIREMENTS. . . . .		174
XX	BREAKDOWN OF INTEGRATED LUMINOSITIES BY TRIGGER LIST VERSION. . . . .		175

## LIST OF TABLES (Continued)

<u>TABLE</u>		<u>PAGE</u>
XXI	FLAVOR COMPOSITION OF MUONIC JETS IN QCD MONTE CARLO FOR DIFFERENT CUTS ON THE MUON IMPACT PARAMETER. . . . .	188
XXII	NUMBER OF OBSERVED AND PREDICTED NEGATIVE TAGS IN THE PRESELECTED SIGNAL SAMPLES. . . . .	202
XXIII	SUMMARY OF $T\bar{T} \rightarrow \text{LEPTON+JETS}$ PRESELECTION EFFICIENCIES IN THE MUON+JETS CHANNEL. THE QUOTED UNCERTAINTIES RESULT ONLY FROM LIMITED MC STATISTICS. . . . .	215
XXIV	SUMMARY OF $T\bar{T} \rightarrow \text{LEPTON+JETS}$ PRESELECTION EFFICIENCIES IN THE ELECTRON+JETS CHANNEL. THE QUOTED UNCERTAINTIES RESULT ONLY FROM LIMITED MC STATISTICS. . . . .	219
XXV	$\varepsilon_{QCD}$ AND $\varepsilon_{SIG}$ AS A FUNCTION OF JET MULTIPLICITY IN THE MUON+JETS CHANNEL. . . . .	222
XXVI	$\varepsilon_{SIG}$ PER JET MULTIPLICITY IN THE ELECTRON+JETS CHANNEL, AND $\varepsilon_{QCD}$ AS A FUNCTION OF THE NUMBER OF JETS AND TRIGGER LIST VERSION. . . . .	223
XXVII	NUMBER OF PRESELECTED EVENTS IN THE MUON+JETS CHANNEL AND EXPECTED CONTRIBUTION FROM QCD AND $W$ -LIKE VERSUS EXCLUSIVE JET MULTIPLICITY. . . . .	223
XXVIII	NUMBER OF PRESELECTED EVENTS IN THE ELECTRON+JETS CHANNEL AND EXPECTED CONTRIBUTION FROM QCD AND $W$ -LIKE EVENTS VERSUS EXCLUSIVE JET MULTIPLICITY.. . . . .	224
XXIX	NUMBER OF SINGLE TAGGED QCD EVENTS IN THE MUON+JETS CHANNEL OBTAINED BY APPLYING THE MATRIX METHOD ON THE TAGGED SAMPLE. . . . .	230
XXX	NUMBER OF DOUBLE TAGGED QCD EVENTS IN THE MUON+JETS CHANNEL OBTAINED BY APPLYING THE MATRIX METHOD ON THE DOUBLE TAGGED SAMPLE. . . . .	231

## LIST OF TABLES (Continued)

<u>TABLE</u>		
XXXI	NUMBER OF EXPECTED SINGLE TAGGED QCD EVENTS IN THE ELECTRON+JETS CHANNEL OBTAINED BY TWO METHODS, USING THE MATRIX METHOD ON THE TAGGED SAMPLE AND USING EVENT TAGGING PROBABILITIES. . . . .	231
XXXII	NUMBER OF EXPECTED DOUBLE TAGGED QCD EVENTS IN THE ELECTRON+JETS CHANNEL OBTAINED BY TWO METHODS, USING THE MATRIX METHOD ON THE TAGGED SAMPLE AND USING EVENT TAGGING PROBABILITIES. . .	232
XXXIII	SUMMARY OF $T\bar{T}$ PRESELECTION EFFICIENCIES IN THE MUON+JETS AND ELECTRON+JETS CHANNELS (%). . . . .	232
XXXIV	SINGLE TAG PROBABILITIES (%) FOR $T\bar{T}$ EVENTS AFTER PRESELECTION. ERRORS ARE STATISTICAL ONLY. . . . .	233
XXXV	DOUBLE TAG PROBABILITIES (%) FOR $T\bar{T}$ EVENTS AFTER PRESELECTION. ERRORS ARE STATISTICAL ONLY. . . . .	233
XXXVI	FRACTION OF THE DIFFERENT $W$ +JETS FLAVOR SUBPROCESSES CONTRIBUTING TO EACH EXCLUSIVE JET MULTIPLICITY BIN. PARTON-JET MATCHING AND PRESELECTION ARE REQUIRED. THE QUOTED UNCERTAINTIES RESULT ONLY FROM LIMITED MC STATISTICS. . . . .	237
XXXVII	SINGLE TAG PROBABILITIES (%) FOR PRESELECTED $W$ +JETS EVENTS. ERRORS ARE STATISTICAL ONLY. . . . .	238
XXXVIII	DOUBLE TAG PROBABILITIES (%) FOR PRESELECTED $W$ +JETS EVENTS. ERRORS ARE STATISTICAL ONLY. . . . .	239
XXXIX	SINGLE TAG PROBABILITIES (%) OBTAINED FROM APPLYING THE LIGHT TAGGING EFFICIENCY PARAMETRIZATION TO THE PRESELECTED SIGNAL SAMPLE. . . . .	239
XL	SUMMARY OF PRESELECTION EFFICIENCIES IN THE MUON+JETS CHANNEL (%). THE QUOTED UNCERTAINTIES RESULT ONLY FROM LIMITED MC STATISTICS. . . . .	241
XLI	SUMMARY OF PRESELECTION EFFICIENCIES IN THE ELECTRON+JETS CHANNEL (%). THE QUOTED UNCERTAINTIES RESULT ONLY FROM LIMITED MC STATISTICS. . . . .	242

## LIST OF TABLES (Continued)

<u>TABLE</u>		<u>PAGE</u>
XLII	SINGLE TAG PROBABILITIES (%) AFTER FULL PRESELECTION FOR PHYSICS BACKGROUNDS OTHER THAN $W + \text{JETS}$ . ERRORS ARE STATISTICAL ONLY. . . . .	243
XLIII	DOUBLE TAG PROBABILITIES (%) AFTER FULL PRESELECTION FOR PHYSICS BACKGROUNDS OTHER THAN $W + \text{JETS}$ . ERRORS ARE STATISTICAL ONLY. . . . .	244
XLIV	SUMMARY OF SYSTEMATIC UNCERTAINTIES AFFECTING THE SIGNAL EFFICIENCY AND/OR BACKGROUND PREDICTION. <i>CORRELATED</i> AND <i>UNCORRELATED</i> REFER TO THE MUON-PLUS-JETS AND ELECTRON-PLUS-JETS CHANNELS.	245
XLV	SUMMARY OF OBSERVED AND PREDICTED NUMBER OF SINGLE TAGGED EVENTS IN THE ELECTRON+JETS AND THE MUON+JETS CHANNELS. ERRORS ARE STATISTICAL ONLY UNLESS STATED OTHERWISE. . . . .	261
XLVI	SUMMARY OF OBSERVED AND PREDICTED NUMBER OF SINGLE TAGGED EVENTS IN THE COMBINED LEPTON+JETS CHANNEL. ERRORS ARE STATISTICAL ONLY UNLESS STATED OTHERWISE. . . . .	262
XLVII	SUMMARY OF OBSERVED AND PREDICTED NUMBER OF DOUBLE TAGGED EVENTS IN THE ELECTRON+JETS AND THE MUON+JETS CHANNELS. ERRORS ARE STATISTICAL ONLY UNLESS STATED OTHERWISE. . . . .	263
XLVIII	SUMMARY OF OBSERVED AND PREDICTED NUMBER OF DOUBLE TAGGED EVENTS IN THE COMBINED LEPTON+JETS CHANNEL. ERRORS ARE STATISTICAL ONLY UNLESS STATED OTHERWISE. . . . .	264
XLIX	SYSTEMATIC UNCERTAINTIES IN THE MUON+JET CHANNEL ONLY, DETERMINED WITH THE NUISANCE PARAMETER LIKELIHOOD. FOR EACH SOURCE OF SYSTEMATIC THE LIKELIHOOD MAXIMIZATION IS REDONE GIVING A NEW CENTRAL VALUE OF THE CROSS SECTION. THE COLUMN LABELED OFFSET GIVES THE DIFFERENCE BETWEEN THE REFITTED CROSS SECTION AND THE CROSS SECTION OBTAINED IN THE STANDARD METHOD. . . . .	269

## LIST OF TABLES (Continued)

<u>TABLE</u>		<u>PAGE</u>
L	SYSTEMATIC UNCERTAINTIES IN THE ELECTRON+JET CHANNEL ONLY, DETERMINED WITH THE NUISANCE PARAMETER LIKELIHOOD. FOR EACH SOURCE OF SYSTEMATIC THE LIKELIHOOD MAXIMIZATION IS REDONE GIVING A NEW CENTRAL VALUE OF THE CROSS SECTION. THE COLUMN LABELED OFFSET GIVES THE DIFFERENCE BETWEEN THE REFITTED CROSS SECTION AND THE CROSS SECTION OBTAINED IN THE STANDARD METHOD. . . . .	270
LI	SYSTEMATIC UNCERTAINTIES IN THE ELECTRON+JET AND MUON+JET CHANNELS COMBINED, DETERMINED WITH THE NUISANCE PARAMETER LIKELIHOOD. FOR EACH SOURCE OF SYSTEMATIC THE LIKELIHOOD MAXIMIZATION IS REDONE GIVING A NEW CENTRAL VALUE OF THE CROSS SECTION. THE COLUMN LABELED OFFSET GIVES THE DIFFERENCE BETWEEN THE REFITTED CROSS SECTION AND THE CROSS SECTION OBTAINED IN THE STANDARD METHOD. . . . .	271
LII	BREAKDOWN OF SYSTEMATIC UNCERTAINTIES IN THE MUON+JET CHANNEL ONLY. THESE SYSTEMATIC UNCERTAINTIES ARE DERIVED WITH THE STANDARD METHOD. . . . .	273
LIII	BREAKDOWN OF SYSTEMATIC UNCERTAINTIES IN THE ELECTRON+JET CHANNEL ONLY. THESE SYSTEMATIC UNCERTAINTIES ARE DERIVED WITH THE STANDARD METHOD. . . . .	274
LIV	BREAKDOWN OF SYSTEMATIC UNCERTAINTIES IN THE ELECTRON+JET AND MUON+JET COMBINED. THESE SYSTEMATIC UNCERTAINTIES ARE DERIVED WITH THE STANDARD METHOD. . . . .	275
LV	DEFINITION OF TOPOLOGICAL VARIABLES CONSIDERED. THE NORMALIZED MOMENTUM TENSOR IS DEFINED IN EQUATION D.1 AND THE THREE EIGENVALUES ARE ORDERED SUCH THAT $\lambda_1 \geq \lambda_2 \geq \lambda_3$ , WITH $\lambda_1 + \lambda_2 + \lambda_3 = 1$ . THE SETS OF VARIABLES CORRESPOND TO VARIABLES PROPORTIONAL TO THE ENERGY PRESENT IN THE EVENT, LEPTON KINETIC VARIABLES, EVENT SHAPE VARIABLES, RATIOS OF ENERGY DEPENDENT VARIABLES, ANGULAR VARIABLES AND A TOPOLOGICAL DISCRIMINANT. . . . .	281

## LIST OF TABLES (Continued)

<u>TABLE</u>		<u>PAGE</u>
LVI	RELATIVE SYSTEMATIC UNCERTAINTIES ON THE SELECTION EFFICIENCY (%) COMMON TO ALL PROCESSES . . . . .	305
LVII	RELATIVE SYSTEMATIC UNCERTAINTIES ON THE $T\bar{T} \rightarrow \text{LEPTON+JETS}$ SELECTION EFFICIENCY (%). . . . .	306
LVIII	RELATIVE SYSTEMATIC UNCERTAINTIES ON THE $T\bar{T} \rightarrow \text{DILEPTON}$ SELECTION EFFICIENCY (%). . . . .	306
LIX	RELATIVE SYSTEMATIC UNCERTAINTIES ON THE SINGLE TOP S-CHANNEL SELECTION EFFICIENCY (%). . . . .	307
LX	RELATIVE SYSTEMATIC UNCERTAINTIES ON THE SINGLE TOP T-CHANNEL SELECTION EFFICIENCY (%). . . . .	307
LXI	RELATIVE SYSTEMATIC UNCERTAINTIES ON THE $WW \rightarrow L\nu JJ$ SELECTION EFFICIENCY (%). . . . .	308
LXII	RELATIVE SYSTEMATIC UNCERTAINTIES ON THE $WZ \rightarrow L\nu JJ$ SELECTION EFFICIENCY (%). . . . .	308
LXIII	RELATIVE SYSTEMATIC UNCERTAINTIES ON THE $WZ \rightarrow LLJJ$ SELECTION EFFICIENCY (%). . . . .	309
LXIV	RELATIVE SYSTEMATIC UNCERTAINTIES ON THE $ZZ \rightarrow LLJJ$ SELECTION EFFICIENCY (%). . . . .	309
LXV	RELATIVE SYSTEMATIC UNCERTAINTIES ON THE $Z \rightarrow \tau^+\tau^-$ SELECTION EFFICIENCY (%). . . . .	310
LXVI	RELATIVE SYSTEMATIC UNCERTAINTY FROM THE JET ENERGY SCALE (%) FOR SINGLE TAGGED EVENTS. . . . .	312
LXVII	RELATIVE SYSTEMATIC UNCERTAINTY FROM THE JET ENERGY SCALE (%) FOR DOUBLE TAGGED EVENTS. . . . .	313
LXVIII	RELATIVE SYSTEMATIC UNCERTAINTY FROM THE JET ENERGY RESOLUTION (%) FOR SINGLE TAGGED EVENTS. . .	314
LXIX	RELATIVE SYSTEMATIC UNCERTAINTY FROM THE JET ENERGY RESOLUTION (%) FOR DOUBLE TAGGED EVENTS. . .	315

## LIST OF TABLES (Continued)

<u>TABLE</u>		
LXX RELATIVE SYSTEMATIC UNCERTAINTY FROM THE JET RECONSTRUCTION AND IDENTIFICATION EFFICIENCY (%) FOR SINGLE TAGGED EVENTS . . . . .		316
LXXI RELATIVE SYSTEMATIC UNCERTAINTY FROM THE JET RECONSTRUCTION AND IDENTIFICATION EFFICIENCY (%) FOR DOUBLE TAGGED EVENTS . . . . .		317
LXXII RELATIVE SYSTEMATIC UNCERTAINTY FROM THE JET TRIGGER (L3) (%) FOR SINGLE TAGGED EVENTS . . . . .		318
LXXIII RELATIVE SYSTEMATIC UNCERTAINTY FROM THE JET TRIGGER (L3) (%) FOR DOUBLE TAGGED EVENTS . . . . .		319
LXXIV RELATIVE SYSTEMATIC UNCERTAINTY FROM THE TAGGABILITY IN DATA (%) FOR SINGLE TAGGED EVENTS . . . . .		320
LXXV RELATIVE SYSTEMATIC UNCERTAINTY FROM THE TAGGABILITY IN DATA (%) FOR DOUBLE TAGGED EVENTS . . . . .		321
LXXVI RELATIVE SYSTEMATIC UNCERTAINTY FROM THE TAGGABILITY FLAVOR DEPENDENCE (%) FOR SINGLE TAGGED EVENTS . . . . .		322
LXXVII RELATIVE SYSTEMATIC UNCERTAINTY FROM THE TAGGABILITY FLAVOR DEPENDENCE (%) FOR DOUBLE TAGGED EVENTS . . . . .		323
LXXVIIIRELATIVE SYSTEMATIC UNCERTAINTY FROM THE INCLUSIVE $B$ -TAGGING EFFICIENCY IN MONTE CARLO (%) FOR SINGLE TAGGED EVENTS . . . . .		324
LXXIX RELATIVE SYSTEMATIC UNCERTAINTY FROM THE INCLUSIVE $B$ -TAGGING EFFICIENCY IN MONTE CARLO (%) FOR DOUBLE TAGGED EVENTS . . . . .		325
LXXX RELATIVE SYSTEMATIC UNCERTAINTY FROM THE SEMILEPTONIC $B$ -TAGGING EFFICIENCY IN MONTE CARLO (%) FOR SINGLE TAGGED EVENTS . . . . .		326

## LIST OF TABLES (Continued)

<u>TABLE</u>		
LXXXI RELATIVE SYSTEMATIC UNCERTAINTY FROM THE SEMILEPTONIC $B$ -TAGGING EFFICIENCY IN MONTE CARLO (%) FOR DOUBLE TAGGED EVENTS . . . . .	327	
LXXXII RELATIVE SYSTEMATIC UNCERTAINTY FROM THE INCLUSIVE $C$ -TAGGING EFFICIENCY IN MONTE CARLO (%) FOR SINGLE TAGGED EVENTS . . . . .	328	
LXXXIII RELATIVE SYSTEMATIC UNCERTAINTY FROM THE INCLUSIVE $C$ -TAGGING EFFICIENCY IN MONTE CARLO (%) FOR DOUBLE TAGGED EVENTS . . . . .	329	
LXXXIV RELATIVE SYSTEMATIC UNCERTAINTY FROM THE SEMILEPTONIC $B$ -TAGGING EFFICIENCY IN DATA (%) FOR SINGLE TAGGED EVENTS . . . . .	330	
LXXXV RELATIVE SYSTEMATIC UNCERTAINTY FROM THE SEMILEPTONIC $B$ -TAGGING EFFICIENCY IN DATA (%) FOR DOUBLE TAGGED EVENTS . . . . .	331	
LXXXVI RELATIVE SYSTEMATIC UNCERTAINTY FROM THE NEGATIVE TAGGING RATE IN DATA (%) FOR SINGLE TAGGED EVENTS . . . . .	332	
LXXXVII RELATIVE SYSTEMATIC UNCERTAINTY FROM THE NEGATIVE TAGGING RATE IN DATA (%) FOR DOUBLE TAGGED EVENTS . . . . .	333	
LXXXVIII RELATIVE SYSTEMATIC UNCERTAINTY FROM THE $SF_{ll}$ (%) FOR SINGLE TAGGED EVENTS . . . . .	334	
LXXXIX RELATIVE SYSTEMATIC UNCERTAINTY FROM THE $SF_{ll}$ (%) FOR DOUBLE TAGGED EVENTS . . . . .	335	
XC RELATIVE SYSTEMATIC UNCERTAINTY FROM THE $SF_{hf}$ (%) FOR SINGLE TAGGED EVENTS . . . . .	336	
XCI RELATIVE SYSTEMATIC UNCERTAINTY FROM THE $SF_{hf}$ (%) FOR DOUBLE TAGGED EVENTS . . . . .	337	

## LIST OF FIGURES

<u>FIGURE</u>	<u>PAGE</u>
1      Virtual top quark loops contributing to the W and Z boson masses. . . . .	10
2      Virtual Higgs boson loops contributing to the W and Z boson masses. . . . .	11
3 $\chi^2$ of the fit to the electroweak data as a function of the top quark mass using LEP data (left) and LEP, hadron collider and neutrino experiment data (right) (14). The dependence on the Higgs mass is weak, since $m_H$ enters only logarithmically in the electroweak fit, whereas $m_t$ enters quadratically. . . . .	11
4      Evolution of the top quark mass prediction and measurement with time (69). . . . .	12
5      Left: Indirect measurement of the Higgs boson mass from all electroweak data together with the 95% confidence level lower limit on the Higgs mass of 114.4 GeV (25). Right: Contour curves of 68% confidence level in the $(m_t, m_W)$ plane, for the corresponding indirect (LEP1, SLD data) and direct (LEP2, $p\bar{p}$ data) determination in a global fit to electroweak precision data (25). Also shown is the correlation between $m_t$ and $m_W$ as expected in the SM for different Higgs boson masses. . . . .	13
6      Parton model description of a hard scattering process. . . . .	15
7      The quark, anti-quark, and gluon momentum densities in the proton as a function of the longitudinal momentum fractions $x$ at $Q^2 = m_t^2$ from CTEQ5D (31). . . . .	16
8      Summary of the values of $\alpha_s$ at various scales $\mu$ and a fit with the $\pm 1\sigma$ limits (79). The data shown in order of increasing $\mu$ correspond to measurements of $\tau$ width, $\Upsilon$ decays, deep inelastic scattering, $e^+e^-$ event shapes at 22 GeV from JADE, shapes at TRISTAN at 58 GeV, $Z$ width, and $e^+e^-$ event shapes at 135 and 189 GeV. . . . .	17
9      Lowest order Feynman diagrams for the production of $t\bar{t}$ pairs at the Tevatron. At Tevatron energies, the diagram involving quark-antiquark annihilation dominates over those involving gluon-gluon fusion. . . . .	19

## LIST OF FIGURES (Continued)

<u>FIGURE</u>		
10	The scale dependence of the $t\bar{t}$ cross section. The exact definition of the terms which are considered in the perturbative expansion referred to as “NNLO” can be found in (39). . . . .	21
11	The top quark mass dependence of the $t\bar{t}$ cross section. The exact definition of the terms which are considered in the perturbative expansion referred to as “NNLO” can be found in (39). . . . .	22
12	QCD predictions for hard scattering cross sections at the Tevatron and the LHC (42). . . . .	23
13	Single top quark production via the weak interaction. The main contributions at the Tevatron arise from the s-channel process (left) and the t-channel (right). . . . .	25
14	Pie chart of the $t\bar{t}$ event decay channels at Born level. . . . .	29
15	Sketch of the production and decay of a $t\bar{t}$ pair in the $\mu$ -plus-jets channel. . . . .	33
16	Feynman diagram for the $W + 0$ parton process. . . . .	33
17	Some examples of Feynman diagrams for the $W + 1$ parton process. . . . .	34
18	Some examples of Feynman diagrams for the $W + 2$ partons process. . . . .	35
19	Feynman diagrams which represent leading order $W$ boson pair production processes. . . . .	38
20	Sketch of a $p\bar{p}$ interaction . . . . .	40
21	Left: $W + 2$ jets process calculated by the matrix element (ME) and one additional jet generated by the parton shower (PS). Right: $W + 3$ jets process calculated by the matrix element and no additional jet generated by the parton shower. Both processes lead to the same final state. . . . .	47
22	Ratio of the real to imaginary parts of the forward hadronic scattering amplitudes, $\rho$ , as a function of $\sqrt{s}$ (79). . . . .	53
23	Total and elastic cross sections for $p\bar{p}$ collision as a function of laboratory beam momentum and total center of mass energy (79). . . . .	54
24	Schematic view of the FERMILAB accelerator chain. . . . .	56

## LIST OF FIGURES (Continued)

<u>FIGURE</u>		<u>PAGE</u>
25	Schematic view of magnetron operation for the hydrogen ion source. . . . .	58
26	Schematic drawing of Linac RF cavity. . . . .	58
27	Simplified drawing of anti-proton production with nickel target and lithium lens. . . . .	61
28	The integrated luminosity per week and total integrated luminosity for Run II from May 2001 until August 2004 in pb <sup>-1</sup> . . . . .	62
29	The initial luminosity for each store for the Tevatron Run II from May 2001 until August 2004. . . . .	63
30	Energy loss through ionization of muons in various energy regimes (79). . . . .	65
31	Side view of the DØ detector. . . . .	67
32	Luminosity Monitor layout. The $r - \phi$ view is shown on the left, the $r - z$ view of the two arrays is shown on the right. . . . .	70
33	The sketch on the left shows the differentiation between inelastic collisions and beam halo. Expected $z$ vertex distribution for inelastic collisions, centered at $z = 0$ cm, $p$ halo centered at $z = -140$ cm and $\bar{p}$ halo centered at $z = 140$ cm (right). . . . .	71
34	Schematic view of the DØ central tracking system, shown with solenoid, preshower detectors, luminosity monitor and calorimeters. . . . .	72
35	Schematic 3D view of the silicon vertex detector. . . . .	73
36	xy-view of the SMT barrel structure with four super-layers. . . . .	74
37	Read out chain of the silicon vertex detector. . . . .	76
38	a) Location of the CFT. b) Closeup view of axial and stereo layers. . . . .	78
39	$y - z$ view of the DØ magnetic field with both the toroid and solenoid magnets at full current. Numbers are in kG (10 kG = 1 T). . . . .	79
40	Perspective view of the solenoid inside the central calorimeter. . . . .	80

## LIST OF FIGURES (Continued)

<u>FIGURE</u>		
41	Invariant mass distributions for the processes $K_s^0 \rightarrow \pi^+\pi^-$ (left) and $\Lambda^0 \rightarrow p^+\pi^-$ (right) shown overlaid with a Gauss distribution plus a straight line fit to the signal and background. The mean and the width of the Gauss fit are also shown (136). . . . .	82
42	Impact parameter resolution measured in data and in simulated single muon events. The lines show fits to data and MC (136). . . . .	82
43	Invariant mass distributions for the processes $\Xi^\pm \rightarrow \Lambda^0\pi^\pm$ (top left) and $\Omega^\pm \rightarrow \Lambda^0K^\pm$ (bottom left). The reconstruction of the processes are examples of events with multiple tracks with impact parameter in the order of centimeters. A sketch of the decay $\Xi^- \rightarrow \Lambda^0\pi^- \rightarrow p^+\pi^-\pi^-$ is also shown (right) (136). . . . .	83
44	Cross section and layout geometry of CPS and FPS scintillator strips. .	84
45	View of the central and two end calorimeters. . . . .	86
46	Schematic view of a quarter of the D $\bar{Q}$ calorimeter showing the transverse and longitudinal segmentation pattern. The shading pattern indicates cells for signal readout. The rays indicate the pseudo-rapidity intervals seen from the center of the detector. . . . .	87
47	Schematic view of a calorimeter cell. . . . .	89
48	Di-electron invariant mass spectrum measured with the calorimeter (left) and the central tracker (right). The $J/\Psi$ and $\Upsilon$ can clearly be seen (94). .	92
49	Invariant di-electron mass distribution of data (dots) and expected background (line) for the $Z$ peak region. Shaded is QCD background (73) .	92
50	A schematic view of the muon system. . . . .	94
51	View of the three drift chamber layers of the muon system. . . . .	96
52	View of the three scintillator layers of the muon system. . . . .	98
53	$\mu^+\mu^-$ invariant mass distributions of various meson resonances: $\omega$ , $\phi$ , $J/\Psi$ , $\Psi'$ and $\Upsilon$ (99). . . . .	100
54	$\mu^+\mu^-$ invariant mass spectrum at the $Z$ mass (74). . . . .	100

## LIST OF FIGURES (Continued)

<u>FIGURE</u>		
55	The FPD: Quadrupole Roman pot detectors are named P or A when placed on the $p$ or $\bar{p}$ side, respectively. Dipole pots, located on the $\bar{p}$ side, are named D. . . . .	102
56	Schematic view of subdetectors with L1 and L2 trigger elements. Horizontal arrows indicate the direction of dataflow. . . . .	104
57	Axial view (looking along the beam-pipe) of a recorded event showing hits and reconstructed tracks. CFT hits are represented by squares, and SMT hits are represented by circles. Hits are colored solid if they are associated with a reconstructed track (solid lines). The curvature of the reconstructed tracks is due to the solenoidal magnetic field, which is pointing out of the page. . . . .	108
58	Left: Corrected muon $p_T$ versus uncorrected muon $p_T$ . Most of the time the correction is small and the $p_T$ 's are very similar. In particular muons with a very high $p_T$ ( $p_T > 200$ GeV) are corrected down. Right: $p_T$ difference: $SF_{CFT\text{-only}} \times p_T - p_T$ (119). . . . .	114
59	$Z \rightarrow \mu\mu$ mass peak fit. The result obtained for data is shown on the left, the Monte Carlo result before tuning, on the right (111). . . . .	116
60	A hollow cone in $R$ , with the inner edge $R_a$ and the outer edge $R_b$ surrounding the muon. Halo(0.1,0.4) is calculated by summing the transverse energies of all calorimeter cells $i$ with $R_i$ : $R_a > R_i > R_b$ . . . . .	118
61	Top: Distributions for rat11 and rattrk for $t\bar{t} \rightarrow \mu\nu_\mu b\bar{b}q\bar{q}$ MC, $W + 3$ jets MC and QCD data. Bottom left: Relative cut efficiencies as a function of the rat11 isolation variable. The rattrk< 0.06 cut has already been applied. Bottom right: Relative cut efficiency as a function of rattrk. The cut on rat11< 0.08 has already been applied. The cuts are indicated by vertical lines (111). . . . .	119
62	Illustration of the Isolation Parameter: $EisoTot$ is the energy in a cone of radius 0.4 (using EM, FH, and CH layers). $EisoCore$ is the energy in a cone of radius 0.2 (using EM layers). The numerator of $iso$ subtracts $EisoCore$ from $EisoTot$ . . . . .	121
63	Illustration of the EM fraction parameter: EM fraction is the ratio between the energy in the CPS plus EM layers, and the energy in the CPS plus EM layers plus hadronic layers. . . . .	122

## LIST OF FIGURES (Continued)

<u>FIGURE</u>	<u>PAGE</u>
64 $Z \rightarrow ee$ mass peak fit. The result obtained for data is shown on the left, the Monte Carlo result before tuning, on the right (114). . . . .	127
65      The fractional electron energy resolution versus the generated energy for electrons in the Central Calorimeter. . . . .	128
66      An illustration of infrared sensitivity in cone jet clustering. Clustering begins around seed particles, shown as arrows with length proportional to energy. Soft radiation (right sketch) between two jets may cause a merging of the jets. . . . .	129
67      An illustration of collinear sensitivity in cone jet clustering. Left two sketches: No seed particle is produced due to the energy splitting among several detector towers (left), whereas a seed is produced without the splitting (right). The right two sketches show the sensitivity of the jet reconstruction to an $E_T$ ordering of seed particles . . . . .	130
68      Left: $\frac{L1SET}{E_T^{reco} \times (1 - CHF)}$ distribution for good jets from a dijet sample and for fake jets from a multijet sample, integrated over the full pseudo-rapidity region. Right: The corresponding survival efficiency for the good vs. the fake jets varying the cut on $\frac{L1SET}{E_T^{reco} \times (1 - CHF)}$ . The CC, ICD and EC regions are defined in the text, the chosen cut values for the three $\eta_{det}$ regions are highlighted by the solid points (111). . . . .	135
69      JES measurement in data. Left: JES correction as a function of uncorrected jet energy (top) and as a function of jet $\eta_{det}$ (bottom). The respective statistical and total uncertainties are shown on the right (121; 122).	140
70      JES measurement in MC. Left: JES correction as a function of uncorrected jet energy (top) and as a function of jet $\eta_{det}$ (bottom). The respective statistical and total uncertainties are shown on the right (121; 122).	141
71      Jet $p_T$ resolutions for different $\eta_{det}$ regions in data. The points below $\sim 50$ GeV are obtained using $\gamma$ +jet events, whereas for $p_T \geq 50$ GeV resolutions are measured using dijet events. Bands of $\pm 1\sigma$ statistical error are also shown. . . . .	144
72      Jet $p_T$ resolutions for different $\eta_{det}$ regions in MC. The points below $\sim 50$ GeV are obtained using $\gamma$ +jet events, whereas for $p_T \geq 50$ GeV resolutions are measured using dijet events. Bands of $\pm 1\sigma$ statistical error are also shown. . . . .	145

## LIST OF FIGURES (Continued)

<u>FIGURE</u>	<u>PAGE</u>
73 $\cancel{E}_T$ resolution in $Z \rightarrow \mu\mu$ events for data, MC and smeared MC with $\geq 0$ jets (left) and $\geq 2$ jets (right) (123). . . . .	148
74      The Secondary Vertex algorithm explicitly reconstructs displaced vertices inside of jets. Tracks with significant Distance of Closest Approach ( $dca$ ) with respect to the Primary Vertex ( $PV$ ) are used to reconstruct secondary vertices within a jet. The cut on the decay length significance of the secondary vertices is tuned to optimize the performance of the algorithm. . . . .	151
75      Left: A schematic drawing showing the definition of the impact parameter ( $dca$ ). The sign of the $dca$ is given by the sign of the inner product of $dca$ and the track-jet momentum. Right: The impact parameter significance distributions for tracks from light and $b$ jets from Monte Carlo. . . . .	153
76      Invariant mass distributions for the processes $\Lambda^0 \rightarrow p^+\pi^-$ (left) and $K_s^0 \rightarrow \pi^+\pi^-$ (right) (136). . . . .	155
77      Muon trigger efficiency as a function of the offline muon $\eta$ for the combined Level 1 condition mu1ptxatlx and Level 2 condition MUON(1,med). The yellow band denotes the statistical error of the spline fit. . . . .	163
78      Jet trigger efficiencies for trigger list v12 in the three detector regions CC (left), ICD (middle) and EC (right). The original parameterizations are overlaid as the solid (blue) curve, the fits used as default are shown in dashed (red) (111). . . . .	166
79      Relative difference in the jet trigger efficiency between the two measurements for jets with and without track-match as a function of offline jet $p_T$ for the Level 1 condition CJT(1,5) (left), for the Level 2 condition JET(1,10) given that the jet already satisfies the Level 1 condition (middle), and the Level 3 condition JET(1,20) given that the jet already satisfies the Level 1 and the Level 2 conditions (right); for trigger version 12, and jets in the CC region (130). . . . .	167

## LIST OF FIGURES (Continued)

<u>FIGURE</u>		
80	Schematic drawing showing the geometric dependance of the taggability. A primary vertex ( $PV$ ) located outside the Silicon Tracker barrels as shown in the picture, may have two reconstructed jets originating from it. In the case of jet 1, the combination of the position along the beam axis ( $PV_Z$ ) and the pseudo rapidity of the jet 1 ( $\eta_1$ ) is such that the track-jet has a high probability to have hits in the SMT. That is not the case for jet 2, where $PV_Z$ and $\eta_2$ are such that the tracks within this jet have a low probability to have SMT hits, thus making it less likely to be taggable for a geometric reason. A combination of $PV_Z$ and the relative sign to the jet $\eta$ takes this geometric dependance into account. . . . .	178
81	Taggability as a function of the position of the Primary Vertex along the beam axis for the case in which the product of $PV_Z$ and jet $\eta$ is positive (left) or negative (right) as observed in a $Wj$ Monte Carlo sample. . . . .	179
82	Taggability as a function of the position of the Primary Vertex along the beam axis for the case in which the product of $PV_Z$ and jet $\eta$ is positive (left) or negative (right) as observed in the lepton plus jets preselected data. The dashed lines correspond to the boundaries between regions. .	180
83	Two dimensional parametrizations of taggability for different ( $PV_Z$ , $PV_Z \times \eta$ ) bins. . . . .	181
84	Validation of the taggability parametrizations applied to the $e+jets$ channel. The predicted and observed jet $p_T$ , jet $\eta$ and $PV_Z$ distribution are in good agreement in all jet multiplicities. . . . .	182
85	Validation of the taggability parametrizations applied to the $\mu+jets$ channel. The predicted and observed jet $p_T$ , jet $\eta$ and $PV_Z$ distribution are in good agreement in all jet multiplicities. . . . .	183
86	Prediction and observation of the number of jets in preselected $e+jets$ data events. . . . .	184
87	Prediction and observation of the number of jets in preselected $\mu+jets$ data events. . . . .	184
88	Predictability of the topological event variable $H_T$ in $e+jets$ preselected data for different jet multiplicities based on the parametrized taggability.	185
89	Predictability of the topological event variable $H_T$ in $\mu+jets$ preselected data for different jet multiplicities based on the parametrized taggability.	186

## LIST OF FIGURES (Continued)

<u>FIGURE</u>		
90	Average track multiplicity in a taggable jet as a function of jet $E_T$ for $b$ , $c$ and light jets in the $Wb\bar{b}$ , $Wc\bar{c}$ and $Wjj$ Monte Carlo samples (136). . . . .	188
91	Ratio of the $b$ to light and $c$ to light jet taggability, measured in a QCD Monte Carlo sample (136). . . . .	189
92	Ratios of taggabilities obtained on enriched $b$ -jet samples to those measured on enriched light flavor jet samples in data and QCD Monte Carlo (136). . . . .	190
93	Semimuonic $b$ -tagging efficiency as a function of jet $p_T$ (left) and jet $\eta$ (middle) measured in data with the System8 method along with the fit and $\pm\sigma$ error band. The right plot shows the combined two-dimensional parameterization. . . . .	194
94	Behavior of the System8 variables ( $\beta$ to the left, $k_b$ in the center and $k_{cl}$ to the right) versus jet $p_T$ observed in Monte Carlo. . . . .	195
95	Inclusive and semimuonic $b$ -tagging efficiency measured in the $t\bar{t}$ Monte Carlo as a function of jet $p_T$ (left) and $\eta$ (right). . . . .	197
96	Inclusive $c$ -tagging efficiency measured in the $t\bar{t}$ Monte Carlo as a function of jet $p_T$ (left) and $\eta$ (middle). The right plot shows the combined two-dimensional parameterization. . . . .	198
97	Negative tagging efficiency as a function of jet $p_T$ (left) and jet $\eta$ (middle). The right plot shows the two-dimensional parameterization. . . . .	200
98	Inclusive $p_T$ (left) and $\eta$ (right) distributions of negatively tagged jets in the EMqcd sample compared with the distributions predicted by the negative tag rate parameterizations. . . . .	201
99	$p_T$ (four left plots) and $\eta$ (four right plots) distributions of negatively tagged jets in the EMqcd sample compared with the distributions predicted by the negative tag rate parametrizations in each jet multiplicity bin. . . . .	202
100	Inclusive $p_T$ (left) and $\eta$ (right) distributions of negatively tagged jets in the combined lepton+jets preselected compared with the distributions predicted by the negative tag rate parameterizations. . . . .	203

## LIST OF FIGURES (Continued)

<u>FIGURE</u>		
101	$p_T$ (four left plots) and $\eta$ (four right plots) distributions of negatively tagged jets in combined lepton+jets preselected compared with the distributions predicted by the negative tag rate parametrizations in each jet multiplicity bin. . . . .	204
102	Correction factors for the contribution of heavy flavor in the negative tag rate ( $SF_{hf}$ , upper plots) and contribution to the mistag rate from long lived light particles ( $SF_{ll}$ , lower plots). The two right plots show the $E_T$ dependence and the two left show the $\eta$ dependence. . . . .	206
103	Leading jet $p_T$ threshold. The simulation includes the corresponding trigger efficiencies (111). . . . .	210
104	The average single tag probability for QCD events as a function of the maximum allowed value of the electron likelihood is shown in the left plot. In the right plot the average tagging probability per jet multiplicity bin for a likelihood requirement of $\leq 0.5$ is shown for single and double tagged events respectively. . . . .	229
105	Ratios of <i>ad-hoc</i> to MLM fractions. Left, center and right columns correspond to $N_{jets} = 1, 2, 3$ , respectively. In each plot, each of the four points shown corresponds to one choice for MLM matching: $(p_T, R) = (5, 0.5), (5, 0.7), (10, 0.5), (10, 0.7)$ (143). . . . .	236
106	Alternative ratios of the $b$ - to light and $c$ - to light jet taggabilities used for the systematics uncertainty calculations (136). . . . .	249
107	Mass dependence of the $t\bar{t}$ preselection efficiencies in the $e+$ jets (left plot) and $\mu+$ jets (right plot) channels. . . . .	254
108	Mass dependence of the $t\bar{t}$ tagging efficiencies in the $e+$ jets (top plots) and $\mu+$ jets (bottom plots) channels. . . . .	255
109	Observed and predicted number of tagged events in the $\mu+$ jets channel. The left plot shows single tagged events and the right plot shows double tagged events. The total error on the background prediction is represented by the dashed blue band and the total error on the sum of the signal and background prediction is represented by the dashed red band.	265
110	The predicted background composition in the $\mu+$ jets channel for single tagged events (left) and double tagged events (right). . . . .	265

## LIST OF FIGURES (Continued)

<u>FIGURE</u>		<u>PAGE</u>
111	Observed and predicted number of tagged events in the $e$ +jets channel. The left plot shows single tagged events and the right plot shows double tagged events. The total error on the background prediction is represented by the dashed blue band and the total error on the sum of the signal and background prediction is represented by the dashed red band.	266
112	The predicted background composition in the $e$ +jets channel for single tagged events (left) and double tagged events (right). . . . .	266
113	Observed and predicted number of tagged events in the combined $l$ +jets channel. The left plot shows single tagged events and the right plot shows double tagged events. The total error on the background prediction is represented by the dashed blue band and the total error on the sum of the signal and background prediction is represented by the dashed red band. . . . .	267
114	The predicted background composition in the combined $l$ +jets channel for single tagged events (left) and double tagged events (right). . . . .	267
115	Top quark mass dependence of the measured cross section compared to the theoretical prediction (39). . . . .	272
116	Comparison of all current $t\bar{t}$ production cross-section measurements from DØ with the theoretical expectation (39; 40). The figure shows the integrated luminosities used and the measured $t\bar{t}$ cross-section. From top to bottom: combined dilepton ( $ee$ , $\mu\mu$ and $e\mu$ ) topological (146), lepton-plus-jets topological (147), combined dilepton-lepton-plus-jets topological (148), combined dilepton ( $ee$ , $\mu\mu$ and $e\mu$ ) topological (52), lepton-plus-jets topological, combined dilepton-lepton-plus-jets topological, lepton-plus-jets using (SVT and CSIP) lifetime $b$ -tagging (149), lepton-plus-jets using (SVT) lifetime $b$ -tagging preliminary result for the summer of 2005 (150), measurement presented in this thesis and the all-jets channel (151).	277
117	Sanity checks for single tagged events in the $l+1$ jet bin. . . . .	282
118	Sanity checks for single tagged events in the $l+2$ jets bin. . . . .	283
119	Sanity checks for single tagged events in the $l+2$ jets bin. . . . .	284
120	Sanity checks for single tagged events in the $l+3$ jets bin. . . . .	285
121	Sanity checks for single tagged events in the $l+3$ jets bin. . . . .	286

## LIST OF FIGURES (Continued)

<u>FIGURE</u>		<u>PAGE</u>
122	Sanity checks for single tagged events in the $l+\geq 4$ jets bin. . . . .	287
123	Sanity checks for single tagged events in the $l+\geq 4$ jets bin. . . . .	288
124	Sanity checks for double tagged events in the $l+2$ jets bin. . . . .	289
125	Sanity checks for double tagged events in the $l+2$ jets bin. . . . .	290
126	Sanity checks for double tagged events in the $l+3$ jets bin. . . . .	291
127	Sanity checks for double tagged events in the $l+3$ jets bin. . . . .	292
128	Sanity checks for double tagged events in the $l+\geq 4$ jets bin. . . . .	293
129	Sanity checks for double tagged events in the $l+\geq 4$ jets bin. . . . .	294

## SUMMARY

A measurement of the top quark pair ( $t\bar{t}$ ) production cross section ( $\sigma_{t\bar{t}}$ ) in  $p\bar{p}$  collisions at a center of mass energy of 1.96 TeV is presented. The measurement is based on data recorded by the DØ Detector at the FERMILAB Tevatron Collider, and preselected in the  $e+$ jets ( $366 \text{ pb}^{-1}$ ) and  $\mu+$ jets ( $363 \text{ pb}^{-1}$ ) channels. The cross section is extracted by applying a lifetime-tagging technique to the data, and yields

$$\sigma_{t\bar{t}} = 6.96^{+1.07}_{-0.98}(\text{stat+syst}) \pm 0.45(\text{lumi}) \text{ pb},$$

for a top quark mass  $m_t = 175$  GeV, in good agreement with the Standard Model prediction.

# CHAPTER 1

## INTRODUCTION

Humans are extremely inquisitive beings. We strive to know defining things like where do we come from and what constitutes us. Through the centuries, humanity relied on science to address questions of this sort with a systematic approach, by the use of logic, creativity and objectivity, that lead us to confront the mind with the findings. The desire to answer a question like “What are things ultimately made of?” gave rise to the Standard Model of Particle Physics, a theory that binds together all the knowledge of elementary particles and their interactions.

Among the fundamental particles of the Standard Model, the top quark, subject of this thesis, is the most recently discovered. The history of the top quark has been a success for the Standard Model, beginning with the prediction of its existence as the electroweak isospin partner of the bottom quark (discovered in 1977), the prediction of its mass from constraints of the electroweak precision data since 1992, and finally its discovery by the CDF and DØ collaborations during FERMILAB Tevatron’s Run I in 1995. However, the study of the top quark is still at its early stages and the Tevatron is, at present, the only place where it can be produced. Top physics gives insights into perturbative Quantum Chromodynamics, into the mechanism of electroweak symmetry breaking, and at the same time, it allows for the search of new physics. These characteristics make the top quark one of the most interesting topics in elementary particle physics today.

The subject of this thesis is the measurement of the rate at which a top-antitop quark pair is produced in  $p\bar{p}$  collisions at a center of mass energy of  $\sqrt{s} = 1.96$  TeV. The data are collected with the DØ detector, a multi-purpose detector operating at the FERMILAB Tevatron collider during Run II.

This thesis is organized as follows:

- The *Theoretical Aspects* of the analysis are detailed in Chapter 2
- The *Experimental Apparatus* describing the Tevatron collider and the DØ Detector is included in Chapter 3.
- The *Event Reconstruction and Object Identification* is given in Chapter 4.
- The *Event Trigger and Data Sample* used for this analysis are discussed in Chapter 5.
- The *Jet Tagging Efficiencies* are detailed in Chapter 6
- The  *$t\bar{t}$  Production Cross-Section* measurement is presented in Chapter 7.
- A *Summary and Conclusion* is given in Chapter 8.

## CHAPTER 2

### THEORETICAL ASPECTS

Our present understanding of quarks, leptons and their interactions is described by the “*Standard Model*” of Elementary Particles. It has been extremely successful in predicting a wide range of fundamental phenomena. The *Standard Model* is a renormalizable gauge theory with local gauge invariance (1). It is characterized by the spectrum of elementary particles which consist of twelve fundamental fermions (six quarks and six leptons), and four fundamental forces mediated by gauge bosons, as shown in Table I. An introduction and discussion of the basic concepts of the *Standard Model* can be found in (2); publications concerning the electroweak theory and Quantum Chromodynamics (QCD) can be found in (3) and (4), respectively.

A brief overview of the *Standard Model* is outlined in Section 2.1. The physics of the top quark in the framework of the *Standard Model* is discussed in Section 2.2. Section 2.3 describes the bottom quark, which is a decay product of the top quark. The signature of signal processes is discussed in Section 2.4. The signature corresponding to different background processes is discussed in Sections 2.5, 2.6, and 2.7. The Monte Carlo simulation of the events is described in Section 2.8, and a discussion about the measurement of the luminosity at hadron colliders is given in Section 2.9.

	Generation		
	I	II	III
leptons:	$\nu_e$ (1953)	$\nu_\mu$ (1962)	$\nu_\tau$ (2000)
	$e$ (1897)	$\mu$ (1936)	$\tau$ (1975)
quarks:	u (1968)	c (1974)	t (1995)
	d (1968)	s (1964)	b (1977)
gauge bosons:	$g_1, \dots, g_s$ (1979)		
	$\gamma$ (1900)		
	$W^\pm, Z^0$ (1983)		

TABLE I

THE THREE GENERATIONS OF THE CONSTITUENTS OF MATTER AND THE GAUGE BOSONS. THE DATES OF DISCOVERY ARE GIVEN IN PARENTHESES.  
(2; 5; 6; 7; 8; 9)

## 2.1 The Standard Model of Elementary Particles

The *Standard Model* (SM) is a gauge theory built on the  $SU(3) \times SU(2) \times U(1)$  symmetry. The requirement of invariance of the Lagrangian under local gauge transformations constrains the kind of interactions allowed in the model. This leads to three forces:  $SU(3)$  accounts for Quantum Chromodynamics (QCD), which describes the strong interaction.  $SU(2) \times U(1)$  corresponds to the electromagnetic and weak interactions. The fourth force, Gravitation, is much weaker than the other three forces and therefore it is negligible in particle physics. It is not described by the SM.

The model, as described so far, does not allow for the presence of mass terms in the Lagrangian. The key for solving this problem is the Higgs mechanism of spontaneous symmetry breaking (10), (11), (12), (13). It accomplishes the generation of the masses of the  $W^\pm$  and  $Z^0$

bosons. The masses of the fermions are introduced as Yukawa couplings, giving the interaction of the Higgs boson with fermions with a strength proportional to the fermion masses.

The SM Lagrangian can be written as:

$$\mathcal{L}_{\text{SM}} = \mathcal{L}_{\text{Gauge}} + \mathcal{L}_{\text{Matter}} + \mathcal{L}_{\text{Higgs}} + \mathcal{L}_{\text{Yukawa}}, \quad (2.1)$$

where  $\mathcal{L}_{\text{Gauge}}$  describes the pure gauge interaction,  $\mathcal{L}_{\text{Matter}}$  the gauge interaction of the fermions,  $\mathcal{L}_{\text{Higgs}}$  the Lagrangian for the Higgs field and  $\mathcal{L}_{\text{Yukawa}}$  the interaction of the Higgs field and the fermions.

The fundamental fermions are leptons and quarks. There are three generations of fermions which differ in mass among themselves. The mixing between the three generation of quarks is parameterized by the Cabibbo-Kobayashi-Maskawa (CKM) matrix. The CKM matrix describes the rotation from the weak to the mass eigenstates of the quarks.

The SM contains nineteen free parameters. Three of them appear as the values of the couplings constants of the gauge symmetry, and two more in the Higgs potential. Neglecting neutrino masses, the other parameters can be found in  $\mathcal{L}_{\text{Yukawa}}$  and correspond to the six quarks and three lepton masses and four parameters of CKM matrix (three mixing angles and one CP-violating phase). The last parameter is a strong CP violating phase that is experimentally determined to be very small.

## **2.2 The Physics of the Top Quark**

The top quark was predicted since the discovery of the bottom quark (1977) as its electroweak isospin partner. The mass of the top quark was constrained since 1992 with continuously increasing precision by electroweak precision data from LEP, SLD, NuTeV and the  $p\bar{p}$  colliders (14).

Discovered at the FERMILAB Tevatron in 1995 (5; 6; 7), the top quark completes the quark sector of the three-generation structure of the SM. It is the heaviest known elementary particle with a mass approximately 40 times larger than the next heaviest quark, the bottom quark. It differs from the other quarks not only by the much larger mass, but also by its lifetime which is too short to build hadronic bound states.

The top quark is one of the least well-studied components of the SM, and the Tevatron, with a center of mass energy of  $\sqrt{s} = 1.96$  TeV, is at present the only accelerator where it can be produced. Studying the top quark is therefore of strong interest due in part to the following considerations:

- The measurement of the production rate of the top quark represent one of the most important tests of the SM, in particular for QCD at the Tevatron.
- The top quark mass is an input for many electroweak analyses, in particular an accurate measurement can be used to constrain the prediction of the Higgs mass.
- The top quark plays an important role in the discovery of new particles, as the Higgs boson coupling to the top quark is stronger than to all other fermions. In addition, background to New Physics consists mainly of events containing top quarks. The understanding of this

main background, its signature and production rate, is crucial for the potential discovery of New Physics.

### **2.2.1 Properties of the Top Quark**

In the SM, the top quark is a spin- $\frac{1}{2}$  fermion of electric charge  $+\frac{2}{3}$  which transforms as a color anti-triplet under the SU(3) gauge group of strong interactions.

#### **Top Quark Mass**

The DØ and CDF experiments have measured the top quark mass to be  $m_t = 178.0 \pm 2.7(stat.) \pm 3.3(syst.)$  GeV in Run I (16) and  $m_t = 172.7 \pm 1.7(stat.) \pm 2.4(syst.)$  GeV in Run II to date (17). The perspectives for the full data set of Run II are to measure the top quark mass to a precision better than 2 GeV. Together with a precision on the  $W$  mass of 20 MeV, the Higgs mass is expected to be constrained to better than 40 % (18). At the Large Hadron Collider (LHC) the mass of the top quark is expected to be measured with a precision of about 1 GeV (19).

#### **Top Quark Charge**

The top quark charge is easily accessible in  $e^+e^-$  production by scanning the center of mass energy of two times the top quark mass and measuring the ratio  $R = \frac{e^+e^- \rightarrow hadrons}{e^+e^- \rightarrow \mu^+\mu^-}$ . However, this region of center of mass energy is not presently accessible so far. At hadron colliders, as the Tevatron, the top quark charge is directly determined by measuring the charge of its decay products. Although the charge of the  $W$  boson is easily accessible through its leptonic decay products, the charge measurement of the associated  $b$  jet is challenging. Current limits to the top quark charge are in agreement with the SM (23).

## ***W* Helicity**

The helicity of  $W$  bosons from top quark decays is predicted by the SM. Studies of the decay angular distributions allow a direct analysis of the  $V - A$  nature of the  $Wtb$  coupling. In the SM, the fraction of decays for longitudinally polarized  $W$  bosons is expected to be  $f_0 = \frac{m_t^2}{2m_W^2 + m_t^2 + m_b^2} \approx 70\%$ . Deviations from this value would bring into question the validity of the Higgs mechanism of spontaneous symmetry breaking. Current measurements (22), using the angular distribution of the objects in the final state, are in good agreement with the expectation.

## **Yukawa Coupling**

The Yukawa coupling is the Higgs coupling to fermions. It relates the fermionic matter content of the SM to the source of mass generation, the Higgs sector (10). In the SM, the Yukawa coupling to the top quark is very close to unity, a theoretically interesting value that leads to speculations that New Physics may be accessed via top quark physics (20). The coupling will be measured in the associated  $t\bar{t}$  Higgs production at the LHC.

## **Spin Correlation**

The Top quark has a very short lifetime of about  $5 \times 10^{-25}$  s, which is  $\mathcal{O}(10)$  times shorter than the characteristic time scale for hadronization. As a consequence, the top quark is the only quark that decays before it has a chance to hadronize, making it the only quark for which its spin is directly observable. The spin information is transferred to the top quark decay products ( $Wb$ ), and can be measured in the leptonic  $W$  boson decay. Limits on  $t\bar{t}$  spin correlations were found in Run I (21).

## Resonances

The invariant mass of the  $t\bar{t}$  system may reveal s-channel resonances predicted by various models. Scans of the  $t\bar{t}$  mass spectrum were performed and no significant peaks were observed so far (24).

### 2.2.2 The Virtual Top Quark

Precise electroweak measurements can be used to check the validity of the SM and get valuable information about its fundamental parameters. The accuracy of the measurements makes them sensitive to the mass of the top quark and the Higgs boson through radiative corrections (14).

All electroweak quantities depend only on five parameters. At leading order, this dependence is reduced to only 3 parameters: two gauge couplings and the Higgs-field vacuum-expectation value. The three best-measured electroweak quantities can be used to determine these three parameters. They are the electromagnetic coupling constant  $\alpha$ , measured at low-energy experiments, the Fermi constant  $G_F$ , determined from the  $\mu$  lifetime (26), and the mass of the  $Z$  boson, measured from  $e^+e^-$  annihilation (27). By defining the Weinberg angle  $\theta_W$  through

$$\sin^2 \theta_W \equiv 1 - \frac{m_W^2}{m_Z^2}, \quad (2.2)$$

the  $W$  mass at tree level can be expressed by:

$$m_W^2 = \frac{\frac{\pi\alpha}{\sqrt{2}G_F}}{\sin^2 \theta_W}. \quad (2.3)$$

Considering also one-loop corrections, the expression in Equation 2.3 is modified to

$$m_W^2 = \frac{\frac{\pi\alpha}{\sqrt{2}G_F}}{\sin^2\theta_W(1 - \Delta r)}, \quad (2.4)$$

where  $\Delta r$  contains all the one-loop corrections. Contributions to  $\Delta r$  originate from the top quark by the one-loop diagrams shown in Figure 1, which contribute to the  $W$  and  $Z$  masses

$$(\Delta r)_{top} \simeq -\frac{3G_F}{8\sqrt{2}\pi^2\tan^2\theta_W} \frac{1}{m_t^2}. \quad (2.5)$$

Also the Higgs boson contributes to  $\Delta r$  via the one-loop diagrams shown in Figure 2

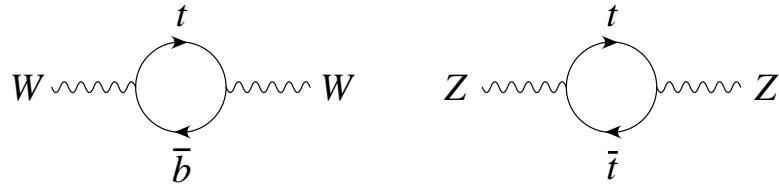


Figure 1. Virtual top quark loops contributing to the  $W$  and  $Z$  boson masses.

$$(\Delta r)_{Higgs} \simeq \frac{11G_F m_Z^2 \cos^2\theta_W}{24\sqrt{2}\pi^2} \ln \frac{m_H^2}{m_Z^2}. \quad (2.6)$$

While the leading  $m_t$  dependence is quadratic, the leading  $m_H$  dependence is logarithmic.

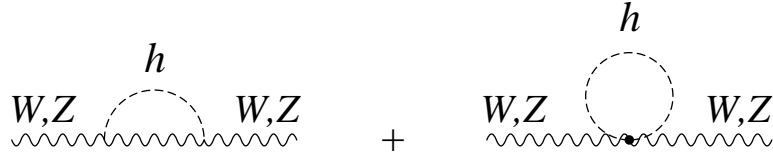


Figure 2. Virtual Higgs boson loops contributing to the  $W$  and  $Z$  boson masses.

Therefore the constraints on  $m_H$  are much weaker than those on  $m_t$ . In addition, neutral current weak interaction data, such as  $e^+e^-$  annihilation near the  $Z$  boson mass,  $\nu N$  and  $eN$  deep-inelastic scattering,  $\nu e$  elastic scattering and atomic parity violation (79) can be used to predict the top quark mass (14) (Figure 3). This was used to successfully predict the top quark mass several years before it was discovered, as shown in Figure 4.

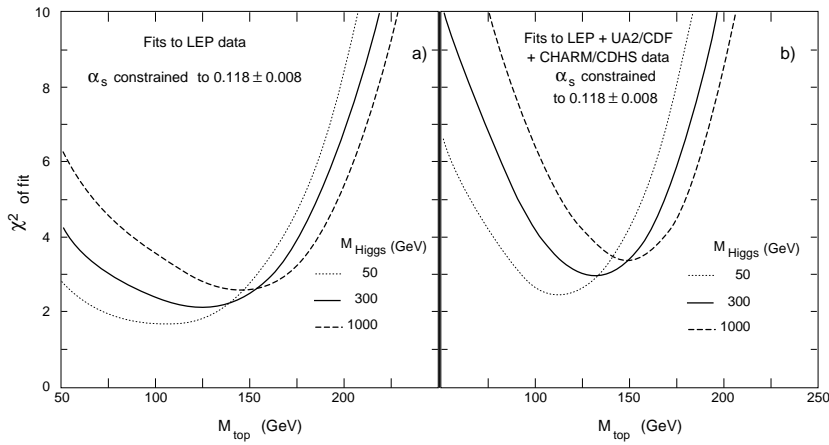


Figure 3.  $\chi^2$  of the fit to the electroweak data as a function of the top quark mass using LEP data (left) and LEP, hadron collider and neutrino experiment data (right) (14). The dependence on the Higgs mass is weak, since  $m_H$  enters only logarithmically in the electroweak fit, whereas  $m_t$  enters quadratically.

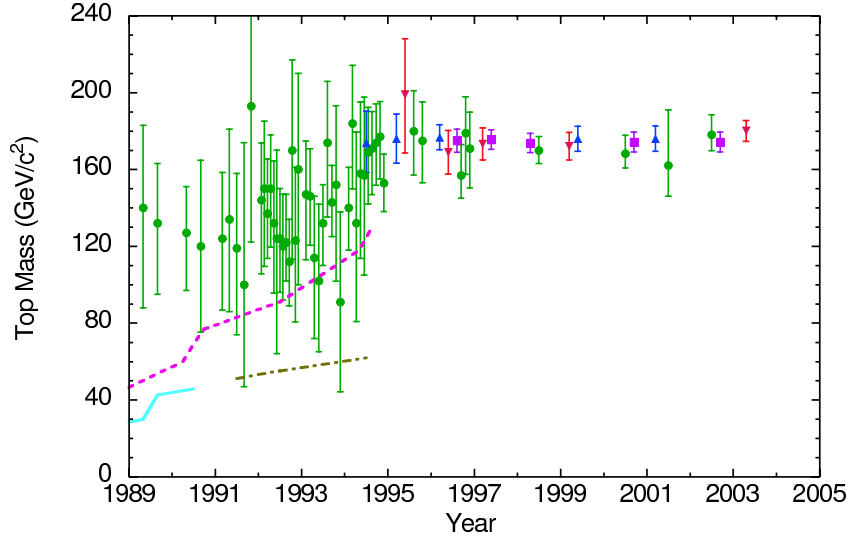


Figure 4. Evolution of the top quark mass prediction and measurement with time (69).

The most recent indirect measurement of the top quark mass using the  $Z$ -pole data together with the direct measurements of the  $W$  mass and total width yields (15)

$$m_t = 173_{-10}^{+13} \text{ GeV}, \quad (2.7)$$

which is in very good agreement with the direct measurement (17):

$$m_t = 172.7 \pm 2.9 \text{ GeV}. \quad (2.8)$$

The successful prediction of the mass of the top quark before its discovery gives confidence to the prediction on the Higgs boson mass from the electroweak global fit to all data, including

the direct measurement of  $m_t$ . Figure 5 (left) shows the result of this fit for the Higgs mass. The most likely value of the Higgs mass, corresponding to the minimum of the curve in Figure 5 (left), is at 114 GeV, with an experimental uncertainty of +69 and -45 GeV (27).

Another representation of the electroweak global fit is given by Figure 5 (right) (27). It shows the direct and indirect measurement of  $m_t$  and  $m_W$ . Also shown are the SM predictions for Higgs masses between 114 and 1000 GeV. As can be seen in the figure, the direct and indirect measurements are in good agreement and prefer a low value for the Higgs mass.

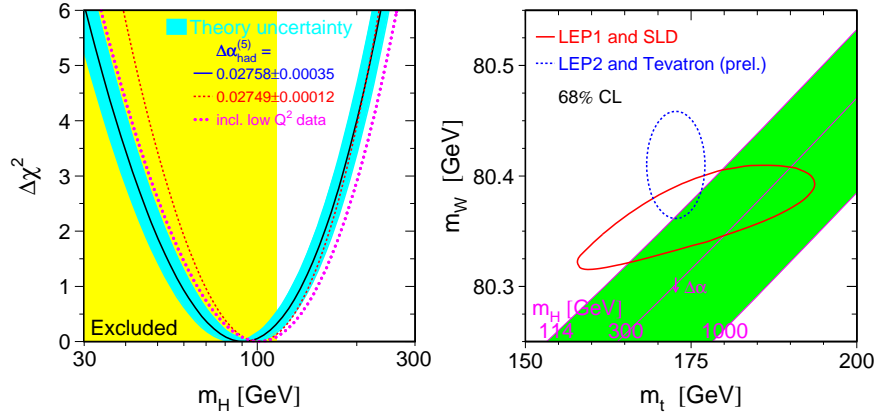


Figure 5. Left: Indirect measurement of the Higgs boson mass from all electroweak data together with the 95% confidence level lower limit on the Higgs mass of 114.4 GeV (25). Right: Contour curves of 68% confidence level in the  $(m_t, m_W)$  plane, for the corresponding indirect (LEP1, SLD data) and direct (LEP2,  $p\bar{p}$  data) determination in a global fit to electroweak precision data (25). Also shown is the correlation between  $m_t$  and  $m_W$  as expected in the SM for different Higgs boson masses.

### 2.2.3 Top Quark Pair Production via the Strong Interaction

The  $t\bar{t}$  production in high energy interactions as in a  $p\bar{p}$  collision is described by Quantum Chromodynamics. In this theory, a hard scattering process between a proton and an antiproton is the result of an interaction between the constituents of the incoming hadrons (quarks and gluons). These hadrons provide broad band beams of partons which possess varying fractions  $x$  of the momenta of their parent hadrons. An illustration of such a  $p\bar{p}$  collision is shown in Figure 6.

#### Factorization of the Cross Section

The  $p\bar{p}$  interaction can be separated into a short distance (hard scattering) cross section of partons of type  $i$  and  $j$ ,  $\hat{\sigma}^{ij}$ , and into long distance pieces which are factored into the parton momentum distribution functions  $f_i(x_i, \mu_F^2)$  (Figure 6). This is called factorization and is set by the factorization scale  $\mu_F^2$  which decides at what scale the separation is made. The remaining short distance cross section involves only high momentum transfer and is calculable in perturbation theory. It is insensitive to the physics of low momentum scale, in particular it does not depend on the hadron wave functions or the type of the incoming hadrons. This factorization property of the cross section can be proven to all orders in perturbation theory (28). The more terms included in the perturbative expansion, the weaker the dependence on this arbitrary scale  $\mu_F^2$ .

The parton distribution function (PDF)  $f_i(x_i, \mu_F^2)$  is the probability density that the parton of flavor  $i$  is participating in the hard scattering interaction at a scale  $\mu_F^2$  with longitudinal momentum fraction  $x_i$  of the incoming hadron. Since the parton distribution functions can

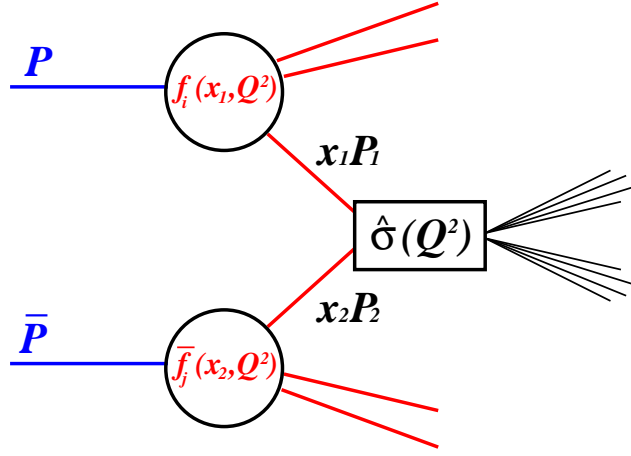


Figure 6. Parton model description of a hard scattering process.

presently not be calculated in perturbative QCD, they are being extracted in global QCD fits at next-to-leading order from data (29; 30). An example parameterization, obtained by the CTEQ collaboration (31), is shown in Figure 7.

### Renormalization and the Running Coupling Constant

A physical observable, such as the  $t\bar{t}$  cross section can be calculated in perturbation theory by including all the virtual loop diagrams. The calculation of this series of diagrams leads to infinities, called ultra-violet divergences. These divergences are removed by a renormalization procedure, which introduces the artificial scale  $\mu_R^2$ . However, it is clear that the physical quantities cannot depend on the arbitrary scale  $\mu_R^2$  and this independence is expressed in terms of a Renormalization Group Equation (32; 4). It can be shown (37; 4) that the solution of

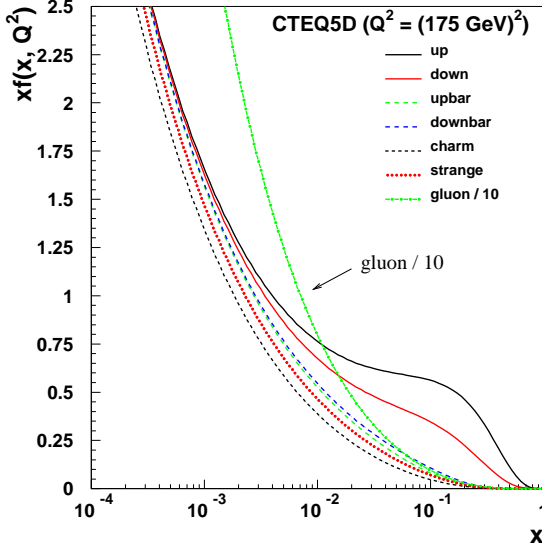


Figure 7. The quark, anti-quark, and gluon momentum densities in the proton as a function of the longitudinal momentum fractions  $x$  at  $Q^2 = m_t^2$  from CTEQ5D (31).

the Renormalization Group Equation implies the running of the coupling constant  $\alpha_s(Q^2)$ .

Neglecting higher orders

$$\alpha_s(Q^2) = \frac{\alpha_s(\mu_R^2)}{1 + \alpha_s(\mu_R^2)b \ln \frac{Q^2}{\mu_R^2}}, \quad (2.9)$$

with  $b = (33 - 2n_f)/12\pi$ , and  $n_f$  the number of active flavors. If  $Q^2/\mu_R^2$  becomes very large, the running coupling  $\alpha_s(Q^2)$  decreases to zero, which is known as asymptotic freedom. A summary of  $\alpha_s$  measurements at various scales is shown in Figure 8. It is common to choose the same scale  $\mu$  both for the factorization and the renormalization scale ( $\mu_F^2 = \mu_R^2 \equiv \mu^2$ ). This convention will be used in the following section.

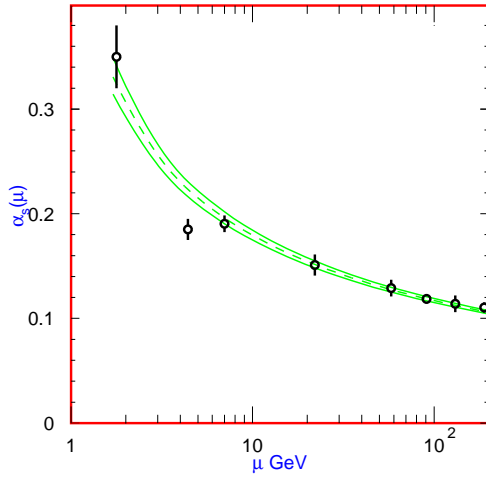


Figure 8. Summary of the values of  $\alpha_s$  at various scales  $\mu$  and a fit with the  $\pm 1\sigma$  limits (79). The data shown in order of increasing  $\mu$  correspond to measurements of  $\tau$  width,  $\Upsilon$  decays, deep inelastic scattering,  $e^+e^-$  event shapes at 22 GeV from JADE, shapes at TRISTAN at 58 GeV,  $Z$  width, and  $e^+e^-$  event shapes at 135 and 189 GeV.

### The $t\bar{t}$ Production Cross Section

The total top quark pair production cross section for a hard scattering process initiated by a  $p\bar{p}$  collision at the center of mass energy  $\sqrt{s}$  can be expressed as

$$\sigma^{p\bar{p} \rightarrow t\bar{t} + X}(s, m_t) = \quad (2.10)$$

$$\sum_{i,j=q,\bar{q},g} \int dx_i dx_j f_i(x_i, \mu^2) \bar{f}_j(x_j, \mu^2) \hat{\sigma}^{ij \rightarrow t\bar{t}}(\rho, m_t^2, \alpha_s(\mu^2), \mu^2).$$

$f_i(x_i, \mu^2)$  and  $\overline{f}_j(x_j, \mu^2)$  are the PDF's for the proton and the antiproton, respectively. The summation indices  $i$  and  $j$  run over all  $q\bar{q}$  and gluon pairs.  $\rho = \frac{4m_t^2}{\hat{s}}$  and  $\hat{s} = x_i \cdot x_j \cdot s$ ,  $\hat{s}$  being the effective center of mass energy squared for the partonic process.

The total short distance cross section can be written as

$$\hat{\sigma}^{ij}(\rho, m_t^2, \alpha_s(\mu^2), \mu^2) \equiv \frac{\alpha_s^2(\mu^2)}{m_t^2} f_{ij}(\rho, \alpha_s(\mu^2), \mu^2/m_t^2). \quad (2.11)$$

The dimensionless functions  $f_{ij}$  are perturbatively computable and have the following expansion in  $\alpha_s$ :

$$\begin{aligned} f_{ij}(\rho, \alpha_s(\mu^2), \mu^2/m_t^2) &= f_{ij}^{(0)}(\rho) + 4\pi\alpha_s(\mu^2) \left[ f_{ij}^{(1)}(\rho) + \overline{f}_{ij}^{(1)}(\rho) \ln \frac{\mu^2}{m_t^2} \right] \\ &\quad + \sum_{n=2}^{\infty} \alpha_s^n(\mu^2) f_{ij}^{(n)}(\rho, \mu^2/m_t^2). \end{aligned} \quad (2.12)$$

The Feynman diagrams of the leading order (LO) subprocesses are shown in Figure 9. The corresponding LO terms  $f_{ij}^{(0)}$  are explicitly given by

$$\begin{aligned} f_{q\bar{q}}^{(0)}(\rho) &= \frac{1}{27}\pi\beta\rho [2 + \rho] \\ &\stackrel{\rho \rightarrow 1}{\simeq} \frac{1}{9}\pi\beta \rightarrow 0, \end{aligned} \quad (2.13)$$

$$\begin{aligned} f_{gg}(\rho) &= \frac{1}{12}\pi\rho \left[ \left(1 + \rho + \frac{\rho^2}{16}\right) \ln \frac{1+\beta}{1-\beta} - \beta \left(\frac{7}{4} + \frac{31}{16}\rho\right) \right] \\ &\stackrel{\rho \rightarrow 1}{\simeq} \frac{7}{192}\pi\beta \rightarrow 0, \end{aligned} \quad (2.14)$$

$$f_{g\bar{q}}^{(0)}(\rho) = f_{g\bar{q}}^{(0)}(\rho) = 0, \quad (2.15)$$

where  $\beta = \sqrt{1 - \rho}$  is the velocity of the top quarks in the  $t\bar{t}$  center-of-mass frame. The limit

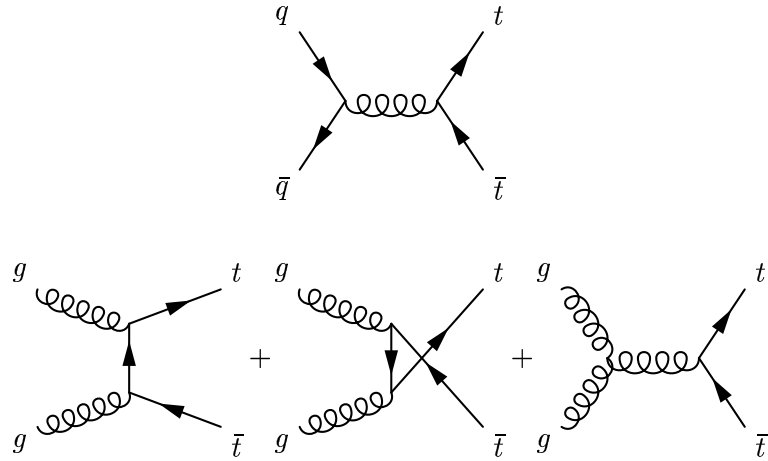


Figure 9. Lowest order Feynman diagrams for the production of  $t\bar{t}$  pairs at the Tevatron. At Tevatron energies, the diagram involving quark-antiquark annihilation dominates over those involving gluon-gluon fusion.

for the  $t\bar{t}$  production near the threshold region is given by  $\hat{s} \rightarrow (2m_t)^2$ , where  $\rho = \frac{4m_t^2}{\hat{s}} \rightarrow 1$

and

$$\frac{f_{q\bar{q}}^{(0)}(\rho)}{f_{gg}(\rho)} \simeq 3. \quad (2.16)$$

Near threshold, and when the parton momenta are equal, one finds  $x_i = x_j = 2m_t/\sqrt{\hat{s}} \simeq 0.18$  for a top quark mass  $m_t = 175$  GeV and  $\sqrt{\hat{s}} = 1.96$  TeV. For these values of  $x$ , the  $q$  and  $\bar{q}$  momentum densities are much larger than the gluon momentum density (Figure 7) which

leads to further enhancement of the  $q\bar{q}$  partonic cross section over the  $gg$  one. As a result, at Tevatron energies, the  $q\bar{q} \rightarrow t\bar{t}$  process dominates, contributing 85% of the cross section. The  $gg \rightarrow t\bar{t}$  process contributes the remaining 15%.

The next-to-leading order (NLO) contributions  $f_{ij}^{(1)}(\rho)$  and  $\overline{f}_{ij}^{(1)}(\rho)$  can only be evaluated numerically (33; 34). While the LO functions  $f_{ij}^{(0)}(\rho)$  vanish for  $\rho \rightarrow 1$  because of phase-space suppression, the NLO functions do not. It can be shown (33; 34) that soft gluon emissions are responsible for the bulk of the NLO correction.

For the most recent calculations of the top quark pair production cross section, the parton-level cross sections include the full NLO matrix elements (33). The complete NLO calculation of the  $t\bar{t}$  cross section is improved with the resummation of leading (LL) (35) and next-to-leading (NLL) soft logarithms (36) appearing at all orders of perturbation theory. The later is equivalent to the incorporation of the dominant contributions originating from the emission of soft gluons.

In what follows, the cross sections are quoted for a top quark mass of 175 GeV. The considered sources of theoretical uncertainties on the  $t\bar{t}$  cross section are the  $\mu$  the scale, PDF, and the  $\alpha_s$  uncertainties. The scale uncertainty is purely theoretical and reflects the dependence on the choice of renormalization ( $\mu_R$ ) and factorization ( $\mu_F$ ) scales. The scale range is set to  $m_t/2 < \mu < 2m_t$ , with  $\mu_R = \mu_F \equiv \mu$ . The dependence of the  $t\bar{t}$  production cross section on the scale  $\mu$  is shown in Figure 10. It can be seen that the dependence decreases with increasing number of orders included in the calculation. The possibility of varying the values of renormal-

ization and factorization scale ( $0.5 < \mu_R/\mu_F < 2$ , with  $0.5 < \mu_{R,F}/m_t < 2$ ) was also considered and found to have a small impact.

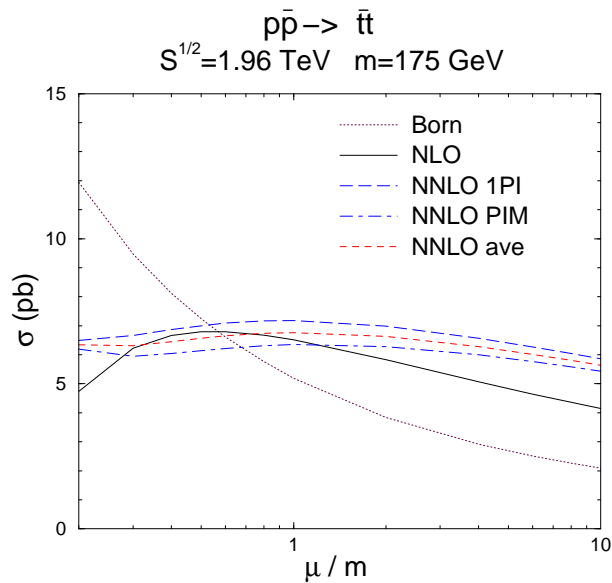


Figure 10. The scale dependence of the  $t\bar{t}$  cross section. The exact definition of the terms which are considered in the perturbative expansion referred to as “NNLO” can be found in (39).

The sets of PDF parameterizations considered are CTEQ6 (29) and MRST 2002 (38). The CTEQ6 and MRST collaborations provide sets of  $\sim 40$  PDF’s which are used to assign systematic uncertainties. Finally, the  $\pm 1\sigma$  uncertainty of  $\alpha_s(M_Z)$  is considered, where  $M_Z$  is the mass of the  $Z$  boson.

The top quark mass dependence of the  $t\bar{t}$  cross section is shown in Figure 11. For the constant center of mass energy of 1.96 TeV, the cross section drops with increasing top quark mass due to the reduced phase space available for the partonic short distance cross section, the lower probability to find a parton with larger  $x \simeq 2m_t/\sqrt{s}$  from the incoming hadron, and the running of  $\alpha_s(Q^2)$ , where  $Q^2 \simeq m_t^2$ .

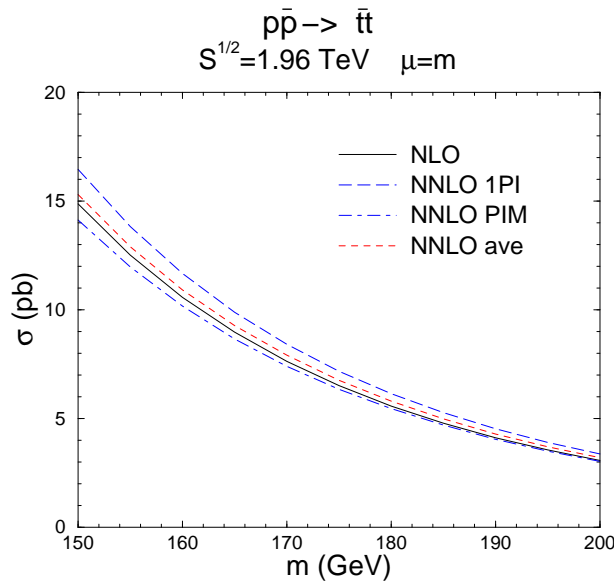


Figure 11. The top quark mass dependence of the  $t\bar{t}$  cross section. The exact definition of the terms which are considered in the perturbative expansion referred to as “NNLO” can be found in (39).

The center of mass energy dependence of the  $t\bar{t}$  cross section is shown in Figure 12. Here the cross section rises with increasing center of mass energy due to the increased phase space

available, and the higher probability to find a parton with larger  $x \simeq 2m_t/\sqrt{s}$  from the incoming hadron. In particular, the contributing fractions from the gluon fusion and the  $q\bar{q}$  partonic subprocesses change as a result of the different PDF's shown in Figure 7. Table II shows the relative contributions to the total  $t\bar{t}$  cross section both for the Tevatron in Run I, Run II and the LHC.

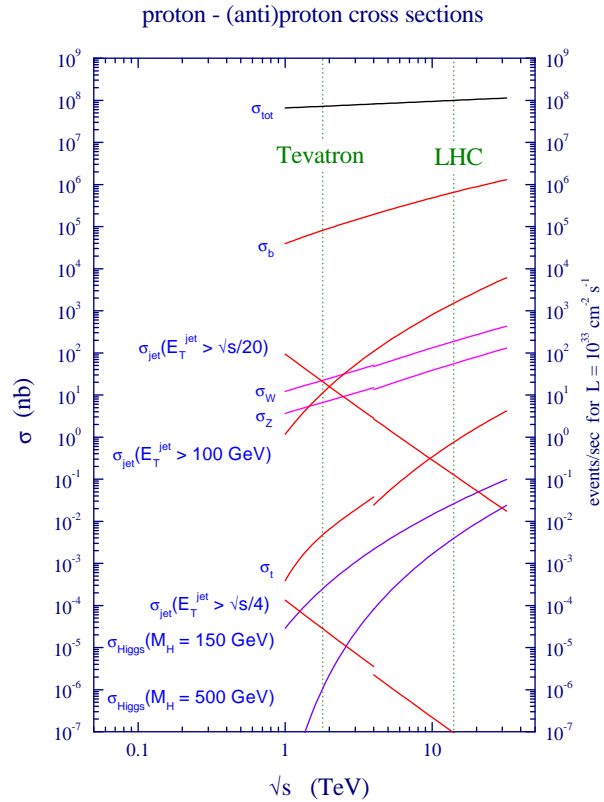


Figure 12. QCD predictions for hard scattering cross sections at the Tevatron and the LHC (42).

	$q\bar{q} \rightarrow t\bar{t}$	$gg \rightarrow t\bar{t}$
Tevatron Run I ( $\sqrt{s} = 1.8$ TeV, $p\bar{p}$ )	90 %	10 %
Tevatron Run II ( $\sqrt{s} = 1.96$ TeV, $p\bar{p}$ )	85 %	15 %
LHC ( $\sqrt{s} = 14.0$ TeV, $pp$ )	10 %	90 %

TABLE II

RELATIVE CONTRIBUTIONS TO THE LEADING ORDER  $t\bar{t}$  CROSS SECTION FOR THE TEVATRON RUN I AND RUN II AND THE LHC. THE HIGHER THE CENTER-OF-MASS, THE HIGHER THE CONTRIBUTION FROM THE GLUON FUSION PROCESS. THIS IS DUE TO THE INCREASED GLUON PROBABILITY DENSITY AT LOWER VALUES OF ACCESSIBLE  $X$ .

Deviations of the measured cross section from the theoretical prediction could indicate effects beyond QCD perturbation theory. Explanations might include substantial non-perturbative effects, new production mechanisms or additional top quark decay modes beyond the SM.

#### 2.2.4 Production of the Top Quark via the Weak Interaction

At present, only the top quark pair production has been observed experimentally. Nevertheless, the SM predicts that top quarks can also be produced singly by electroweak interactions. In this case, a virtual  $W$  boson interacts with a bottom quark producing a top quark in the final state as shown in Figure 13.

Despite its name, the electroweak single top production is of similar strength as the strong  $t\bar{t}$  production, the reason being that the production of a real  $W$  boson is allowed, and there is no CKM mixing suppression since  $V_{tb} \approx 1$ . However, the single top production is experimentally

more challenging, since its topology is closer to the background's and the level of background is higher for the lower jet multiplicity final states.

The s-channel process (left diagram in Figure 13) has the least theoretical uncertainties. This process is very similar to the direct production of an on-shell  $W$  boson. However, to decay into a top quark and a bottom quark, the  $W$  boson has to be off-shell. The large virtuality of the  $W$  boson heavily reduces the cross section. It is predicted to be  $0.88 \pm 0.07$  pb (41) at the Tevatron. In the  $W$ -gluon fusion t-channel process, a gluon splits into a  $b\bar{b}$  pair. The bottom quark interacts with a virtual  $W$  boson emitted from a quark from the other hadron and turns into a top quark. This process has larger theoretical uncertainties from the gluon PDF, but a larger cross section. Its predicted value is  $1.98 \pm 0.21$  pb (41). In Run I, an upper limit on the electroweak top quark production has been set by the CDF and DØ experiments (43; 44), first Run II limits exist (45; 46) with improved sensitivity compared to Run I.

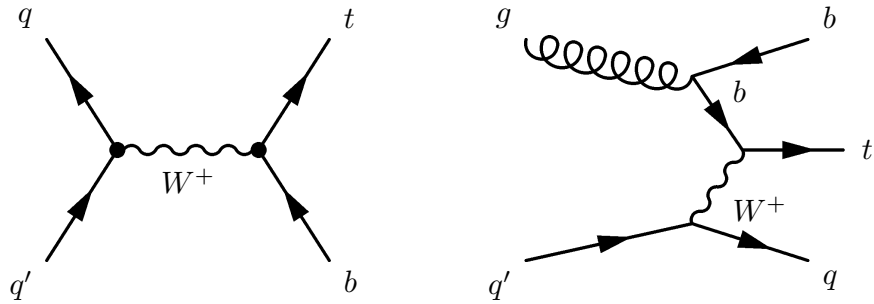


Figure 13. Single top quark production via the weak interaction. The main contributions at the Tevatron arise from the s-channel process (left) and the t-channel (right).

### 2.2.5 Decay of the Top Quark

The top quark decays via weak interaction, according to the electroweak vertex  $\frac{-ig}{2\sqrt{2}} \bar{t} \gamma^\mu (1 - \gamma^5) V_{tb} b W_\mu$ . The SM predicts a branching fraction  $BR(t \rightarrow Wb) > 0.998$ , because  $|V_{tb}| \simeq 1$ . Neglecting the mass of the  $b$  quark and higher order terms, the total width of the top quark,  $\Gamma_t$ , can be expressed as

$$\begin{aligned} \Gamma_t &= \frac{G_F m_t^3}{8\pi\sqrt{2}} \left(1 - \frac{m_W^2}{m_t^2}\right)^2 \left(1 + 2\frac{m_W^2}{m_t^2}\right) \left[1 - \frac{2\alpha_s}{3\pi} \left(\frac{2\pi^2}{3} - \frac{5}{2}\right)\right] \\ &\simeq 1.50 \text{ GeV , (for } m_t = 175.0 \text{ GeV)} . \end{aligned} \quad (2.17)$$

Note that  $\Gamma_t$  increases with the top quark mass and is known with a precision better than 2%. The two-loop QCD corrections have also been calculated (47), thereby improving the overall theoretical accuracy to better than 1%.  $\Gamma_t$  corresponds to the very short lifetime of the top quark of about  $5 \times 10^{-25}$  s.

The next most likely top quark decay modes are the off-diagonal CKM decays  $t \rightarrow Ws$  and  $t \rightarrow Wd$ . A measurement of the ratio of branching fractions,  $R = BR(t \rightarrow Wb)/BR(t \rightarrow Wq)$  was performed in Run I (48) and preliminary results in Run II exist (49), both consistent with the SM expectation. Within the SM,  $R$  can be expressed in terms of CKM matrix elements

$$R = \frac{|V_{tb}|^2}{|V_{tb}|^2 + |V_{ts}|^2 + |V_{td}|^2} . \quad (2.18)$$

Assuming three generations of quarks and unitarity of the CKM matrix,  $R$  represents a measurement of  $|V_{tb}|$ . Once a single top signal has been established the magnitude of  $V_{tb}$  could also be extracted directly by measuring the cross section for single top quark production via the weak interaction, which is proportional to  $|V_{tb}|^2$ .

The SM also predicts very small rates for flavor changing neutral current (FCNC) decays of the top quark. Their observation would indicate the presence of *New Physics*. Limits on the top quark decay modes  $t \rightarrow q\gamma$  and  $t \rightarrow qZ$  were set in Run I (50); the decay  $t \rightarrow qg$  will be accessible at the LHC (19).

Searches for top quark decays into charged Higgs bosons  $t \rightarrow H^+ b$  in  $t\bar{t}$  production were performed in Run I (51), where the  $H^+$  preferably decays to either  $cs$  or  $\tau\nu$ , resulting in a final state different from the SM expectation. As a consequence, a significant contribution from  $t \rightarrow H^+ b$  would give rise to a visible SM cross sections lower than the expectation (assuming that non-SM contributions to  $t\bar{t}$  production are negligible).

For the present analysis, the top quark is considered to decay to a bottom quark and a  $W$  boson 100% of the time.

### **2.2.6 Signature of $t\bar{t}$ Events**

As discussed in Section 2.2.5, the top quark decays to a  $W$  boson and a  $b$  quark nearly 100% of the time. The  $W$  boson can decay to a charged lepton and a neutrino or to a  $q\bar{q}'$  pair. While all three lepton generations ( $e, \mu, \tau$ ) are allowed, the hadronic  $W$  decay modes are kinematically limited to the production of first and second generation  $q\bar{q}'$  pairs. At Born level all three leptonic  $W$  decay modes have the same probability, but each of the two hadronic

modes is three times more likely due to the color factor of three. Altogether, there are nine potential decay paths which have all the same probability of  $1/9$  at Born level. Due to higher order corrections this symmetry between the decay modes is slightly broken. A summary of the  $W$  decay modes is shown in Table III. The resulting final states for  $t\bar{t}$  events are shown in Figure 14.

decay mode	$BR$ at Born level	$BR$ (79)
$W^+ \rightarrow e^+ \nu_e$	$1/9$	$(10.68 \pm 0.12)\%$
$W^+ \rightarrow \mu^+ \nu_\mu$	$1/9$	$(10.68 \pm 0.12)\%$
$W^+ \rightarrow \tau^+ \nu_\tau$	$1/9$	$(10.68 \pm 0.12)\%$
$W^+ \rightarrow u\bar{d}, c\bar{s}$	$2 \cdot 3 \cdot 1/9 = 6/9$	$(67.96 \pm 0.35)\%$

TABLE III

LEADING ORDER AND BEST KNOWN BRANCHING FRACTIONS OF THE REAL  $W^+$  BOSON DECAY, ASSUMING LEPTON UNIVERSALITY. IDENTICAL FOR THE CHARGE CONJUGATES OF THE MODES ABOVE ( $W^-$ ).  
(79)

Three signatures can be distinguished arising from a  $t\bar{t}$  event: in the **dilepton** channel, both  $W$  bosons decay leptonically. The signature is two charged leptons, two neutrinos and two  $b$  quarks, i.e.  $l\nu l'\nu' + \geq 2$  jets; in the **lepton-plus-jets** channel, one  $W$  boson decays leptonically and one hadronically resulting in one charged lepton, one neutrino, a  $q\bar{q}'$  pair, and two  $b$  quarks,

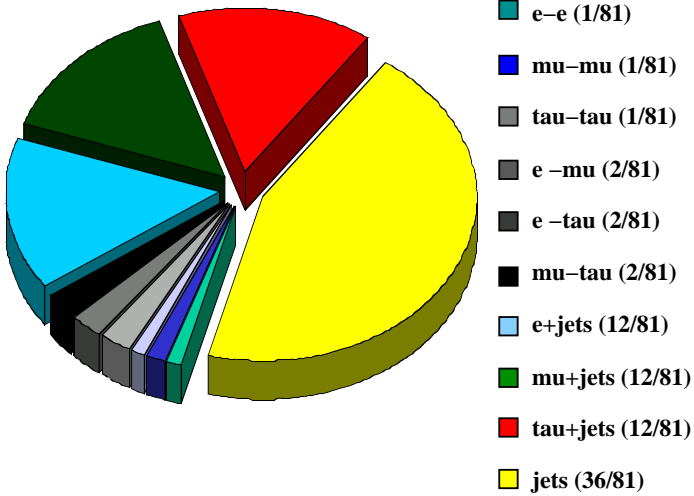


Figure 14. Pie chart of the  $t\bar{t}$  event decay channels at Born level.

i.e.  $l\nu+ \geq 4$  jets; finally, in the **all-jets** channel, both  $W$  bosons decay hadronically giving rise to two  $q\bar{q}'$  pairs and two  $b$  quarks, i.e.  $\geq 6$  jets.

Only the all-jets channel and the decay channels where the charged lepton is an electron or a muon have been analyzed so far (the identification of  $\tau$  leptons is difficult and work is in progress). However, a fraction of the  $\tau$  leptons decays leptonically to an electron or muon, and two neutrinos. These events have the same signature as the events where the  $W$  boson decays directly to an electron or a muon, and are treated as part of the signal in these channels. The leptonic  $\tau$  decay modes are summarized in Table IV. At present, the following decay channels are considered: three  $t\bar{t}$  decay channels of the dilepton category ( $ee$ ,  $\mu\mu$  and  $e\mu$ ), two of the lepton-plus-jets category ( $e+jets$  and  $\mu+jets$ ), and one all-jets category. They are summarized in Table V.

	decay mode	$BR$
$\tau^-$	$\rightarrow e^- \bar{\nu}_e \nu_\tau$	$(17.84 \pm 0.06)\%$
$\tau^-$	$\rightarrow \mu^- \bar{\nu}_\mu \nu_\tau$	$(17.36 \pm 0.06)\%$

TABLE IV

BRANCHING FRACTIONS OF THE REAL  $\tau^-$  LEPTON DECAY. IDENTICAL FOR THE CHARGE CONJUGATES OF THE MODES ABOVE ( $\tau^+$ ).  
(79)

channel	decay mode	$BR$ at Born level	$BR$ (79)
$ee$	$t\bar{t} \rightarrow e^+ \nu_e e^- \bar{\nu}_e b\bar{b}$	1/81	$(1.14 \pm 0.02)\%$
	$t\bar{t} \rightarrow e^+ \nu_e \mu^- \bar{\nu}_\mu b\bar{b}$	2/81	$(2.28 \pm 0.04)\%$
	$t\bar{t} \rightarrow \mu^+ \nu_\mu \mu^- \bar{\nu}_\mu b\bar{b}$	1/81	$(1.14 \pm 0.02)\%$
	$t\bar{t} \rightarrow e_{(\tau)}^+ e_{(\tau)}^- b\bar{b} + \nu' s$	-	$(1.58 \pm 0.03)\%$
	$t\bar{t} \rightarrow e_{(\tau)}^+ \mu_{(\tau)}^- b\bar{b} + \nu' s$	-	$(3.16 \pm 0.06)\%$
	$t\bar{t} \rightarrow \mu_{(\tau)}^+ \mu_{(\tau)}^- b\bar{b} + \nu' s$	-	$(1.57 \pm 0.03)\%$
$e+\text{jets}$	$t\bar{t} \rightarrow e^+ \nu_e q\bar{q}' b\bar{b}$	12/81	$(14.52 \pm 0.09)\%$
	$t\bar{t} \rightarrow \mu^+ \nu_\mu q\bar{q}' b\bar{b}$	12/81	$(14.52 \pm 0.09)\%$
	$t\bar{t} \rightarrow e_{(\tau)}^+ q\bar{q}' b\bar{b} + \nu' s$	-	$(17.11 \pm 0.11)\%$
	$t\bar{t} \rightarrow \mu_{(\tau)}^+ q\bar{q}' b\bar{b} + \nu' s$	-	$(17.04 \pm 0.11)\%$
all-jets	$t\bar{t} \rightarrow q\bar{q}' q\bar{q}' b\bar{b}$	36/81	$(46.19 \pm 0.46)\%$
	$t\bar{t} \rightarrow \tau$ final states	17/81	$(20.21 \pm 0.13)\%$

TABLE V

$t\bar{t}$  DECAY CHANNELS, BORN LEVEL AND BEST KNOWN BRANCHING FRACTIONS. THE CHARGE CONJUGATED FINAL STATES ARE IMPLIED.  $\ell_{(\tau)}$ , WITH  $\ell = (e, \mu)$ , INCLUDE BOTH THE DECAY MODES  $W \rightarrow \ell\nu$  AND  $W \rightarrow \tau\nu \rightarrow \ell + \nu\nu\nu$ . THE BRANCHING FRACTIONS CONSIDERED FOR THE DØ ANALYSES ARE DENOTED BY  $e e$ ,  $\mu\mu$  AND  $e \mu$ ,  $e + \text{JETS}$  AND  $\mu + \text{JETS}$ , AND ALL-JETS.  
(79) (52) (53)

### **2.3 The Physics of the Bottom Quark**

There are two  $b$  quarks in the final state of a  $t\bar{t}$  event which distinguishes the  $t\bar{t}$  final state from most of the background processes. As a consequence, identifying the bottom flavor of the corresponding jet can be used as a selection criteria. The hadronization of the bare  $b$  quark leads to  $b$  hadrons. In many aspects, these  $b$  hadrons are significantly different from most other particles as they have a long lifetime, large mass, high decay multiplicity, and substantial leptonic branching ratio, typically  $\sim 10\%$  per lepton. The most important property for the selection of  $b$  hadrons is their lifetime, which is around 1.6 ps ( $c\tau \sim 450\mu\text{m}$ ). This means that flight distances are of the order of 5 mm for a typical  $b$  hadron originating from a top quark decay.

The  $b$  quark contains most of the momentum of the  $b$  hadron. In the spectator model the decay of the  $b$  hadron is independent of the light quark in the hadron. This implies that the lifetime of all  $b$  hadrons should be the same, which is approximately the case (79). The  $b$  quark decays via the weak interaction into a  $c$  quark and a  $W$  boson of high virtuality, due to the large mass difference between the  $b$  quark and the  $W$  boson.

Hadrons composed of  $c$  quarks have a 2-3 times shorter lifetime. Due to the smaller mass difference between the  $c$  quark and the light quark in the hadron, a  $W$  boson can be exchanged allowing for additional decay modes which lead to a shorter lifetime. In addition, the CKM matrix elements are larger than the allowed CKM matrix elements for the  $b$  quark (the top quark decay in the latter is highly suppressed due to the limited phase space).

The top quark, however, is much heavier than the  $W$  boson and decays promptly due to the large phase space available. Light quarks dominantly hadronize into neutral and charged pions. The neutral pions decay through the electromagnetic interaction ( $\pi^0 \rightarrow \gamma\gamma$ ) in about  $10^{-16}$  seconds. This is not the case for the charged pions that decay through the weak interaction. This results in a very long lifetime of  $2.6 \times 10^{-8}$  seconds, which causes the charged pions to interact with the detector before they decay.

#### **2.4 Signature for $t\bar{t}$ Events in the Lepton + Jets Final State**

The signature of  $t\bar{t}$  events in the lepton-plus-jets final states can be described as:

- One charged lepton ( $e$  or  $\mu$ ) from a leptonic  $W$  boson decay with high transverse momentum.
- Missing transverse energy ( $\cancel{E}_T$ ) from the neutrino emission of the leptonic  $W$  boson decay.
- Two  $b$  jets, from the hadronization of the  $b$  quarks.
- Two non- $b$  jets ( $u, d, s, c$ ) from the hadronic  $W$  decay.
- Additional jets due to initial (ISR) and final state radiation (FSR).

A sketch of a  $t\bar{t}$  event with a muon in the final state is shown in Figure 15. Both the charged lepton and the neutrino are produced in the central region.

#### **2.5 Electroweak $W$ Boson Production in Association with Jets**

The main source of  $W$  bosons at a hadron collider like the Tevatron is the direct electroweak production through  $q\bar{q}'$  annihilation, as shown in the Feynman diagram in Figure 16. Bosons produced in this Drell-Yan process have no transverse momentum and are almost fully polarized

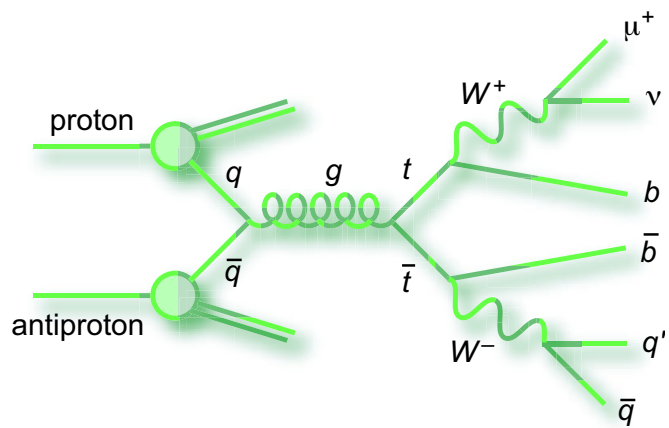


Figure 15. Sketch of the production and decay of a  $t\bar{t}$  pair in the  $\mu$ -plus-jets channel.

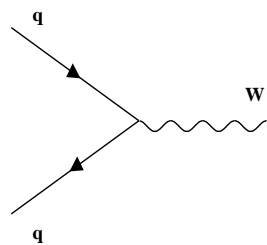


Figure 16. Feynman diagram for the  $W + 0$  parton process.

along the antiproton direction due to the  $V - A$  coupling (37). However, a gluon emitted from one of the initial quarks can give transverse momentum to the  $W$  boson and add a gluon to the final state. At order  $\alpha_s$ , an initial gluon can split into a quark-antiquark pair, one of these quarks interacts with an initial quark from the other hadron to produce the  $W$  boson together with a quark in the final state. The corresponding Feynman diagrams are depicted in Figure 17.  $W$  boson production with two partons in the final state is shown in Figure 18.

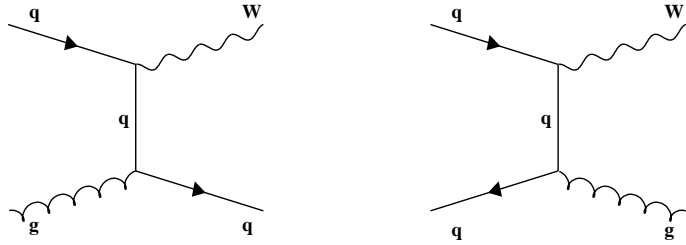


Figure 17. Some examples of Feynman diagrams for the  $W + 1$  parton process.

With each additional parton a vertex proportional to  $\sqrt{\alpha_s}$  is added. The lowest order matrix elements for the production of a  $W$  boson in association with up to four partons at hadron colliders have been computed (56) using various techniques to control the rapid growth of the number of contributing Feynman diagrams as the number of partons increases. The cross section is computed by Monte Carlo integration of the final state parton phase space.

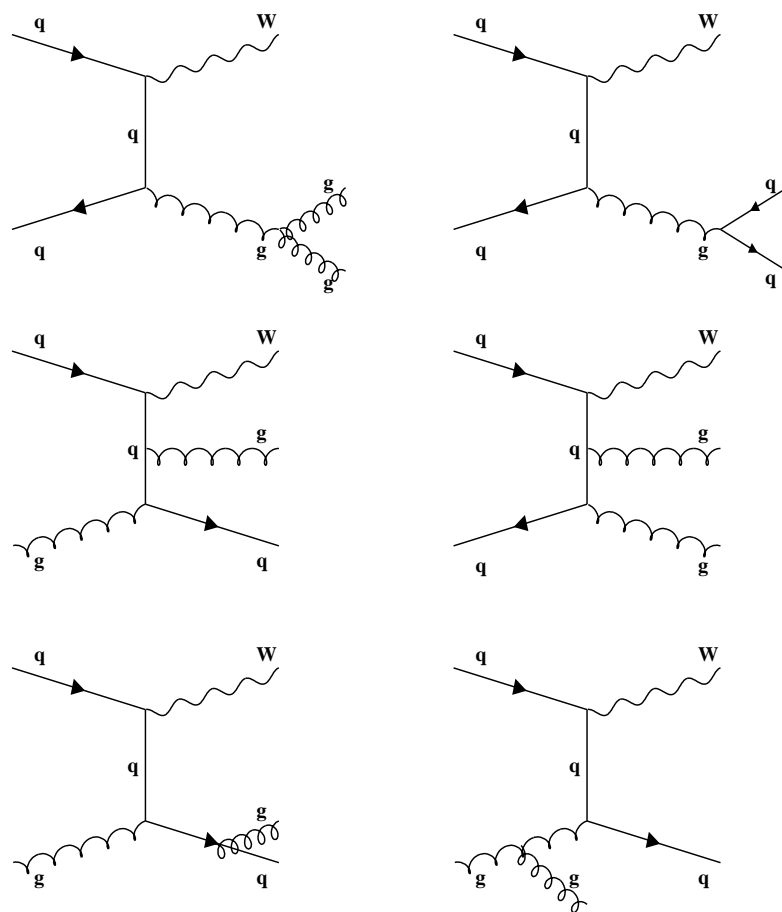


Figure 18. Some examples of Feynman diagrams for the  $W + 2$  partons process.

Two out of three valence quarks in the proton are up quarks and only one is a down quark, thus the  $u$  quark carries a larger momentum fraction than the  $d$  quark as shown in Figure 7. This results in a charge asymmetry for  $W$  bosons from direct production, i.e. the  $W^+$  ( $W^-$ ) boson are more likely boosted in the proton (antiproton) direction.  $W$  bosons produced in the top decay do not show this asymmetry and are produced centrally. The  $W$  bosons from the top quark decay have, on average, a larger transverse momentum than the  $W$  bosons produced via the weak interaction, due to the large top quark mass. These properties are transferred to the leptons from the  $W$  boson decay which have a larger transverse momentum and are produced at lower  $|\eta|$  in  $t\bar{t}$  events. The jets produced in association with the electroweak  $W$  boson originate mainly from QCD bremsstrahlung. The corresponding cross section is infrared and collinear divergent, resulting in jets with low transverse momenta and with large values of  $|\eta|$ .

The signature of the electroweak  $W$  boson production with a subsequent leptonic decay in association with four jets in the final state is similar to the lepton-plus-jets signature of the  $t\bar{t}$  decay, discussed in Section. 2.4. It is found to be the dominant background to the  $t\bar{t}$  process in the lepton-plus-jets channel.

## **2.6 QCD Multijet Production**

One of the largest cross sections at the Tevatron corresponds to the QCD multijet production through the strong interaction. The production mechanisms for additional jets are the same as in the  $W$ -plus-jets production, through QCD bremsstrahlung, i.e. gluon emission and gluon to  $q\bar{q}$  splitting. The cross section for QCD-multijets production decreases with each additional jet due to  $\alpha_s < 1$ .

Electromagnetically fluctuating jets can fake electrons in the detector.  $c$  and  $b$  quarks have a substantial branching ratio to decay modes which involve both a charged lepton and a neutrino in the final state. The muon originating from this semi-leptonic heavy quark decay can appear to be isolated if the remaining part of the jet is too soft to be reconstructed. The neutrino from the heavy quark decay, the misreconstruction of the jet and the mismeasurement of the muon momentum lead to  $\cancel{E}_T$  in the detector. These effects can lead to the same signature as the signal  $t\bar{t}$  events, making QCD multijet production the second most important background to the  $t\bar{t}$  process in the lepton-plus-jets channel.

## **2.7 Additional Background Processes**

Other small contributions to the background of the  $t\bar{t}$  process with lepton-plus-jets final states are discussed in the following sections.

### **2.7.1 Single Top Production**

Single top quark production via the weak interaction is discussed in Section 2.2.4. For a leptonic decay of the  $W$  boson originating from the top quark decay, the experimental signature is one charged lepton,  $\cancel{E}_T$  from the neutrino, and two  $b$  jets. For the t-channel, there is an additional light jet. Initial and final state radiation can produce even more jets, which leads to the same detector signature as the lepton-plus-jets final state of the  $t\bar{t}$  decay.

### 2.7.2 Vector Boson Pair Production

At leading order, pair production of  $W$  bosons occurs primarily through interactions represented by diagrams in Figure 19. The cross section is measured in Run II (55) to be

$$\sigma_{p\bar{p} \rightarrow W^+ W^- + X} = 13.8^{+4.3}_{-3.8} (\text{stat.})^{+1.2}_{-0.9} (\text{syst.}) \pm 0.9 (\text{lumi.}) \text{ pb},$$

in good agreement with the next-to-leading order calculation (54) given in Table VI. The cross sections for the production of  $Z$  boson pairs, and for the production of a  $W$  boson in association with a  $Z$  boson are also calculated at next-to-leading order and given in Table VI. Decay modes where one of the two bosons decays leptonically and one hadronically can lead to similar final state signatures as the one of the signal  $t\bar{t}$  process.

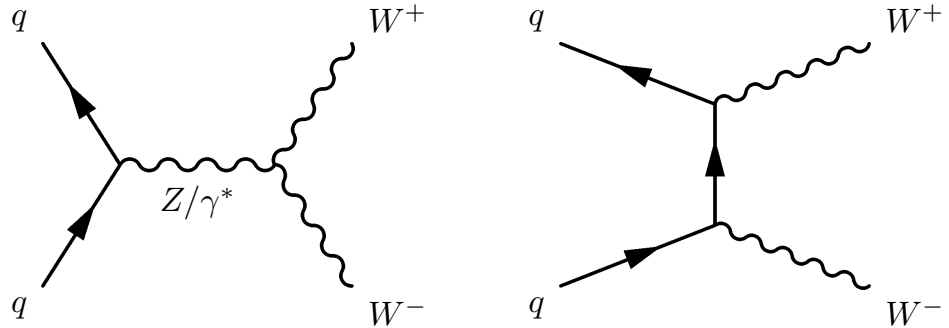


Figure 19. Feynman diagrams which represent leading order  $W$  boson pair production processes.

$W^+W^-$	$ZW^+$ or $ZW^-$	$ZZ$
13.0-13.5 pb	1.95-2.01 pb	1.56-1.60 pb

TABLE VI

TOTAL NLO CROSS SECTION FOR THE GIVEN DI-BOSON PROCESSES FOR A  $p\bar{p}$  CENTER-OF-MASS ENERGY OF 2 TEV.  
(54)

### 2.7.3 $Z/\gamma^* \rightarrow \tau\tau$ Production in Association with Jets

$Z/\gamma^*$  production is described by the same Feynman diagrams as the electroweak  $W$  boson production (Figure 16-Figure 18), by replacing the  $W$  by a  $Z/\gamma^*$ . The  $Z$  production rate, where the  $Z$  boson decays into two  $\tau$ s, is roughly a factor of ten smaller than the corresponding  $W$  rate (72). In the case when one of the two charged leptons is not detected due to the limited acceptance, the detector signature of the  $Z/\gamma^*$  production in association with jets is the same as the lepton-plus-jets signature of the  $t\bar{t}$  decay.

### 2.8 Monte Carlo Simulation

The study of the signature of the signal and background processes, the optimization of the event selection, as well as the accurate measurement of selection and tagging efficiencies require the Monte Carlo simulation of the data events, including the hard scattering interaction, hadronization, detector response, and digitization.

The simulation of a  $p\bar{p}$  collision is factorized in a short distance hard scattering interaction, calculable in perturbative QCD, and the long range physics; the latter includes the parton

momentum distributions and the additional soft physics interaction, referred to as the *underlying event*. As discussed in Section 2.2.3, this separation introduces the artificial factorization scale  $Q^2$ . Additional effects can occur such as *multiple proton interactions* and *pile-up* in the detector.

Figure 20 shows a sketch of the  $p\bar{p}$  interactions. The full chain of the simulation is described next.

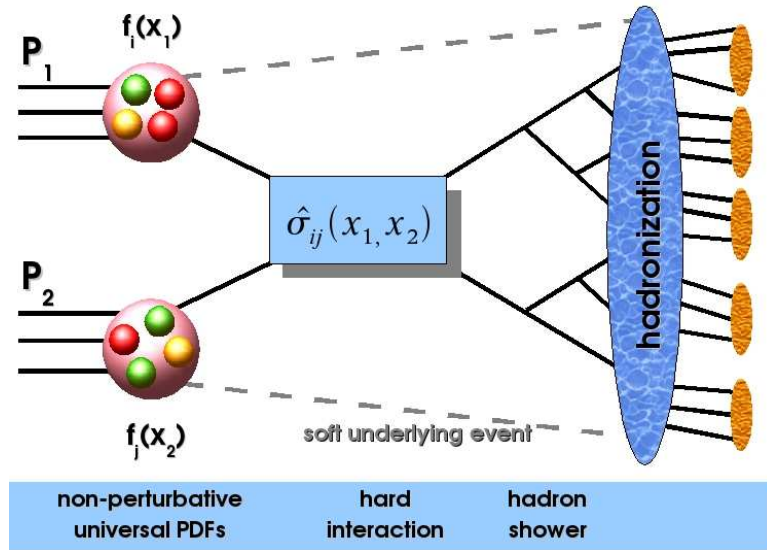


Figure 20. Sketch of a  $p\bar{p}$  interaction

The **hard scatter interaction** is described by calculating the leading order matrix element using ALPGEN (57). The set of parton distribution functions used is CTEQ 5L (31) and

CTEQ 6.1M (29). The latter was derived at NLO, which is in principle not adequate to use in association with a leading order matrix element. However, proper PDF uncertainties are at present only available for NLO PDFs, and because the change in the  $t\bar{t}$  cross section due to different PDFs is found to be small, CTEQ 6.1M is used for this analysis.

The **underlying event** consists of a hard and a soft component. The hard component describes the particles that arise from initial and final state radiation and from the outgoing hard scattered partons. The soft component consists of *beam-beam remnants* and *multiple parton interactions*. The **beam-beam remnant** describes the outgoing partons of the  $p\bar{p}$  interaction, which did not take part in the hard scattering process. The color connection between these spectator partons and the two partons from the hard scattering is the origin of this soft interaction and is hard to model. The **multiple parton interactions** describe the possibility that a hard scattering event also contains semi-hard interactions between the remaining partons from the identical  $p\bar{p}$  pair. Again, there is a color connection between the “semi-hard” and the hard scattering partons, and in addition a dependence on the  $p_T$  of the hard scattering partons. The *transverse* region, defined as the phase space around the plane orthogonal to the jet with highest  $p_T$  in the event, is sensitive to the underlying event. A data to Monte Carlo comparison of the average charged particle density and  $p_T$  distribution in the transverse region leads to a measurement of the underlying event and a tuning of its MC modeling, so-called “Tune A” (58). PYTHIA 6.202 (59), including multiple parton interactions, is used to model the underlying event.

**Multiple interactions** can occur when more than one  $p\bar{p}$  hard scatter takes place in the same bunch crossing. The multiple interactions are simulated by superimposing minimum bias data events to the generated MC event. Minimum bias events are defined as events which show a minimum activity in the detector, i.e. not being triggered by a high  $p_T$  lepton, jet or  $\cancel{E}_T$ . The number of added events is taken from a Poisson distribution with a mean between 0.5 and 0.8 events, depending on the instantaneous luminosity being simulated.

**Pile-up** describes overlapping  $p\bar{p}$  interactions from consecutive bunch crossings in the detector, which are reconstructed in the same event.

The resulting collection of partons is then hadronized into colorless mesons and baryons in a process called **hadronization**. Different approaches are used by the event generators. The model implemented in PYTHIA (59) splits gluons into  $q\bar{q}$  pairs and turns them into hadrons via the string fragmentation model. HERWIG (60) uses an approach where colorless clusters are formed from quarks and gluons with low invariant mass, which are turned into hadrons.

The Monte Carlo simulation also includes the **detector response**. The passage of the particles through the detector and the response of the different detector components is simulated using the software package *d0gstar*. The description of the detector material and geometry is handled by the GEANT3 program (61), that takes into account the present understanding of the detector and test beam results.

The next step is the simulation of the **digitization** of the detector response, performed by the software package *d0sim*. After this step, events from collider data and MC simulation are on the same level, called raw data, and can be treated identically.

For each event, the digitized information of nearly one million channels of detector response is processed by the **reconstruction** program  $D\bar{O}$  *reco*. The reconstruction defines higher level objects and their properties, from which the event kinematics can be inferred, as described in Section 4.

The **analysis tool** used to study reconstructed events is TopAnalyze (62), a software-package which processes the reconstructed events further and produces manageable ROOT (63) files. All software packages used are from versions of the p14  $D\bar{O}$  software release.

The Monte Carlo samples used for the analyses presented are discussed next.

### **2.8.1 $t\bar{t}$ Signal Simulation**

The production and decay of the  $t\bar{t}$  signal is simulated with the Monte Carlo settings and parton cuts prescribed by the “Common Alpgen-Pythia Study” (CAPS) group, using ALPGEN 1.3 (57). It includes the complete  $2 \rightarrow 6$  Born level matrix elements, followed by PYTHIA 6.2 (59) to simulate the underlying event, including “Tune A”, and the hadronization. This procedure takes advantage of the full spin correlation information for top quarks that is provided in ALPGEN 1.3. The top quark mass is set to 175 GeV. EVTGEN (65), known to successfully describe the spin correlations between the decay particles, is used to provide the various branching fractions and lifetimes for the following  $b$  quark states:  $B^0$ ,  $B^+$ ,  $B_s^0$ ,  $B_c^+$ , and  $\Lambda_b$ . The factorization scale for the calculation of the  $t\bar{t}$  process is set to  $Q = m_t$ .

MC samples are generated separately for the signatures dilepton, lepton-plus-jets, and all-jets, according to the decay of the  $W$  bosons. Leptons include  $e$ ,  $\mu$ , and  $\tau$ , with  $\tau$ s decaying

inclusively using TAUOLA (66). The main generation parameters are summarized in Table VII.

Generation Parameters	$t\bar{t}$	$W$ -plus-jets
PDF	CTEQ6.1M	CTEQ6.1M
$Q^2$	$m_t^2$	$(\frac{M_W}{2})^2$
Underlying event	Tune A	none
$p_T(\text{parton})$	none	$> 12 \text{ GeV}$
$ \eta(\text{parton}) $	none	$< 2.7$
$\Delta R(\text{parton}, \text{parton})$	none	$> 0.4$
$p_T(l)$	none	$> 12 \text{ GeV}$
$ \eta(l) $	none	$< 2.7$
$p_T(\nu)$	none	8 GeV
No. of min bias events	0.8	0.5

TABLE VII

MAIN GENERATION PARAMETERS FOR  $t\bar{t}$  AND  $W$ -PLUS-JETS.

### 2.8.2 $W$ -plus-jets Background Simulation

The  $W$ +jets background is simulated using ALPGEN 1.3 (57) followed by PYTHIA 6.2 (59) to simulate the underlying event and the hadronization. It includes the correct masses for  $c$  and  $b$  quarks. Each data sample ( $\mu$ -plus-jets and  $e$ -plus-jets) is subdivided into four disjoint event samples with 1, 2, 3 and  $\geq 4$  jets in the final state. Moreover, since the present analysis makes use of  $b$ -tagging, it is necessary to generate the following exclusive samples:

- $Wjjjj$ ,  $Wcjjj$ ,  $Wc\bar{c}Jj$  and  $Wb\bar{b}Jj$ ,

- $W_{jjj}, W_{cjj}, W_{c\bar{c}J}$  and  $W_{b\bar{b}J}$ ,
- $W_{jj}, W_{cj}, W_{c\bar{c}}$  and  $W_{b\bar{b}}$ ,
- $W_j$  and  $W_c$ ,

where  $j$  is either a  $u, d, s$ , or  $g$  parton, and  $J$  is either a  $u, d, s, c$ , or  $g$  parton ( $W_{c\bar{c}c\bar{c}}, W_{b\bar{b}c\bar{c}}$ , and  $W_{b\bar{b}b\bar{b}}$  processes are not included; their cross sections are negligible). The main generation parameters for these samples are summarized in Table VII. No parton-level cuts are applied on the heavy quarks ( $c$  or  $b$ ), except for the  $c$  quark in the single  $c$  quark production. The corresponding production cross sections for the  $W$ -plus-jets MC samples are summarized in Table VIII.  $W$  bosons are forced to decay to leptons, combining  $W \rightarrow e\nu$ ,  $W \rightarrow \mu\nu$ , and  $W \rightarrow \tau\nu$  decays;  $\tau$ s are forced to semileptonic decays using TAUOLA (66). The respective fraction of  $W \rightarrow \tau\nu$  is adjusted in the overall sample, to correctly reflect the contributions to the  $e$  and  $\mu$  channels.

process	$\sigma$ (pb)	process	$\sigma$ (pb)	process	$\sigma$ (pb)	process	$\sigma$ (pb)
$W_j$	1600	$W_{jj}$	517	$W_{jjj}$	163	$W_{jjjj}$	49.5
$W_c$	51.8	$W_{cj}$	28.6	$W_{cjj}$	19.4	$W_{cjjj}$	3.15
		$W_{b\bar{b}}$	9.85	$W_{b\bar{b}J}$	5.24	$W_{b\bar{b}Jj}$	2.86
		$W_{c\bar{c}}$	24.3	$W_{c\bar{c}J}$	12.5	$W_{c\bar{c}Jj}$	5.83

TABLE VIII

$W$ +JETS PROCESSES IN ALPGEN AND THEIR CROSS-SECTIONS FOR THE LEPTONIC  $W$  BOSON DECAY,  $\sigma \equiv \sigma_{P\bar{P} \rightarrow W+JETS} BR(W \rightarrow e\nu)$ , WHERE  $j = u, d, s, g$  AND  $J = u, d, s, g, c$ .

### 2.8.2.1 Jet-Parton Matching

The leading order parton level calculations performed by ALPGEN need to be consistently combined with the partonic evolution given by the shower MC program PYTHIA. The problem that occurs in this merging process can be denoted as *double counting* of configurations leading to the same final state. Since this analysis treats exclusive jet multiplicity bins as independent channels, the jet-parton matching procedure is a simplification of the matching schemes proposed and used for the combination of inclusive  $W/Z + n$  jet MC events (67; 68). The parton shower MC programs serve to model the higher order corrections to the leading order matrix element calculation at each order of  $\alpha_s$ . Two sources of double counting can be identified:

- The parton shower MC programs transform the leading order matrix element of  $W + (n - m)$  jets with exclusively  $(n - m)$  jets in the final state into a final state involving  $n$  jets by adding  $m$  jets due to initial and final state radiation. This implies a double counting of events with  $n$  reconstructed jets in the final state from all leading order matrix element calculations of  $W + (n - m)$  jets, where the parton evolution leads to the reconstruction of  $m$  additional jets, with  $0 \leq m \leq n$ . This is illustrated in Figure 21 for  $n = 3$  and  $m = 0, 1$ .
- The detector acceptance, response and the jet selection criteria lead also to the migration of  $W + (n + k)$  jet events to events with  $n$  reconstructed jets in the final state, where  $k \geq 0$ . In particular, the  $k$  jets can be too soft or too forward to be reconstructed or selected.

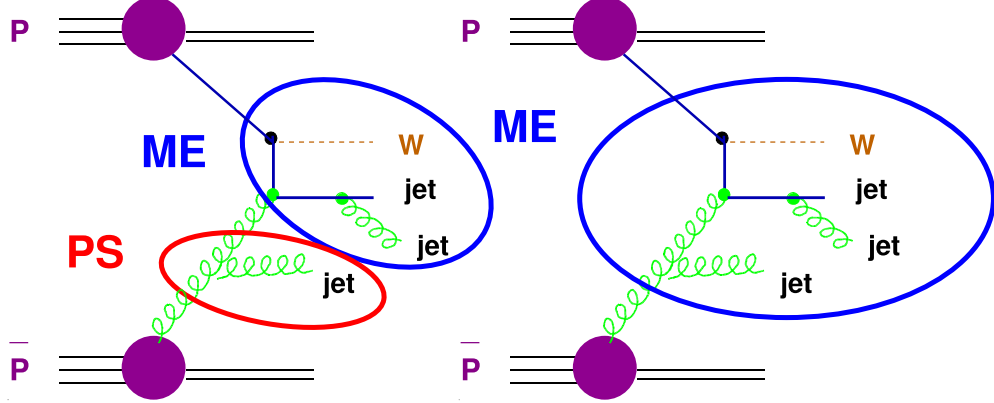


Figure 21. Left:  $W + 2$  jets process calculated by the matrix element (ME) and one additional jet generated by the parton shower (PS). Right:  $W + 3$  jets process calculated by the matrix element and no additional jet generated by the parton shower. Both processes lead to the same final state.

A matching of partons, produced by the matrix element calculation, and reconstructed jets is performed in order to eliminate the double counting. This matching procedure also reduces the sensitivity of the parton-level cross sections, predicted by ALPGEN, to the parton generation cuts. Two matching procedures have been developed. In the **CKKW matching**, the multijet matrix elements are merged with the shower development by reweighting the matrix elements weights with Sudakov form factors and vetoing shower emissions in regions of phase space already covered by the parton level configurations (67). The matching procedure is named after the initials of the authors (S. Catani, F. Krauss, R. Kuhn and B. R. Webber). On the other hand, in the **MLM matching**, matrix element partons are matched to parton jets (68), proposed and named after M. L. Mangano.

An approximation of the MLM matching is used in the present analysis. Since the parton jets are not available, the matching is performed between matrix element partons and reconstructed jets.

The  $W$ -plus-jets MC samples are classified according to the number of heavy flavor ( $c$  or  $b$ ) jets as follows:

- $W+$  light jets, events without  $c$  or  $b$  jets
- $Wc$ : events with one  $c$  jet due to single  $c$  production,
- $W(c\bar{c})$ : events with one  $c$  jet due to double  $c$  production where two  $c$  quarks are merged in one jet or one of the  $c$  jets is outside of the acceptance region,
- $Wc\bar{c}$ : events with two  $c$  jets,
- $W(b\bar{b})$ : events with one  $b$  jet due to double  $b$  production where two  $b$  quarks are merged in one jet or one of the  $b$  jets is outside of the acceptance region (single  $b$  production is highly suppressed and neglected),
- $Wb\bar{b}$ : events with two  $b$  jets.

The jet flavor in the MC is determined by a matching with the generated heavy flavor hadrons. A reconstructed jet is considered a  $b$  jet if it is matched to a  $b$  hadron,  $\Delta R(jet, hadron) < 0.5$ ; it is considered a  $c$  jet if it is matched to a  $c$  hadron,  $\Delta R(jet, hadron) < 0.5$ , and not to a  $b$  hadron; and it is a **light** jet if it is neither matched to a  $c$  nor to a  $b$  hadron.

### Approximated MLM Jet-Parton Matching

Events that do not satisfy the following conditions, are rejected from the MC samples:

- The number of reconstructed jets is required to be equal to the number of matrix element partons, where  $(c\bar{c})$  and  $(b\bar{b})$  are treated as one parton.
- Light jets and  $c$  jets from  $Wc$  events are required to be matched to matrix element partons, i.e.  $\Delta R(jet, parton) < 0.5$ .

As the fourth jet multiplicity bin is inclusive, all events with  $\geq 4$  reconstructed jets are considered independently of the number of additional non-matched light jets.

### **2.8.3 Additional Backgrounds**

The backgrounds originating from boson pair production are evaluated using samples generated with ALPGEN followed by PYTHIA with inclusive  $\tau$  decays. Since the cross sections provided by ALPGEN correspond to LO calculations, correction factors are applied in order to scale them up to the NLO cross sections (54).

Samples for single top were generated with CompHEP interfaced to PYTHIA.

The  $Z/\gamma^* \rightarrow \tau\tau$  sample was generated with PYTHIA containing inclusive  $\tau$  decays.

Table IX summarizes the generated processes with the corresponding cross sections and NLO correction factors where applicable. In the case of  $Z/\gamma^* \rightarrow \tau\tau$ , the NNLO cross section (64) corresponding to the mass range  $60 < M_Z < 130$  GeV is used. For single top processes, the cross sections shown are at NLO.

process	$\sigma$ (pb)	NLO correction	Branching ratio	
			$e$	$\mu$
$tb \rightarrow \ell\nu bb$	0.88	-	0.1259	0.1253
$tbq \rightarrow \ell\nu bbj$	1.98	-	0.1259	0.1253
$WW \rightarrow \ell\nu jj$	2.04	1.31	0.3928	0.3912
$WZ \rightarrow \ell\nu jj$	0.61	1.35	0.3928	0.3912
$WZ \rightarrow jj\ell\ell$	0.18	1.35	0.4417	0.4390
$ZZ \rightarrow jj\ell\ell$	0.16	1.28	0.4417	0.4390
$Z/\gamma^* \rightarrow \tau\tau; 60 < M_{\tau\tau} < 130 \text{ GeV}$	253	-	0.3250	0.3171

TABLE IX

CROSS SECTIONS FOR BACKGROUND PROCESSES AND THE CORRESPONDING NLO CORRECTION FACTORS (WHERE APPLICABLE) USED IN THE CURRENT ANALYSIS.

## 2.9 Measurement of the Luminosity

In a collider, the event rate  $R$  is proportional to the interaction cross section  $\sigma_{int}$ ; the factor of proportionality is called the instantaneous luminosity  $\mathcal{L}$

$$R = \mathcal{L} \cdot \sigma_{int}. \quad (2.19)$$

For a cross section measurement, as the one presented in this thesis, both the instantaneous luminosity and the interaction rate have to be measured. The instantaneous luminosity is determined by measuring the rate of a reference interaction with known cross section. The process of choice at the Tevatron is the inelastic  $p\bar{p}$  cross section, which is related to the total and the elastic cross section through

$$\sigma_{inelastic} \equiv \sigma_{total} - \sigma_{elastic}. \quad (2.20)$$

In contrast to  $e^+e^-$  or  $e\gamma$  colliders, where the reference cross section can be calculated with high precision, at hadron colliders both the total and the elastic cross section are measured separately to determine the inelastic cross section. The total cross section can be determined from event rates only, without knowing the luminosity, by using the optical theorem described below. The measurement of the inelastic event rate with the DØ luminosity system is discussed in Section 3.3.2.

### **2.9.1 The Total $p\bar{p}$ Cross Section and the Optical Theorem**

According to Equation 2.19 and Equation 2.20 the total cross section can be written as

$$\sigma_{total} = \frac{1}{\mathcal{L}}(R_{el} + R_{inel}). \quad (2.21)$$

On the other hand, the optical theorem relates the total cross section to the imaginary part of the forward elastic scattering amplitude

$$\sigma_{total} = \frac{4\pi}{k} ImF(\Theta)^{\Theta=0}, \quad (2.22)$$

where  $k$  is the momentum of the incoming hadron. Squaring of Equation 2.22 yields

$$\sigma_{total}^2 = \frac{16\pi^2}{k^2} \frac{ImF(0)^2}{ImF(0)^2 + ReF(0)^2} \cdot |F(0)|^2. \quad (2.23)$$

The scattered outgoing flux in the solid angle  $d\Omega$  is the product of the scattering cross section and the incident flux. For elastic scattering, incident and outgoing flux are the same and therefore

$$|F(\Theta)|^2 = \left( \frac{d\sigma}{d\Omega} \right)_{el}^\Theta. \quad (2.24)$$

For forward scattering,  $\Theta = 0$ . By introducing the Mandelstam variable  $t = -2k^2(1 - \cos \Theta)$  and using  $d\Omega = 2\pi d\cos \Theta = \frac{2\pi}{2k^2}dt$ , Equation 2.24 can be written as

$$|F(0)|^2 = \left( \frac{d\sigma}{d\Omega} \right)_{el}^{\Theta=0} = \frac{1}{\mathcal{L}} \frac{2k^2}{2\pi} \left( \frac{dR_{el}}{dt} \right)_{t=0}. \quad (2.25)$$

Using  $\rho = \frac{ReF(0)}{ImF(0)}$  as the ratio of the real to the imaginary part of the forward scattering amplitude, Equation 2.23 can be written as

$$\sigma_{total}^2 = \frac{16\pi}{1 + \rho^2} \frac{1}{\mathcal{L}} \left( \frac{dR_{el}}{dt} \right)_{t=0}, \quad (2.26)$$

and by dividing Equation 2.26 by Equation 2.21 the total cross section can be expressed as a function of measurable quantities

$$\sigma_{total} = \frac{16\pi}{1 + \rho^2} \frac{\left( \frac{dR_{el}}{dt} \right)_{t=0}}{R_{el} + R_{inel}}, \quad (2.27)$$

without knowing the instantaneous luminosity. Measurements of  $\rho$  are shown in Figure 22. Measured total cross sections as a function of the center of mass energy are shown in Figure 23

together with the elastic cross section, which can be determined experimentally. Both cross sections can be inserted in Equation 2.20 to obtain the inelastic  $p\bar{p}$  cross section, which was measured in Run I at  $\sqrt{s} = 1.8$  TeV by the E710, E811 and CDF collaborations. The average of the three measurements is scaled up to  $\sqrt{s} = 1.96$  TeV (70) and is found to be (83)

$$\sigma_{inel} = 60.7 \pm 2.4 \text{ mb}. \quad (2.28)$$

This value is then used via Equation 2.19 to measure the instantaneous luminosity.

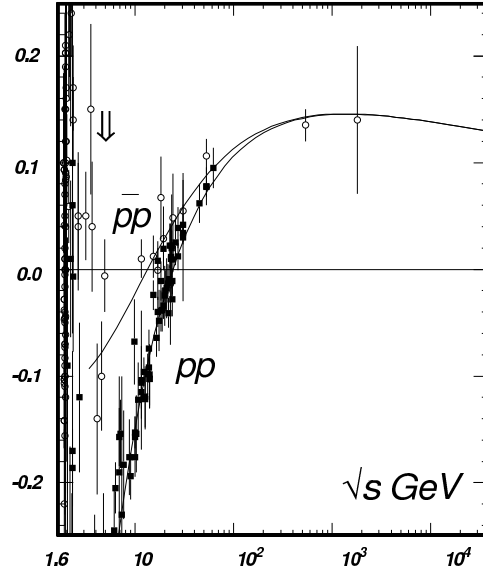


Figure 22. Ratio of the real to imaginary parts of the forward hadronic scattering amplitudes,  $\rho$ , as a function of  $\sqrt{s}$  (79).

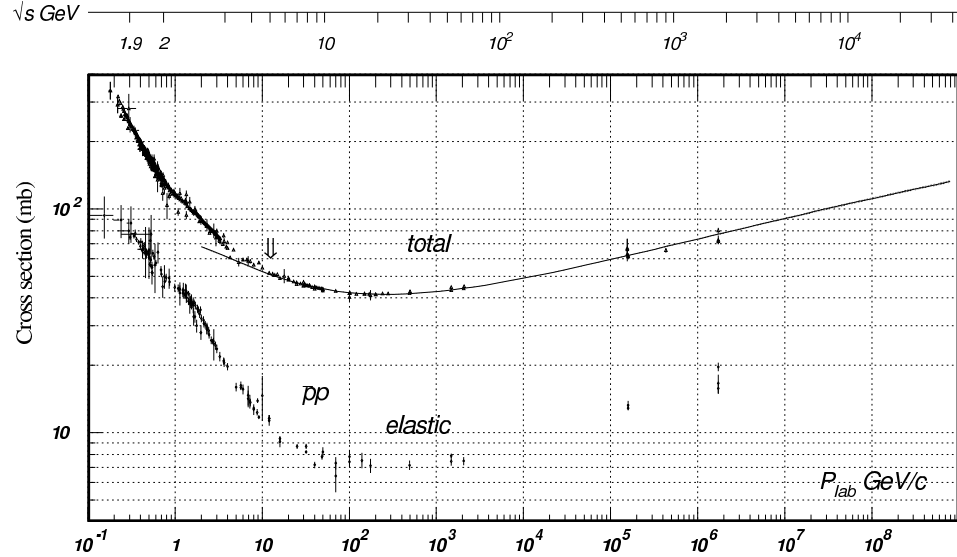


Figure 23. Total and elastic cross sections for  $p\bar{p}$  collision as a function of laboratory beam momentum and total center of mass energy (79).

For many precision measurements the uncertainty on the luminosity measurement will be the limiting factor at the end of Run II. The aim is to use simultaneous  $W$  boson and  $Z$  boson event counts (71) to determine the luminosity. The theoretical cross sections for these processes are very well known (72) and have been measured (73; 74), however, the cross sections are orders of magnitude smaller than the inelastic  $p\bar{p}$  cross section and thus the rates are lower.

## CHAPTER 3

### EXPERIMENTAL APPARATUS

The *Tevatron* is currently the highest energy proton-antiproton collider in the world. It operates at the Fermi Nacional Accelerator Laboratory (FNAL, or FERMILAB). In this chapter, the chain of accelerators needed to achieve a center of mass collision energy of 1.96 TeV is described. An overview of the DØ detector is also given.

#### 3.1 The Fermilab Accelerators

The Tevatron is the final stage in a sequence of seven accelerators (75; 76; 77). A Cockcroft-Walton *pre-accelerator*, a linear accelerator (*Linac*) and a synchrotron (*Booster*) provide a source of 8 GeV protons. The antiproton *Debuncher* and *Accumulator* are two components of the *Antiproton Source*. The *Main Injector* serves as the final boosting stage before injecting protons and antiprotons into the Tevatron. It also provides the necessary source of energetic protons which are needed in the Antiproton Source. Figure 24 gives an overview of the FERMILAB accelerator complex.

#### **The Pre-accelerator**

The purpose of the pre-accelerator is to produce negatively charged hydrogen ions ( $H^-$ ) with an energy of 750 keV, which are then transferred into the Linac. Hydrogen gas ( $H_2$ ) enters a magnetron surface-plasma source (Figure 25). Due to the electric field between the anode (negatively charged) and cathode (positively charged), the electrons are stripped away from

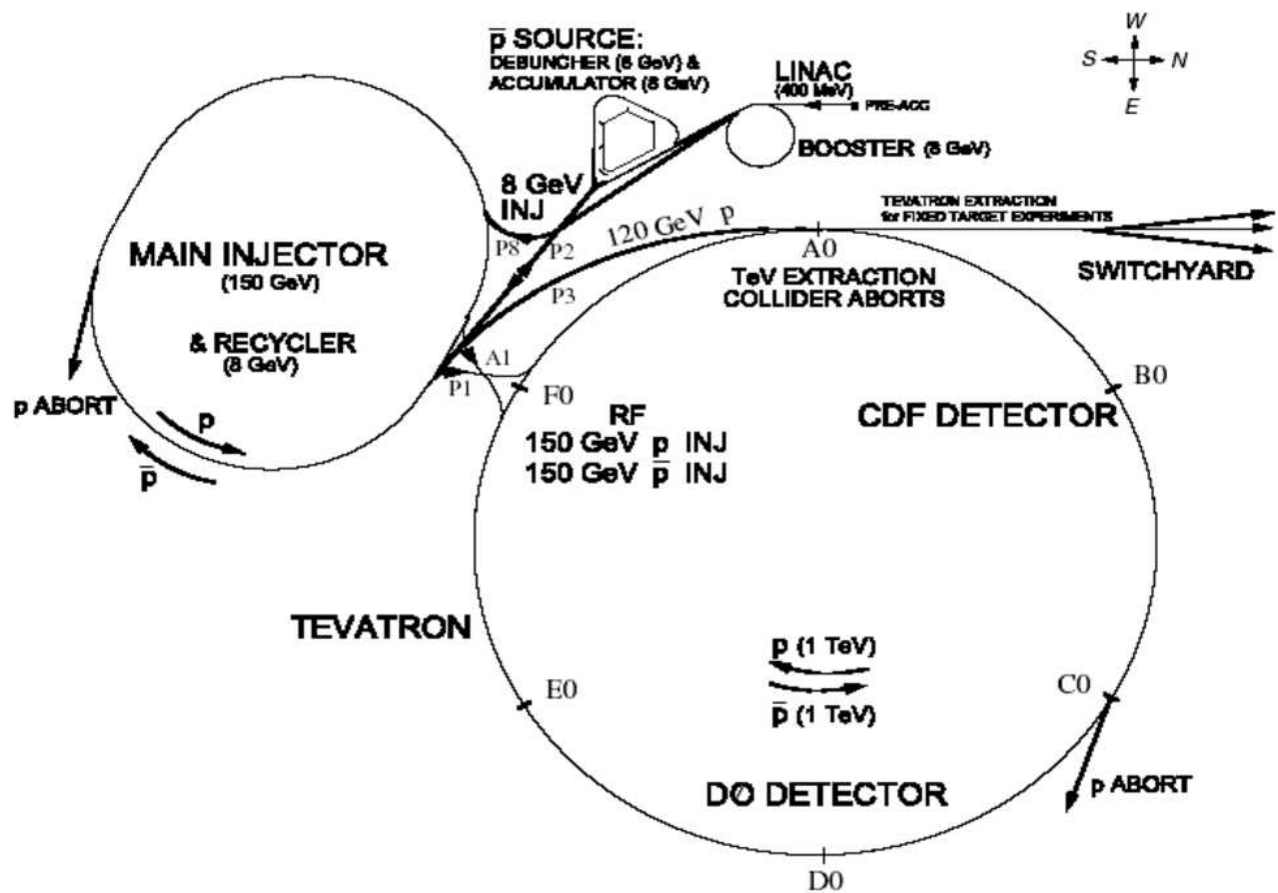


Figure 24. Schematic view of the FERMILAB accelerator chain.

the hydrogen atoms to create a plasma. The positively charged hydrogen ions then strike the surface of the cathode to collect extra electrons and thereby form negatively charged hydrogen ions. The  $H^-$  ions are extracted through the anode aperture with an electric field of 18 kV applied by the extractor plate (Figure 25).

A commercial Cockcroft-Walton Generator produces a 750 kV potential difference by charging capacitors in parallel from an AC voltage source and discharging them in series, via diodes. The Cockcroft-Walton Generator is used to further accelerate the  $H^-$  ions to an energy of 750 keV. After exiting the Cockcroft-Walton device, the  $H^-$  ions travel through a transfer line. Before entering the Linac the continuous stream of  $H^-$  ions passes through a single gap radio frequency (RF) cavity which bunches the beam at the RF frequency of the Linac (201.24 MHz).

## The Linac

The Linac receives bunches of 750 keV  $H^-$  ions from the pre-accelerator and accelerates them further to an energy of 400 MeV using RF cavities (Figure 26). The RF cavities are contained within a collection of steel tanks which hold a sequence of drift tubes separated from each other by gaps. In order to accelerate  $H^-$  ions, the cavities are designed in such a way that particles traveling in the gaps experience an acceleration, while particles traveling in the drift tubes are shielded from the RF. After passing through the Linac, bunches of 400 MeV  $H^-$  ions are transferred into the Booster.

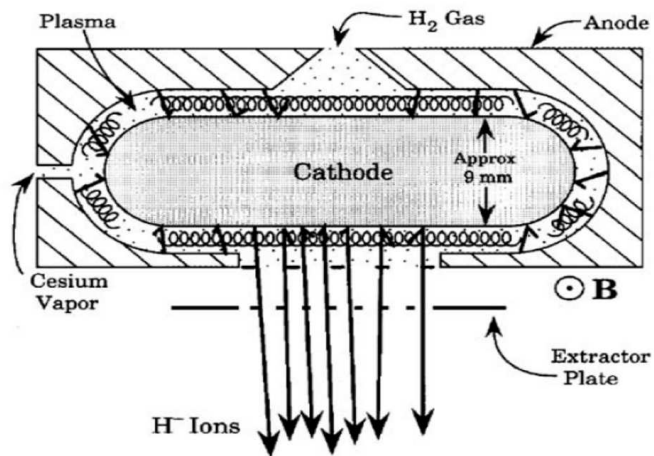


Figure 25. Schematic view of magnetron operation for the hydrogen ion source.

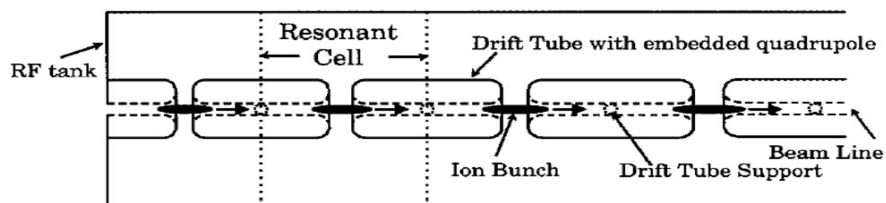


Figure 26. Schematic drawing of Linac RF cavity.

## The Booster

The Booster is the first synchrotron in the chain of accelerators. It consists of a sequence of dipole and quadrupole magnets and 17 RF cavities arranged in a circle with a diameter of 151 m, and accelerates protons to an energy of 8 GeV. Negatively charged  $H^-$  ions coming from the Linac are merged with protons ( $H^+$  ions) circulating in the Booster with the help of dipole magnets. The electrons are subsequently stripped from the  $H^-$  ions by letting the combined beam pass through a carbon foil.

Once the Booster is filled with proton bunches, the RF cavities provide an acceleration up to 8 GeV. At the same time, the field strength in the dipole magnets is adjusted accordingly in order to maintain a constant radius for the circulating particles. Once the protons have reached an energy of 8 GeV, they are transferred into the Main Injector.

## The Main Injector

The Main Injector is a circular synchrotron with a diameter of 1 km. It can accelerate both protons (coming from the Booster) and antiprotons (coming from the Antiproton Source) from 8 GeV to 150 GeV before injecting them into the Tevatron. It also delivers 120 GeV protons to the Antiproton Source.

## The Antiproton Source

The Antiproton Source consists of three major components: the *Target Station*, the *De-buncher*, and the *Accumulator*. In the first step, the Target Station receives 120 GeV protons from the Main Injector and diverts them onto a Nickel Target. This produces a shower of secondary particles (including antiprotons) at many different angles and with a large spread

in particle momentum. A Lithium lens and bending magnets are used to focus the beam and remove positively charged particles (Figure 27). A process called *stochastic cooling* is used in both the Debuncher and the Accumulator to reduce the spread in momentum and position of the antiprotons, thereby “cooling” them.

Both the Debuncher and Accumulator are located in a rounded-triangle shaped tunnel with a circumference of about 51 m. Antiprotons coming from the Target Station are transferred into the Debuncher where the momentum spread of the particles is reduced. It is technically very challenging to accumulate a large quantity of antiprotons. On average, for every 1 million protons that hit the Nickel target, only about 20 antiprotons can be gathered. Therefore the Accumulator stores antiprotons until a sufficient amount has been generated to be transferred into the Main Injector. The Accumulator must be capable of storing antiprotons over many hours.

### **The Tevatron**

The Tevatron is the final stage in the sequence of proton and antiproton acceleration. It has a diameter of 2 km and uses superconducting magnets which operate at liquid helium temperature providing magnetic fields of up to 4 Tesla. Protons and antiprotons are accelerated to 980 GeV, leading to a center-of-mass collision energy of 1.96 TeV.

Protons and antiprotons travel in groups of particles (*bunches*) in opposite directions while sharing the same beam pipe. A full revolution (*turn*) takes  $\approx 21 \mu s$ . The Tevatron injects 36 bunches of both protons and antiprotons for each store. A three fold symmetry is imposed by separating the 36 bunches into three superbunches. Overall, this leads to a time structure

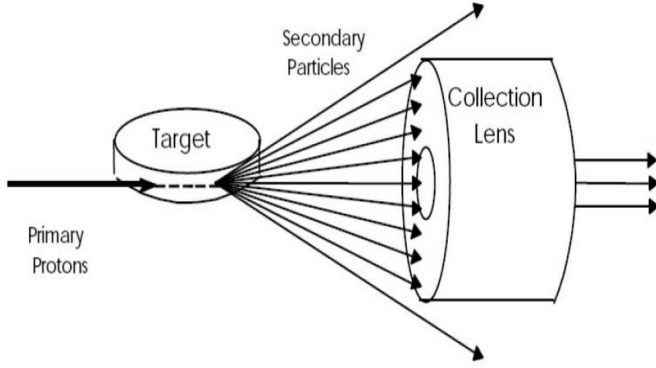


Figure 27. Simplified drawing of anti-proton production with nickel target and lithium lens.

where bunches of protons and antiprotons (*live bunch crossings* or *zero bias events*) collide at 1.7 MHz (78).

Figure 28 shows the integrated luminosity per week and total integrated luminosity for Run II from May 2001 until August 2004. The initial luminosity for each store is shown in Figure 29.

### **3.2 Interactions of Energetic Particles with Matter**

The DØ detector is built around one of the interaction regions where protons and antiprotons collide. It records the kinematics of the collision by examining the position and energies of its long lived products. Those relevant to this thesis are electrons, muons, hadronic particles and neutrinos.

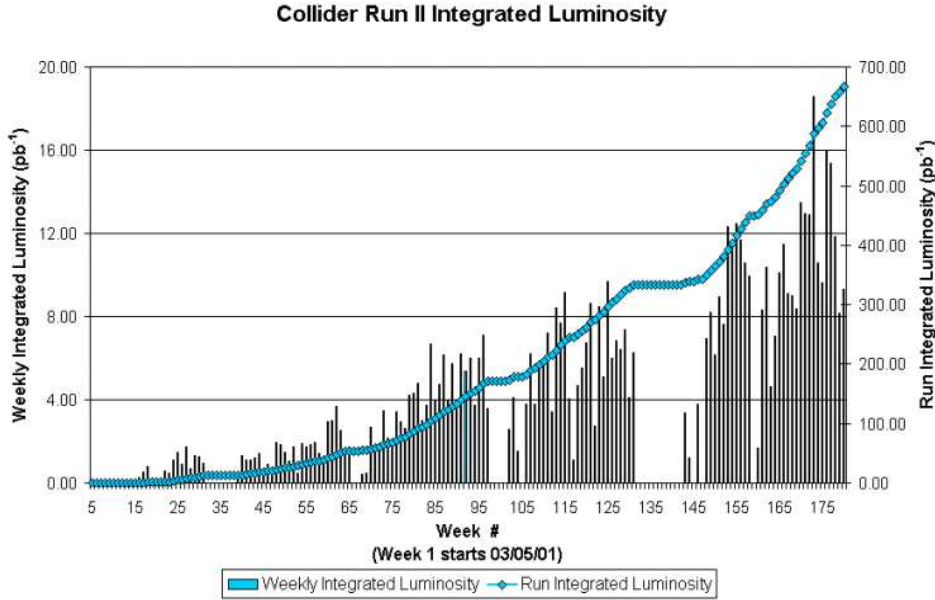


Figure 28. The integrated luminosity per week and total integrated luminosity for Run II from May 2001 until August 2004 in  $\text{pb}^{-1}$ .

The interaction of these particles with detector subsystems results in energy loss which can be detected and measured. Tracking detectors are designed to measure the particle positions with minimal energy loss. Calorimeters are constructed to fully absorb the particles and their showers, and thus their energy, in the process of measurement. The interactions of the different types of particles with the DØ detector are described below.

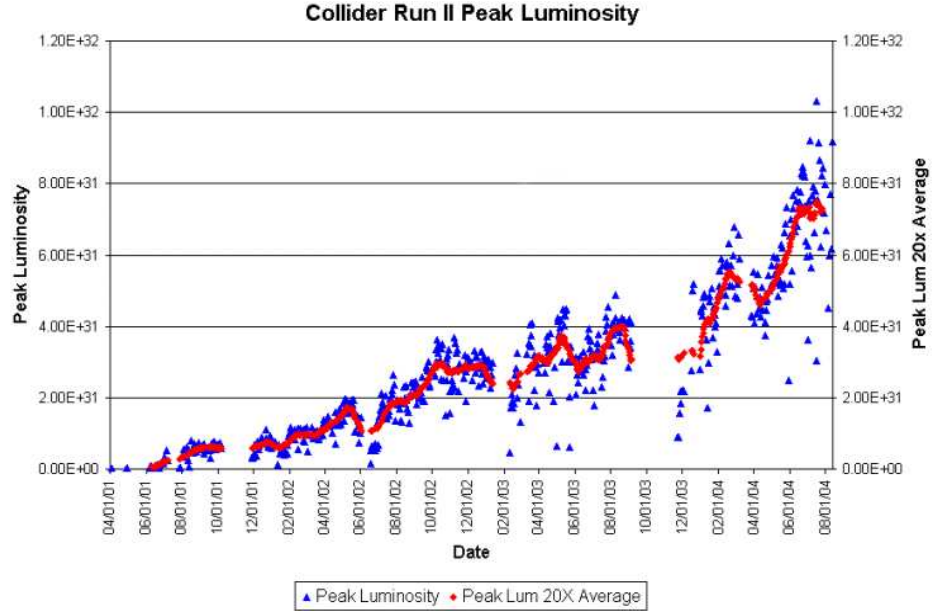


Figure 29. The initial luminosity for each store for the Tevatron Run II from May 2001 until August 2004.

## Electrons and Photons

Electrons passing through matter loose energy primarily through ionization and bremsstrahlung.

Above a critical energy (79)

$$E_c = \frac{800}{Z + 1.2} \text{ MeV}, \quad (3.1)$$

bremsstrahlung is the dominant process <sup>1</sup>. The emitted photons produce electron-positron pairs, which in turn emit photons. The resulting shower of electrons and photons grows until

---

<sup>1</sup>Z corresponds to the atomic number of the medium in Equation 3.1.

the energy of the electrons falls below the critical energy. They subsequently interact primarily through ionization. The mean distance over which an electron loses all but  $1/e$  of its energy is called the radiation length  $X_0$  (79)

$$X_0 = \frac{716.4 A}{Z(Z + 1) \ln(287/\sqrt{Z})} \text{ g cm}^{-2}, \quad (3.2)$$

where  $A$  is the atomic mass of the medium in  $\text{g mol}^{-1}$ .

Photons interacting with matter produce electron-positron pairs, and hence an electromagnetic shower.

## Muons

Muons interact through bremsstrahlung at a much lower rate than electrons due to their larger mass. Their energy loss is primarily through ionization. Figure 30 shows the energy loss per unit of material for muons in various energy regimes. Muons at the Tevatron have energies of the order of GeV, and hence are minimum ionizing particles, also called MIP. They deposit only minimal energy in the detector and leave it essentially unperturbed, in contrast to all other particles (with the exception of neutrinos).

## Hadronic Particles

These particles interact inelastically with the nuclei of the detector elements, producing primarily pions and nucleons. At high energies, the resulting particles interact similarly with nearby nuclei, producing a shower of hadronic particles. The characteristic length scale is the

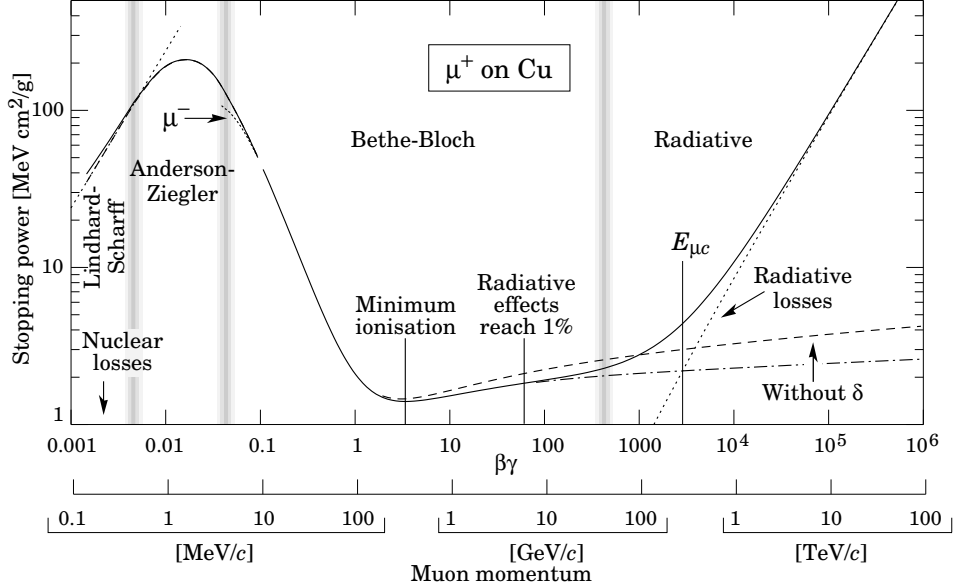


Figure 30. Energy loss through ionization of muons in various energy regimes (79).

nuclear interaction length, which depends on the material density and atomic mass and is roughly independent of energy

$$\lambda_I \approx 35 A^{1/3} \text{ g cm}^{-2}. \quad (3.3)$$

A significant fraction of energy of the initial hadron escapes the hadronic cascade in form of neutral pions, which produce a secondary cascade. A smaller fraction results in invisible energy lost through unbinding of nuclei by spallation, non-ionizing collisions and uncaptured energy of neutrinos.

## Neutrinos

Being uncharged leptons, neutrinos interact only weakly via  $W$  and  $Z$  boson exchange, making their energy loss negligible and their direct detection impossible at DØ. Their presence can be inferred, however, from transverse momentum conservation requirements.

### 3.3 The DØ Detector

The DØ detector (80; 81) is a large multi-purpose detector designed to identify and to precisely measure the four-momenta of the particles discussed in Section 3.2. It consists of three major subsystems. At the core of the detector, a magnetized tracking system records precisely the angles of charged particles and measures their transverse momenta. A hermetic, finely grained Uranium and Liquid Argon calorimeter measures the energy of electromagnetic and hadronic showers. A muon spectrometer measures the momenta of muons. Figure 31 shows an overview of the detector. The following subsections describe each component in detail.

#### 3.3.1 Coordinate System

The cartesian coordinate system used for the DØ detector is right-handed with the  $z$  axis parallel to the direction of the beam such that the protons flow in the positive  $z$  direction. The  $y$  axis is then vertical, and the  $x$  axis points towards the center of the accelerator ring. Another useful set of coordinates are the standard polar coordinates  $(r, \phi)$ . The coordinate  $r$  denotes the perpendicular distance from the  $z$  axis,

$$r = \sqrt{x^2 + y^2}, \quad (3.4)$$

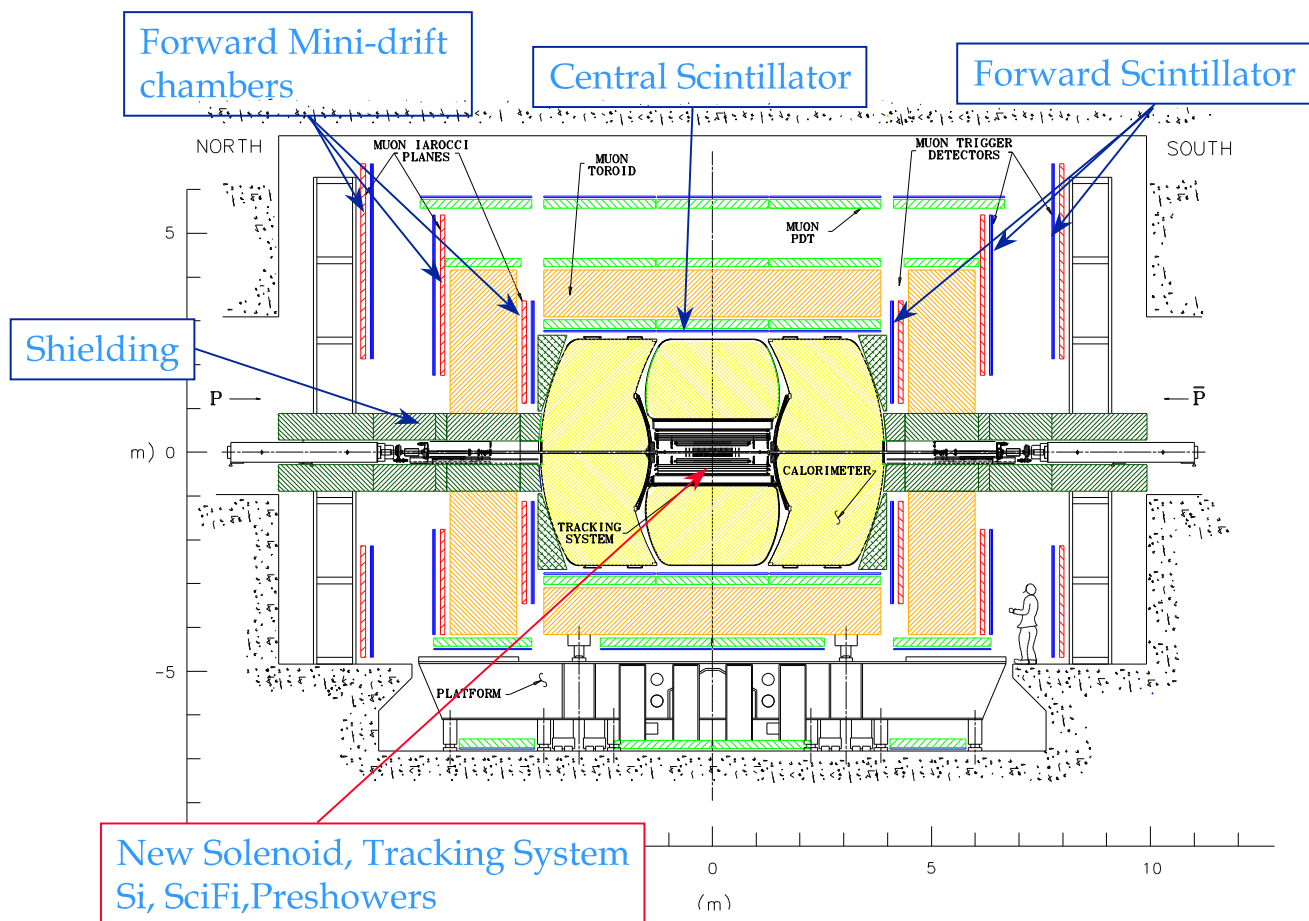


Figure 31. Side view of the DØ detector.

and  $\phi$  is the azimuthal angle

$$\phi = \arctan \frac{y}{x}. \quad (3.5)$$

In addition, a particular reformulation of the polar angle  $\theta = \arccos \frac{z}{\sqrt{x^2+y^2+z^2}}$  is given by the pseudo-rapidity  $\eta$ , defined as

$$\eta = -\ln \tan \frac{\theta}{2}. \quad (3.6)$$

The pseudo-rapidity, obtained from the rapidity  $y = \frac{1}{2} \ln \left( \frac{E+p_z}{E-p_z} \right)$  when particle masses are neglected, is a convenient choice at a hadron collider as the multiplicity of high energy particles is roughly constant in  $\eta$ . In addition, rapidity intervals are Lorentz-invariant under boosts along the  $z$  axis.

Depending on the choice of the origin of the coordinate system, the coordinates are referred to as physics coordinates when the origin is the reconstructed vertex of the interaction ( $\phi$  and  $\eta$ ), and they are referred to as detector coordinates ( $\phi_{det}$  and  $\eta_{det}$ ) when the origin is chosen to be the center of the DØ detector.

In many cases some of the products of a proton-antiproton collisions escape down the beam pipe, which makes it difficult to measure momentum components along the  $z$ -axis accurately. In addition, the initial longitudinal momentum of the collision is not known, as the colliding partons carry only a fraction of the proton or the antiproton momentum. Therefore it is more

convenient to use the momentum vector projected onto a plane perpendicular to the beam axis (*transverse momentum*)

$$p_T = p \cdot \sin\theta. \quad (3.7)$$

In a similar fashion *transverse energy* is defined as

$$E_T = E \cdot \sin\theta. \quad (3.8)$$

Unless stated otherwise, the four-momentum vectors for objects observed in the calorimeter are calculated using energies measured by the calorimeter.

### 3.3.2 Luminosity Monitor

The main purpose of the Luminosity Monitor (LM) (82) is to make an accurate determination of the Tevatron collider luminosity at the DØ interaction region (83). It consists of two arrays of twenty-four plastic scintillation counters with photomultiplier readout. A schematic drawing of the system is shown in Figure 32. The arrays are located in front of the end calorimeters at  $z = \pm 140$  cm, and occupy the region between the beam pipe and the Forward Preshower Detector (see Section 3.3.4). The counters are 15 cm long and cover the pseudo-rapidity range  $2.7 < |\eta_{det}| < 4.4$ .

The luminosity is measured by detecting inelastic  $p\bar{p}$  collisions in the Luminosity Monitor, and determined as

$$\mathcal{L} = \frac{R}{\varepsilon A \sigma_{inel}}, \quad (3.9)$$

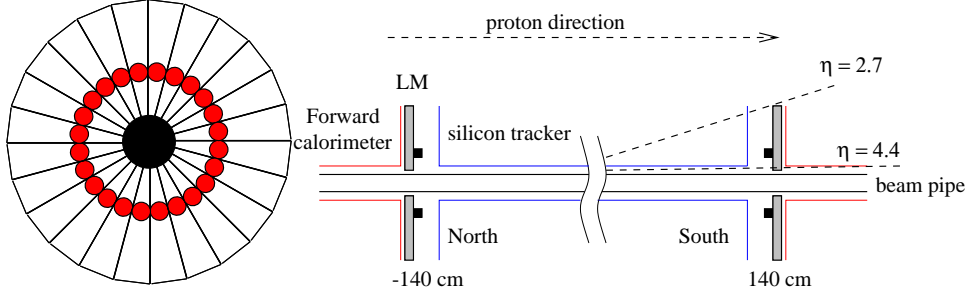


Figure 32. Luminosity Monitor layout. The  $r - \phi$  view is shown on the left, the  $r - z$  view of the two arrays is shown on the right.

whith  $R$  being the event rate. The determination of  $\sigma_{inel}$  is discussed in Section 2.9 and given by Equation 2.28. The event rate has to be corrected for the efficiency  $\varepsilon$  and the acceptance  $A$  of the LM detector for inelastic  $p\bar{p}$  collisions.

Multiple  $p\bar{p}$  collisions can occur in a single beam crossing. The number of interactions per bunch crossing is described by Poisson statistics. Collision products arrive at each set of scintillators roughly in coincidence, while beam halo products passing through the detector appear distinctly separated. Time-of-flight information from the two luminosity arrays and the  $z$  vertex distribution (see Figure 33) is utilized to separate these processes. The rate  $R$  is corrected for these two effects.

### 3.3.3 The Central Tracking System

The purpose of the central tracking system is to measure the momentum, direction and the sign of the electric charge for particles produced in a collision. It is surrounded by a solenoid which provides a nearly uniform magnetic field of  $B = 2$  T parallel to the beam axis. Charged

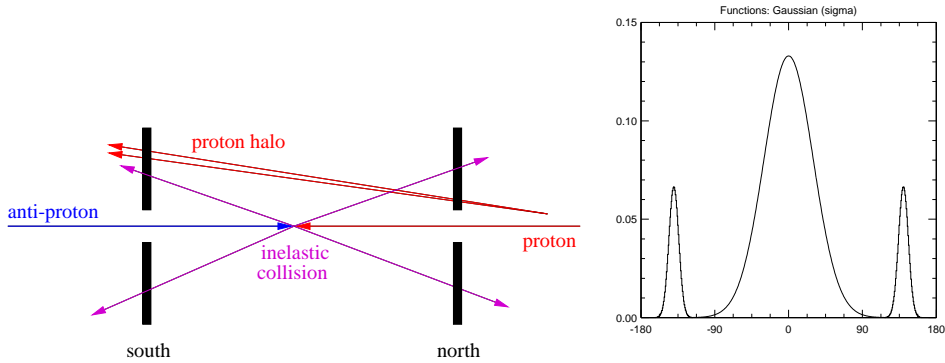


Figure 33. The sketch on the left shows the differentiation between inelastic collisions and beam halo. Expected  $z$  vertex distribution for inelastic collisions, centered at  $z = 0$  cm,  $p$  halo centered at  $z = -140$  cm and  $\bar{p}$  halo centered at  $z = 140$  cm (right).

particles produced in a collision are bent around the field lines. The radius  $r$  of the curvature allows the measurement of the transverse momentum through

$$p_T[\text{GeV}] = 0.3 \cdot r[\text{m}] \cdot B[\text{T}]. \quad (3.10)$$

The track direction in the  $r - z$  plane completes the measurement of the three-dimensional momentum vector of the particle.

Closest to the beam pipe is the Silicon Microstrip Tracker (SMT), which allows for an accurate determination of impact parameters and identification of secondary vertices. Surrounding the SMT is the Central Fiber Tracker (CFT), composed of 16 layers of scintillating fiber. The CFT extends to a radius of 50 cm, giving a lever arm long enough to provide effective transverse momentum resolution. The DØ central tracking system is shown in Figure 34.

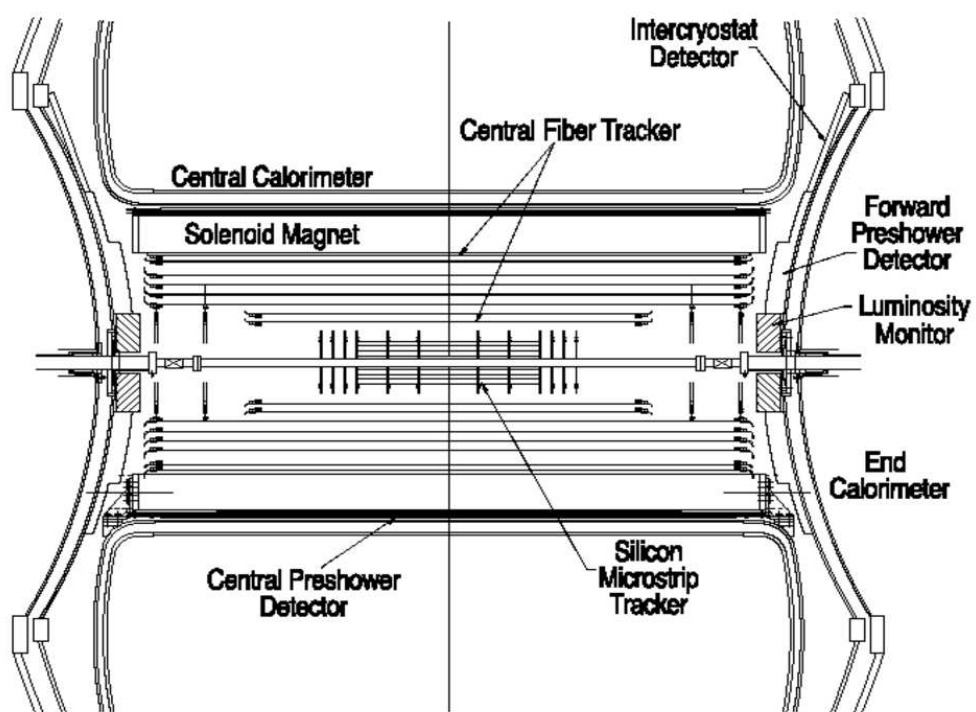


Figure 34. Schematic view of the DØ central tracking system, shown with solenoid, preshower detectors, luminosity monitor and calorimeters.

## The Silicon Microstrip Tracker

The Silicon Microstrip Tracker (SMT) is the innermost system in the D $\emptyset$  detector (81). The length of the interaction region ( $\sigma \approx 25$  cm) sets the length scale of the device in  $z$ . With an extended interaction region, it is difficult to deploy detectors such that the tracks are generally perpendicular to detector surfaces for all  $\eta$ . This led to the design of barrel modules interspersed with disks in the center, and assemblies of disks in the forward and backward regions. The barrel detectors measure primarily the  $r - \phi$  coordinate, and the disk detectors measure  $r - z$  as well as  $r - \phi$ . Thus vertices for high  $\eta$  particles are reconstructed in three dimensions by the disks, and vertices of particles at small values of  $\eta$  are measured in the barrel.

A view of the SMT is shown in Figure 35.

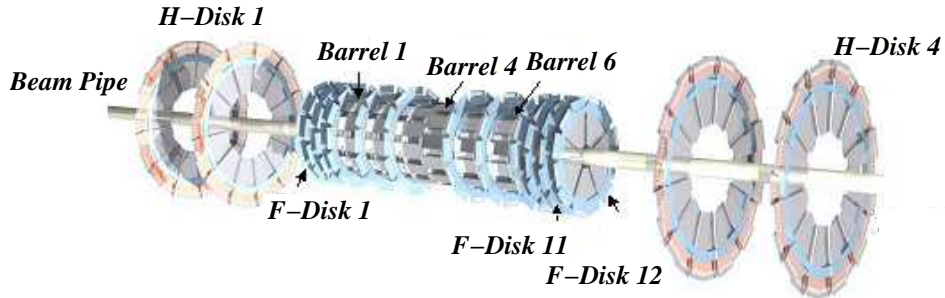


Figure 35. Schematic 3D view of the silicon vertex detector.

The detector has six barrels in the central region. Each barrel has four silicon readout layers, each layer having two staggered and overlapping sub-layers, as shown in Figure 36. The outer barrels have single sided and double sided  $2^\circ$  stereo ladders. The four inner barrels have double sided  $90^\circ$  stereo and double sided  $2^\circ$  stereo ladders. Each barrel is capped at high  $|z|$  with a disk of twelve double sided wedge detectors, called an “F-disk”. In the far forward and backward regions, a unit consisting of three F-disks and two large-diameter “H-disks” provides tracking at high  $|\eta_{det}| < 3.0$ . The H-disks are made of 24 pairs of single sided detectors glued back to back. Table X lists some specifications of the SMT (84).

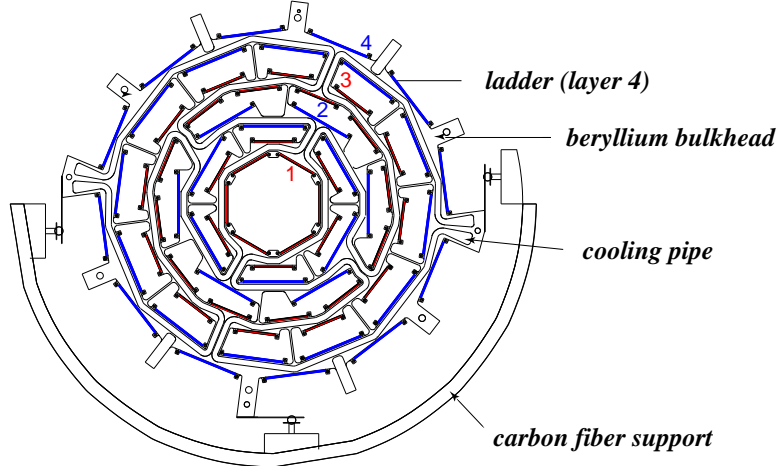


Figure 36. xy-view of the SMT barrel structure with four super-layers.

	Barrels	F-Disks	H-Disks
#Channels	387 072	258 048	147 456
Sensors	s/d-sided	double-sided	single-sided
Stereo	$0^\circ, 2^\circ, 90^\circ$	$\pm 15^\circ$	$\pm 7.5^\circ$
#Modules	432	144	96 pairs
Si area	$1.3 \text{ m}^2$	$0.4 \text{ m}^2$	$1.3 \text{ m}^2$
Inner radius	2.7 cm	2.6 cm	9.5 cm
Outer radius	9.4 cm	10.5 cm	26 cm
Maximal $ z $	38.4 cm	54.8 cm	120 cm

TABLE X  
SPECIFICATIONS OF THE SILICON VERTEX DETECTOR.

Assemblies made of kapton flex circuits laminated to Be substrates (high density interconnects or HDIs) are used to hold the SVXIIe (85) read out chip and supporting electronic components. The SVXIIe chip has 128 channels, each with 32 cell analog pipeline and an 8-bit ADC. It features 53 MHz read out speed, sparsification, down-loadable ADC ramp, pedestal, and bandwidth setting.

Figure 37 shows the read out chain of the silicon vertex detector. The HDIs are connected by 2.5 m long kapton flex cables to adaptor cards (AC) located at the face of the central calorimeter. The ACs transfer the signal and power supplies of HDIs to 10 m long high mass cables which connect to interface boards (IB). The IBs supply and monitor power to the SVXIIe chips, distribute bias voltage to the sensors and refresh data and control signals traveling between the HDIs and the sequencers. The sequencers control the operation of the chips and convert their

data into optical signals carried over 1 GB/s optical links to VME read out Buffer boards. The VME readout buffers receive and hold the data pending a Level-2 trigger decision.

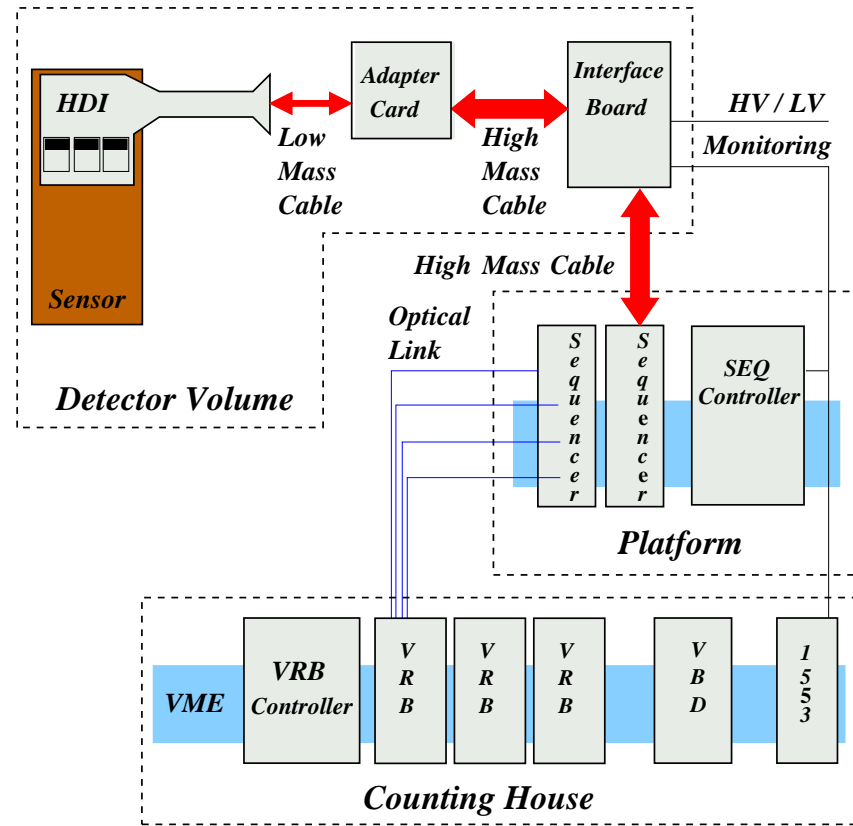


Figure 37. Read out chain of the silicon vertex detector.

Charged particles passing through the  $300 \mu\text{m}$  thick wafers of *n*-type silicon which conform the SMT produce pairs of electrons and holes. The ionized charge is collected by strips of

*p*-type or *n*<sup>+</sup>-type silicon, whose separation (between  $\sim 50\mu\text{m}$  and  $\sim 150\mu\text{m}$  pitch) provide for the measurement of the hits position. The axial hit resolution is of the order of  $10\ \mu\text{m}$ , the *z* hit resolution is  $35\ \mu\text{m}$  for  $90^\circ$  stereo and  $450\ \mu\text{m}$  for  $2^\circ$  stereo ladders.

### Central Fiber Tracker

The scintillating fiber detector, CFT, (81; 86; 87) consists of  $835\ \mu\text{m}$  scintillating fibers mounted on eight concentric support cylinders and occupies the radial space from 20 to 52 cm from the center of the beam pipe. The two innermost cylinders are 1.66 m long, and the outer six cylinders are 2.52 m long. Each cylinder supports one doublet layer of fibers oriented along the beam direction and a second doublet layer at a stereo angle of alternating  $+3^\circ$  and  $-3^\circ$ . The two layers of fibers are offset by half a fiber width to provide improved coverage. The small fiber diameter gives the CFT a cluster resolution of about  $100\ \mu\text{m}$  per doublet layer.

Light production in the fibers is a multistep process. When a charged particle traverses one of the fibers, the scintillator emits light at  $\lambda = 340\ \text{nm}$  through a rapid fluorescence decay. A wave-shifting dye absorbs the light at  $\lambda = 340\ \text{nm}$  and emits it at  $\lambda = 530\ \text{nm}$ . The light is then transmitted by total internal reflexion to the end of the scintillating fibers, where the light is transferred through an optical connection to clear fiber waveguides of identical diameter which are 7.8 to 11.9 m long. The light is only observed from one end of each scintillating fiber. The opposite end of each of the scintillating fibers is mirrored by sputtering with an aluminum coating that provides a reflectivity of 85 to 90 %. The clear fiber waveguides carry the scintillation light to visible light photon counters (VLPCs), which convert it to an electronic pulse which is read out.

The visible light photon counters are situated in a liquid Helium cryostat and operate at a temperature of 9 K. They detect photons with a quantum efficiency of 85 % and provide charge of about 30 to 60 k electrons per photon. A minimum ionizing particle creates an average of eight photo-electrons per layer, depending on the angle between the scintillating fiber and the particle trajectory. Figure 38 shows a schematic view of the CFT.

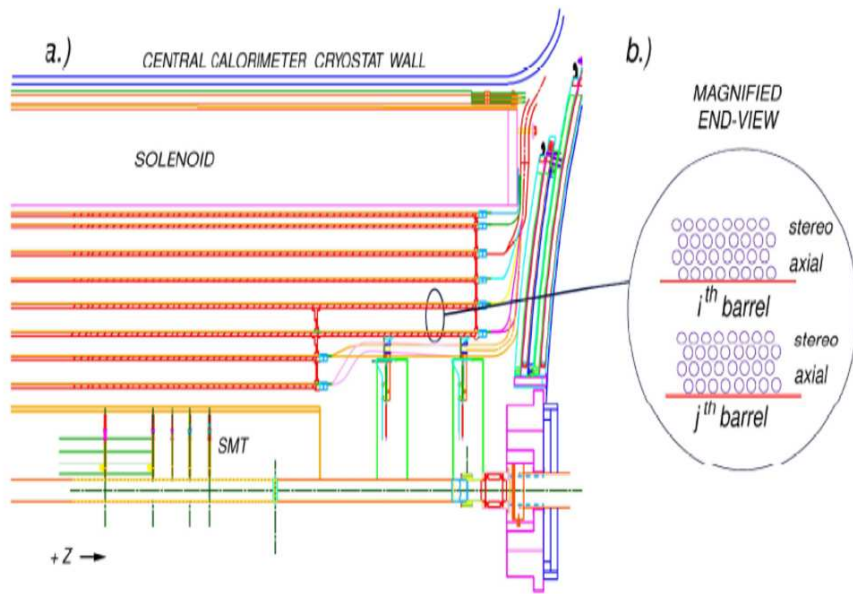


Figure 38. a) Location of the CFT. b) Closeup view of axial and stereo layers.

## Solenoid Magnet

The momenta of charged particles are determined from their curvature in the 2 Tesla magnetic field (Figure 39) provided by a 2.7 m long superconducting solenoid magnet (88). The

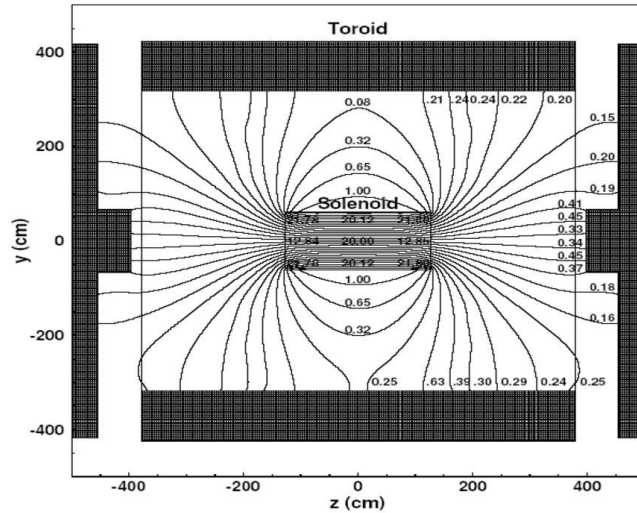


Figure 39.  $y - z$  view of the DØ magnetic field with both the toroid and solenoid magnets at full current. Numbers are in kG ( $10 \text{ kG} = 1 \text{ T}$ ).

superconducting solenoid, a two layer coil with mean radius of 60 cm, has a stored energy of 5 MJ and operates at 10 K. Inside the tracking volume, the magnetic field along the trajectory of any particle reaching the solenoid is uniform within 0.5%. The uniformity is achieved in the absence of a field-shaping iron return yoke by using two grades of conductor. The supercon-

ducting solenoid coil plus cryostat wall has a thickness of about 0.9 radiation lengths. Figure 40 shows a perspective view of the solenoid inside the central calorimeter with its chimney and control dewar.

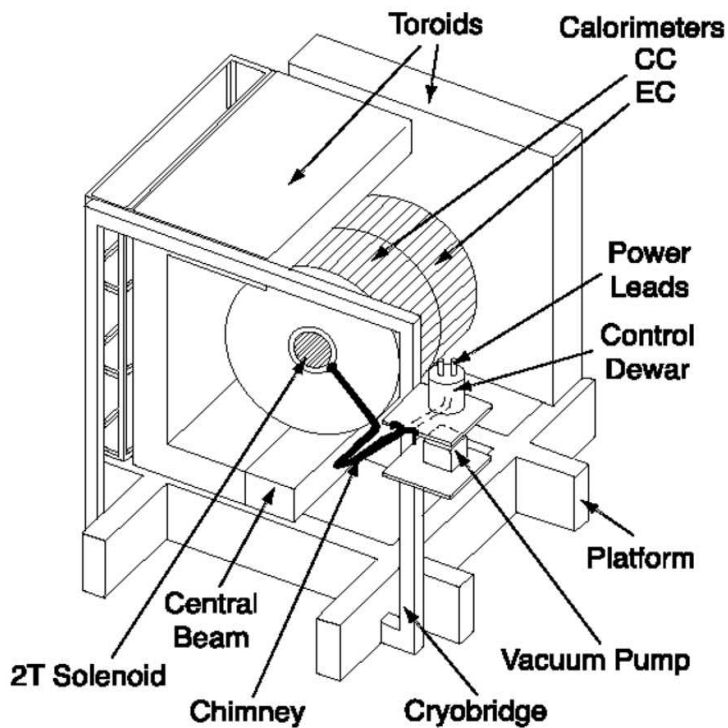


Figure 40. Perspective view of the solenoid inside the central calorimeter.

## Tracking Performance

Hits from both tracking detectors are combined to reconstruct tracks. The momentum resolution of the tracker for minimum ionizing particles can be parameterized as

$$\sigma(p^{-1}) = \frac{\sqrt{(S \cdot \sqrt{\cosh \eta})^2 + (C \cdot p_T)^2}}{p}, \quad (3.11)$$

where  $p$  is the particle momentum and  $\eta$  is the pseudo-rapidity.  $S$  accounts for the multiple scattering term and  $C$  represents the resolution term. A study (135) of  $Z \rightarrow \mu^+ \mu^-$  events has found  $S = 0.015$  and  $C = 0.0018$ .

Meson and baryon resonances are used to calibrate the tracker. The process  $K_s^0 \rightarrow \pi^+ \pi^-$  is measured with a width of  $\sigma = 7.3$  MeV and  $\Lambda^0 \rightarrow p^+ \pi^-$  with  $\sigma = 2.6$  MeV (Figure 41). The reconstruction of secondary vertices is crucial to identify  $b$  hadrons. The impact parameter resolution is shown as a function of transverse momentum in Figure 42. As an example, the reconstruction of processes  $\Xi^\pm \rightarrow \Lambda^0 \pi^\pm$  and  $\Omega^\pm \rightarrow \Lambda^0 K^\pm$  is shown in Figure 43, where multiple tracks with impact parameter of the order of centimeters are reconstructed.

### 3.3.4 The Calorimeter System

The calorimeter system was designed to measure the energy of electrons, photons, jets and neutrinos by inducing them to produce electromagnetic and hadronic showers. Passive layers of dense material in which the shower begins are followed by active layers, where the surviving fraction of the shower energy is sampled. The calorimeter system is segmented longitudinally into electromagnetic and hadronic calorimeters. The electromagnetic calorimeter measures the

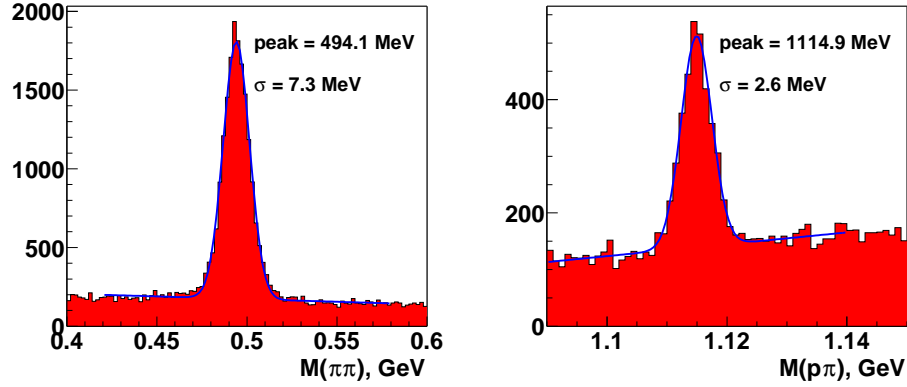


Figure 41. Invariant mass distributions for the processes  $K_s^0 \rightarrow \pi^+\pi^-$  (left) and  $\Lambda^0 \rightarrow p^+\pi^-$  (right) shown overlaid with a Gauss distribution plus a straight line fit to the signal and background. The mean and the width of the Gauss fit are also shown (136).

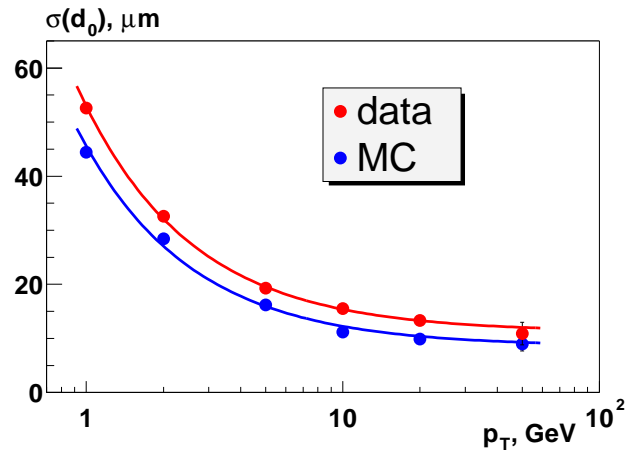


Figure 42. Impact parameter resolution measured in data and in simulated single muon events. The lines show fits to data and MC (136).

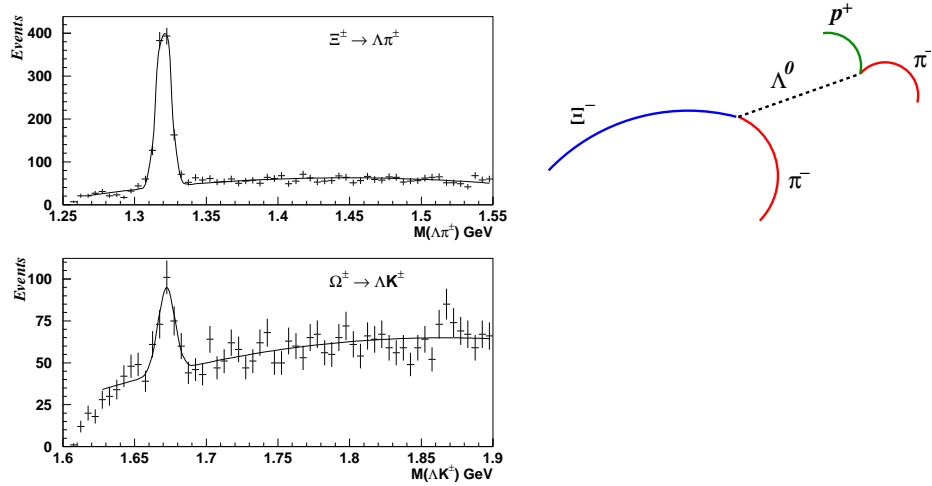


Figure 43. Invariant mass distributions for the processes  $\Xi^\pm \rightarrow \Lambda^0 \pi^\pm$  (top left) and  $\Omega^\pm \rightarrow \Lambda^0 K^\pm$  (bottom left). The reconstruction of the processes are examples of events with multiple tracks with impact parameter in the order of centimeters. A sketch of the decay  $\Xi^- \rightarrow \Lambda^0 \pi^- \rightarrow p^+ \pi^- \pi^-$  is also shown (right) (136).

energy of electrons and photons. The hadronic calorimeter measures the energy of hadrons as they interact with the material of the calorimeter. Muons only deposit a small amount of energy due to ionization. Neutrinos deposit no energy in the detector, but the absence of energy deposition results in a momentum imbalance in the transverse plane. The imbalance is called missing transverse energy.

### The Preshower Detectors

The preshower detectors (89; 90) are designed to improve the identification of electrons and photons, and to correct for their upstream energy losses during offline event reconstruction. Scintillators are used to detect both position and energy of charged particles. In contrast to the

scintillators used in the CFT, preshower scintillators are triangular shaped (Figure 44). This arranges scintillator layers without creating any dead space and thereby improves the accuracy of position measurements. The center of each scintillator carries a wavelength-shifting fiber which collects the light created by passing charged particles. The light is transmitted via clear fibers to VLPCs for readout.

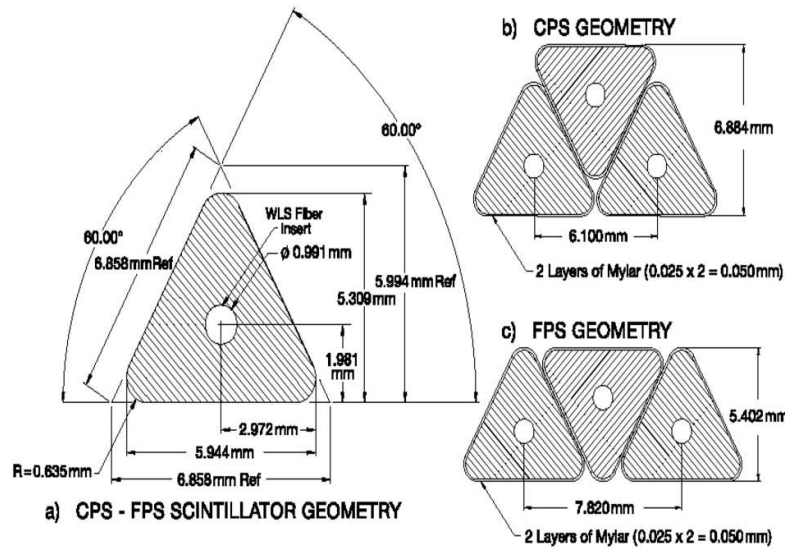


Figure 44. Cross section and layout geometry of CPS and FPS scintillator strips.

The Central Preshower Detector (CPS) is located in the 5 cm gap between the solenoid and the central calorimeter, covering the region  $|\eta| < 1.3$  (Figure 34). It consists of a layer of

lead radiator which has a thickness corresponding to approximately one radiation-length ( $X_0$ ), followed by three layers of triangular scintillator strips. The scintillating layers are arranged in an axial- $u$ - $v$  geometry, with a  $u$  stereo angle of  $23.8^\circ$  and a  $v$  stereo angle of  $24.0^\circ$ . Each layer has a total number of 2,560 readout channels.

The two Forward Preshower Detectors (FPS) are attached to the faces of the end calorimeters and cover a region of  $1.5 < |\eta| < 2.5$  (Figure 34). Each detector consists of an upstream double layer of scintillator strips (minimum ionizing particle layers, or MIP layers), followed by a lead-stainless-steel absorber layer and another double layer of scintillator strips behind it (shower layers).

### **The Liquid Argon Calorimeter**

The Liquid Argon calorimeter (86; 81; 91) is designed to identify and measure the energy for electrons, photons, taus and jets, and establish the transverse energy balance in an event. The device is also sensitive to MIPs and therefore can serve to identify muons. The calorimeter itself (i.e. the modules) is unchanged from Run I and depicted in Figure 45. However, there is significantly more material in front of the calorimeter ( $2 \leq X_0 \leq 4$ , depending on the  $\eta$ ) and the electronics is rebuilt.

As shown in Figure 46, the Liquid Argon calorimeter is subdivided into the central calorimeter (CC) covering roughly  $|\eta_{det}| < 1$  and two end calorimeters (EC) extending the coverage to  $|\eta_{det}| \approx 4$ . Each calorimeter contains an electromagnetic (EM) section closest to the interaction region followed by fine and coarse hadronic sections whose module size increases with the distance from the interaction region. The active medium for all of the calorimeters is liquid

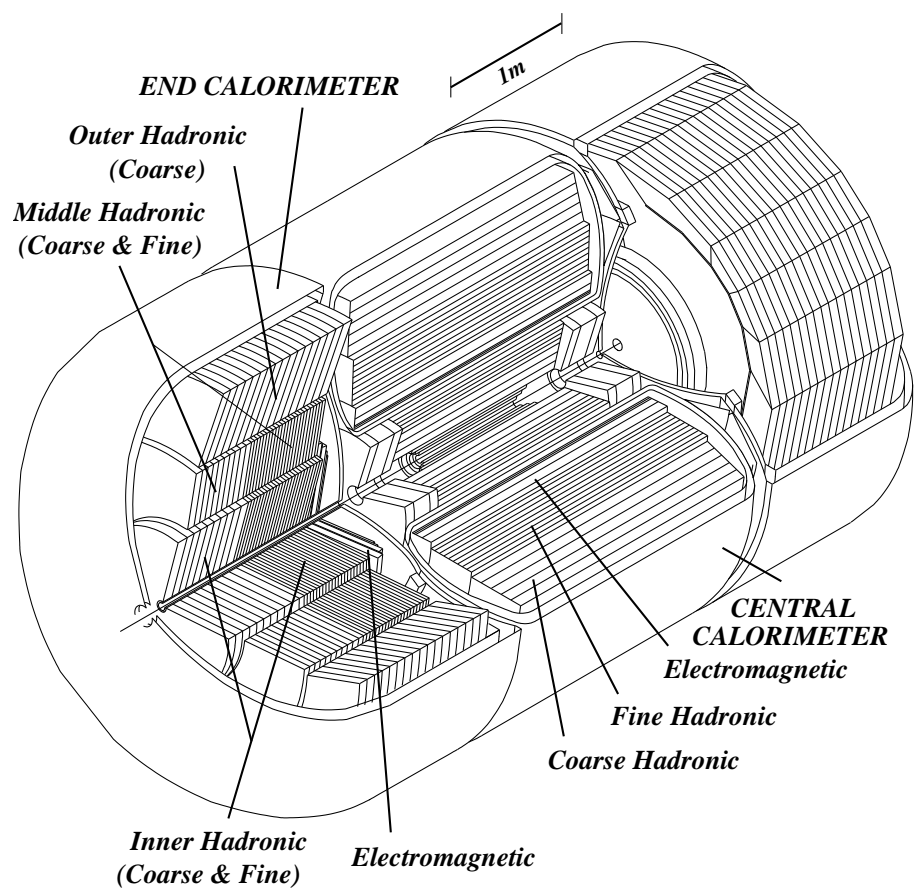


Figure 45. View of the central and two end calorimeters.

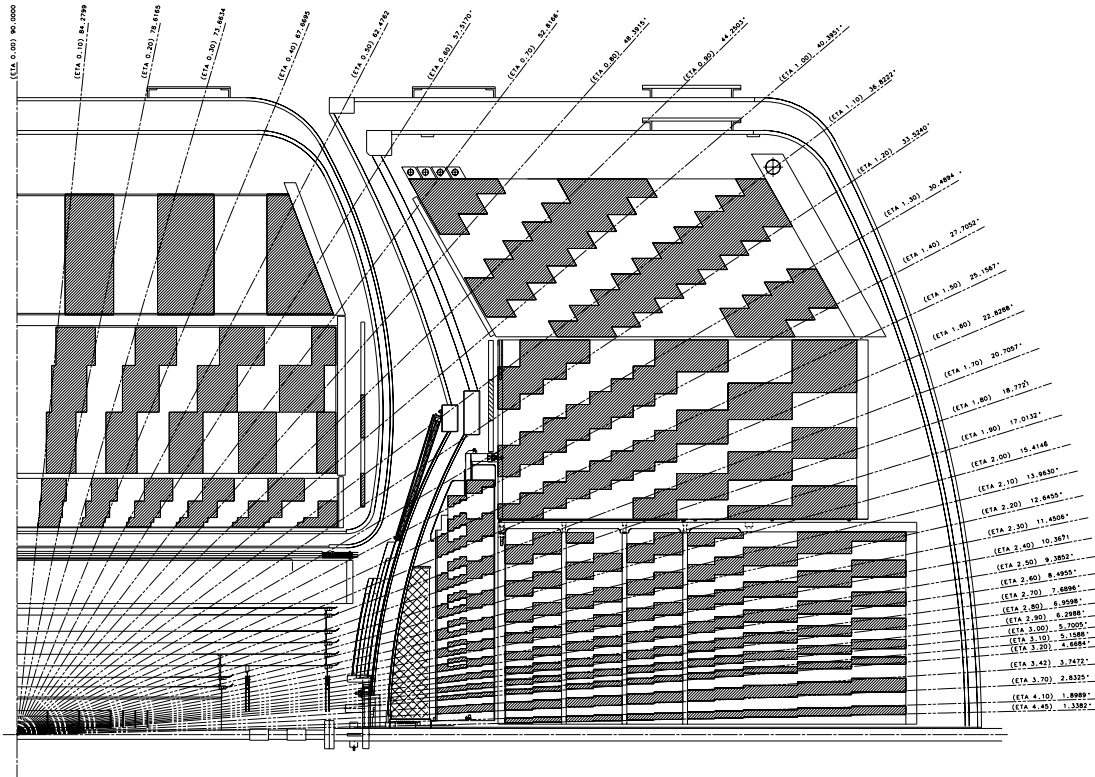


Figure 46. Schematic view of a quarter of the DØ calorimeter showing the transverse and longitudinal segmentation pattern. The shading pattern indicates cells for signal readout. The rays indicate the pseudo-rapidity intervals seen from the center of the detector.

Argon. Each of the three calorimeters is located within a cryostat that maintains the temperature at approximately 80 K. In order to achieve the same energy response for electromagnetic and hadronic particles ( $e/h \approx 1$ , compensating calorimeter), different absorber plates are used in different locations. The EM sections use thin 3 or 4 mm plates, made from nearly pure depleted Uranium. The fine hadronic sections are made from 6-mm-thick Uranium-Niobium alloy. The coarse hadronic modules contain relatively thick 46.5 mm plates of Copper in the CC and stainless steel in the EC.

The elements are combined in a basic unit (calorimeter cell, shown in Figure 47) which contains the absorber plates, the active medium, and a Copper readout pad laminated to G10 and covered in resistive epoxy for collecting the ionization. The electric field is established by grounding the absorber plates and holding the resistive surface of the pad at typically 1.6 kV. The electron drift time across the 2.3 mm gap is approximately 450 ns. Several such pads are ganged together in depth to form a readout cell (Figure 46).

The readout cells are arranged and sized such that each covers roughly an area of  $\Delta\eta \times \Delta\phi = 0.1 \times 0.1$ , comparable to the transverse sizes of showers: 1-2 cm for EM showers and about 10 cm for hadronic showers. Typical cone sizes of jets are  $\Delta R = \sqrt{\Delta\eta^2 + \Delta\phi^2} \approx 0.5$ . Segmentation finer than this is useful in probing the shapes of jets. Longitudinal subdivisions are useful since longitudinal shower profiles help distinguish electrons and hadrons. There are four separate depth layers for the EM modules in the CC and EC. The first two layers are approximately two radiation lengths ( $X_0$ ) thick and help measure the transverse shower development. The third layer is placed where the shower is expected to reach its maximum and the cells measure

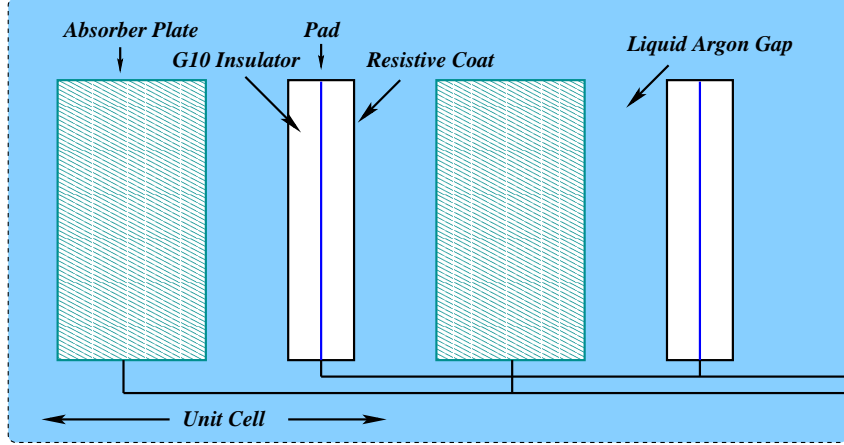


Figure 47. Schematic view of a calorimeter cell.

$\Delta\eta \times \Delta\phi = 0.05 \times 0.05$  to provide improved spatial resolution. The electromagnetic section contains in total 65.6 mm of Uranium, which represents approximately 20 radiation lengths ( $X_0^{Ur} \approx 3.2$  mm) to capture the overwhelming fraction of the electromagnetic energy. As the nuclear interaction length is much larger than the radiation length, ( $\lambda_I^{Ur} \approx 10.5$  cm  $\approx 30X_0^{Ur}$ ), hadronic particles typically deposit most of their energy in the hadronic section of the calorimeter, which contains approximately  $6.4\lambda_I$  of Uranium and Copper.

### The Inter-Cryostat Detectors

Given that the calorimeter system is contained in three separate cryostats, it provides incomplete coverage in the pseudorapidity region  $0.8 < |\eta_{det}| < 1.4$ , as can be seen in Figure 46. Additional layers of sampling detectors are added in the form of scintillating counters between the CC and EC cryostats. These counters are called Inter-Cryostat Detector or ICD (86; 81; 91). They have a segmentation of  $\Delta\eta \times \Delta\phi = 0.1 \times 0.1$ , that matches exactly the Liquid Argon

calorimeter geometry. In addition, separate single-cell scintillator structures, called *massless gaps* (86; 81; 91) are installed, both in the central calorimeter and in the end cap calorimeters. The ICD allows sampling of the region between the Central and End Calorimeters improving the energy resolution.

### Calorimeter Performance

The energy resolution of the electromagnetic and hadronic calorimeter modules was studied in Run I using pions and electrons from a test beam (92) with energies between 10 and 150 GeV, typical energies for production in Tevatron collisions. The relative energy resolution can be parameterized as

$$\frac{\sigma(E)}{E} = \sqrt{C^2 + \left(\frac{S}{\sqrt{E}}\right)^2 + \left(\frac{N}{E}\right)^2}. \quad (3.12)$$

The dominant effect in the energy resolution comes from sampling fluctuations which are of Poisson nature and is represented by  $S$ .  $N$  represents contributions from Uranium and electronics noise, and  $C$  originates from calibration errors and other systematic effects. The results are summarized in Table XI.

The measurement of the Run II energy resolution of the electromagnetic calorimeter is performed utilizing the three resonances  $J/\Psi$ ,  $\Upsilon$ , and  $Z$  that decay to two electrons. The central tracking system provides the momentum measurement from which the energy can be inferred. Figure 48 shows the di-electron invariant mass spectrum measured with the calorimeter (left) and the central tracker (right). Figure 49 shows the di-electron invariant mass spectrum

Particle	C	S	N
e	$0.0115^{+0.0027}_{-0.0036}$	$0.135 \pm 0.005\sqrt{\text{GeV}}$	0.43 GeV
$\pi$	$0.032 \pm 0.004$	$0.45 \pm 0.04\sqrt{\text{GeV}}$	0.975 GeV

TABLE XI

CALORIMETER ENERGY RESOLUTION PARAMETERS, MEASURED WITH ELECTRONS FOR THE ELECTROMAGNETIC SECTION ( $C$  FROM THE  $Z \rightarrow e e$  MASS RESOLUTION,  $S$  FROM THE TEST BEAM AND  $N$  FROM  $W \rightarrow e \nu$ ) AND WITH PIONS FROM THE TEST BEAM FOR THE HADRONIC SECTION.

in the region of the  $Z$  boson mass. The events can be selected with high statistics and with high purity and represent three independent measurements allowing to constrain the  $S$ ,  $C$  and  $N$  terms in Equation 3.12.

The energy resolution of the hadronic calorimeter in Run II is measured by randomly selecting collisions (so-called *zero-bias* events). Most of the time no hard-scatter interaction will occur. The central tracking system is then used to identify single tracks representing isolated charged particles, which are dominantly charged pions. The tracking system provides a momentum measurement which is used to determine the expected energy deposition of the particle in the calorimeter. Preliminary studies (94) suggest a decreased calorimeter response compared to Run I, mainly due to the following reasons:

- The electron drift time of 450 ns provides a challenge for signal charge integration for a roughly 5 times larger beam crossing frequency occurring every 396 ns in Run II instead of every 2  $\mu\text{s}$  in Run I. Only 70 % of the signal charge is integrated for the shorter time in

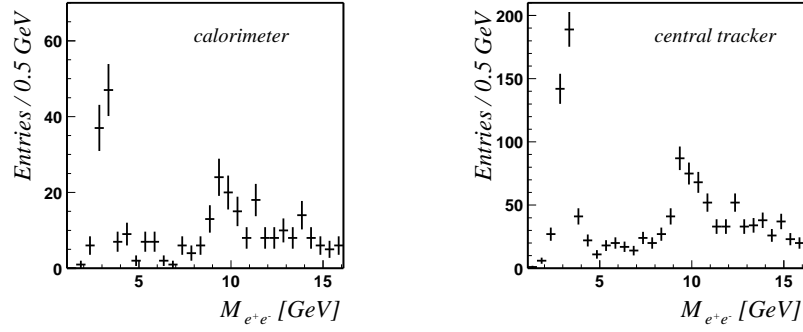


Figure 48. Di-electron invariant mass spectrum measured with the calorimeter (left) and the central tracker (right). The  $J/\Psi$  and  $\Upsilon$  can clearly be seen (94).

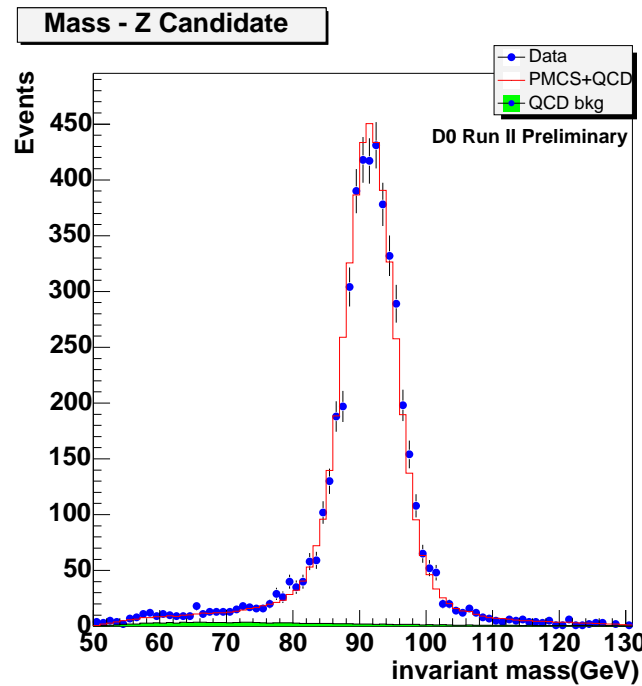


Figure 49. Invariant di-electron mass distribution of data (dots) and expected background (line) for the  $Z$  peak region. Shaded is QCD background (73)

Run II leading to larger sensitivity to fluctuations. In particular, the contribution from slow nuclear products from the hadronic shower is lost. Also, the mechanical tolerances with which the calorimeter was built met the requirements of the Run I integration time but are too large for Run II. All this involves a degradation of the  $S$  and  $N$  terms in Equation 3.12.

- The new electronics used in Run II is found to have a worse noise performance, affecting mainly the  $N$  term in Equation 3.12.
- The energy response of the cells differs by up 10 % (94). This cell to cell miscalibration affects the  $C$  term in Equation 3.12.
- The new tracking system detector components, the solenoid magnet and the preshower detector installed for Run II in front of the calorimeter have radiation lengths  $2 \leq X_0 \leq 4$ , depending on the  $\eta$  of the particle. As a consequence, the term  $S$  in Equation 3.12 degrades.

### **3.3.5 The Muon System**

Muons originating from a  $p\bar{p}$  collision penetrate the tracking system and the calorimeter essentially unperturbed. The DØ muon detection system is the outermost part of the DØ detector. It is placed around the calorimeter as shown in Figure 50, and it serves to identify and trigger on these muons and to provide a crude measurement of their momenta and charge.

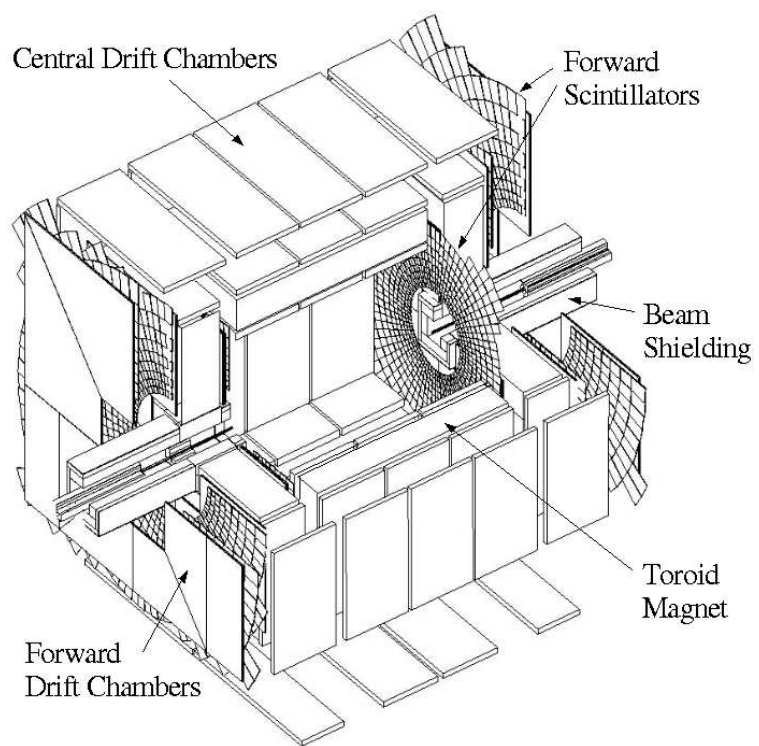


Figure 50. A schematic view of the muon system.

It consists of a system of proportional drift tubes (PDTs), mini drift tubes (MDTs) and scintillation counters. The PDTs cover  $|\eta_{det}| < 1.0$ , the planes of MDTs extend the muon detection to  $|\eta_{det}| = 2.0$ . The scintillator counters are used for triggering and for cosmic and beam related muon rejection. Toroidal magnets and special shielding complete the muon system. Each sub-system has three layers called A, B, and C. The A layer is innermost and located between the calorimeter and the iron of the toroid magnet. B and C layers are located outside the iron. In the region directly below the calorimeter, only partial coverage by muon detectors is possible as the support structure for the DØ detector and the readout electronics are located in this region.

The average energy loss of a muon in the calorimeter is 1.6 GeV, and about 1.7 GeV in the iron. The momentum measurement is corrected for this energy loss. In the following sections the subsystems of the muon spectrometer are discussed.

### **Toroid Magnet**

A 1973 ton toroid magnet (88), located between layer A and B, allows a measurement of the muon momentum. It is a square annulus 109 cm thick, in radial distance of 317.5 cm from the beam line. In order to give access to the inner portions of the DØ detector, the central toroid is split in 3 parts. A bottom section gives support for the calorimeter and tracking detectors. The central toroid is completed by two movable c-shaped shells. The two forward toroid magnets are located at  $447 \leq |z| \leq 600$  cm. The coils carry currents of 1500 A and result in an internal field of 1.8 T.

## Proportional Drift Tubes

The PDTs (95) are rectangular volumes, filled with gas covering  $|\eta_{det}| < 1$ . The ionization created by a passing charged particle is collected and amplified by a  $50 \mu\text{m}$  gold-plated tungsten sense wire which runs through the center of the chamber. Vernier cathode pads are located above and below the wires to provide information on the hit position along the wire. A measurement of the arrival time of the pulse from the sense wire and a calibration of the drift time of the gas allows for calculation of the radial distance from the sense wire. A comparison of arrival times from adjacent wires provides a rough measurement of the position of the ionization along the wire.

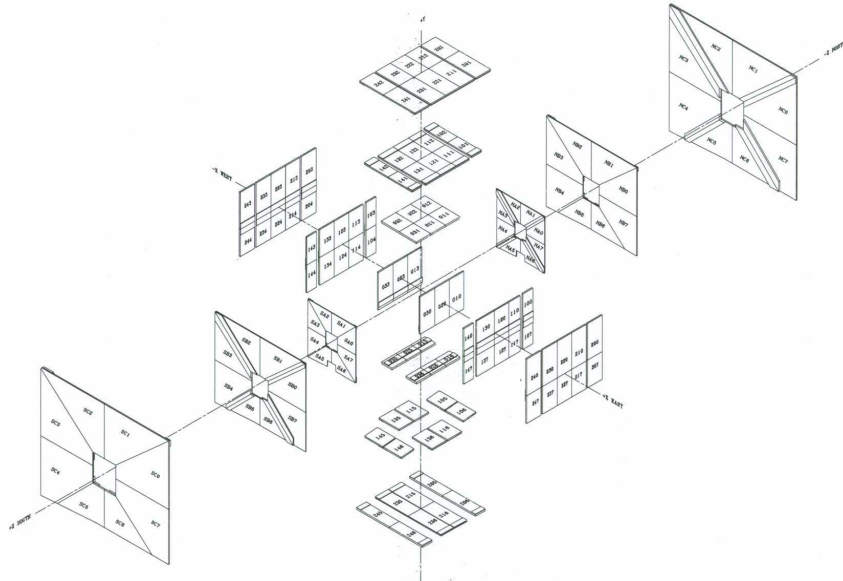


Figure 51. View of the three drift chamber layers of the muon system.

PDTs are constructed of extruded aluminum coated with steel foil and filled with a mixture of 84 % Argon, 8 %  $CH_4$  and 8 %  $CF_4$ . The gas flow rate is 500 liters per hour. The drift velocity is approximately 10 cm/ $\mu$ s, for a maximum drift time of about 500 ns. The coordinate resolution of the radial distance to the sense wire is approximately 3 mm.

### **Mini Drift Tubes**

The MDTs (96) extend the muon detection to  $|\eta_{det}| = 2$ . They have a shorter electron drift time compared to the PDTs (40-60 ns, depending on the inclination of the tracks), a better coordinate resolution ( $\approx 0.7$  mm), are radiation hard, and have a high segmentation, thus a low occupancy. They are filled with a mixture of 90 %  $CF_4$  and 10 %  $CH_4$ . Figure 51 shows an expanded view of the drift tubes.

### **Scintillation Counters**

Sheets of scintillating pixels accompany each layer of drift tubes, with the exception of the B layer in the central system. Designed to cover  $4.5^\circ$  in  $\phi$ , they provide additional position measurement, and are used for triggering, cosmic ray veto, beam related muon rejection and track reconstruction. Figure 52 shows an expanded view of the scintillation counters (97). The pixels consist of a slab of scintillator in which light-collecting fibers are set in grooves. A photomultiplier tube collects the light and provides an analog voltage pulse to the digitizing electronics.

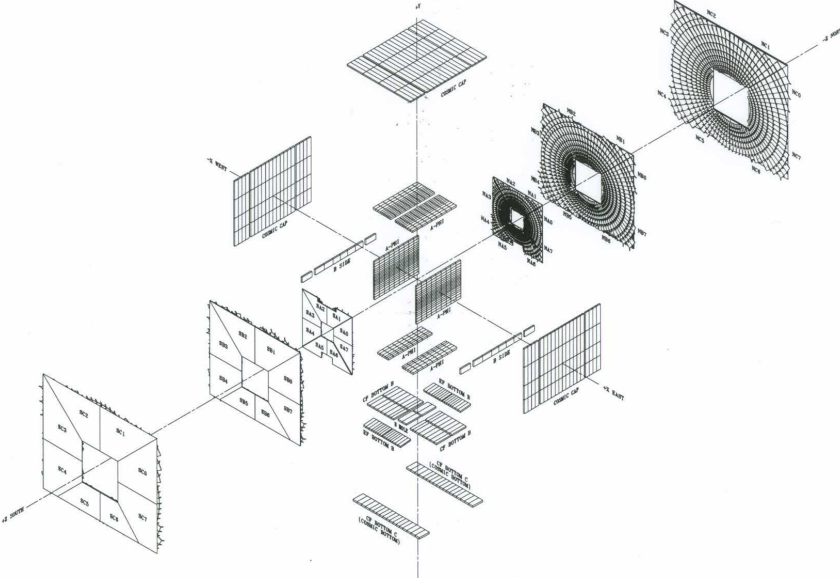


Figure 52. View of the three scintillator layers of the muon system.

## Shielding

The shielding consists of layers of iron, polyethylene and lead in a steel structure surrounding the beam pipe and low beta quadrupole magnets. Three different sources contribute to background in the central and forward muon system:

- Scattered proton and antiproton fragments that interact with the end of the calorimeter or with the beam pipe produce background in the central and forward A layer.
- Proton and antiproton fragments, mostly muons from pion decays created by proton and antiproton interactions upstream of the detector, interacting with the low beta quadrupole magnets produce hits in the B and C layers of the forward system.

- Beam halo interactions affect both the central and the forward muon system.

Iron is used as the hadronic and electromagnetic absorber, polyethylene is a good absorber for neutrons due to its high hydrogen content, and lead is used to absorb gamma rays.

## Performance

The performance of the muon system combined with the central tracker is shown in Figure 53 and Figure 54, where the di-muon invariant mass is shown at the  $\omega$ ,  $\phi$ ,  $J/\Psi$ ,  $\Psi'$ ,  $\Upsilon$  and at the  $Z$  mass.

The momentum resolution of the muon system has been studied using reconstructed muons with an associated central track. The muon momentum resolution,  $\sigma(p_T)/p_T$ , as measured by the muon system, varies between 0.1 for low-momentum muons and 0.5 for muons with  $p_T > 50 \text{ GeV}$  (98). The overall muon momentum resolution, including information from the silicon vertex detector and the central fiber tracker, is defined by the central tracking system for muons with momentum up to approximately 100 GeV. The muon system measurement improves the resolution only for higher momentum muons (81).

### **3.3.6 The Forward Proton Detector**

The Forward Proton Detector (FPD) (100) is a series of momentum spectrometers that make use of accelerator magnets in conjunction with position detectors along the beam line in order to determine the kinematic variables  $t$  and  $\xi$  of the scattered  $p$  and  $\bar{p}$ , where  $|t|$  is the four-momentum transfer of the scattered proton or antiproton, and  $\xi = 1 - x_p$ , where  $x_p$  is the fractional longitudinal momentum of the scattered particle with respect to the incoming proton. The FPD covers the region  $0 \leq t \leq 4.5 \text{ GeV}^2$ .

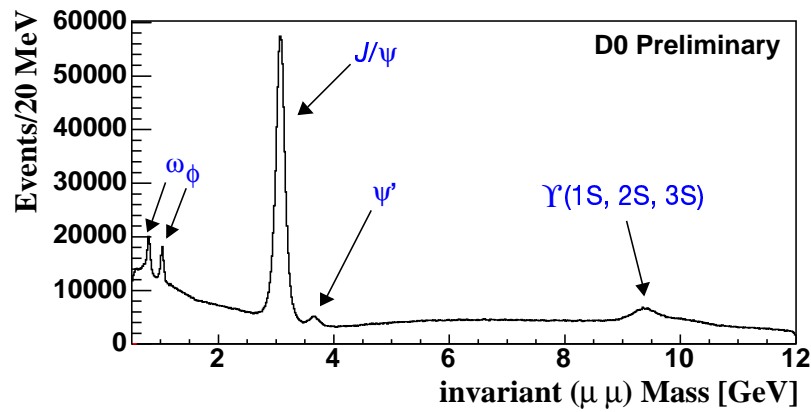


Figure 53.  $\mu^+ \mu^-$  invariant mass distributions of various meson resonances:  $\omega$ ,  $\phi$ ,  $J/\Psi$ ,  $\Psi'$  and  $\Upsilon$  (99).

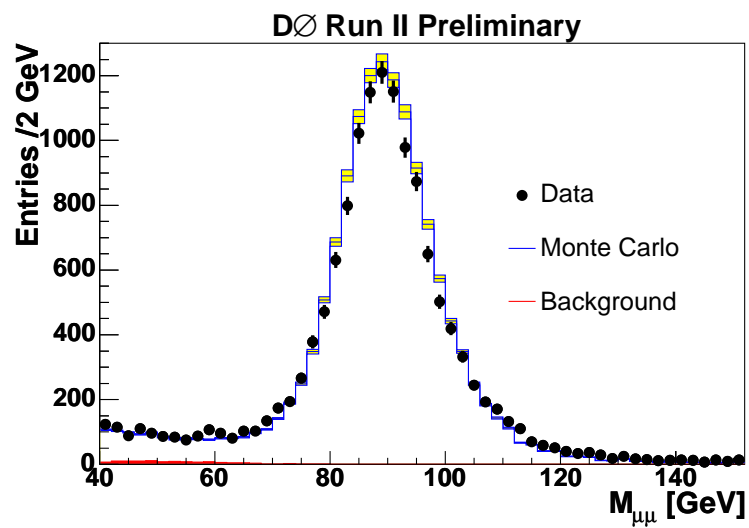


Figure 54.  $\mu^+ \mu^-$  invariant mass spectrum at the  $Z$  mass (74).

The position detectors must operate a few millimeters from the beam and have to be moved away during the injection of protons in the accelerator. Special devices, called Roman pots (134), are designed to house the position detectors allowing for remotely controlled movement with an accuracy in the order of tens of microns.

The Roman pots are housed in stainless steel chambers called castles. The FPD, shown in Figure 55, consists of 18 Roman pots arranged in six castles, where the detectors placed in each castle can approach the beam from up, down, inside and outside directions with respect to the Tevatron ring. Four castles are located downstream of the low beta quadrupole magnets on each side of the colliding point: two on the proton side (P1 and P2) and two on the antiproton side (A1 and A2). The FPD is not used in the present analysis.

### **3.3.7 The Trigger System**

The proton antiproton crossings at the D $\emptyset$  location result in collisions that in the majority of cases are of little interest. In particular, collisions which produce massive particles such as  $W$ ,  $Z$ , the top quark or those which might provide evidence of *New Physics* occur extremely rarely. To accumulate a large sample of events of interest without having to store and reconstruct a staggering number of uninteresting collisions, D $\emptyset$  employs an event trigger which decides whether to store an event or to discard it. At the Tevatron, an input bunch crossing rate of 2.5 MHz must be reduced to the final rate of 50 Hz, a limit given by the offline reconstruction capabilities.

The trigger system is a three tiered pipelined system; each tier examines the event in more detail than lower tiers while restricting the rate of events to higher tiers. An event can fail the

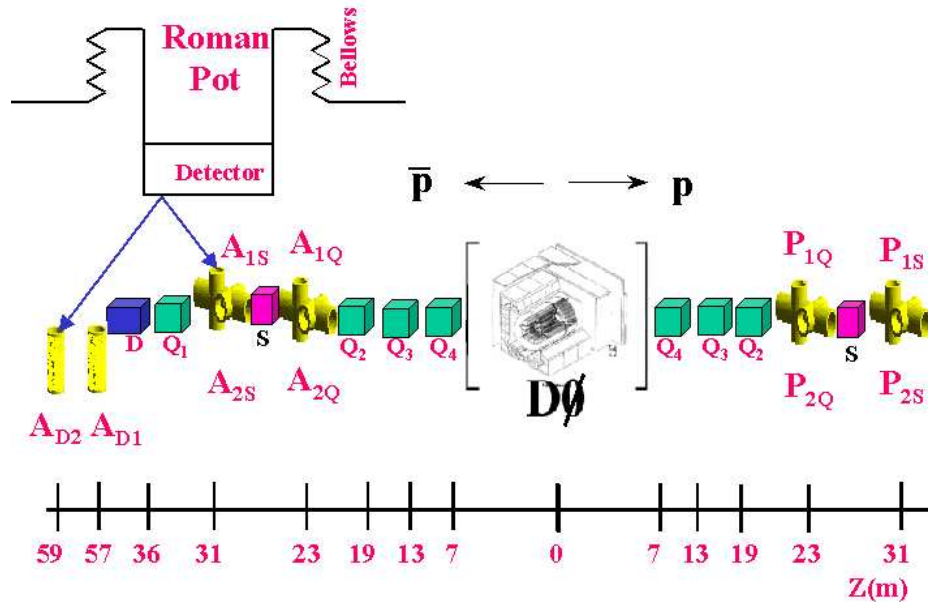


Figure 55. The FPD: Quadrupole Roman pot detectors are named P or A when placed on the  $p$  or  $\bar{p}$  side, respectively. Dipole pots, located on the  $\bar{p}$  side, are named D.

trigger because it was recognized as a less interesting process, because it was mistaken for a less interesting process (trigger inefficiency), or because the trigger or data acquisition systems were busy processing previous collisions (dead time).

### The Level 1 Trigger

The first trigger stage (Level 1 or L1) is a hardware trigger that consists of a framework built of field programmable gate arrays (FPGAs), which take inputs consisting of simple objects provided by the individual subdetectors (luminosity monitor, calorimeter and muon system).

It has a pipeline, which allows to make a decision within  $4.2 \mu\text{s}$ , resulting in a trigger accept rate of about 2 kHz.

The luminosity system provides an indication that a collision occurred with a position on the  $z$  axis which would place it within the DØ detector. The calorimeter employs a special path which performs a very quick summation of electromagnetic and hadronic towers at a resolution of  $\Delta\eta \times \Delta\phi = 0.2 \times 0.2$ , excluding the coarse hadronic section due to a higher noise rate. The trigger requires that the energy in these towers be above a certain threshold. Based on signal to noise considerations, only the trigger towers for  $|\eta_{det}| < 3.2$  are used. Some of the data used in the analyses presented are triggered with a limited trigger coverage,  $|\eta_{det}| < 2.4$ . Additional trigger terms are possible for global quantities such as the total sum of all tower energies,  $\sum E_T$ , and the missing transverse energy,  $\cancel{E}_T$ . The muon trigger requires a coincidence between the scintillators in the A and B or C layers.

### **The Level 2 Trigger**

In the second stage (Level 2 or L2), hardware engines associated with specific subdetectors process information that is then used by a global processor to determine correlations between different detectors, e.g. matching tracks and leptons. Level 2 has an accept rate of 1 kHz at a maximum dead-time of 5%, and a maximum latency of  $100 \mu\text{s}$ . The Level 2 trigger passes events to the Level 3 system.

Figure 56 shows the design of the DØ Level 1 and Level 2 trigger system.

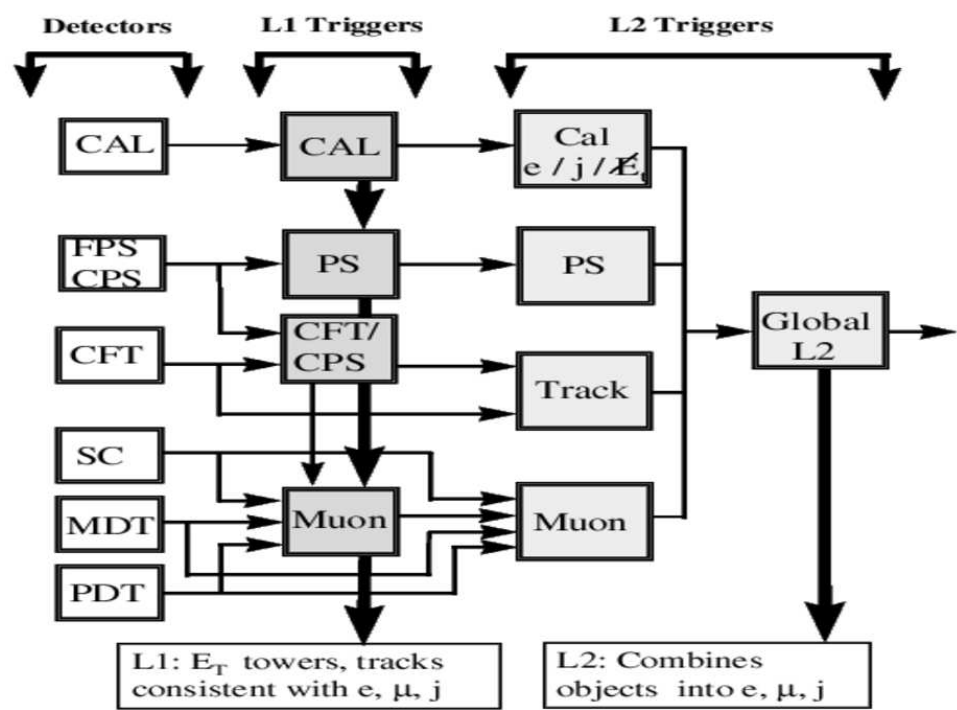


Figure 56. Schematic view of subdetectors with L1 and L2 trigger elements. Horizontal arrows indicate the direction of dataflow.

### The Level 3 Trigger

The third stage (Level 3 or L3) uses a collection of approximately 100 farm nodes to perform a limited reconstruction of the event and make a trigger decision using the full event information (complete physics objects as well as their correlations). The nominal 1 kHz input rate is reduced to 50 Hz for data recorded for offline analyses.

## CHAPTER 4

### EVENT RECONSTRUCTION AND OBJECT IDENTIFICATION

The D $\emptyset$  detector collects information consisting of nearly a million input channels. These channels have to be processed carefully for evidence of the products of a collision, from which the kinematics of the collision can be inferred.

A collection of software algorithms called *d0reco* (101) is used to reduce the huge amount of information and to define basic physics objects and their properties, representing the particles originating from a  $p\bar{p}$  collision. The detector design allows to distinguish and to define fundamental objects such as tracks, primary vertices, electrons, photons, muons, jets and their flavor, and missing transverse energy ( $\cancel{E}_T$ ).

In general, the object reconstruction and identification is optimized for efficiency and purity, and to provide the best possible measurement of the magnitude and direction of the object's momentum. However, other objects in the event, like particles not originating from the collision or noise in the detector components or the readout electronics, can mimic the object signature, degrading the purity. In particular for the analysis presented, the object identification is optimized to isolate  $t\bar{t}$  events from background events.

In this chapter, strategies for reconstructing these objects from the detector responses and the respective selection criteria are described.

## 4.1 Charged Tracks

The central tracking system accounts for a large fraction of the event data. Scanning through all of its channels for signals of charged particles is one of the most time consuming tasks of the reconstruction chain. Charged particles, curving through the magnetic field, leave traces in the central tracking system from which tracks are reconstructed.

The reconstruction is divided in two parts: **hit clustering**, that groups individual channels that are likely to represent the passage of an individual particle, and **track finding**, which finds groups of clusters located along a physical path. Particles passing through the SMT will deposit charge in a number of strips. A particle traversing the CFT will illuminate a number of fibers. In both cases, a cluster is defined as a group of adjacent strips above a noise threshold. The track finding is subdivided into two algorithms: pattern recognition and track fitting. The pattern recognition creates sets of clusters which lie along physical paths. The track fitting uses sophisticated algorithms (Kalman fitter (102)) to fit a candidate charged particle track to a physical path, using a  $\chi^2$  test. Figure 57 shows an example of hits and reconstructed tracks.

## 4.2 Primary Vertex

The location of a  $p\bar{p}$  collision is referred to as the Primary Vertex (PV). The precise determination of the PV position is crucial for all  $b$ -tagging algorithms and to determine if a lepton originates from it. Details of the PV reconstruction and its performance on Monte Carlo and data can be found in (103), and are briefly described below.

The reconstruction of Primary Vertices consists of two major steps (two-pass algorithm):

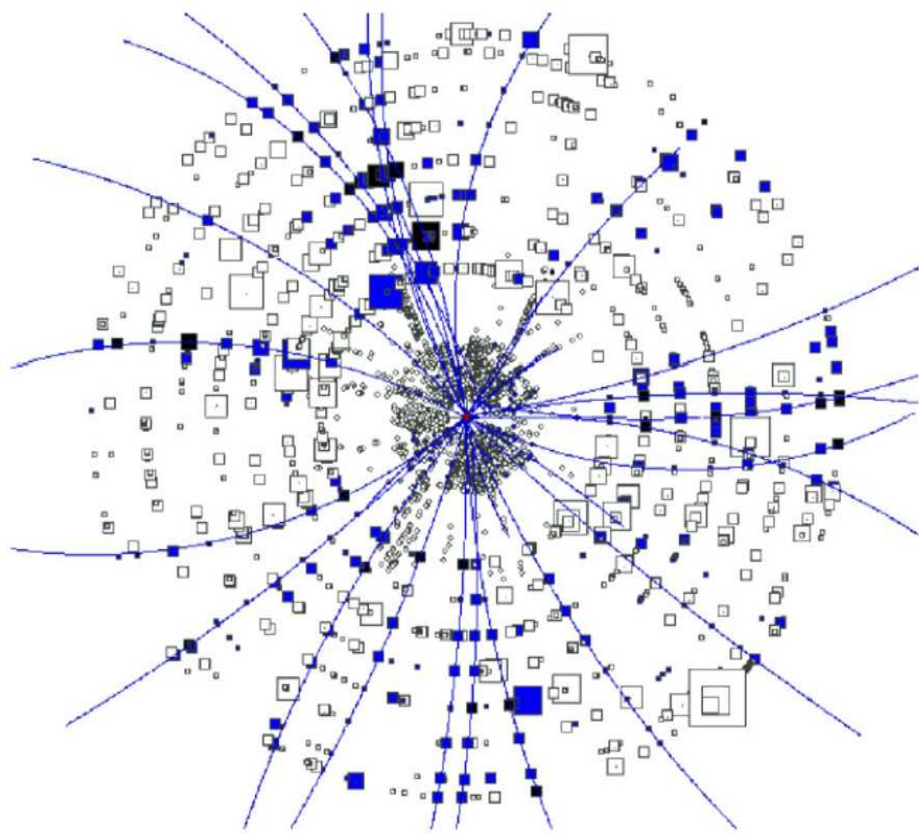


Figure 57. Axial view (looking along the beam-pipe) of a recorded event showing hits and reconstructed tracks. CFT hits are represented by squares, and SMT hits are represented by circles. Hits are colored solid if they are associated with a reconstructed track (solid lines). The curvature of the reconstructed tracks is due to the solenoidal magnetic field, which is pointing out of the page.

1. the algorithm locates the position of the beam spot center. At this step, all tracks with distance of closest approach ( $dca$ ) significance  $S_{(0,0)} < 100$ , calculated with respect to  $(x, y) = (0, 0)$  in the transverse plane, are fitted to the PV. The result of the fit is the list of possible primary vertices.
2. at the second pass, the track  $dca$  significance is calculated with respect to the position of these first-pass vertices. Only tracks with at least two SMT hits, surviving a tight  $dca$  significance cut, are fitted to the final primary vertices.

The final step is the selection of the hard scatter vertex from the list of reconstructed vertices. The method used is described in detail in (104). It is based on the fact that tracks from minimum bias interactions have smaller transverse momenta than tracks from hard scatter interactions. The  $\log_{10} p_T$  distribution of tracks from minimum bias processes is used to define a probability for a track to come from a minimum bias vertex. For each vertex, the product of the probabilities of each track divided by the total number of tracks is calculated, thus forming the probability for a vertex to originate from a minimum bias interaction. The PV with the lowest minimum bias probability is chosen as the hard scatter PV.

There are two implementations of the PV algorithms, so-called “DØreco” and “DØroot”. The momenta of calorimeter objects in the event (jets, electromagnetic clusters, and the  $E_T$ ) are reconstructed with respect to the DØreco PV. For tracking related quantities, the  $dca$ 's of leptons, and the reconstruction of secondary vertices for  $b$ -tagging, the DØroot PV algorithm is used since it has a better performance.

The DØreco vertex finder and the DØroot vertex finder are very similar and show comparable performance in terms of reconstruction efficiency and in the reconstructed  $x$ ,  $y$  and  $z$  coordinate of the vertex. The two algorithms share the vertex selection procedure but differ in the track-selection and fitting techniques. The main characteristics of both algorithms regarding track selection at the second pass are summarized in Table XII. The DØroot algorithm has an additional step which is performed before the two-pass approach. It starts from clustering tracks along the  $z$ -coordinate. The clustering algorithm starts from the track with highest  $p_T$  and adds the track with closest vertex, which is within 2 cm from the first one. The position of the cluster of tracks is recalculated with every additional track. Clusters of tracks are the input for the two-pass algorithm.

Track variable	DØreco	DØroot
$p_T$	$\geq 0.5 \text{ GeV}$	$\geq 0.5 \text{ GeV}$
SMT hits	$\geq 2$ (Data) $\geq 0$ (Monte Carlo)	$\geq 2$
$dca$ significance	$\leq 5.0$	$\leq 3.0$

TABLE XII

TRACK SELECTION OF THE TWO VERTEX ALGORITHMS AT THE SECOND PASS.

The average number of tracks per DØroot-PV in QCD multijet events is 20 and the average efficiency of the PV reconstruction is 98% (107). The efficiency of the PV reconstruction is about

100% in the central  $|z|$  region and drops quickly outside the SMT fiducial volume ( $|z| < 36$  cm for the barrel) due to the requirement of two SMT hits per track forming the PV. The resolutions (convoluted with the beam spot size) of  $x, y$  and  $z$  coordinates of the reconstructed PV depend on the number of tracks,  $N_{trksPV}$ , fitted into the PV, and are completely dominated by the beam spot starting from  $N_{trksPV} > 15$ . The resolution is about  $35\ \mu\text{m}$  in the transverse plane.

To ensure a high reconstruction quality the following additional PV selection is required:

- $|z_{PV}| \leq 60$  cm.
- At least three tracks fitted into the PV:  $N_{trksPV} > 2$ .
- The DØreco PV and the DØroot PV are required to have a  $z$ -separation of less than 5 cm.

### 4.3 Muons

Muons are reconstructed using information from two independent detector systems: the muon detector and the central tracker. A *local* track in the muon system is the basis of the muon identification. Muons are required to have hits in all three layers of the muon system (both inside and outside the toroid). The muon identification criteria are presented in Section 4.3.1. The superior track resolution from the central tracker is used to improve the knowledge of the kinematic properties of the muon, and to have a confirmation that the muon originated from the primary vertex. A refinement of the track  $p_T$  measurement is presented in Section 4.3.2. The muon momentum scale and resolution in MC is adjusted to the values found in the data, as discussed in Section 4.3.3. Section 4.3.4 describes the variables used to determine how well a muon is isolated from other physics objects in the event.

### 4.3.1 Muon Identification Criteria

The following standard Muon ID requirements are used:

- Muon candidates are required to be of ' $|nseg| = 3$  medium' quality, according to the following Muon ID criteria (105):
  - at least two wire hits in the A segment,
  - at least one scintillator hit in the A segment,
  - at least two wire hits in the BC segment,
  - at least one scintillator hit in the BC segment, (except for central muons with less than four wire hits in the BC segment).
- A loose cut against cosmics is applied, based on timing information from scintillator hits associated with the muon that requires A-layer and BC-layer scintillator times  $|t_A| < 10$  ns and  $|t_{BC}| < 10$  ns.
- the muon is required to be at  $|\eta| < 2.0$ .

In addition a *central track* match is required. This means that the muon tracks are extended to the point of closest approach (PCA) to the beam and their parameters are compared with those of tracks in the central tracker at the PCA. A global fit is performed with all central tracks within 1 radian in azimuthal and polar angle of a muon track at PCA. The central track with the highest  $\chi^2$ -probability is considered to belong to the muon candidate. The measurement of the muon track parameters are taken from the central tracking system. The following additional quality requirements are applied to the central track:

- $\chi^2_{track}/NDF < 4$  for the central track fit, to remove bad track fits.
- A distance  $|\Delta z(\mu, \text{PV})| < 1$  cm between the track and the primary vertex, to further reduce background from cosmics and badly reconstructed tracks
- $dca$  significance less than 3 standard deviations away from zero,  $dca/\sigma(dca) < 3$ , in order to reject muons from semi-leptonic heavy flavor decays.

Tracks that fail the  $\chi^2_{track}/NDF$  or  $\Delta z(\mu, \text{PV})$  quality cuts have a larger probability to give a very high  $p_T$  measurement ( $> 200$  GeV). Applying these cuts significantly reduce fake high  $p_T$  muons. The remaining high  $p_T$  muons can be explained by genuine muons, for which the track curvature  $q/p_T$  is well measured within the finite resolution of the central tracker.

#### 4.3.2 Muon Momentum Correction

A correction is applied to the momentum of muons matched to CFT-only tracks, i.e. those tracks where no hits are found in the SMT subdetector. The procedure considers the primary vertex as a constraint for the fit (105). The track is refitted such that the  $dca$  in  $x$  and  $y$  remains 0 (106). The correction factor is given by:

$$\text{SF}_{\text{CFT-only}} = 1 - dca/q_{opt} \cdot (\text{ERR}(r, q_{opt})/\text{ERR}(r, r)),$$

where  $dca$  is the muon  $r\phi$  distance of closest approach to the primary vertex,  $q_{opt}$  is the muon charge divided by the muon  $p_T$ ,  $\text{ERR}(r, q_{opt})$  and  $\text{ERR}(r, r)$  represent the respective error matrix entries where  $r$  is the  $r\phi$  impact parameter relative to  $(x, y, z) = (0, 0, 0)$ .

Roughly 18% of the muons are subject to this correction. In the central region much fewer muons are affected. The size of the correction is shown in Figure 58.

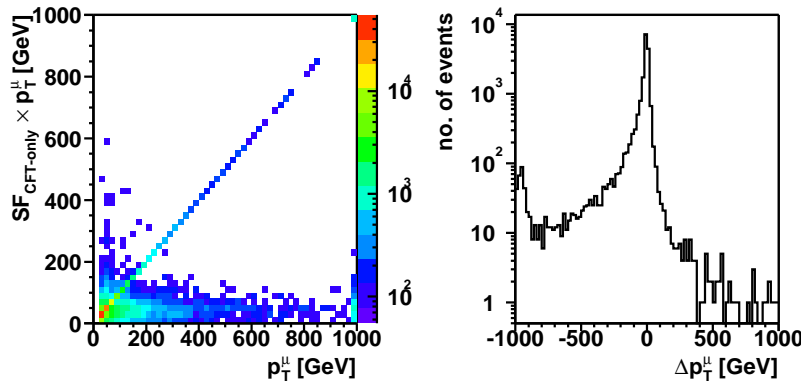


Figure 58. Left: Corrected muon  $p_T$  versus uncorrected muon  $p_T$ . Most of the time the correction is small and the  $p_T$ 's are very similar. In particular muons with a very high  $p_T$  ( $p_T > 200$  GeV) are corrected down. Right:  $p_T$  difference:  $SF_{CFT\text{-only}} \times p_T - p_T$  (119).

#### **4.3.3 Muon Momentum Scale and Resolution**

A comparison of the dimuon invariant mass distribution in  $Z$  candidate events shows (107) that the muon momentum scale and resolution in MC is better than in data, and the position of the  $Z$ -peak in MC is also shifted from that in data. Therefore, additional tuning is applied to the MC. The muon momentum is corrected by:

$$\frac{1}{p_T} \rightarrow \frac{1}{\alpha p_T} + G(0, \sigma_\xi), \quad (4.1)$$

where  $\alpha$  is the scale factor which accounts for the overall calibration, and  $G(0, \sigma_\xi)$  is a random variable drawn from a Gaussian distribution with a mean of 0 and a width  $\sigma_\xi$ .

The transformation from Equation 4.1 is performed for different parameter values of  $(\alpha, \sigma_\xi)$ ; this is done by systematically scanning the relevant parameter space in small steps. The optimum scale  $\alpha$  and the width of the Gaussian,  $\sigma_\xi$ , are obtained simultaneously from a Kolmogorov-Smirnov goodness-of-fit test (108) for the  $Z$  mass distribution in data and Monte Carlo.

The level of agreement between data and Monte Carlo is found to be dependent on the muon detector pseudo-rapidity,  $\eta_{det}$ . Due to the limited statistics, only two pseudo-rapidity regions are considered. First, the procedure is applied only to the events with both muons in the central region, defined as  $|\eta_{det}| < 1.62$ . Next, events with one muon in the central and the other one in the forward region were considered. In this case, the smearing applied to the central muon was fixed to the one obtained for central-central events and only the parameters of the forward muon were allowed to vary.

The result of this optimization procedure is summarized in Table XIII. Two different mass windows around the  $Z$  peak are considered,  $70 < m_{\mu\mu} < 110$  GeV and  $75 < m_{\mu\mu} < 105$  GeV. The same result is found, irrespective of the choice of mass window cuts.

A comparison of the position and the width of the  $Z \rightarrow \mu\mu$  peak in data and Monte Carlo before smearing is shown in Figure 59. The transverse momenta of muons in the simulation are corrected according to Equation 4.1 using the numbers for  $\sigma_\xi$  and  $\alpha$  from Table XIII. The details of the procedure for determining the scale and over-smearing for MC muons can be found in (107).

	$\alpha$	$\sigma_\xi$
central	0.991	$0.0025 \text{ GeV}^{-1}$
forward	0.996	$0.0043 \text{ GeV}^{-1}$

TABLE XIII

RESULT OF THE KOLMOGOROV-SMIRNOV GOODNESS-OF-FIT TESTS FOR MUONS IN THE CENTRAL REGION ( $|\eta_{DET}| < 1.62$ ) AND MUONS IN THE FORWARD REGION ( $1.62 \leq |\eta_{DET}| \leq 2.00$ ).  $\alpha$  REPRESENTS THE TRANSVERSE MOMENTUM SCALE CORRECTION AND  $\sigma_\xi$  IS THE WIDTH OF THE GAUSSIAN OVERSMEARING.

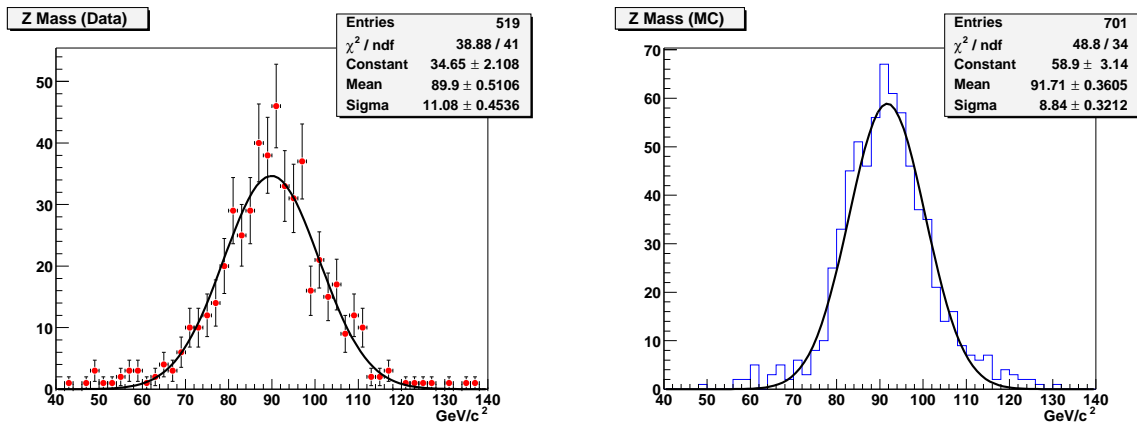


Figure 59.  $Z \rightarrow \mu\mu$  mass peak fit. The result obtained for data is shown on the left, the Monte Carlo result before tuning, on the right (111).

#### 4.3.4 Muon Isolation Criteria

The main background for identification of muons comes from semileptonic decays in heavy quark jets. Compared to muons originating from the leptonic decay of a  $W$  boson, those muons tend to be non-isolated and have a lower transverse momentum. Muon isolation is used to distinguish muons from these two different sources. A loose isolation criteria is defined by demanding that a muon is separated from a jet,  $\Delta R(\mu, \text{jet}) > 0.5$ .

In previous  $t\bar{t}$  cross-section measurements (109) the following variables and cuts were used as a measure of muon isolation (110):

- $\text{Halo}(0.1,0.4) < 2.5$  GeV, where  $\text{Halo}(0.1,0.4)$  is the sum of the  $E_T$  of calorimeter clusters in a hollow cone between  $\Delta R = 0.1$  and  $\Delta R = 0.4$  away from the muon, as illustrated in Figure 60. In forming this sum, cells in the electromagnetic and fine hadronic calorimeters are considered. Due to an enhanced noise level, the coarse hadronic calorimeter is excluded from the sum.
- $\text{TrkCone}(0.5) < 2.5$  GeV, where  $\text{TrkCone}(0.5)$  is the sum of the  $p_T$  of all tracks within a cone of radius  $\Delta R = 0.5$  surrounding the muon. The track matched to the muon is excluded from this sum.

It was found (111) that the separation between the two classes of muons mentioned above could be improved by using the difference between their  $p_T$  spectra. Thus, more powerful isolation variables were defined, taking the ratio of the above isolation variables and the transverse momentum of the muon,  $p_{T_\mu}$ :

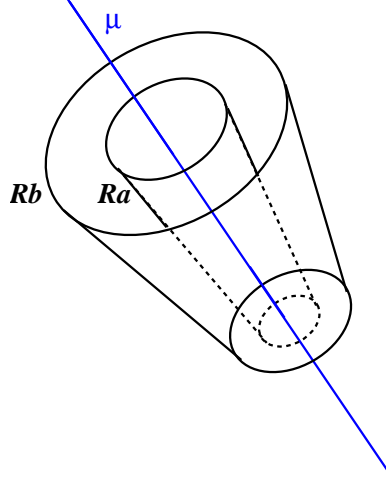


Figure 60. A hollow cone in  $R$ , with the inner edge  $R_a$  and the outer edge  $R_b$  surrounding the muon.  $\text{Halo}(0.1,0.4)$  is calculated by summing the transverse energies of all calorimeter cells  $i$  with  $R_i$ :  $R_a > R_i > R_b$ .

- $\text{Rat11} \equiv \text{Halo}(0.1,0.4)/p_{T\mu} < 0.08$  and
- $\text{Rattrk} \equiv \text{TrkCone}(0.5)/p_{T\mu} < 0.06$ .

Typical distributions and relative survival probabilities for these two variables are shown in Figure 61 for  $t\bar{t}$ ,  $W$ +jets and QCD events.

#### 4.4 Electrons

Electromagnetic candidates (EM objects), such as electrons and photons, are initially identified based on calorimeter information. Since photons are particles with no charge, they do not leave signals in the tracking system. Thus, a track matched to the energy deposit in the calorimeter provides a tool to distinguish electrons from photons. The electron reconstruction and identification criteria are presented in Section 4.4.1. The electron energy scale is discussed

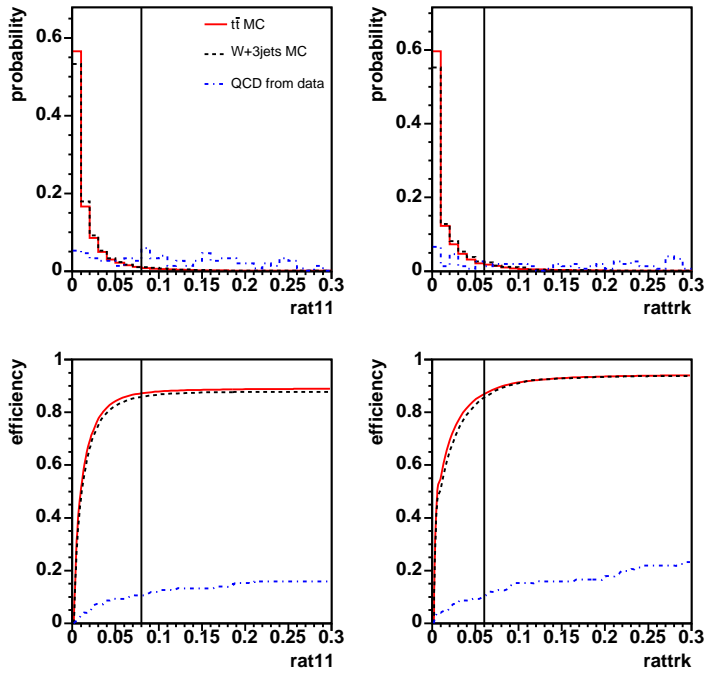


Figure 61. Top: Distributions for  $\text{rat11}$  and  $\text{rattrk}$  for  $t\bar{t} \rightarrow \mu\nu_\mu b\bar{b}q\bar{q}\ell$  MC,  $W + 3\text{jets MC}$  and QCD data. Bottom left: Relative cut efficiencies as a function of the  $\text{rat11}$  isolation variable. The  $\text{rattrk} < 0.06$  cut has already been applied. Bottom right: Relative cut efficiency as a function of  $\text{rattrk}$ . The cut on  $\text{rat11} < 0.08$  has already been applied. The cuts are indicated by vertical lines (111).

in Section 4.4.2, and a discussion of the corresponding energy resolution is presented in Section 4.4.3.

#### **4.4.1 Electron Reconstruction and Identification**

Electrons are reconstructed from information in two subdetectors, the calorimeter and the tracker. This typically proceeds in two stages: a cluster is formed in the calorimeter and subsequently confirmation is sought from the tracker. A simple cone algorithm clusters calorimeter cells based on precision readout data around seeds with  $E_T > 1.5$  GeV in a cone of radius  $\Delta R = \sqrt{\Delta\eta^2 + \Delta\phi^2} < 0.2$ . Various parameters are calculated for every EM cluster that is formed by the simple-cone algorithm. This gives flexibility when defining EM objects.

**ID:** all EM clusters are assigned an ID of 10. If in addition a cluster has a track loosely matched (in  $\eta$  and  $\Phi$ ) to it, it is assigned an ID of  $\pm 11$  (“+” for electrons, “-” for positrons).

**Isolation:** the isolation of an identified cluster is defined by the following variable

$$EM_{iso} = \frac{E_{tot}(R < 0.4) - E_{EM}(R < 0.2)}{E_{EM}(R < 0.2)}, \quad (4.2)$$

where  $E_{EM}(R < 0.2)$  is the EM energy within a cone of radius  $R < 0.2$  (based on EM layers), and  $E_{tot}(R < 0.4)$  is the total energy within a cone of radius  $R < 0.4$  (based on EM, FH, and CH layers). Figure 62 illustrates the definition of the isolation parameter. All initial EM clusters are required to have an isolation of less than 0.15. The isolation parameter gives a measure of how deep and narrow a given cluster is. EM objects tend to deposit most of their

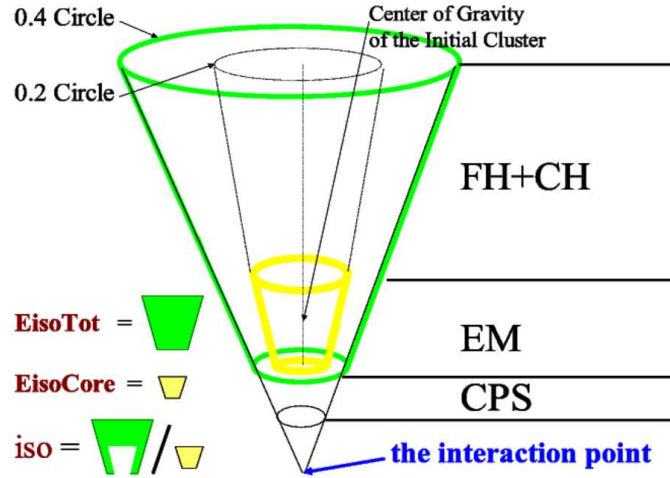


Figure 62. Illustration of the Isolation Parameter:  $EisoTot$  is the energy in a cone of radius 0.4 (using EM, FH, and CH layers).  $EisoCore$  is the energy in a cone of radius 0.2 (using EM layers). The numerator of  $iso$  subtracts  $EisoCore$  from  $EisoTot$ .

energy in a narrow region of the EM layers, while hadrons deposit their energies in the hadronic layers in a much wider radius.

**Electromagnetic Fraction:** the electromagnetic fraction ( $EM_f$ ) discriminates between EM and hadronic calorimeter energy deposits. It takes advantage of the fact that EM showers are almost entirely contained within the EM layers of the calorimeters. EM fraction is defined as

$$EM_f = \frac{E_{EM}(R < 0.2)}{E_{tot}(R < 0.2)}, \quad (4.3)$$

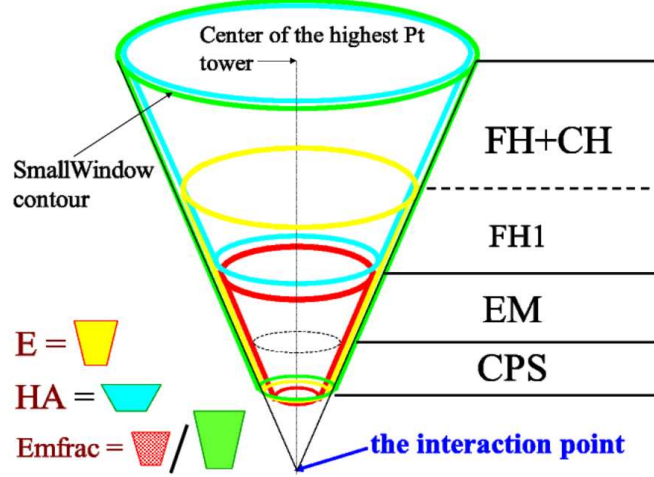


Figure 63. Illustration of the EM fraction parameter: EM fraction is the ratio between the energy in the CPS plus EM layers, and the energy in the CPS plus EM layers plus hadronic layers.

where  $E_{EM}(R < 0.2)$  is the EM energy within a cone of radius  $R < 0.2$  (based on EM layers), and  $E_{tot}(R < 0.2)$  is the total energy within a cone of radius  $R < 0.2$  (based on EM, FH, and CH layers). Figure 63 illustrates the definition of the EM fraction parameter. Electromagnetic clusters are required to have a large EM fraction ( $EM_F > 0.9$ ).

**H-Matrix:** the H-Matrix distinguishes between EM and hadronic energy deposits, by analyzing the longitudinal and transverse shape of the showers. Based on MC generated electrons, a covariance matrix ( $M$ ) is defined using a set of seven discriminant variables

$$M_{ij} = \frac{1}{N} \sum_{n=1}^N (x_i^n - \langle x_i \rangle) (x_j^n - \langle x_j \rangle), \quad (4.4)$$

where  $x_i^n$  is the value of variable  $i$  for electron  $n$ , and  $\langle x_i \rangle$  is the mean value of variable  $i$ . The seven variables that are used are listed below:

- Shower energy fractions in 1<sup>st</sup>, 2<sup>nd</sup>, 3<sup>rd</sup>, and 4<sup>th</sup> EM layer of the calorimeter.
- Cluster size in  $r - \Phi$  based on the 3<sup>rd</sup> EM layer of the calorimeter (EM showers typically deposit the bulk of their energy in the 3<sup>rd</sup> EM layer).
- Total shower energy.
- Primary vertex position.

The H matrix is defined as the inverse of the covariance matrix  $M$

$$H \equiv M^{-1}. \quad (4.5)$$

Using the H matrix, a  $\chi^2$ -like variable is calculated that gives a measure of the likelihood that a given shower  $k$  is consistent with an EM object shower

$$\chi^2 = \sum_{ij} (x_i^k - \langle x_i \rangle) H_{ij} (x_j^k - \langle x_j \rangle). \quad (4.6)$$

Electromagnetic clusters are required to have  $Hmx < 50$ .

**Track Matching:** requiring that a track is associated with a calorimeter EM cluster is a powerful discriminant between electrons and photons. In this analysis, *global tracks* are used

for tracking confirmation, i.e. tracks based on information from both the CFT and SMT subdetectors. Using calorimeter and tracking information, the following  $\chi^2$  variable is calculated

$$\chi^2 = \left( \frac{\Delta\Phi}{\sigma_\Phi} \right)^2 + \left( \frac{\Delta z}{\sigma_z} \right)^2, \quad (4.7)$$

where in Equation 4.7:

- $\Delta\Phi$  ( $\Delta z$ ) is the difference in  $\Phi$  ( $z$ ) between the EM cluster position in the 3<sup>rd</sup> EM calorimeter layer and the extrapolation of the track to the same layer.
- $\sigma_\Phi$  and  $\sigma_z$  are the root-mean-squares of the experimental measurements of each quantity.

A track is considered matched to an EM cluster if the track matching  $\chi^2$  probability is  $P(\chi^2) > 0$ .

**Electron Likelihood:** a likelihood method is a more efficient way of separating good electrons from background than square cuts, since it uses information in the signal and background shapes to distinguish between electrons and background. The likelihood (112) used in this analysis is based on seven variables:

- EM fraction .
- $H$ -matrix.
- The ratio of the calorimeter transverse energy of the cluster to the transverse momentum of the matched track,  $E_T^{Cal}/p_T^{trk}$ . This ratio is a good discriminator since it does not tend toward 1 for background objects.
- The above mentioned track matching  $\chi^2$  probability,  $Prob(\chi_{SpatialEM-trk}^2)$ . Background events tend to have a worse spatial match between the track and the calorimeter positions.

- Distance of closest approach, i.e. the shortest distance of the selected track to the line parallel to the z-axis which passes through the primary vertex.
- Number of tracks in a  $\Delta R < 0.05$  cone. This is a good variable for removing photon conversions since such events tend to have two tracks very close together instead of just one track like a good electron.
- The sum of the  $p_T$  of all tracks in a  $\Delta R < 0.4$  cone around the associated track. It is intended to remove jets, which tend to have several significant tracks in this cone.

Smoothed, normalized distributions for each of these variables are made for both signal and background samples. Then, to distinguish electrons from background objects, the following likelihood discriminant is build

$$\mathcal{L}(\mathbf{x}) = \frac{P_{sig}(\mathbf{x})}{P_{sig}(\mathbf{x}) + P_{bkg}(\mathbf{x})}, \quad (4.8)$$

where  $P_{sig}$  and  $P_{bkg}$  are the probabilities for a given EM object to be signal or background. The electron likelihood selection cut is  $\mathcal{L} > 0.85$ . A detailed study of the electron reconstruction and identification can be found in (113).

#### 4.4.2 Electron Energy Scale

A comparison of the dielectron invariant mass distribution in  $Z$  candidate events shows (107) that the electron energy resolution in MC is better than in data, and the position of the  $Z$ -peak

in MC is also shifted from that in data. Therefore, additional tuning is applied to the MC. The energy resolution of electrons can be parametrized as

$$\frac{\sigma(E)}{E} = C \oplus \frac{S}{\sqrt{E}} \oplus \frac{N}{E}, \quad (4.9)$$

where,  $C$ ,  $S$ , and  $N$  represent the constant, sampling and noise terms, respectively. Therefore one may use the following parametrization to adjust the scale and width of the MC electron's energy distribution

$$\begin{aligned} E' &= E \times [\alpha + \xi_1 = Gaus(0, \sigma = \alpha c) \\ &\quad + \xi_2 = Gaus(0, \sigma = s\sqrt{\alpha/E}) \\ &\quad + \xi_3 = Gaus(0, \sigma = n/E)], \end{aligned} \quad (4.10)$$

where  $\alpha$  is the scale factor, and  $\xi_1$ ,  $\xi_2$  and  $\xi_3$  provide additional smearing to the width, and are random corrections drawn from a Gaussian distribution with mean zero and standard deviation  $\sigma$ . The variables  $c$ ,  $s$  and  $n$  are the over-smearing coefficients in the constant, sampling and noise terms. It has been observed (114) that the scale factor and the oversmearing provided by  $\sigma = \alpha c$  alone is sufficient to tune the electron energy in MC to that in data. A comparison of the position and the width of the  $Z \rightarrow ee$  peak in data and Monte Carlo before tuning is shown in Figure 64. The details of the procedure for determining the scale and over-smearing for MC electrons can be found in (107).

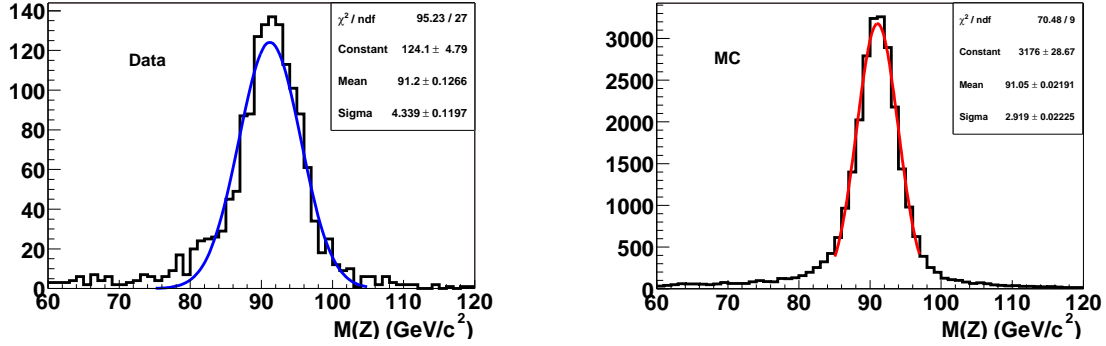


Figure 64.  $Z \rightarrow ee$  mass peak fit. The result obtained for data is shown on the left, the Monte Carlo result before tuning, on the right (114).

#### 4.4.3 Electron Energy Resolution

Once the MC electron energy has been scaled and over-smeared as discussed in the previous section, the electron energy resolution is determined by comparing the energy of the generated electron to that of a matched reconstructed electron in a  $\Delta R$  ( $\equiv \sqrt{\Delta\eta^2 + \Delta\phi^2}$ ) cone of 0.4. A Gaussian is fit to the reconstructed energy distribution in the range  $\pm 3\text{RMS}$  from the mean of the distribution. The fitted *mean* and the *width* are then extracted. Figure 65 shows the ratio of the width to the fitted mean, as a function of different values of the generated energy ( $E_{true}$ ), used to obtain the energy resolution curve. This curve is then fitted to the functional form in Equation 4.9 resulting in a value of  $0.044 \pm 0.0002$  for the constant term,  $C$ , and  $0.224 \pm 0.0018 \sqrt{\text{GeV}}$  for the sampling term,  $S$ . Since this analysis uses high- $p_T$  electrons, the fit is not sensitive to the noise term,  $N$  (107).

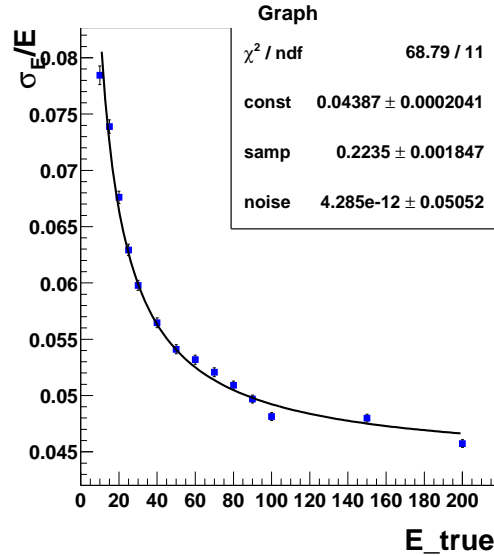


Figure 65. The fractional electron energy resolution versus the generated energy for electrons in the Central Calorimeter.

#### 4.5 Jets

Hadronic particles are reconstructed as jets in the calorimeter; the algorithm for the reconstruction is presented in Section 4.5.1. An additional algorithm (T42), used to reduce contributions from noisy cells to the jet, is discussed in Section 4.5.2. In order to be considered a good jet, reconstructed jets have to meet identification criteria that are given in Section 4.5.3. Electromagnetic objects might also be reconstructed as jets; the method used to separate them is subject of Section 4.5.4. The reconstructed energy in a jet cone is not equal to the original

particle level energy. The necessary corrections are discussed in Section 4.5.5. The measurement of the jet energy resolution is presented in Section 4.5.6.

#### 4.5.1 The Jet Reconstruction Algorithm

The interaction of hadronic particles with the calorimeter, explained in Section 3.2, results in a shower of hadronic particles which has typically the shape of a cone. The ideal jet algorithm should reconstruct the kinematic properties of the initial hadronic particle. In particular, it should be infrared (see Figure 66) and collinear safe (see Figure 67), independent of the detailed detector geometry and granularity, have a maximal reconstruction efficiency and require a minimal CPU time.

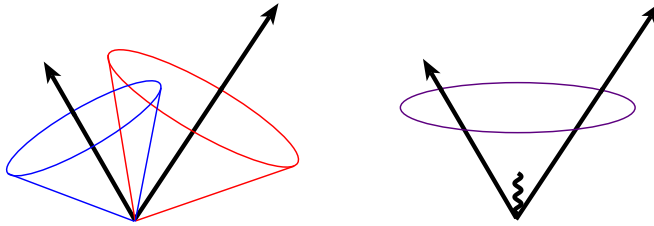


Figure 66. An illustration of infrared sensitivity in cone jet clustering. Clustering begins around seed particles, shown as arrows with length proportional to energy. Soft radiation (right sketch) between two jets may cause a merging of the jets.

The jet algorithm associates adjacent particles, reconstructed as clusters of energy in the calorimeter, into jets. The *improved legacy cone* algorithm (115) comes closest to the ideal jet reconstruction, as discussed above, and is used for the analysis presented.

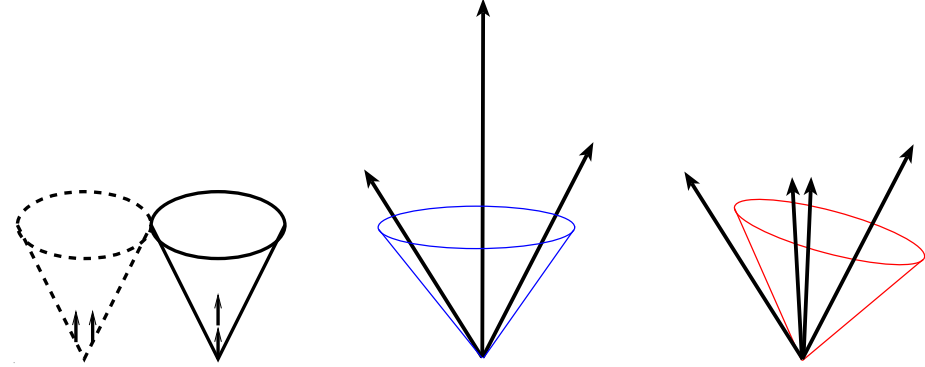


Figure 67. An illustration of collinear sensitivity in cone jet clustering. Left two sketches: No seed particle is produced due to the energy splitting among several detector towers (left), whereas a seed is produced without the splitting (right). The right two sketches show the sensitivity of the jet reconstruction to an  $E_T$  ordering of seed particles

The first step of the algorithm is to find seeds, represented by calorimeter towers above a minimum seed threshold,  $E_T^{tower} > E_T^{seed}$ , where a tower is defined as the sum of all cells sharing the same pseudo-rapidity and azimuthal angle. Cells in the coarse hadronic calorimeter, the end cap massless gap, or the end cap hadronic layer 16 or 17, are not considered as seeds due to an enhanced noise level.

Proto-jets are created with a simple cone algorithm from an  $E_T$  ordered list of seeds. A seedless algorithm is found to be infrared safe and is therefore preferred over an algorithm with seeds, however, it is expensive computationally. An approximation of a seedless algorithm is achieved by the addition of midpoints,  $E_T$  weighted centers between pairs of proto-jets. These centroids are also considered as proto-jets. Overlapping cones are separated with a split and merge procedure.

The jet algorithm specifications can be summarized as:

- $R_{cone} = 0.5$ ,
- $E_T^{seed} = 0.5$  GeV,
- add midpoints after the cone clustering,
- split and merge proto-jets,
- keep all jets with more than  $E_T^{reco} = 8$  GeV.

#### **4.5.2 The T42 Algorithm**

The T42 algorithm has been introduced (116) to enhance the treatment of the calorimeter noise. This leads to an improvement in the reconstruction of different objects (electrons, photons, jets,  $\cancel{E}_T$ ), whose identification and energy measurement relies mainly on the calorimeter.

Calorimeter noise, generally defined as energy deposition not related to the hard interaction, can be schematically classified as “hot”, “warm” or “normal”: **Hot noise:** Hot cells are related to detector problems (hardware failure, abnormal electronic noise), or to physics processes like backscattering of particles interacting in the beampipe outside of the vertex interaction region into the calorimeter. Their energy is typically large,  $> 1$  GeV. **Warm noise:** Warm cells are due to pedestal subtraction problems or hardware deficiencies. The cell energy levels are typically lower, on the order of hundred of MeV, however, they might appear in great numbers in a definite region of the detector, creating so-called warm zones. **Normal noise:** Normal noise cells appear due to Gaussian electronic noise surviving the zero suppression. They are at

lower energies, typically below  $4\text{-}5\sigma$ , where  $\sigma$  is the RMS of the pedestal. Typically, between 1000 and 3000 such cells appear per event.

The T42 algorithm is implemented in the TopAnalyze code (62) and is applied before reconstructing the calorimeter objects. It aims to reject “normal” noise cells. For the T42 algorithm, an isolated cell is considered a noise cell and thus discarded if it is not “signal-like”. A cell is considered “signal-like” if its energy is positive (negative energy cells can originate from electronics noise and from pile-up which is baseline subtracted) and above a high threshold of  $+4\sigma$ , or if its energy is above  $+2.5\sigma$  and the energy of a neighboring cell is above  $+4\sigma$ . The acronym T42 stands for “threshold  $4\sigma - 2\sigma$ ”, however, the current implementation corresponds to “threshold  $4\sigma - 2.5\sigma$ ”, resulting in the name T42.5.

The first electromagnetic layer (layer 1), and the layers 8, 9 and 10 of the intercryostat region are not considered by the algorithm; so all cells in those layers with positive energy are kept in the event, and are not used as neighbors. A detailed description of the current implementation of the T42 algorithm can be found in (117).

The ratio of rejected cells by T42 over the number of cells in the event ranges from 30% to 60%. In the main part of the calorimeter ( $|\eta| < 3.2$ ), the fraction of cells rejected by T42 corresponds to the number of cells expected from noise between  $2.5$  and  $4\sigma$ , assuming a Gaussian distribution (118). This is a good indication that T42 is indeed reducing mainly noise cells. In the forward region, more cells than expected are rejected, since cells from pile-up effects accumulate close to the beam-pipe (118); however, this has no influence on high  $p_T$  physics, which is the subject of the analysis presented.

### 4.5.3 Jet Identification

Once jets are clustered following the cone algorithm, further quality selection cuts are applied to each jet. The following criteria are aimed at removing jets which are not reconstructed from hadronic particles from the hard interaction:

- To remove isolated electromagnetic particles, a cut on the energy fraction, deposited in the electromagnetic section of the calorimeter ( $EMF$ ) is applied at  $0.05 < EMF < 0.95$ .
- To remove jets which predominantly deposit their energy in the coarse hadronic section of the calorimeter, a cut on the fraction of the jet energy deposited therein ( $CHF$ ) is applied at  $CHF < 0.4$ . The noise level is higher in the coarse hadronic section; this cut is essentially aimed at removing those jets which clustered around noise in the coarse hadronic section.
- To remove jets clustered from hot cells, a cut on the ratio of the highest to the next-to-highest transverse energy cell in the calorimeter ( $HotF$ ) is applied at  $HotF < 10$ .
- To remove those jets clustered from a single hot tower, the number of towers containing 90% of the jet energy ( $n90$ ) is required to be greater than 1.
- The minimum  $p_T$  requirement for jets after the jet energy scale correction (see Section 4.5.5) is 15 GeV.

The cut values for these variables were determined from data by defining samples which contain predominantly jets which should be kept (denoted as *good* jets), and samples which are

enriched in jets reconstructed from noise denoted as *fake* jets. The cuts aim to reject the latter jets, while keeping a high identification efficiency for the good jets.

#### 4.5.3.1 L1 Jet Confirmation

Residual noise in identified jets is removed by the L1 Jet Confirmation.

Fake jets originating from noise in the calorimeter readout are found to have the largest contribution to the remaining fake jets. An alternative calorimeter readout, the L1 trigger readout chain, is therefore utilized to confirm the presence of good jets. The comparison of the energy in the L1 compared to precision readout is found to be the most powerful discriminant against noise, which does not appear simultaneously in the two readout chains.

A new variable,  $L1SET$ , is defined for a given jet as the scalar sum of the trigger towers  $E_T$  inside the jet cone of  $R = 0.5$ . To quantify the agreement of the transverse energy measurement of the two readout chains, and thus confirm the quality of the jet, the ratio of the two energy measurements is built

$$\frac{L1SET}{E_T^{reco} \cdot (1 - CHF)} . \quad (4.11)$$

The  $L1SET$  measurement is not corrected for the JES and it does not include the coarse hadronic calorimeter section. In order to get the best correlation between the energy measured in the precision and L1 readout, the uncorrected jet  $E_T$  from the precision readout is used for the ratio,  $E_T^{reco}$ , subtracting the coarse hadronic energy fraction  $CHF$ .

The level of noise is found to be dependent of the  $|\eta_{det}|$  of the jet; different cut values are therefore chosen for the three regions of pseudo-rapidity corresponding to the geometry of the calorimeter (CC, ICD and EC, see Section 3.3.4).

Figure 68 shows the distribution for  $\frac{L1SET}{E_T^{reco} \times (1-CHF)}$  for good jets and for fake jets and the survival efficiencies for cutting on this variable. The cut values on  $\frac{L1SET}{E_T^{reco} \times (1-CHF)}$  were chosen to have a high efficiency ( $> 99\%$ ) and to reject the maximum amount of alledged fake jets (Figure 68); the cut values are summarized in Table XIV.

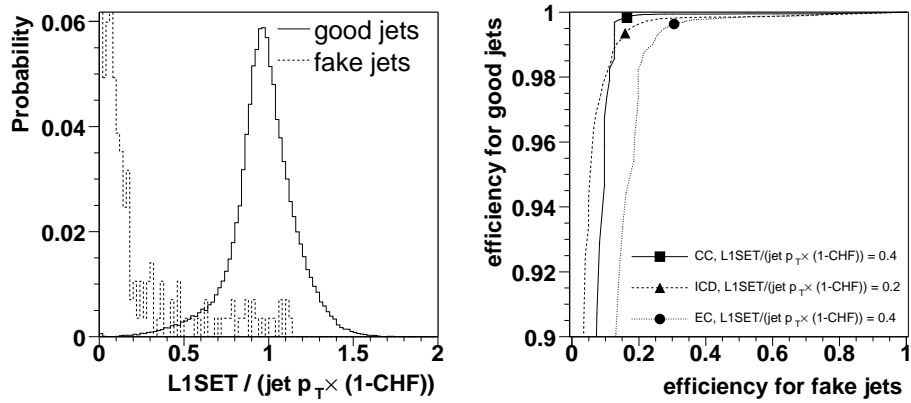


Figure 68. Left:  $\frac{L1SET}{E_T^{reco} \times (1-CHF)}$  distribution for good jets from a dijet sample and for fake jets from a multijet sample, integrated over the full pseudo-rapidity region. Right: The corresponding survival efficiency for the good vs. the fake jets varying the cut on  $\frac{L1SET}{E_T^{reco} \times (1-CHF)}$ . The CC, ICD and EC regions are defined in the text, the chosen cut values for the three  $\eta_{det}$  regions are highlighted by the solid points (111).

	CC	ICD	EC
$\frac{L1SET}{E_T^{reco} \times (1 - CHF)}$	0.4	0.2	0.4

TABLE XIV

ADDITIONAL JET IDENTIFICATION CRITERION: CUT VALUES ON  $\frac{L1SET}{E_T^{RECO} \times (1 - CHF)}$  FOR THE THREE CALORIMETER REGIONS.

#### 4.5.4 Separation of Jets from Electromagnetic Objects

Electrons and photons with transverse energy greater than 8 GeV are also reconstructed as jet objects in the calorimeter. This represents a twofold challenge: how to discriminate between real jets and electromagnetic objects, and how to apply the appropriate energy correction for the type of interaction with the calorimeter (i.e. electromagnetic vs. nuclear).

The reconstructed EM jet objects are classified in three groups: regular jets, photons and electrons. Regular jets generally have some nearby energy in the hadronic layers of the calorimeter, or a shower shape inconsistent with that of a photon or electron. These jets should be corrected by the jet energy scale and classified as jets. The second class would pass cuts which mark them as dominated by energy from an electromagnetic shower from an electron-like particle (ie. a photon), and they are usually the result of jets fragmenting to a leading  $\pi^0$ . These objects should also be classified as jets, but the EM scale is a more appropriate energy correction. The last category are not jets, and should be corrected by the EM scale.

Reconstructed and identified (see Section 4.5.3) jet candidates are not considered as jets but as electron candidates if they overlap with an electromagnetic object ( $\Delta R(jet, EM) < 0.5$ ) with the following selection criteria:

- $p_T > 15.0$  GeV (after jet energy scale correction),
- $|\eta_{det}| < 2.5$ ,
- $EMF > 0.9$ ,
- $f_{\text{iso}} < 0.15$ ,
- $H\text{-matrix}7 < 50$ .

#### **4.5.5 Jet Energy Scale**

The calorimeter is very effective at absorbing the hadronic energy of the jet. However there are several mechanisms which cause the energy of the cells clustered into a jet to deviate from the energy of the initial parton. The most important ones are summarized below:

**Calorimeter Response (R):** hadronic showers may lose energy in ways which do not leave any ionization; electromagnetic and hadronic particles may therefore be imbalanced. Furthermore, the measured jet energy can be distorted due to a different response of the calorimeter to different particles, a non-linear response of the calorimeter to the particle energies, un-instrumented regions of the detector, or dead material.

**Energy Offset (O):** energy in the clustered cells which is due to the underlying event, multiple interactions, energy pile-up, electronics noise and noise from the Uranium absorber can provide an offset to the energy of the jet.

**Showering Corrections (S):** a fraction of the jet energy is excluded due to the finite size of the cone used for clustering. The Jet Energy Scale (JES) corrections attempt to correct the reconstructed jet energy,  $E^{reco}$ , back to the particle level energy,  $E^{corr}$ , as it was before interacting with the calorimeter. The correction may be written as

$$E^{corr} = \frac{E^{reco} - O}{R \times S},$$

where  $R$  is the calorimeter response to a jet,  $O$  is the energy offset, and  $S$  is the fraction of shower leakage outside the jet cone in the calorimeter.

$R$  is determined by examining QCD Compton events (111). The energy of the photon is purely electromagnetic and its electromagnetic energy scale can be calibrated independently using  $Z \rightarrow ee$  events. The transverse energy of the jet should therefore balance the transverse energy of the photon.  $O$  is determined from energy densities in events which are triggered when a minimum activity in the luminosity monitor is reported (so-called minimum bias triggered events).  $S$  is determined from measured energy profiles of jets.

Since not all of these different effects might be modeled accurately in the simulation, a separate JES correction is provided for data and MC. In the current analysis the JetCorr v5.3 package (122) is used. The corrections applied to data and MC are shown in Figure 69 and Figure 70 respectively.

The total systematic uncertainty assigned to the JES correction is estimated conservatively as:

$$\sigma = \sqrt{\sigma_{stat,data}^2 + \sigma_{syst,data}^2 + \sigma_{stat,MC}^2 + \sigma_{syst,MC}^2}. \quad (4.12)$$

The statistical and the total (quadratic sum of statistical and systematic) uncertainties are shown in Figure 69 for the data and in Figure 70 for the MC. The quadratic sum of the systematic uncertainties on the data  $\sigma_{syst,data}^2$  and the MC  $\sigma_{syst,MC}^2$  in Equation 4.12 is known to lead to an overestimation of the systematic uncertainty, since the systematics are correlated for the most part among data and MC, and the systematics relevant to the analysis presented arise only from the relative systematic uncertainty between data and MC. These correlations are currently unknown and therefore, conservatively, no correlations are assumed in Equation 4.12.

The JES corrections are expected to depend also on the flavor of the jet. In particular,  $b$  jets may have a different response and also a different showering correction due to their harder fragmentation. For the analysis presented, only one additional class of jets is considered: jets containing a muon ( $\Delta R(\mu, jet) < 0.5$ ). The hypothesis is that the muon originates from a semileptonic  $b$  decay, which produces a neutrino along with the muon. As an approximation, it is assumed that the neutrino carries the same momentum as the muon, and the jet is corrected in addition for these two particles.

#### **4.5.6 Jet Energy Resolution**

The jet energy resolutions are measured using a dijet event sample consisting of two jets that pass all jet ID cuts. No  $\cancel{E}_T$  cut is imposed on the sample. The details of the event selection

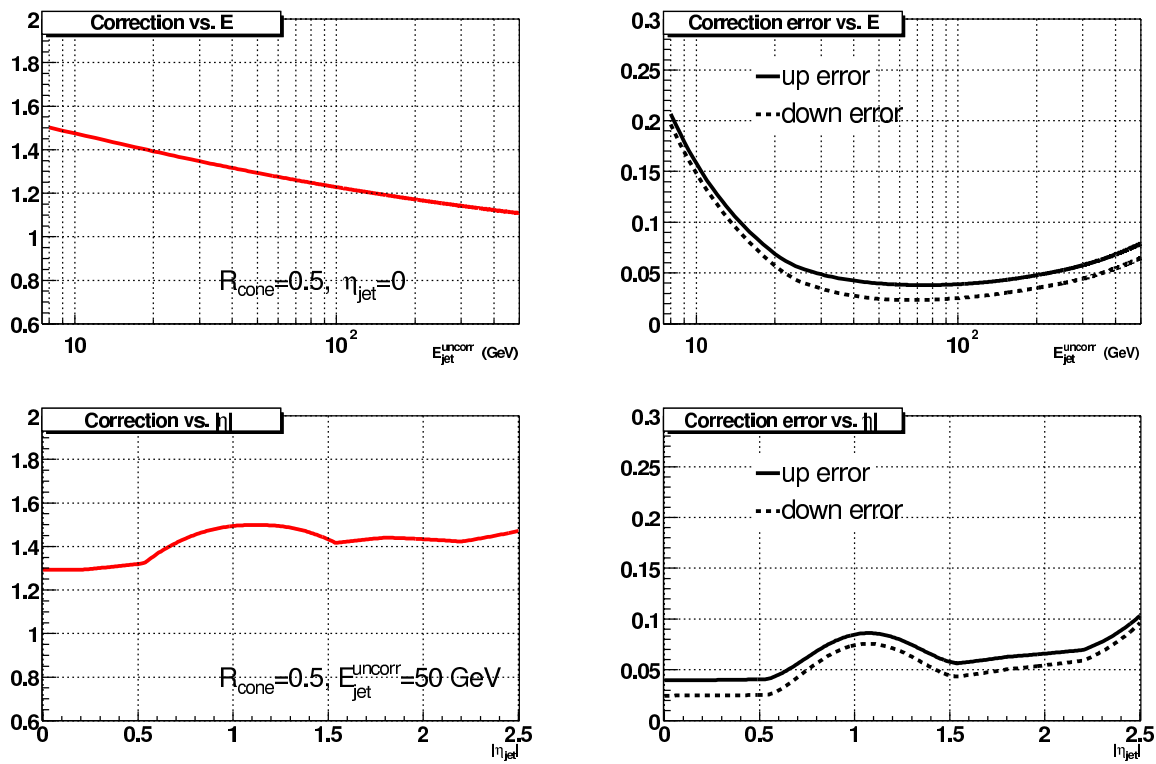


Figure 69. JES measurement in data. Left: JES correction as a function of uncorrected jet energy (top) and as a function of jet  $\eta_{\text{det}}$  (bottom). The respective statistical and total uncertainties are shown on the right (121; 122).

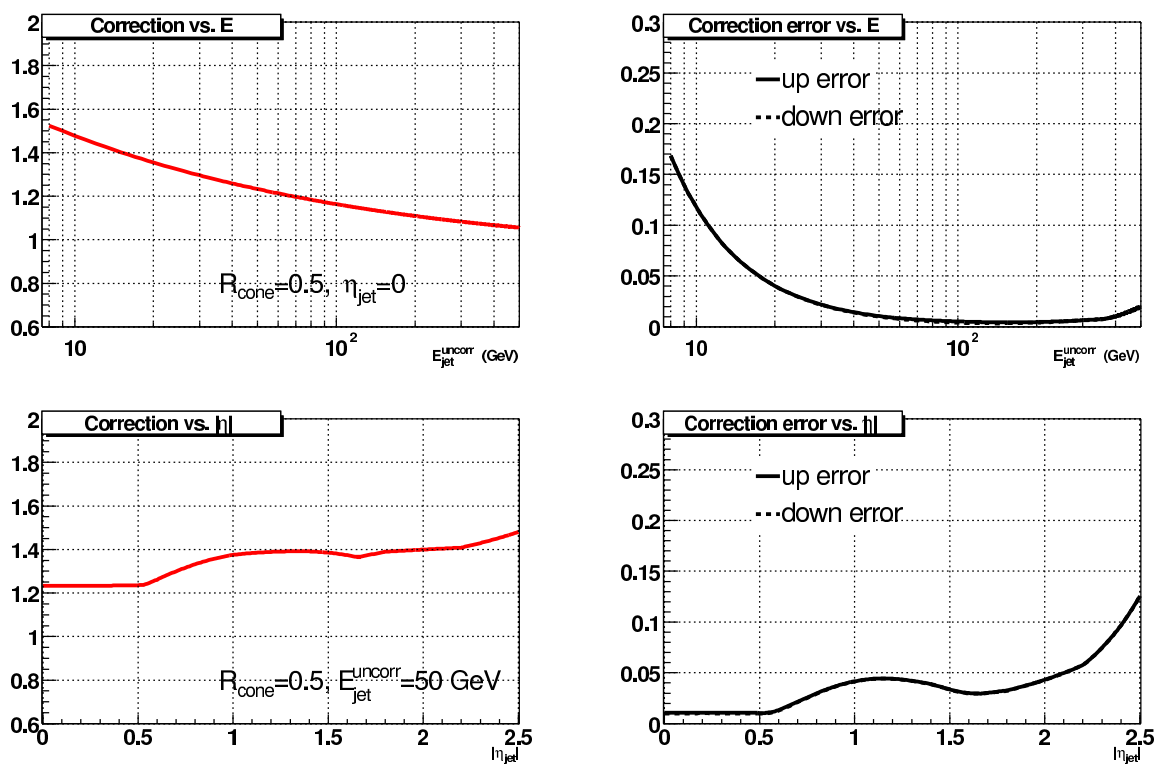


Figure 70. JES measurement in MC. Left: JES correction as a function of uncorrected jet energy (top) and as a function of jet  $\eta_{det}$  (bottom). The respective statistical and total uncertainties are shown on the right (121; 122).

can be found in (122). The single jet trigger used becomes fully efficient for a jet  $p_T$  above 40 GeV. Therefore this dijet data is used to measure the jet energy resolutions only above this threshold.

The sample is split in several bins of average  $p_T$  of the dijet system,  $\langle p_T \rangle = (p_{T1} + p_{T2})/2$ , and for each  $\langle p_T \rangle$  bin the distribution of the transverse momentum asymmetry variable

$$A = \frac{|p_{T1} - p_{T2}|}{p_{T1} + p_{T2}} \quad (4.13)$$

is studied. The width of the  $A$  distribution,  $\sigma_A$ , obtained from a Gaussian fit with a mean value set to zero, gives the jet  $p_T$  resolution through the formula

$$\frac{\sigma_{p_T}}{p_T} = \sqrt{2} \sigma_A. \quad (4.14)$$

In order to derive the resolution for the jet  $p_T$  in the range below 50 GeV, QCD Compton events are used. The events are triggered by a single EM trigger with no track requirement. In the case of QCD Compton events, the asymmetry variable is defined as

$$A_{pj} = \frac{p_T^{jet} - p_T^\gamma}{p_T^\gamma}. \quad (4.15)$$

$ \eta_{det} $ range	$N$	$S$	$C$
$0.0 <  \eta_{det}  < 0.5$	5.05	0.753	0.0893
$0.5 <  \eta_{det}  < 1.0$	0.	1.20	0.0870
$1.0 <  \eta_{det}  < 1.5$	2.24	0.924	0.135
$1.5 <  \eta_{det}  < 2.0$	6.42	0.	0.0974

TABLE XV  
JET ENERGY RESOLUTION COEFFICIENTS FOR DATA.

Given that the resolution of the photon is much better than the resolution of the hadronic jet,

$\sigma_{p_T^\gamma}$  can be ignored compared to  $\sigma_{p_T^{jet}}$ , and the jet resolution can be expressed as

$$\frac{\sigma_{p_T^{jet}}}{p_T^{jet}} = \sigma_{A_{pj}} \times R_{pj}, \quad (4.16)$$

where  $R_{pj} = p_T^\gamma / p_T^{jet}$  is a factor that corrects the imbalance between the average jet  $p_T$  and the photon  $p_T$  in each  $p_T$  bin.  $R_{pj}$  is found to be compatible with unity given the systematic uncertainties on the JES.

The results obtained from the dijet and the QCD Compton samples are put together and fitted using the formula

$$\frac{\sigma(p_T)}{p_T} = \sqrt{C^2 + \left(\frac{S}{\sqrt{p_T}}\right)^2 + \left(\frac{N}{p_T}\right)^2}; \quad (4.17)$$

see Equation 3.12 and Section 3.3.4 for the meaning of the coefficients  $C$ ,  $S$  and  $N$ . The combined results are shown in Figure 71 and Figure 72, for the data and MC, respectively. The fit parameters are summarized in Table XV and Table XVI.

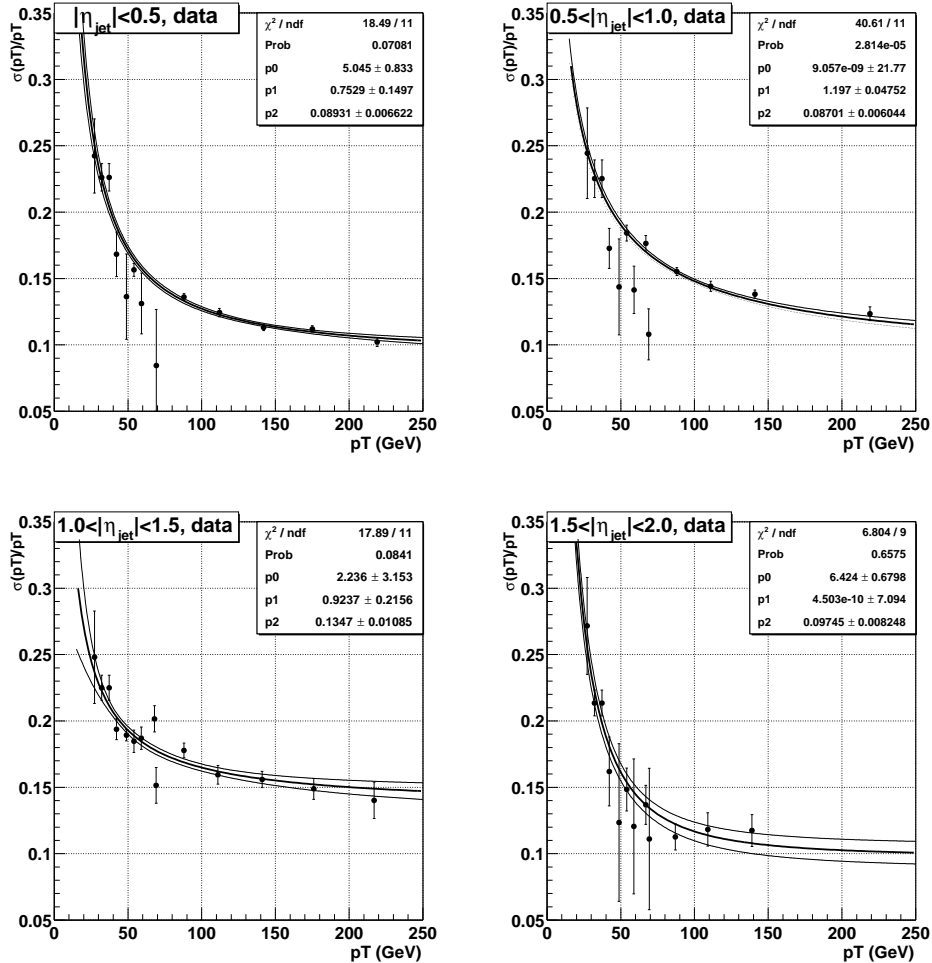


Figure 71. Jet  $p_T$  resolutions for different  $\eta_{\text{det}}$  regions in data. The points below  $\sim 50$  GeV are obtained using  $\gamma + \text{jet}$  events, whereas for  $p_T \geq 50$  GeV resolutions are measured using dijet events. Bands of  $\pm 1\sigma$  statistical error are also shown.

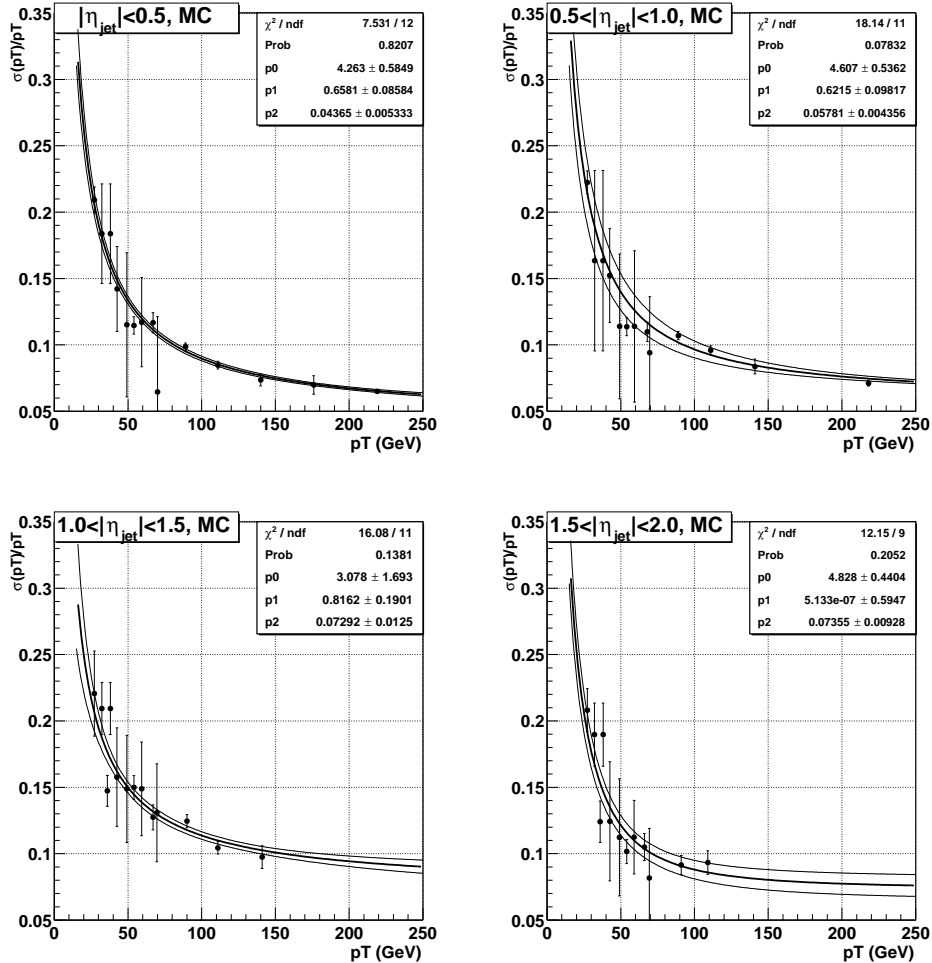


Figure 72. Jet  $p_T$  resolutions for different  $\eta_{\text{det}}$  regions in MC. The points below  $\sim 50$  GeV are obtained using  $\gamma + \text{jet}$  events, whereas for  $p_T \geq 50$  GeV resolutions are measured using dijet events. Bands of  $\pm 1\sigma$  statistical error are also shown.

$ \eta_{det} $ range	$N$	$S$	$C$
$0.0 <  \eta_{det}  < 0.5$	4.26	0.658	0.0436
$0.5 <  \eta_{det}  < 1.0$	4.61	0.621	0.0578
$1.0 <  \eta_{det}  < 1.5$	3.08	0.816	0.0729
$1.5 <  \eta_{det}  < 2.0$	4.83	0.	0.0735

TABLE XVI  
JET ENERGY RESOLUTION COEFFICIENTS FOR MC.

Jets in the simulation are corrected by applying an additional smearing according to a random Gaussian distribution with a width

$$\sigma(p_T) = \sqrt{\sigma_{p_T}^{data}(p_T)^2 - \sigma_{p_T}^{MC}(p_T)^2} \quad (4.18)$$

using the resolution found in the simulation,  $\sigma_{p_T}^{MC}(p_T)$ , and in the data,  $\sigma_{p_T}^{data}(p_T)$ .

#### 4.6 Missing $E_T$

The presence of a neutrino in the final state can be detected only from the imbalance of the energy in the transverse plane. The missing  $E_T$  ( $\cancel{E}_T$ ) is reconstructed from the vector sum of the transverse energies of all cells surviving the T42 algorithm, except for those in the coarse hadronic layer which are treated separately due to their high level of noise. The only cells of the coarse hadronic calorimeter which are used in the  $\cancel{E}_T$  sum are those clustered within good jets. The vector opposite to this total visible momentum vector is denoted the missing energy vector and its modulus is the raw missing transverse energy ( $\cancel{E}_{Traw}$ ).

The response of electromagnetic particles such as photons, electrons or  $\pi^0$ 's is different from that of hadrons and in particular, from that of jets. In events with both electromagnetic objects and jets, this imbalance translates directly into missing transverse energy. As a JES correction is derived for all good jets, it can also be applied to the missing transverse energy. In order to do so, the JES correction (limited to the response part of such correction) applied to all good jets is subtracted from the  $\cancel{E}_{Traw}$  vector. In the same way the EM correction for electromagnetic objects ( $p_T > 15.0$  GeV,  $|\eta_{det}| < 2.5$ ,  $EMF > 0.9$ ,  $f_{iso} < 0.15$ ,  $H\text{-matrix7} < 50$ ) is applied to the  $\cancel{E}_{Traw}$  vector. The resulting modulus is denoted the calorimeter missing transverse energy ( $\cancel{E}_{TCAL}$ ).

As a muon is a minimum ionizing particle throughout the entire detector, it will deposit only a small amount of energy in the calorimeter. Its presence can thus also fake  $\cancel{E}_{TCAL}$ . The transverse momentum of all track matched muons present in the event is subtracted from the missing transverse energy vector after deduction of the expected energy deposition of the muon in the calorimeter (taken from GEANT simulation look-up tables) and this is called  $\cancel{E}_T$ .

#### 4.6.1 $\cancel{E}_T$ Resolution

The  $\cancel{E}_T$  resolution is studied in events where no  $\cancel{E}_T$  is expected.  $Z$ -plus-jets events with a muonic  $Z$  decay can be selected with a high efficiency and purity and are expected to have no  $\cancel{E}_T$ . The  $\cancel{E}_T$  resolution in data is found to be worse than in MC as shown in Figure 73 for events with  $\geq 0$  and  $\geq 2$  jets. The Monte Carlo is further smeared in order to bring it in agreement with data, as described in (123). A  $\cancel{E}_T$  oversmearing parameter is defined by calculating the difference in quadrature of the  $\cancel{E}_T$  resolutions in data and Monte Carlo and

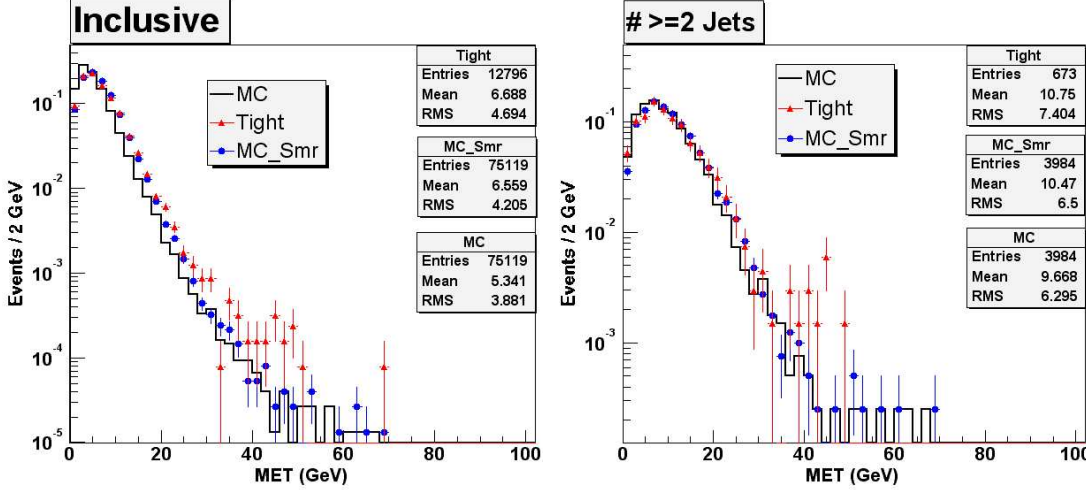


Figure 73.  $E_T$  resolution in  $Z \rightarrow \mu\mu$  events for data, MC and smeared MC with  $\geq 0$  jets (left) and  $\geq 2$  jets (right) (123).

then fitting this vs  $\Sigma E_{Tunclus}$ , the event scalar  $E_T$  (clustered and unclustered) minus the  $E_T$ 's of all the reconstructed (clustered) objects. No jet multiplicity dependence is observed. The  $E_T$  oversmearing correction is instrumented by the following transformation of  $\Sigma E_{Tunclus}$ :

$$\Sigma E_{Tunclus} \rightarrow \Sigma E_{Tunclus} + G(0, \sigma_{E_T}(\Sigma E_{Tunclus})) , \quad (4.19)$$

where  $G(0, \sigma_{E_T}(\Sigma E_{Tunclus}))$  is a random variable drawn from a Gaussian distribution with a mean of 0 and a width  $\sigma_{E_T}(\Sigma E_{Tunclus})$  parameterized as

$$\sigma_{E_T}(\Sigma E_{Tunclus}) = 2.553 + 0.008951 \times \Sigma E_{Tunclus} .$$

The resulting oversmeared  $\cancel{E}_T$  is also shown in Figure 73. The smearing of the Monte Carlo improves the agreement with data particularly in the core of the  $\cancel{E}_T$  distribution. The effect of the oversmearing is most pronounced for events with few jets in the event (left plot in Figure 73), and is much less pronounced for events with  $\geq 2$  jets in the event (right plot in Figure 73). It is expected to be even less pronounced for events with  $\geq 4$  jets, the relevant region for the  $t\bar{t}$  signal events. For this reason no  $\cancel{E}_T$  oversmearing is applied in this analysis.

#### 4.7 $b$ Jets

Reconstructed jets passing the identification criteria described in Section 4.5 can be further classified by their flavor, depending if they originate from the decay and hadronization of a light flavor quark or gluon ( $u, d, s, g$ ), a  $c$  quark or a  $b$  quark. The corresponding jets are called light flavor jets,  $c$  jets or  $b$  jets. Two techniques have been developed to distinguish jets by their flavor: **Soft Lepton Tagging (SLT)**, where the presence of a soft electron or muon within the jet cone indicates a semileptonic  $b$  or  $c$  hadron decay with a branching ratio of typically  $\sim 10\%$  per lepton; **Lifetime tagging**, where charged tracks significantly displaced from the primary vertex are identified as originating from the finite lifetime of the  $c$  or  $b$  hadron decay.

Four lifetime tagging algorithms have been developed at DØ for the identification of  $b$  jets: **Counting Signed Impact Parameter (CSIP)** requires a minimum number of tracks with large impact parameter significance with respect to the primary vertex; **Jet Lifetime Probability (JLIP)** calculates the probability that a jet does not originate from the primary vertex using the impact parameter information of tracks seen in the SMT layers; the **Secondary Vertex Tagger (SVT)** algorithm does an explicit reconstruction of secondary vertices with

a large decay length significance with respect to the primary vertex (137); **Neural Network Tagger (NN)** uses variables determined by the above mentioned algorithms as inputs to a neural network tool trained to discriminate heavy flavor jets. The SVT algorithm has been used to identify  $b$  jets in this analysis, as described in Chapter 6.

#### **4.7.1 Secondary Vertex Tagger Algorithm**

The secondary vertex b-tagging algorithm identifies jets arising from  $b$  quark hadronization by explicitly reconstructing the decay vertex of long-lived  $B$  hadrons within jets. The decay of a long-lived hadron produces several charged particles emanating from a secondary vertex, displaced from the primary  $p\bar{p}$  interaction point.

According to the Pythia Monte Carlo simulation (59),  $B$  hadron decays in top quark events have an average number of 5 charged particles and a decay length of 3mm. The tertiary charm  $D$ -meson decay vertex has a mean charged track multiplicity of 2.2 and its decay length with respect to the  $B$  hadron is 0.16cm. MC studies also show that 99% of the  $B$  decay particles are produced within a cone of size  $\Delta R = 0.5$  around the direction of the  $B$ -Meson. We find that for  $B$  mesons with decay length greater than 1mm, more than 70% of the  $b$ -jets have at least 2 displaced tracks with an impact parameter significance ( $dca/\sigma(dca)$ ) greater than 3. A diagram of the algorithm showing the relevant variables used is included in Figure 74.

The Secondary Vertex Tagger algorithm consists of three main steps: reconstruction and identification of the primary interaction vertex (described in Section 4.2), reconstruction of track-jets and secondary vertex finding. The last two steps are described below.

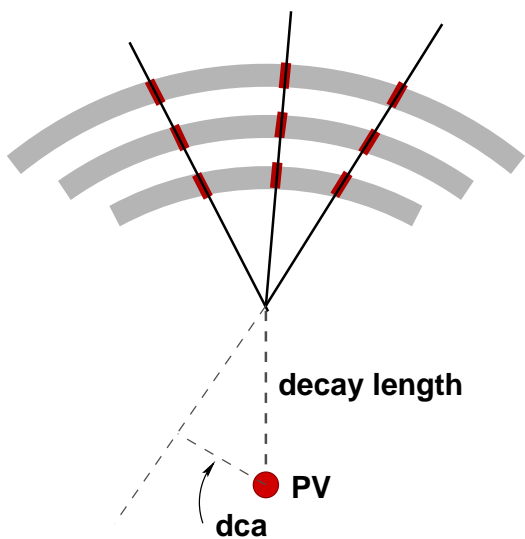


Figure 74. The Secondary Vertex algorithm explicitly reconstructs displaced vertices inside of jets. Tracks with significant Distance of Closest Approach ( $dca$ ) with respect to the Primary Vertex ( $PV$ ) are used to reconstruct secondary vertices within a jet. The cut on the decay length significance of the secondary vertices is tuned to optimize the performance of the algorithm.

#### 4.7.1.1 Track-Jets

On average, 2/3 of the particles within a jet are electrically charged and therefore detected as tracks in the central tracking system. An algorithm has been developed to reconstruct these “track-jets” from charged tracks. The procedure can be subdivided into 3 steps:

1.  **$z$  pre-clustering:** tracks are clustered according to their  $z$  of closest approach with respect to  $z = 0$ . Looping in descendant order of track  $p_T$ , tracks are added to the pre-cluster if  $\Delta z < 2$  cm, where  $\Delta z$  is the difference between the  $z$  of the closest approach of the track and the pre-cluster.
2. **Track selection:** for every pre-cluster, the closest reconstructed primary vertex is identified and tracks are selected satisfying the following criteria:  $p_T > 0.5$  GeV,  $\geq 1$  SMT hits,  $|dca| < 0.20$  cm and  $|zdca| < 0.4$  cm, where  $dca$  refers to the distance of closest approach to the reconstructed primary vertex.
3. **Jet clustering:** for every pre-cluster, the selected tracks are clustered in the  $(\eta, \phi)$ -plane using a simple cone jet algorithm with seed  $p_T > 1$  GeV, requiring at least two tracks.

#### 4.7.1.2 Secondary Vertex Finding

The secondary vertex finding is applied to every track-jet in the event; the method consists of several steps and is described below.

1. **Track selection:** a loop over all tracks is performed and only tracks with  $p_T > 1.0$  GeV and (signed) impact parameter significance ( $|dca|/\sigma(dca)$ )  $> 3.5$  are selected. The sign of the impact parameter is given by the sign of its projection onto the track-jet axis, (see

Figure 75 for a schematic drawing).  $dca$  and  $\sigma(dca)$  are computed with respect to the selected primary vertex. The signed impact parameter significance distribution is shown in Figure 75 for tracks within track-jets with at least two selected tracks, for *light* and *b* jets as predicted by the Monte Carlo simulation. A clear excess at positive impact parameter significance is observed for *b* jets. The contribution to the negative impact parameter significance is caused by random overlap of tracks which are displaced from the primary vertex due to tracking errors and resolution effects (Section 6.4).

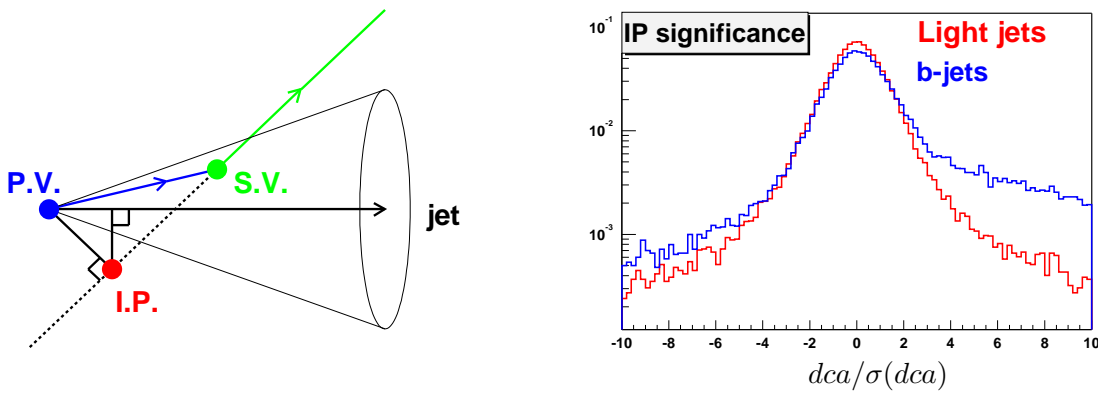


Figure 75. Left: A schematic drawing showing the definition of the impact parameter ( $dca$ ). The sign of the  $dca$  is given by the sign of the inner product of  $dca$  and the track-jet momentum. Right: The impact parameter significance distributions for tracks from light and *b* jets from Monte Carlo.

2. **Vertex finding and fitting:** the algorithm searches for a secondary vertex using a *Build-Up* method that looks for *seed* vertices by fitting all combinations of pairs of selected tracks within a track-jet. It then attempts to attach additional tracks to the *seed* vertices if it improves the resulting  $\chi^2$  contribution to the vertex. The process is repeated until no more tracks can be associated to seeds. This procedure results in vertices that might share tracks.
3. **Vertex selection:** the secondary vertices found are required to have track multiplicity  $\geq 2$ , the vertex transverse decay length  $|L_{xy}| = |\vec{r}_{SV} - \vec{r}_{PV}|$  is required to satisfy  $|L_{xy}| < 2.6$  cm and  $|L_{xy}/\sigma(L_{xy})| > 7.0$ ,  $\chi^2_{L_{xy}}/\text{dof} < 10$  and  $|\text{collinearity}| > 0.9$ . The collinearity is defined as the inner product of  $\vec{L}_{xy}$  and the vertex momentum, computed as the vector sum of the momenta of all attached tracks after the constrained fit to the Secondary Vertex. The sign of the transverse decay length is given by the sign of the collinearity.
4.  **$V^0$  removal:** secondary vertices composed of two tracks with opposite sign are required to be inconsistent with a  $V^0$  hypothesis. The hypotheses tested by the algorithm include  $K_s^0 \rightarrow \pi^+\pi^-$ ,  $\Lambda^0 \rightarrow p^+\pi^-$  and the photon conversion ( $\gamma \rightarrow e^+e^-$ ). Secondary vertices are rejected if the invariant di-track mass, given the  $V^0$  hypothesis, is consistent with the corresponding  $V^0$  mass in a mass window defined by  $\pm 3\sigma$  of the measured  $V^0$  mass resolution. The reconstructed invariant mass distribution for  $K_s^0$  and  $\Lambda^0$  are shown in Figure 76.

The algorithm is tuned to identify  $b$  jets with high efficiency, referred to as  $b$ -tagging efficiency, while keeping low the probability to tag a light jet (from a  $u$ ,  $d$ ,  $s$  quark or a gluon),

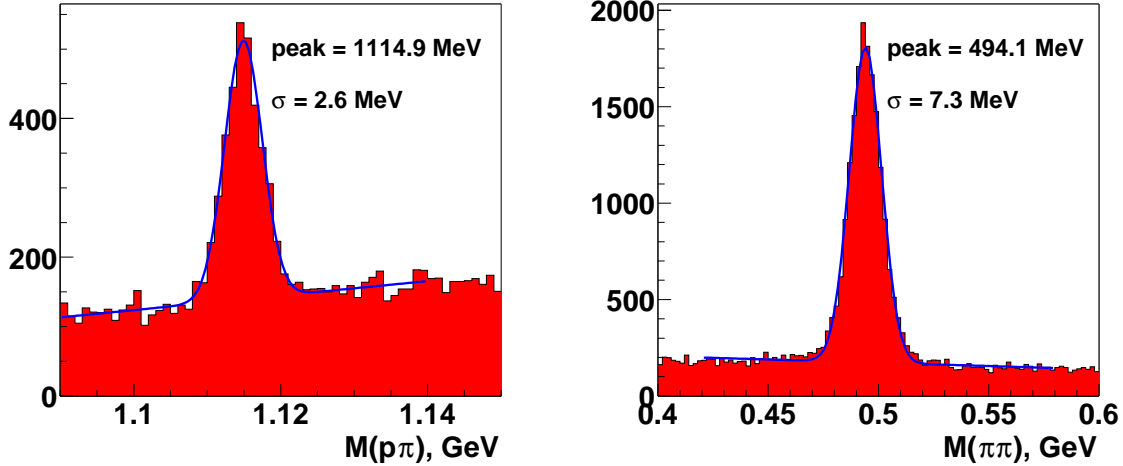


Figure 76. Invariant mass distributions for the processes  $\Lambda^0 \rightarrow p^+\pi^-$  (left) and  $K_s^0 \rightarrow \pi^+\pi^-$  (right) (136).

referred to as mis-tagging efficiency. The efficiency to tag a  $c$  jet is referred to as  $c$ -tagging efficiency. A calorimeter jet is identified as a  $b$  jet (also called “tagged” or “having a  $b$ -tag”) if it contains a reconstructed secondary vertex with  $L_{xy} > 0$  within  $\Delta R < 0.5$ . Events containing one or more tagged jets are referred to as “tagged events”.

## CHAPTER 5

### EVENT TRIGGER AND DATA SAMPLE

At the Tevatron, collisions occur at intervals of 396 ns. The amount of data produced is far beyond the capabilities of the data recording. Moreover, most of events of interest occur rarely. This motivates the use of a trigger system, as discussed in Section 3.3.7, that selects the events of interest. The  $t\bar{t}$  signature of the lepton-plus-jets events is one lepton (electron or muon), one neutrino and  $\geq 4$  jets as discussed in Section 2.4. To ensure that the relevant data are recorded, a trigger to select both a lepton and a jet was designed. The treatment of the different triggers used in the present analysis is discussed in Section 5.1. The quality selection and luminosity of the data sample are presented in Section 5.2.

#### 5.1 Trigger Efficiency Measurement

The data sample was collected using seven different trigger list versions ranging from v8 to v13. A trigger list version consists of a well defined set of triggers. All the signal triggers used to select events for this analysis have in common that a lepton and a jet must be detected already at trigger level. However, the required quality criteria differ between trigger list versions.

Table XVII and Table XVIII summarize the triggers used for the muon-plus-jets and electron-plus-jets channels, respectively, and specify the trigger terms at each trigger level. The trigger conditions that appear in Table XVII and Table XVIII are:

##### **Level 1:**

Trigger List	Trigger Name	L1	L2	L3
$\geq v8.2$	MU_JT20_L2M0	mu1ptxatxx_CJT(1,5)	MUON(1,med)	JET(1,20)
v9	MU_JT20_L2M0	mu1ptxatxx_CJT(1,5)	MUON(1,med)	JET(1,20)
v10	MU_JT20_L2M0	mu1ptxatxx_CJT(1,5)	MUON(1,med)	JET(1,20)
v11	MU_JT20_L2M0	mu1ptxatxx_CJT(1,5)	MUON(1,med)	JET(1,20)
v12	MU_JT25_L2M0	mu1ptxatxx_CJT(1,3)	MUON(1,med) JET(1,10)	JET(1,25)
v13.0 – v13.1	MUJ2_JT25	mu1ptxatlx_CJT(1,5)_ncu	MUON(1,med) JET(1,8)	JET(1,25)
v13.2	MUJ2_JT25_LM3	mu1ptxatlx_CJT(1,5)_ncu	MUON(1,med) JET(1,8)	JET(1,25) MUON(1,3.,loose)

TABLE XVII. SUMMARY OF TRIGGERS USED IN TRIGGER LISTS V8 TO V13 IN THE MUON-PLUS-JETS CHANNEL.

Trigger List	Trigger Name	L1	L2	L3
v8.2 through v11	EM15_2JT15	CEM(1,10)_CJT(2,5)	EM(.85,10)_JET(2,10)	ELE_LOOSE_SH_T(1,15)_JET(2,15)
v12	E1_SHT15_2J20	CEM(1,11)	-	ELE_NVL_SHT(1,15)_JET(2,20)
v13	E1_SHT15_2J_J25	CEM(1,11)	CALEM(1,15)	ELE_NVL_SHT(1,15)_JET(2,20)_JET(1,25)

TABLE XVIII. SUMMARY OF TRIGGERS USED IN TRIGGER LISTS V8 TO V13 IN THE ELECTRON-PLUS-JETS CHANNEL.

- mulptxatxx: level 1 muon passing tight scintillator requirements,
- mulptxatlx: in addition to the previous requirement, a loose PDT wire hit must be present.,
- CEM(1,X): one calorimeter EM tower with EM  $E_T > X$  GeV,
- CJT(N,X):  $N$  calorimeter trigger towers with uncorrected  $E_T > X$  GeV,  $|\eta_{det}| < 2.4$  for v8-v10, and  $|\eta_{det}| < 3.2$  for v11-v13.

### **Level 2:**

- MUON(1,med): level 2 medium muon as described in (124),
- EM(.85,10): level 2 EM candidate with  $EM_f > 0.85$  and  $E_T > 10$  GeV,
- CALEM(1,15): requires a standard level 2 EM cluster with  $E_T > 15$  GeV,
- JET(N,X):  $N$  level 2 jets with uncorrected  $E_T > X$  GeV.

### **Level 3:**

- MUON(1,3.,loose): one muon found passing loose quality requirements at level 3 within  $|\eta_{det}| < 2.5$  and  $p_T > 3$  GeV. Due to a mistake in the data handling, the information associated with level 3 muon objects is lost in the p14 software release. Therefore no efficiency can be calculated for this particular trigger requirement and it is assumed that all muons passing the level 1 & level 2 will also pass this level 3 requirement. Any possible bias introduced by this assumption is limited to the v13.2 trigger list, which corresponds to approximately 4% of the total amount of data analyzed.

- ELE\_LOOSE\_SH\_T(1,15): one electron ( $|\eta| < 3.0$ ) with  $E_T > 15$  GeV passing loose requirements, including a cut on the transverse shower shape,
- ELE\_NVL\_SHT(1,15): requires one electron ( $|\eta| < 3.6$ ) with  $E_T > 15$  GeV with tight shower shape requirements. Non-linearity and vertex corrections are also used.
- JET(N,X):  $N$  level 3 jets with uncorrected  $E_T > X$  GeV.

The trigger efficiency can be measured in two different ways, either by simulating the trigger requirements on Monte Carlo simulated events using the program **TrigSimCert** (125), or folding into Monte Carlo simulated events the per-electron, per-muon and per-jet efficiency of satisfying individual trigger conditions at Level 1, Level 2 and Level 3 in the data. The probability of a single object (electron, muon, jet) to satisfy a particular trigger requirement is measured in data.

Although correlations and overlap between triggers are automatically taken into account using the first method, currently, the Monte Carlo modeling of trigger objects and trigger quantities is not adequate to be used for precision measurements of the trigger efficiency. Therefore the second method based on trigger efficiencies derived from data is chosen.

The approach used to combine single object trigger efficiencies to calculate the probability of an event to satisfy a specific trigger is described in (126) and briefly summarized below.

The total event probability ( $P(L1, L2, L3)$ ) is calculated as the product of the probabilities for the event to satisfy the trigger conditions at each triggering level,

$$P(L1, L2, L3) = P(L1) \cdot P(L2|L1) \cdot P(L3|L1, L2) \quad (5.1)$$

where  $P(L2|L1)$  and  $P(L3|L1, L2)$  represent the conditional probability for an event to satisfy a set of criteria given it has already passed the requirements imposed at the previous triggering level(s).

The total probability of an event to satisfy a set of trigger requirements is obtained assuming that the probability for a single object to satisfy a specific trigger condition is independent of the presence of other objects in the event. Under this assumption, the contributions from different types of objects to the total event probability can be factored out such that

$$P_{(object_1 \& object_2)} = P_{object_1} \cdot P_{object_2}. \quad (5.2)$$

Furthermore, under this assumption, the probability ( $P$ ) for at least one object to satisfy a particular trigger condition, out of a total of  $N$  objects present in an event, is given by

$$P = 1 - \prod_{i=1}^N (1 - P_i), \quad (5.3)$$

where  $P_i$  represents the single object probability (the probability for an electron to fire a jet trigger and vice versa is also considered in the corresponding product).

The total trigger efficiency is calculated as the luminosity weighted average of the event probability associated to the trigger requirements contained in each individual trigger list.

The probability of a single object to satisfy a particular trigger requirement is measured using the following general procedure (127). The first step consists of identifying a sample of events, unbiased with respect to the trigger requirement under study. Offline reconstructed

objects are then identified in the events. The efficiency is obtained by calculating the fraction of these offline reconstructed objects that satisfy the trigger condition under study. Single object efficiencies are in general parameterized as a function of the kinematic variables  $p_T$ ,  $\eta$  and  $\phi$  of the offline reconstructed objects.

In order to take into account major changes in the trigger system and thus in the trigger response, many single object trigger efficiencies are measured separately for the different trigger lists v8 to v13. Data recorded using different trigger lists, for which no changes to a particular subdetector and associated trigger system occurred, are combined. A detailed document describing these studies and summarizing the results can be found in (128). A short summary is included below.

### **5.1.1 Muon Trigger**

A *tag-and-probe* method is used on  $Z \rightarrow \mu\mu$  events to calculate the fraction of offline muons that pass the trigger requirement under study. Events triggered by one of the single muon triggers in each of the trigger list versions are further selected by requiring the presence of two offline muons. Muons are identified in this sample of events using the offline selection criteria (see Section 4.3). The invariant mass of the two offline muons is required to be within a small window around the  $Z$  mass:  $80 \text{ GeV} < m_{\mu\mu} < 100 \text{ GeV}$ . One muon is randomly chosen (*tag*) and required to satisfy the single muon trigger requirement. The second offline muon (*probe*) is then used to calculate the efficiency of a particular trigger criteria.

Figure 77 shows the combined probability of an offline muon to satisfy the Level 1 requirement `mulptxatlx` and the Level 2 requirement `MUON(1,med)` given it has fired the Level 1

condition as a function of the offline muon  $\eta$ . Cubic splines are fitted to the measured efficiencies. For a muon with  $p_T > 15$  GeV, the Level 1 and Level 2 trigger efficiencies are found to be constant as a function of  $p_T$ . The statistical uncertainty of the fits to the muon trigger efficiencies measured in data is used as an estimate for the systematic uncertainty on the total signal efficiency arising from the muon trigger weight calculation.

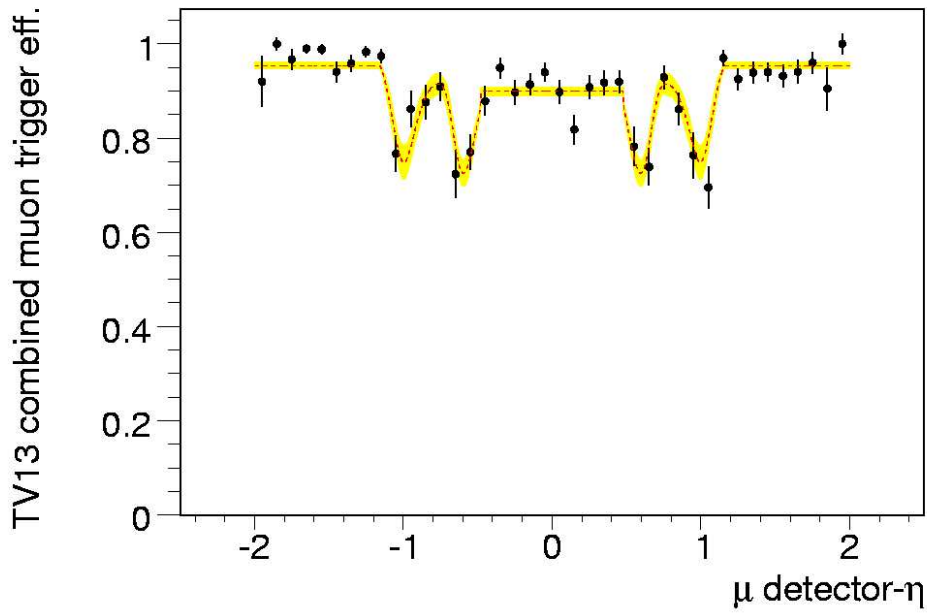


Figure 77. Muon trigger efficiency as a function of the offline muon  $\eta$  for the combined Level 1 condition `mulptxatlx` and Level 2 condition `MUON(1,med)`. The yellow band denotes the statistical error of the spline fit.

### 5.1.2 Electron Trigger

The efficiency for an offline electron to pass a specific trigger requirement is obtained from a sample of  $Z \rightarrow ee$  events, using the tag-and-probe method. Events triggered by one of the single electron triggers in each of the trigger list versions were further selected by requiring the presence of two offline reconstructed electrons. In addition, the invariant mass of the two electrons was required to be within 75 and 105 GeV. One electron is then randomly chosen (tag) and required to satisfy one of the single electron trigger requirements. The second offline electron (probe) is then used to calculate the trigger efficiency for a particular trigger criteria.

The Level 1 single electron efficiency is found to be constant as function of  $\eta$  in the region of interest. The trigger efficiency in general reaches a maximum constant value for electrons with  $p_T$  about twice that of the L1 energy threshold. For electrons with  $p_T > 20$  GeV, the efficiency for both CEM(1,10) and CEM(1,11) is approximately 98%.

The single electron efficiency for the L2 condition requiring one electron with an EM fraction greater than 0.85 and  $p_T > 10$  GeV for electrons that have satisfied the CEM(1,10) condition has been shown to be fully efficient (129) for trigger versions 8 to 11. No L2 trigger condition was used in this analysis for trigger version 12. The L2 trigger condition CALEM(1,15) used for version 13 is fully efficient for  $p_T > 40$  GeV and half efficient for  $p_T = 13$  GeV.

The efficiency for a reconstructed offline electron to pass a L3 electron condition is obtained by only considering offline electrons that are matched to L1 trigger towers with a minimum threshold required by the associated L1 condition. This ensures that the L3 electron efficiency is calculated for offline electrons that have already passed the L1 electron condition. This

scheme does not take into account the possibility of having an electron pass the L3 requirement but failed the L1 condition, which is ruled out in data by matching the offline signal electron to L1, L2 and L3 objects.

The statistical uncertainty of the fits to the electron trigger efficiencies measured in data is used as an estimate for the systematic uncertainty on the total signal efficiency arising from the electron trigger weight calculation.

### 5.1.3 Jet Trigger

Since jet samples are available with large statistics, the jet trigger efficiencies are calculated individually for each trigger list version, even if the trigger condition did not change from one trigger list version to another.

The jet trigger efficiencies are parameterized as function of the JES corrected jet  $p_T$  in three regions of the calorimeter: CC ( $|\eta_{det}| < 0.8$ ), ICR ( $0.8 \leq |\eta_{det}| < 1.5$ ) and EC ( $|\eta_{det}| \geq 1.5$ ). These efficiencies are measured in a sample of data events which fired one of the many muon triggers present in the trigger list version under study. The function used to parameterize the jet trigger efficiency at L1, L2 and L3 is

$$f(p_T) = 0.5 \cdot A2 \cdot \left( 1 + \frac{2}{\sqrt{\pi}} \cdot \int_0^{\frac{p_T - A0}{\sqrt{p_T \cdot A1}}} \exp(-t^2) dt \right). \quad (5.4)$$

A closure test of the jet trigger parameterizations is performed (111) by measuring the trigger efficiency in data for jets which pass the trigger conditions at all three trigger levels at the same time. The product of the parameterizations obtained for each trigger level individually

should then reproduce this data. As the agreement observed is not optimal, the jet turn-on curves are refit and the new parametrizations are used as default. The relative change in the estimated  $t\bar{t}$  signal efficiency is below 0.2 %. This small change can be explained by the presence of many jets in  $t\bar{t}$  events, which cause the probability for at least one of the jets to fire the trigger to be close to unity. However, a slight improvement in the description of the jet  $p_T$  spectra for events with low jet multiplicities is observed. In this case, the influence of each individual jet is higher. Figure 78 shows the measured jet trigger efficiency in CC, ICD and EC for v12, where both parameterizations are overlayed.

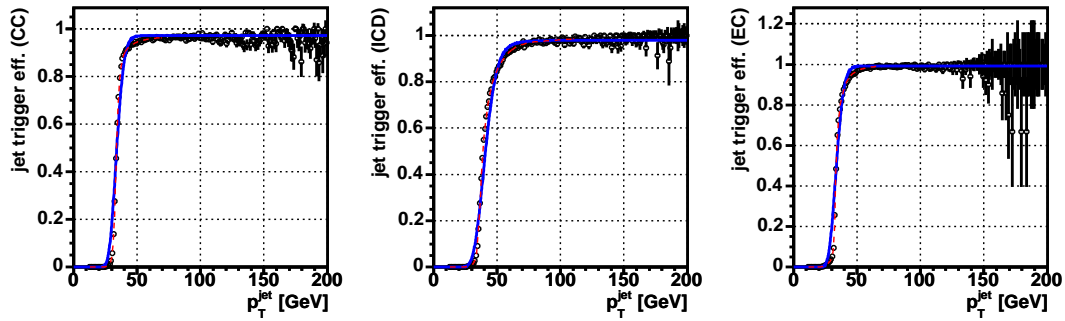


Figure 78. Jet trigger efficiencies for trigger list v12 in the three detector regions CC (left), ICD (middle) and EC (right). The original parameterizations are overlaid as the solid (blue) curve, the fits used as default are shown in dashed (red) (111).

The jet turn-on curves are measured with a large data sample which results in a small statistical uncertainty on the trigger efficiency measurements. Possible systematic effects associated to the method used for measuring the trigger efficiencies could, however, be of the same size or even larger than the statistical uncertainties. In order to quantify possible effects due to the jet quality used in measuring the efficiencies, all the trigger turn-on curves are remeasured requiring a track-match for every jet and thereby improving the purity of the jet samples. The relative systematic uncertainties derived from the difference between the two efficiencies, shown in Figure 79, go up approximately to 10 % for low  $p_T$  jets and decrease to a few % for high  $p_T$  jets.

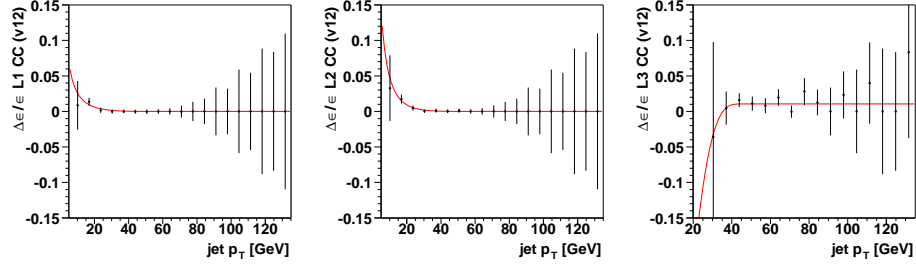


Figure 79. Relative difference in the jet trigger efficiency between the two measurements for jets with and without track-match as a function of offline jet  $p_T$  for the Level 1 condition CJT(1,5) (left), for the Level 2 condition JET(1,10) given that the jet already satisfies the Level 1 condition (middle), and the Level 3 condition JET(1,20) given that the jet already satisfies the Level 1 and the Level 2 conditions (right); for trigger version 12, and jets in the CC region (130).

### 5.1.4 Event Trigger Efficiency

#### Muon + Jets Trigger

The probability of an event ( $P_{vXX}(\mu + jets)$ ) to pass the trigger in each trigger list version is calculated by multiplying the probability of an event to pass the muon requirements and the probability of an event to pass the jet requirements.

$$P_{\mu+jets} = P_\mu \cdot P_{JET} \quad (5.5)$$

where  $P_\mu$  ( $P_{JET}$ ) represents the probability for the event to satisfy the muon-type (jet-type) conditions. These probabilities can be further sub-divided into individual trigger requirements such that,

$$v8 - v11 : \quad P_\mu = P_{\text{mu1ptxatxx}} \cdot P_{\text{MUON}(1,\text{med})}$$

$$P_{JET} = P_{\text{CJT}(1,5)} \cdot P_{\text{JET}(1,20)}$$

$$v12 : \quad P_\mu = P_{\text{mu1ptxatxx}} \cdot P_{\text{MUON}(1,\text{med})}$$

$$P_{JET} = P_{\text{CJT}(1,3)} \cdot P_{\text{JET}(1,10)} \cdot P_{\text{JET}(1,25)}$$

$$v13.0 - v13.1 : \quad P_\mu = P_{\text{mu1ptxatlx}} \cdot P_{\text{MUON}(1,\text{med})}$$

$$P_{JET} = P_{\text{CJT}(1,5)} \cdot P_{\text{JET}(1,8)} \cdot P_{\text{JET}(1,25)}$$

$$v13.2 : \quad P_\mu = P_{\text{mu1ptxatlx}} \cdot P_{\text{MUON}(1,\text{med})} \cdot P_{\text{MUON}(1,3.,\text{loose})}$$

$$P_{JET} = P_{\text{CJT}(1,5)} \cdot P_{\text{JET}(1,8)} \cdot P_{\text{JET}(1,25)}$$

Signal trigger efficiencies in the  $\mu$ -plus-jets channel are shown in Chapter 7, Table XXIII.

### **Electron + Jets Trigger**

The probability of an event ( $P_{\text{vXX}}(e + jets)$ ) to pass the trigger in each trigger list version is calculated by multiplying the probability of an event to pass the electron requirements and the probability of an event to pass the jet requirements.

$$P_{\text{vXX}}(e+jets) = P_{\text{vXX}}(e) \cdot P_{\text{vXX}}(\geq 1jet) = P_{\text{vXX}}(e) \cdot (1 - \prod_{jets} (1 - P_{\text{vXX}}(jet))) \quad (5.6)$$

As the events used in this analysis contain one tight offline electron with  $p_T > 20$  GeV it is assumed that this object will satisfy both the EM and one of the JET conditions at each trigger level. Thus, the probability of an event to satisfy the trigger is calculated as:

In trigger list versions 8 to 11,

$$\begin{aligned} P_{\text{v8-11}}(e) &= P_{\text{v8-11}}(L1|e) \cdot P_{\text{v8-11}}(L2|L1, e) \cdot P_{\text{v8-11}}(L3|L1, L2, e) \\ &= P(CEM(1, 10)|e) \cdot P(EM(1, 10)|CEM(1, 10), e) \cdot \\ &\quad P(ELE\_LOOSE\_SH\_T(1, 15)|EM(1, 10), CEM(1, 10), e) \\ P_{\text{v8-11}}(jet) &= P_{\text{v8-11}}(L1|jet) \cdot P_{\text{v8-11}}(L2|L1, jet) \cdot P_{\text{v8-11}}(L3|L1, L2, jet) \\ &= P(CJT(1, 5)|jet) \cdot P(JET(1, 10)|CJT(1, 5), jet) \cdot \\ &\quad P(JET(1, 15)|CJT(1, 5), JET(1, 10), jet) \end{aligned}$$

In trigger list version 12,

$$\begin{aligned}
 P_{v12}(e) &= P_{v12}(L1|e) \cdot P_{v12}(L3|L1, e) \\
 &= P(CEM(1, 11)|e) \cdot P(ELE\_NLV\_SHT(1, 15)|CEM(1, 11), e) \\
 P_{v12}(jet) &= P_{v12}(L3|jet) \\
 &= P(JET(1, 20)|jet)
 \end{aligned} \tag{5.7}$$

In trigger list version 13,

$$\begin{aligned}
 P_{v13}(e) &= P_{v13}(L1|e) \cdot P_{v13}(L2|L1, e) \cdot P_{v13}(L3|L1, L2, e) \\
 &= P(CEM(1, 11)|e) \cdot P(CALEM(1, 15)|CEM(1, 11), e) \cdot \\
 &\quad P(ELE\_NLV\_SHT(1, 15)|CALEM(1, 15), CEM(1, 11), e) \\
 P_{v13}(jet) &= P_{v13}(L3|jet) \\
 &= \begin{cases} P(JET(1, 20)|jet) & \text{if } p_T^{electron} > 25\text{GeV} \\ P(JET(1, 25)|jet) & \text{if not} \end{cases}
 \end{aligned}$$

Signal trigger efficiencies in the electron-plus-jets channel are shown in Chapter 7, Table XXIV. More details about the triggering can be found in (128).

## 5.2 Data Sample

The analysis presented makes use of the data recorded with the DØ detector between August 2002 and March 2004.

In the muon-plus-jets channel, the data sample is derived from the 1MUloose CSG skim (138) and further skimmed requiring one muon candidate with  $p_T > 15.0$  GeV and  $\Delta R(\mu, jet) > 0.5$  and one jet with  $p_T > 15.0$  GeV. In the electron-plus-jets channel, the EM1TRK CSG skim (138) was used requiring, in addition, one electron candidate with  $p_T > 15.0$  GeV and at least one jet with  $p_T > 15.0$  GeV. In addition to the signal samples, the following samples are selected for various studies:

- muon-in-jet: at least two reconstructed jets and a medium muon with  $\Delta R(\mu, jet) < 0.5$ .
- muon-in-jet-away-jet-tagged: a subset of the muon-in-jet sample where the jet opposite to that with a muon is tagged by SVT.
- EMqcd: this sample requires  $e+jets$  signal trigger, at least one electromagnetic object with  $p_T > 20$  GeV, at least one reconstructed jet, and  $E_T \leq 10$  GeV.

In the following the data quality selection (Section 5.2.1) and the luminosity of the data sample are discussed (Section. 5.2.2).

### **5.2.1 Data Quality Selection**

Only a fraction of the data delivered by the Tevatron is recorded by the DØ detector. Out of this data only the fraction for which all detector systems are functioning well is used for the data analysis. Finally, only the fraction of the data which is reconstructed is actually used for the analysis presented. This amounts for approximately 80% of the data delivered by the Tevatron.

The data quality monitoring is performed on two levels, online and offline. It is crucial for a high data taking efficiency to catch the malfunction of detector components, of the readout

or the triggering as early as possible. Online data quality monitoring guarantees an immediate reaction to a problem, thus maximizing the good data that gets recorded.

However, there are data quality issues which are not recognized online. The remaining deficient data is eliminated by offline data quality monitoring. The idea is to compare basic distributions of physics objects or other variables that describe the detector performance of the data taken with canonical distributions. In a second step, a list of possible data corruption methods is identified, quality measures are defined with a maximum discrimination power between usable and unusable data, and criteria are defined to classify the data quality. Since the corruption of the data can occur on time scales much smaller than the length of a whole run, the classification is preferably done on the smallest possible units of data.

The data quality selection required for the data events analyzed is broken down on a run based, a luminosity block number (LBN) based (corresponding to approximately one minute of data taking and several thousand events recorded) and an event-by-event based selection.

**Run quality selection:** The good run selection is based on information stored in DØ's Run Quality Database (131). The requirements are summarized in Table XIX. It is guaranteed that no hardware failures are known during a run for all detector systems of importance to this analysis. The tracking quality is particularly important as it contributes to the identification of leptons originating from the PV, it is crucial for the  $b$ -tagging, and is also used to build the kinematic variables of the event. **Luminosity block quality selection:** a grounding problem in the calorimeter, for the most part resolved, can cause a  $\phi$ -ring of energy referred to as *ring-of-fire*. This leads to a large missing energy signature in the event. Events which show

the characteristic pattern for the ring-of-fire activity are eliminated from the data sample. The selection is based on the luminosity block number (LBN). In addition, the following requirements on the average  $\cancel{E}_T$  and average scalar  $E_T$  are made to reject events with *bad JETMET LBN*:

- - shift in average  $\cancel{E}_T$ :  $\sqrt{\langle \cancel{E}_{Tx} \rangle^2 + \langle \cancel{E}_{Ty} \rangle^2} < 6 \text{ GeV}$ ,
- - average RMS of  $\cancel{E}_T$ :  $\sqrt{RMS(\cancel{E}_{Tx})^2 + RMS(\cancel{E}_{Ty})^2} < 20 \text{ GeV}$ ,
- - average scalar  $E_T$ :  $\langle \text{scalar } E_T \rangle > 60 \text{ GeV}$ .

Files consist of groups of approximately 20 consecutive LBN's. To have a sufficient number of events the data quality selection is based on these files. **Event quality selection:** the selection of  $t\bar{t}$  events involves requirements of jets and  $\cancel{E}_T$ , both of which are highly susceptible to backgrounds from calorimeter readout malfunctions. Although the signatures for these problems tend to be fairly obvious when looking at event displays, care must be taken in devising an event-wide quality variable which is immune to variations in an event's real (as opposed to instrumentally originating) scalar  $E_T$  or number of jets. This is particularly true for  $t\bar{t}$  events in which large scalar transverse energies can arise. A study to arrive at such an event quality selection is described in (133). If an event shows significant differences in energy deposition in the precision readout and the Level 1 readout then the event is suspect. A similar quantity is already used for the jet identification, see Section 4.5.3. In order to be immune against events with many jets or large scalar transverse energy, the comparison between the L1 readout and the precision readout is carried out only for trigger towers with Level 1 energy of less than 2 GeV. An event is rejected if it does not pass the requirement on the Level 1 and the precision

readout information (133), and if it is flagged as *coherent noise*, a flag based on precision readout occupancy and RMS within ADC cards (132).

MUON	Reasonable
SMT	Not Bad
CFT	Not Bad
CAL	Not Bad
CTT	Any

TABLE XIX

## RUN QUALITY REQUIREMENTS.

### 5.2.2 Integrated Luminosity of the Data Samples

Only good luminosity blocks, i.e. luminosity blocks for which the luminosity can be calculated, are used in this analysis. Table XX summarizes the integrated luminosity for the different trigger lists.

The measurement of the luminosity is discussed in Section 2.9, the total uncertainty on the integrated luminosity is 6.5% (83).

Trigger List	$\int \mathcal{L} (\text{pb}^{-1})$	
	$e + jets$	$\mu + jets$
v8	19.4	20.1
v9	21.2	21.2
v10	15.1	15.3
v11	54.9	57.3
v12	209.8	209.8
v13	45.8	39.7
total	366.2	363.4

TABLE XX

BREAKDOWN OF INTEGRATED LUMINOSITIES BY TRIGGER LIST VERSION.

## CHAPTER 6

### JET TAGGING EFFICIENCIES

The current version of the D $\emptyset$  Monte Carlo simulation does not describe well the tagging efficiencies observed in data. Among the reasons for this deficiency are the inadequate description of dead detector material and noise in the central tracking system. This results in an overestimated tracking efficiency in the Monte Carlo, in particular within jets. For this reason, straightforward Monte Carlo based calculation of tagging efficiencies does not give a correct result. A method developed to measure the jet tagging efficiencies is described below.

#### 6.1 Taggability

The tagging efficiencies depend on the quality of the jet to be tagged. For instance, a fake jet made of noisy cells in the calorimeter, or a high  $p_T$  photon reconstructed as a jet, have no tracks pointing to them and cannot be tagged. The probability to identify a  $b$  jet using lifetime tagging is conveniently broken down into two components: the probability for a jet to be “taggable”, also called “taggability”, and the probability for a taggable jet to be effectively tagged, also called “tagging efficiency”. This breaking down of the probability to identify  $b$  jets serves to decouple the tagging efficiency from issues related to tracking inefficiencies and calorimeter noise problems, which are therefore absorbed into the taggability. This also facilitates the comparison in performance among different  $b$ -tagging algorithms.

A calorimeter jet passing the identification criteria defined in Sect.4.5 is considered taggable if it is matched within  $\Delta R \leq 0.5$  to a track-jet (Sect. 4.7.1.1). The tracks in the track-jet are required to have at least one hit in the SMT barrel or F-disk. Since the SMT fiducial volume covered by the F-disks is smaller ( $\approx 38$  cm) than the DØ luminous region ( $\approx 54$  cm), the taggability is expected to have a strong dependence with the position of the primary vertex of the event. Moreover, particular combinations of the position of the Primary Vertex along the beam axis and the  $\eta$  of the jet would enhance or reduce the probability that a track-jet passes through the SMT, as is shown schematically in Figure 80.

Because of the geometric constraints imposed by the tracking system, in particular the Silicon Tracker, the position of the Primary Vertex along the beam axis ( $PV_Z$ ) has to be taken into account when determining jet taggabilities. Moreover, the relative sign between the  $PV_Z$  and the jet  $\eta$  must also be considered. Figure 81 shows the behavior of taggability observed in a  $W + jets$  Monte Carlo sample as a function of  $PV_Z$  for the case in which this relative sign is positive or negative.

Taggability is measured from the combined lepton+jets preselected data as no statistically significant difference between the taggability measured in the e+jets and  $\mu$ +jets preselected samples has been observed. The taggability is parametrized as a function of jet  $p_T$  and  $\eta$  in 6 bins of  $PV_Z$  to account for the dependance on the position of the Primary Vertex. The resulting efficiency is shown in Figure 82, where the drop in taggability at the edges of the SMT barrels and the effect of the relative sign between  $PV_Z$  and jet  $\eta$  is clearly noticeable . If the product of  $PV_Z$  and jet  $\eta$  is negative, the taggability decreases for  $PV_Z \geq 38$  cm. This effect is much more

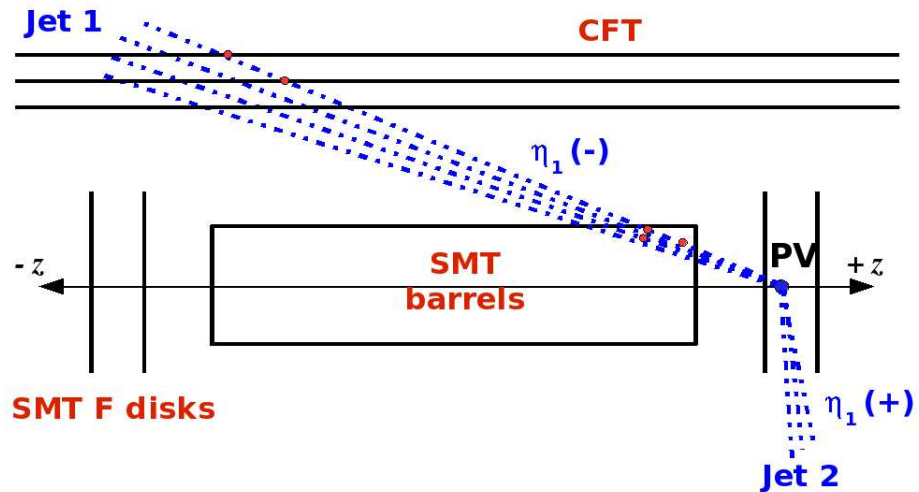


Figure 80. Schematic drawing showing the geometric dependance of the taggability. A primary vertex ( $PV$ ) located outside the Silicon Tracker barrels as shown in the picture, may have two reconstructed jets originating from it. In the case of jet 1, the combination of the position along the beam axis ( $PV_Z$ ) and the pseudo rapidity of the jet 1 ( $\eta_1$ ) is such that the track-jet has a high probability to have hits in the SMT. That is not the case for jet 2, where  $PV_Z$  and  $\eta_2$  are such that the tracks within this jet have a low probability to have SMT hits, thus making it less likely to be taggable for a geometric reason. A combination of  $PV_Z$  and the relative sign to the jet  $\eta$  takes this geometric dependance into account.

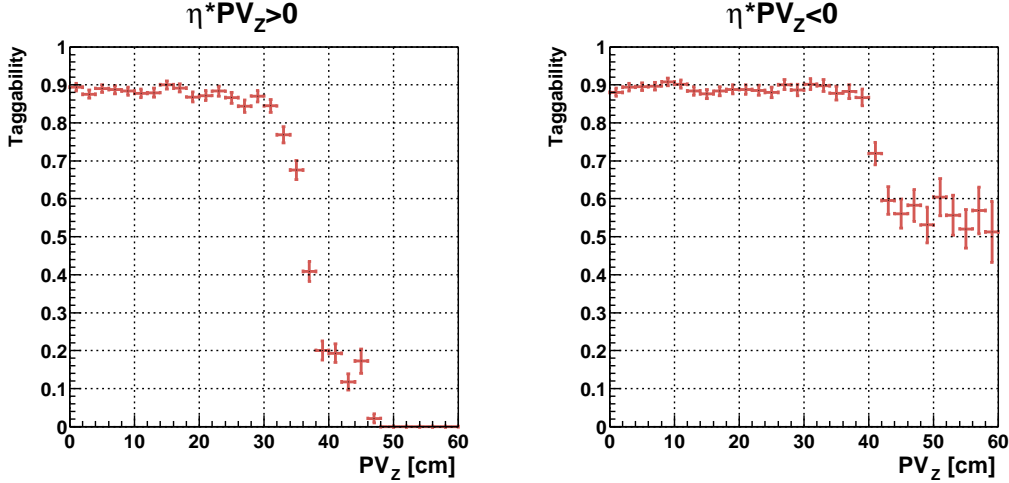


Figure 81. Taggability as a function of the position of the Primary Vertex along the beam axis for the case in which the product of  $PV_Z$  and jet  $\eta$  is positive (left) or negative (right) as observed in a  $Wj$  Monte Carlo sample.

pronounced for the case in which this relative sign is positive. The regions shown in Figure 82 where chosen by taking into consideration the edge of the SMT barrels, the amount of data available for the fits and the “flatness” of the taggability in each region.

Figure 83 shows the parametrization of taggability as a function of jet  $p_T$  and  $\eta$  for the different regions determined by the position of the Primary Vertex and the relative sign with the jet  $\eta$ . In each of these six bins, the parameterization is obtained for the  $p_T$  and the  $\eta$  dependence separately. A two-dimensional parameterization is derived by assuming that the dependence is factorizable, so that  $\varepsilon(p_T, \eta) = C\varepsilon(p_T)\varepsilon(\eta)$ . The normalization factor  $C$  is calculated so that the total number of predicted taggable jets obtained as the sum over all

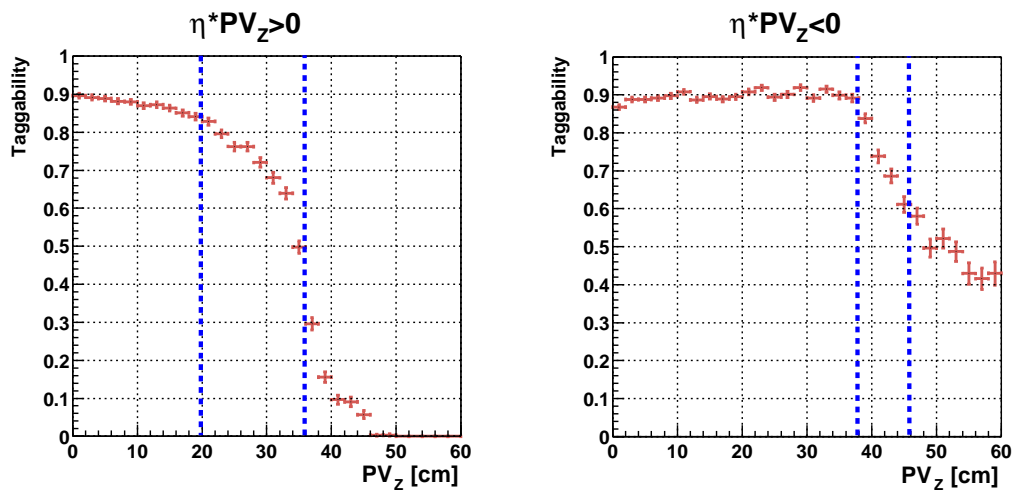


Figure 82. Taggability as a function of the position of the Primary Vertex along the beam axis for the case in which the product of  $PV_Z$  and jet  $\eta$  is positive (left) or negative (right) as observed in the lepton plus jets preselected data. The dashed lines correspond to the boundaries between regions.

reconstructed jets weighted with  $\varepsilon(p_T, \eta)$  according to their  $p_T$  and  $\eta$  is equal to the total number of observed taggable jets.

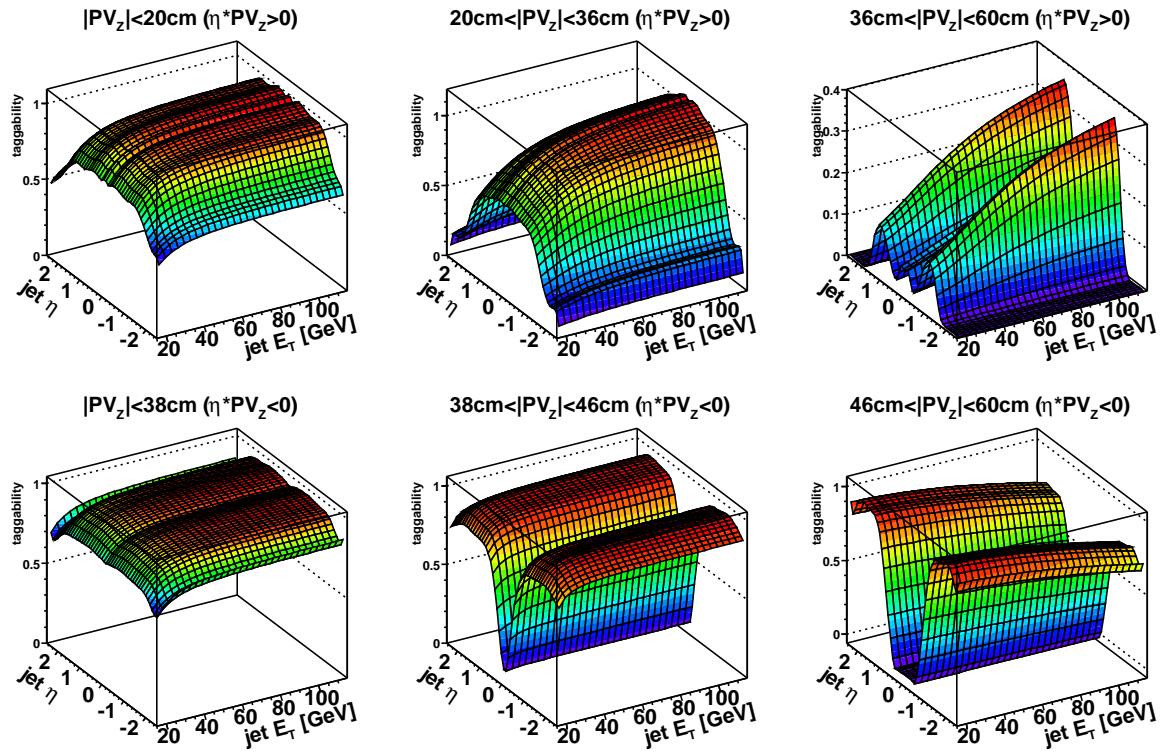


Figure 83. Two dimensional parametrizations of taggability for different ( $PV_Z$ ,  $PV_Z \times \eta$ ) bins.

The assumption that the taggability can be factorized in this way is verified through the corresponding validation test that compares the number of predicted and the number of ob-

served taggable jets as a function of different variables. The validation tests were done by applying the combined  $l+jets$  taggability parametrizations separately to the  $e+jets$  and  $\mu+jets$  preselected data as a weight for each jet. Statistical uncertainties of the fits used to derive the parametrizations are assigned as errors to the taggability. Figure 84 and Figure 85 show the validation of the kinematic distributions of jets together with the good agreement between predicted and observed Primary Vertex position along the beam axis ( $PV_Z$ ) in the  $e+jets$  and  $\mu+jets$  channel, respectively.

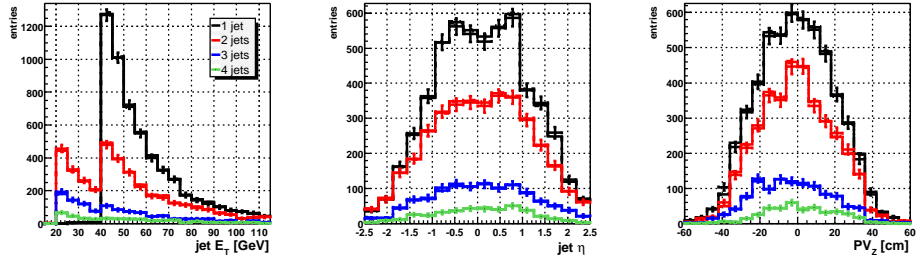


Figure 84. Validation of the taggability parametrizations applied to the  $e+jets$  channel. The predicted and observed jet  $p_T$ , jet  $\eta$  and  $PV_Z$  distribution are in good agreement in all jet multiplicities.

A validation of the parametrized taggability is also done by comparing the prediction with the observation for event variables. Figure 86 and Figure 87 show the predictability of the jet multiplicities for the case in which the event has exactly one taggable jet, events with at least

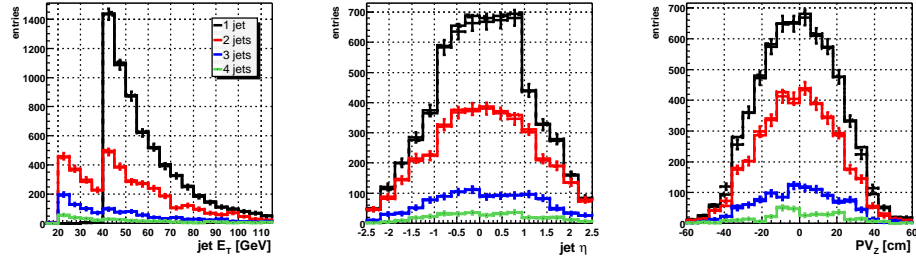


Figure 85. Validation of the taggability parametrizations applied to the  $\mu$ +jets channel. The predicted and observed jet  $p_T$ , jet  $\eta$  and  $PV_Z$  distribution are in good agreement in all jet multiplicities.

two taggable jets, and the inclusive case, for the  $e$ +jets and  $\mu$ +jets channels, respectively. A validation of a topological event variable such as the sum of the scalar transverse energy of all jets in the event, namely  $H_T$ , is shown in Figure 88 and Figure 89 for the electron and muon channels respectively, as an example of the good agreement between predicted and observed taggability.

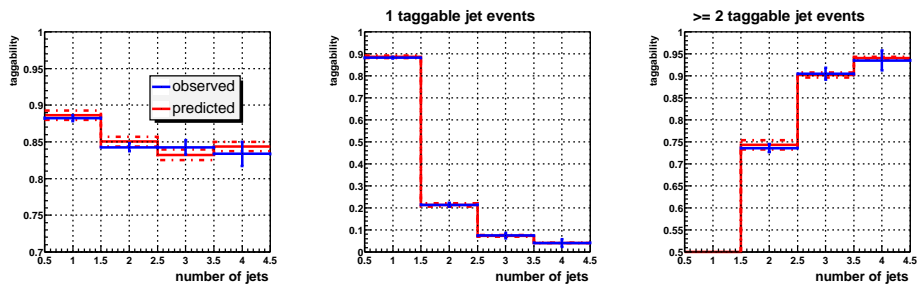


Figure 86. Prediction and observation of the number of jets in preselected  $e+jets$  data events.

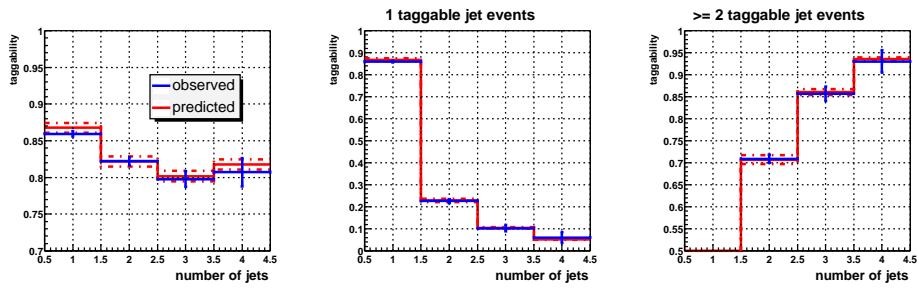


Figure 87. Prediction and observation of the number of jets in preselected  $\mu+jets$  data events.

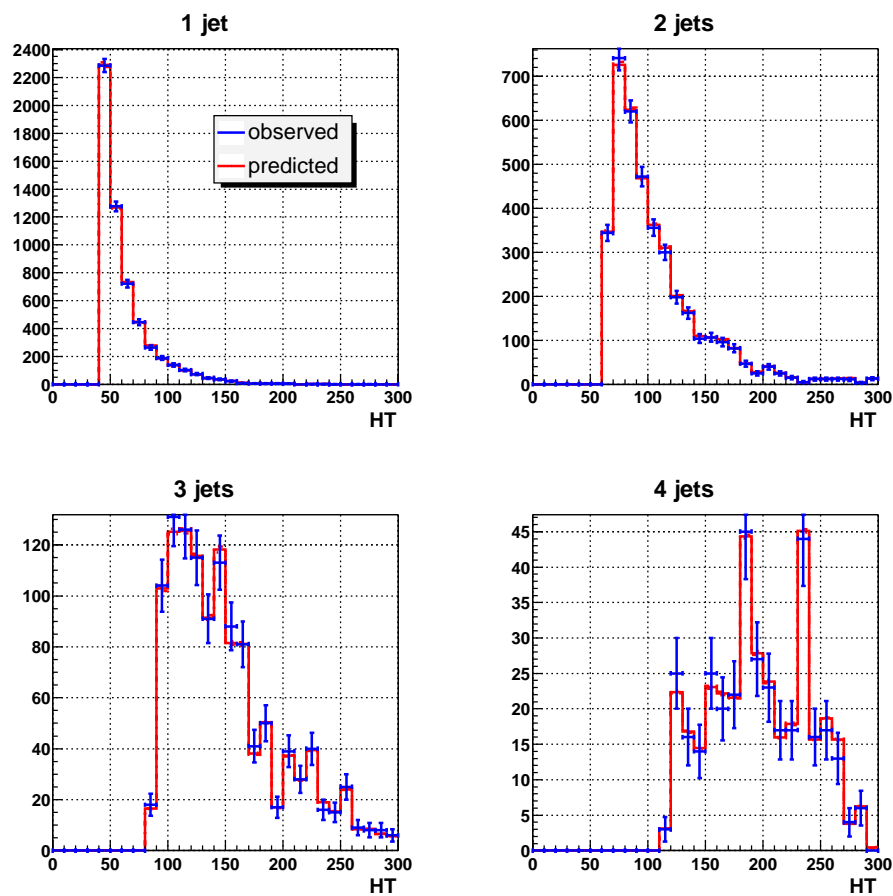


Figure 88. Predictability of the topological event variable  $H_T$  in  $e+jets$  preselected data for different jet multiplicities based on the parametrized taggability.

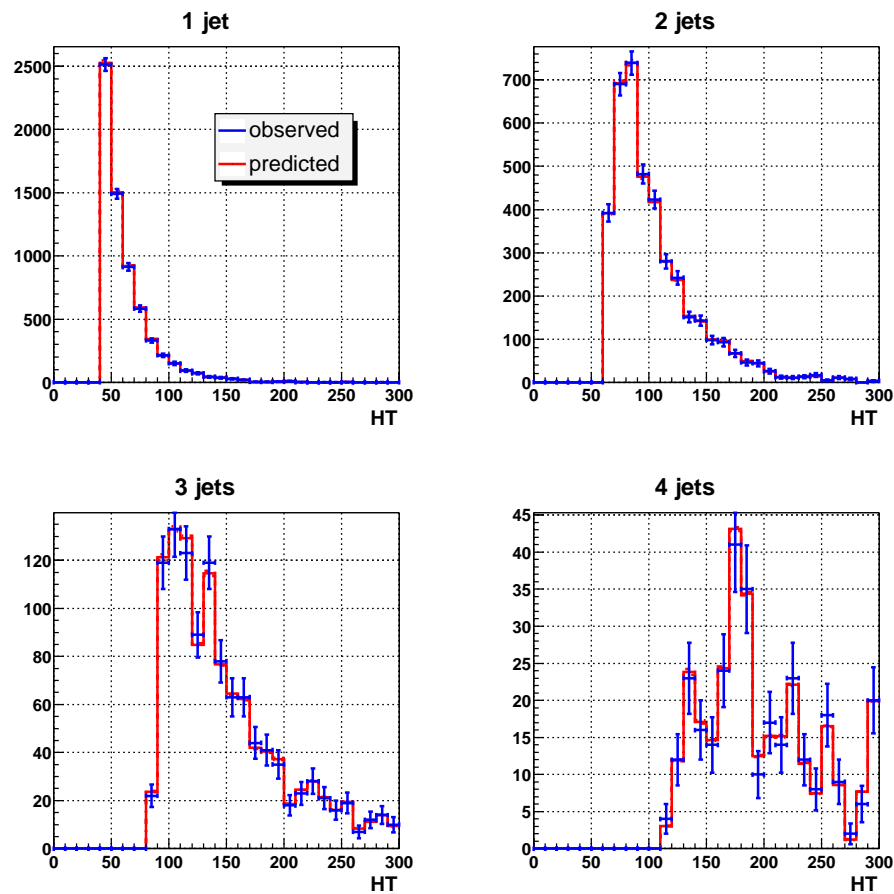


Figure 89. Predictability of the topological event variable  $H_T$  in  $\mu+$ jets preselected data for different jet multiplicities based on the parametrized taggability.

### 6.1.1 Jet Flavor Dependence of Taggability

The taggability measured in data is dominated by the light jet contribution since the heavy flavor content in the low jet multiplicity bins is small. It therefore describes the taggability for light flavor jets. Figure 90 shows that the average track multiplicity is larger for heavy flavor jets than for light jets. This leads to an increased taggability for  $b$  and  $c$  jets. The ratios of  $b$  to light and  $c$  to light taggabilities as a function of jet  $E_T$  and  $\eta$  observed in a QCD Monte Carlo sample are shown in Figure 91. The largest difference in taggability, of approximately 10 %, is observed between  $b$  and light jets in the low  $p_T$  region corresponding to jets with low track multiplicity. The  $\eta$  dependence is relatively soft. The fits to the ratios are used as flavor dependent correction factors to the taggability.

The flavor dependence of the taggability has been checked on data using two samples with significantly different fractions of heavy flavors. The muon-in-jet sample is expected to contain a large fraction of events that originated from QCD heavy flavor production. The  $b$ -content of the sample was further increased by requiring a large positive impact parameter significance of the muon,  $\sigma_{DCA} > 3$ . The complementary sample, enriched in light flavor content, was obtained by applying an opposite cut on the impact parameter significance of the muon,  $\sigma_{DCA} < 3$ . The effect of these cuts on the heavy flavor composition of  $\mu$ -jets was estimated on a muon-in-jet QCD Monte Carlo, where events with only  $\mu$ -jets were considered. These cuts effectively separate light jets from  $b$  jets as can be seen from the resulting fractions shown in Table XXI. Ratios of taggabilities obtained from muon-in-jet data and QCD Monte Carlo samples with  $\sigma_{DCA}$  cuts are shown in Figure 92. Although the cut on  $\sigma_{DCA}$  does not separate completely  $b$

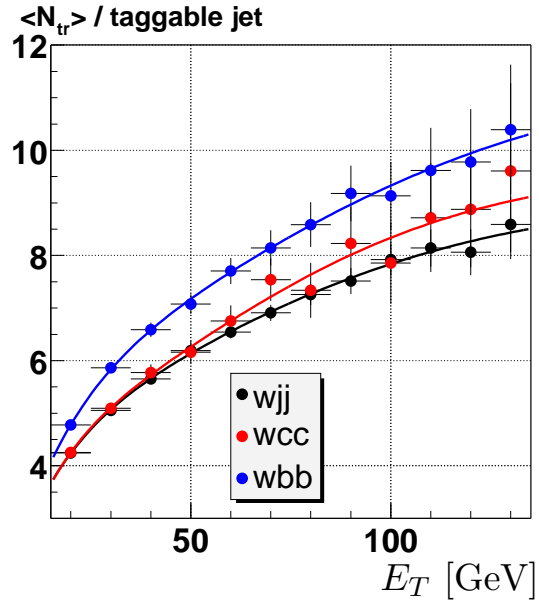


Figure 90. Average track multiplicity in a taggable jet as a function of jet  $E_T$  for  $b$ ,  $c$  and light jets in the  $Wb\bar{b}$ ,  $Wc\bar{c}$  and  $Wjj$  Monte Carlo samples (136).

	light	c	b
$\sigma_{DCA} < 3$	82%	10%	8%
$\sigma_{DCA} > 3$	24%	23%	53%

TABLE XXI

FLAVOR COMPOSITION OF MUONIC JETS IN QCD MONTE CARLO FOR DIFFERENT CUTS ON THE MUON IMPACT PARAMETER.

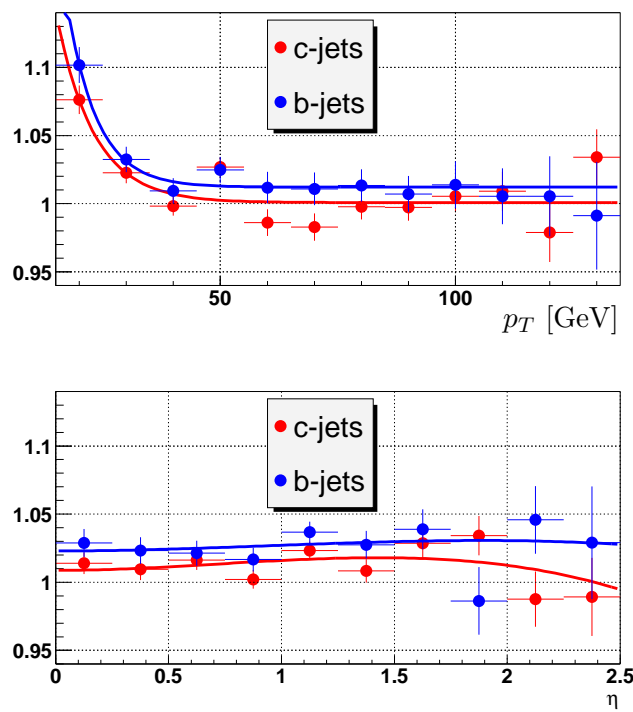


Figure 91. Ratio of the  $b$  to light and  $c$  to light jet taggability, measured in a QCD Monte Carlo sample (136).

and light flavor jets, the ratio of taggabilities obtained on these two samples reveals the same tendency as seen in Figure 91. The increase of taggability at low jet  $p_T$  in the  $b$ -jets enriched sample is considered as a qualitative proof of the validity of making use of the taggability flavor dependence obtained from the Monte Carlo.

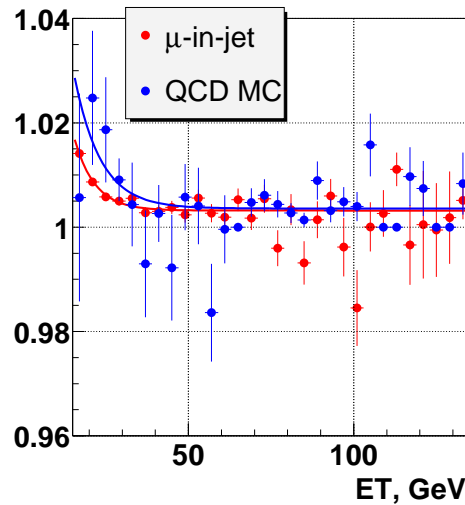


Figure 92. Ratios of taggabilities obtained on enriched  $b$ -jet samples to those measured on enriched light flavor jet samples in data and QCD Monte Carlo (136).

The taggability derived in the combined lepton + jets data sample, dominated by light jets, is then corrected by the ratios of the  $b$  to light and  $c$  to light jet taggabilities (Figure 92) measured in a QCD Monte Carlo sample for  $b$  and  $c$  jets separately.

## 6.2 *b*-Tagging Efficiency

The measurement of the *b*-tagging efficiency in data requires the knowledge of the number of taggable *b* jets before and after applying the tagging algorithm. As a pure sample of taggable *b*-jets in data is not available, the *b*-tagging efficiency is measured in a sample enriched in taggable jets. The data sample of choice is the muon-in-jet sample, derived from the 1MUloose CSG skim (138), which is selected requiring:

- $N_{jet} \geq 2$ ,
- $\geq 1$  medium muon with  $\Delta R(\mu, jet) < 0.5$ ,

representing a sample enriched in semimuonic heavy flavor quark decays, as indicated in Section 6.1.1.

The following section describes the method used to measure the *b*-tagging efficiency in data. It is designed to measure the *b*-tagging efficiency solely for taggable *b* jets with a semimuonic *b* decay ( $b \rightarrow \mu$ ) where  $\Delta R(\mu, jet) < 0.5$ .

### 6.2.1 System8 Method

The System8 method (139) is used to measure the *b*-tagging efficiency purely from data. It allows for the determination of selection efficiencies for signal and one or more backgrounds by measuring the inclusive selection efficiencies for one or more samples with varying signal and background compositions. The problem can be represented by a system of equations. The system is solvable if

- the samples have different fractions of signal and backgrounds,

- the selection criteria have different efficiencies for these signal and backgrounds,
- the different selection criteria are decorrelated to allow the factorization of the efficiencies,
- the number of constraints  $\geq$  the number of unknowns.

Two data samples are used for the measurement of the  $b$ -tagging efficiency, the muon-in-jet ( $n$ ) and the muon-in-jet-away-jet-tagged sample ( $p$ ). The signal is given by  $b$  jets, and only one background is considered, non- $b$  jets ( $c$  and light). The two selection criteria used are the SVT  $b$ -tagging (Section 4.7) and the SLT  $b$ -tagging, that requires the presence of a muon with  $\Delta R(\mu, jet) < 0.5$  and  $p_T^{rel} > 0.7$  GeV, where  $p_T^{rel}$  refers to the fraction of the muon momentum transverse to the momentum of the jet-muon system. A system of eight equations can be formed:

$$\begin{aligned}
 n &= n_b + n_{non-b} \\
 p &= p_b + p_{non-b} \\
 n^{SVT} &= \varepsilon_b^{SVT} n_b + \varepsilon_{non-b}^{SVT} n_{non-b} \\
 p^{SVT} &= \varepsilon_b^{SVT} p_b + \varepsilon_{non-b}^{SVT} p_{non-b} \\
 n^{SLT} &= \varepsilon_b^{SLT} n_b + \varepsilon_{non-b}^{SLT} n_{non-b} \\
 p^{SLT} &= \beta \varepsilon_b^{SLT} p_b + \alpha \varepsilon_{non-b}^{SLT} p_{non-b} \\
 n^{SVT,SLT} &= \varepsilon_b^{SVT} \varepsilon_b^{SLT} n_b + \varepsilon_{non-b}^{SVT} \varepsilon_{non-b}^{SLT} n_{non-b} \\
 p^{SVT,SLT} &= \beta \varepsilon_b^{SVT} \varepsilon_b^{SLT} p_b + \alpha \varepsilon_{non-b}^{SVT} \varepsilon_{non-b}^{SLT} p_{non-b}
 \end{aligned}$$

The terms on the left hand side of the equations are measured in data and correspond to the total number of jets in each sample before tagging ( $n$  for the muon-in-jet sample and  $p$  for the muon-in-jet-away-jet-tagged sample) and after applying the corresponding tagger ( $n^{SVT}$ ,  $n^{SLT}$ ,  $n^{SVT,SLT}$ ,  $p^{SVT}$ ,  $p^{SLT}$  and  $p^{SVT,SLT}$ ). The eight unknowns on the right hand side of the equations consist of the number of  $b$  and non- $b$  jets in the two samples ( $n_b$ ,  $n_{non-b}$ ,  $p_b$ ,  $p_{non-b}$ ), and the tagging efficiencies for taggable  $b$  and non- $b$  jets for the two tagging algorithms SVT and SLT. The system is solved for each  $(p_T, \eta)$  bin separately.

The  $b$ -tagging efficiency measurement is affected by uncertainties due to the assumption of the decorrelation between the SVT and the SLT algorithm for  $b$ -jets

$$\kappa_b = \frac{\varepsilon_b^{SVT,SLT}}{\varepsilon_b^{SVT} \varepsilon_b^{SLT}}, \quad (6.1)$$

for non- $b$ -jets

$$\kappa_{cl} = \frac{\varepsilon_{non-b}^{SVT,SLT}}{\varepsilon_{non-b}^{SVT} \varepsilon_{non-b}^{SLT}}; \quad (6.2)$$

the sample dependence of the SVT tagging efficiency for  $b$  jets

$$\beta = \frac{\varepsilon_b^{SVT} \text{ measured in the muon in jet away jet tagged sample}}{\varepsilon_b^{SVT} \text{ measured in the muon in jet sample}}, \quad (6.3)$$

and for non- $b$  jets

$$\alpha = \frac{\varepsilon_{non-b}^{SVT} \text{ measured in the muon in jet away jet tagged sample}}{\varepsilon_{non-b}^{SVT} \text{ measured in the muon in jet sample}}, \quad (6.4)$$

particularly originating from the assumption that the non- $b$  background composition (i.e. the fraction of  $c$  and light jets) of the two samples is the same.

The average jet  $b$ -tagging efficiency measured in data using the System8 method is  $32.8 \pm 0.3\%$ .

The corresponding parametrizations are shown in Figure 93. The fit to the two dimensional

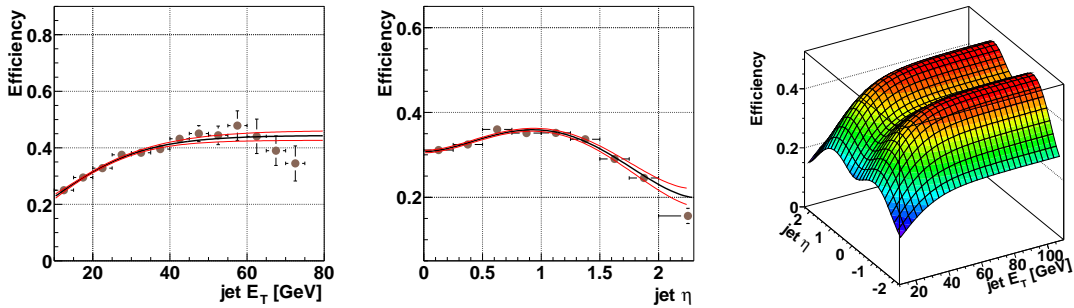


Figure 93. Semimuonic  $b$ -tagging efficiency as a function of jet  $p_T$  (left) and jet  $\eta$  (middle) measured in data with the System8 method along with the fit and  $\pm\sigma$  error band. The right plot shows the combined two-dimensional parameterization.

$b$ -tagging parametrization shown in Figure 93 gives the statistical uncertainty. The corresponding systematic uncertainties are obtained as follows: Figure 94 shows  $\beta$ ,  $k_b$  and  $k_{cl}$  plotted as a

function of jet  $p_T$  as obtained from a Monte Carlo sample containing  $Z \rightarrow b\bar{b} \rightarrow \mu$  (for the first two coefficients),  $Z \rightarrow c\bar{c}$  and  $Z \rightarrow q\bar{q}$  (for  $k_{cl}$ ). To evaluate the contribution to the systematic uncertainty on the  $b$ -tagging efficiency measurement related to  $\beta$  and  $k_{cl}$ , the values of these parameters are varied by  $\pm 1\sigma$  and  $\pm 3\sigma$  respectively, where  $\sigma$  corresponds to the error on the constant fits shown in Figure 94. The variation of  $k_b$  of  $\pm 0.4\%$  is determined from the difference of the values obtained from  $Z \rightarrow b\bar{b}$  and  $t\bar{t}$  Monte Carlo samples compared to that obtained from the combined sample. The value of  $\alpha$  is arbitrarily chosen to be  $1 \pm 0.8$ . The variation in the  $b$ -tagging efficiency is defined as the systematic error.

Another source of systematic uncertainty is the  $p_T^{rel}$  cut chosen for the muon tagger. A cut value of 0.7 GeV is used when solving System8. The variation of the efficiency due to a change of this cut is assigned as another source of systematic uncertainty. The total systematic uncertainty on the  $b$ -tagging efficiency is 2.2%.

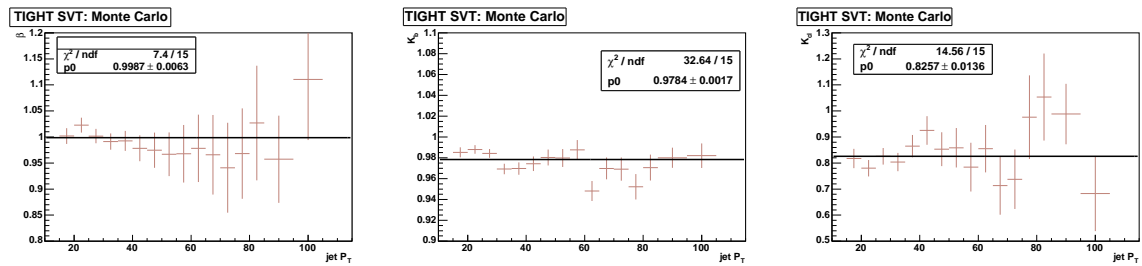


Figure 94. Behavior of the System8 variables ( $\beta$  to the left,  $k_b$  in the center and  $k_{cl}$  to the right) versus jet  $p_T$  observed in Monte Carlo.

### 6.2.2 Inclusive $b$ -Tagging Efficiency

The System8 method was used to measure the  $b$ -tagging efficiency for semimuonic  $b$  decays ( $\varepsilon_{b \rightarrow \mu}$ ) in data. Because of the inadequate description of dead detector material and noise in the central tracking system, the tagging efficiencies are expected to be higher in the Monte Carlo. The  $b$ -tagging efficiency in the Monte Carlo is obtained from a  $t\bar{t} \rightarrow W^+ b W^- \bar{b}$ , sample. The jet flavor is determined by matching the direction of the reconstructed jet to the meson flavor within the cone  $\Delta R < 0.5$ . If there is more than one meson found within the cone, the jet is considered to be a  $b$ -jet if the cone contains at least one  $B$ -meson. It is called a  $c$ -jet if there is at least one  $C$ -meson in the cone and no  $B$ -meson. Light jets are required to have no  $B$ - or  $C$ -mesons within  $\Delta R < 0.5$ .

The efficiency to tag a given jet flavor is defined as the ratio of tagged to taggable jets of that particular flavor and it is parameterized as a function of jet  $E_T$  and  $\eta$ . In order to calibrate the  $b$ -tagging efficiency in Monte Carlo to that measured in data, we define the scale factor as:

$$SF_{b \rightarrow \mu}(p_T, \eta) = \frac{\epsilon_{b \rightarrow \mu}^{data}(p_T, \eta)}{\epsilon_{b \rightarrow \mu}^{MC}(p_T, \eta)}, \quad (6.5)$$

where  $\epsilon_{b \rightarrow \mu}^{MC}$  is the semileptonic  $b$ -tagging efficiency in Monte Carlo. Figure 95 shows the difference between the inclusive ( $\varepsilon_b^{MC}$ ) and the semimuonic ( $\varepsilon_{b \rightarrow \mu}^{MC}$ )  $b$ -tagging efficiencies.

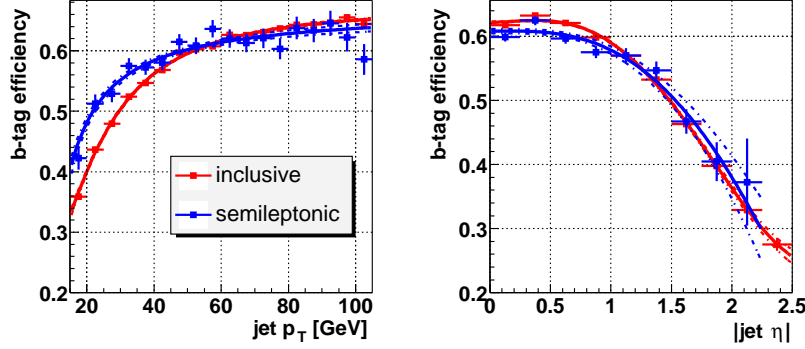


Figure 95. Inclusive and semimuonic  $b$ -tagging efficiency measured in the  $t\bar{t}$  Monte Carlo as a function of jet  $p_T$  (left) and  $\eta$  (right).

We assume that the scale factor for inclusive  $b$ -decays is the same as for semileptonic ones,  $SF_b = SF_{b \rightarrow \mu}$ , and define the calibrated Monte Carlo tagging efficiency for inclusive  $b$ -decays as

$$\epsilon_b(p_T, \eta) = \epsilon_b^{MC}(p_T, \eta) SF_b(p_T, \eta), \quad (6.6)$$

where  $\epsilon_b^{MC}$  is the inclusive  $b$ -tagging efficiency in Monte Carlo.

### 6.3 $c$ -Tagging Efficiency

The  $c$ -tagging efficiency can be written as:

$$\epsilon_c(p_T, \eta) = \epsilon_c^{MC}(p_T, \eta) SF_c(p_T, \eta), \quad (6.7)$$

where  $SF_c(p_T, \eta)$  has been taken to be equal to  $SF_b(p_T, \eta)$ .  $\varepsilon_c^{MC}(p_T, \eta)$  is shown in Figure 96.

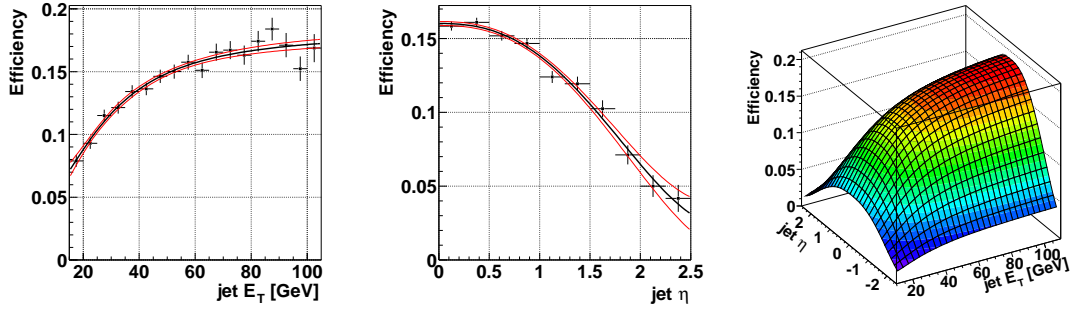


Figure 96. Inclusive  $c$ -tagging efficiency measured in the  $t\bar{t}$  Monte Carlo as a function of jet  $p_T$  (left) and  $\eta$  (middle). The right plot shows the combined two-dimensional parameterization.

Both  $SF_b$  and  $SF_c$  have been measured in Monte Carlo, calibrated to make the track multiplicity look like the one found in data by randomly removing tracks (140). Systematic uncertainties are evaluated due to the assumption that  $SF_c(p_T, \eta) = SF_b(p_T, \eta)$ , by making the replacement

$$SF_{b/c}(p_T, \eta) \equiv \frac{\varepsilon_{b/c}^{data}(p_T, \eta)}{\varepsilon_{b/c}^{MC}(p_T, \eta)} \rightarrow SF_{b/c}^{rtr}(p_T, \eta) \equiv \frac{\varepsilon_{b/c}^{MC,rtr}(p_T, \eta)}{\varepsilon_{b/c}^{MC}(p_T, \eta)}, \quad (6.8)$$

where  $\varepsilon_{b/c}^{MC,rtr}(p_T, \eta)$  represents the  $b/c$ -tagging efficiency measured in the calibrated Monte Carlo. Discrepancies of up to 16% are found as  $SF_c^{rtr} \sim 0.84 SF_b^{rtr}$ , and assigned as a systematic uncertainty.

#### 6.4 Mis-Tagging Rate

Mistags are defined as light flavor jets that have been tagged by the  $b$ -tagging algorithm. They are caused by random overlap of tracks which are displaced from the primary vertex due to tracking mistakes and resolution effects. In addition, there are contributions from  $K_s^0$  and  $\Lambda^0$  decays, photon conversion ( $\gamma \rightarrow e^+e^-$ ) and nuclear interactions, not completely removed by the  $V^0$  filter discussed in Section 4.7.1.

Figure 75 shows the impact parameter significance distributions for tracks from light and  $b$  jets from Monte Carlo. Light jets occur approximately at the same rate for  $dca/\sigma(dca) > 0$  and for  $dca/\sigma(dca) < 0$ . Since the SVT algorithm is symmetric in its treatment of both the impact parameter and the  $L_{xy}$  significance, the mistags should occur at the same rate for  $L_{xy} > 0$  (defined as a tag or “positive tag”) and  $L_{xy} < 0$ , referred to as “negative tag”. Therefore a good estimate for the (positive) mis-tagging efficiency can be obtained from the negative tagging efficiency.

The negative tagging efficiency is measured in the EMqcd data sample which is dominated by QCD multijet production. This sample is selected by requiring:

- $e +$  jets signal trigger,
- at least one electromagnetic object (ID = 10 or 11) with  $p_T \geq 20$  GeV,

- at least one reconstructed and identified jet,
- $E_T \leq 10$  GeV.

Figure 97 shows the parametrizations of the negative tagging efficiency as a function of the jet transverse momentum and rapidity.

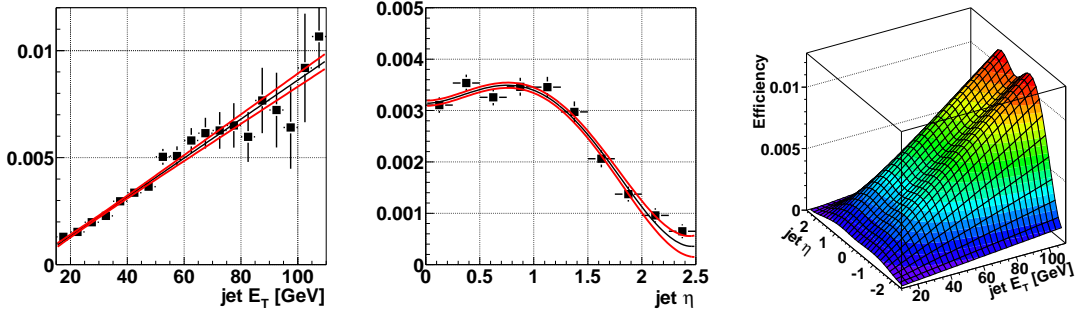


Figure 97. Negative tagging efficiency as a function of jet  $p_T$  (left) and jet  $\eta$  (middle). The right plot shows the two-dimensional parameterization.

To validate these parametrizations, a closure test is done where the predicted rate of negative tags is compared to the observed one in the same sample. This is shown in Figure 98 for the inclusive sample and in Figure 99 for each jet multiplicity bin separately. Good agreement is observed in all distributions.

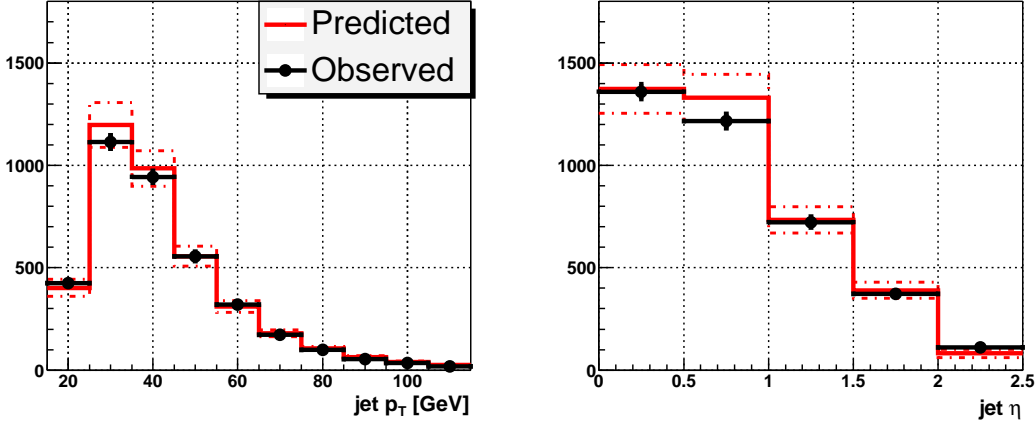


Figure 98. Inclusive  $p_T$  (left) and  $\eta$  (right) distributions of negatively tagged jets in the EMqcd sample compared with the distributions predicted by the negative tag rate parameterizations.

The parameterized negative tag rate was also applied to all taggable jets in the preselected signal samples and the prediction was compared to the actual number of observed negative tags. The result can be found in Table XXII . Figure 100 and Figure 101 show the agreement between the observed transverse momentum and rapidity of jets in the lepton+jets preselected sample and the prediction based on the negative tagging efficiency derived in the EMqcd sample for inclusive and exclusive jet multiplicities, respectively. Good agreement is found between prediction and observation when the parametrized negative tagging rate shown in Figure 97 is applied to the signal sample.

Two factors need to be taken into account to extract the mis-tagging efficiency from the negative tagging rate: the contamination of heavy flavor (hf) and the presence of long lived

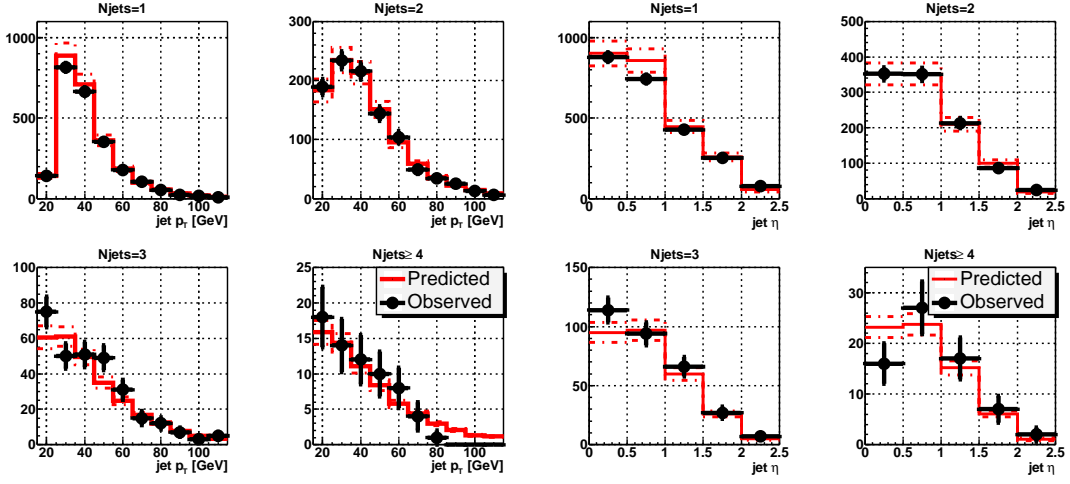


Figure 99.  $p_T$  (four left plots) and  $\eta$  (four right plots) distributions of negatively tagged jets in the EMqcd sample compared with the distributions predicted by the negative tag rate parametrizations in each jet multiplicity bin.

	1 jet	2 jet	3 jet	$\geq 4$ jet
$\mu + \text{jets}$ channel				
$N^{\text{pred}}$	$34.3 \pm 5.9$	$17.5 \pm 4.2$	$4.55 \pm 2.13$	$1.44 \pm 1.20$
$N^{\text{obs}}$	32	13	6	1
$e + \text{jets}$ channel				
$N^{\text{pred}}$	$24.6 \pm 5.0$	$13.4 \pm 3.7$	$3.89 \pm 1.97$	$1.54 \pm 1.24$
$N^{\text{obs}}$	22	16	5	4
$l + \text{jets}$ channel				
$N^{\text{pred}}$	$58.9 \pm 7.7$	$30.9 \pm 5.6$	$8.4 \pm 2.9$	$2.98 \pm 1.73$
$N^{\text{obs}}$	54	29	11	5

TABLE XXII

NUMBER OF OBSERVED AND PREDICTED NEGATIVE TAGS IN THE PRESELECTED SIGNAL SAMPLES.

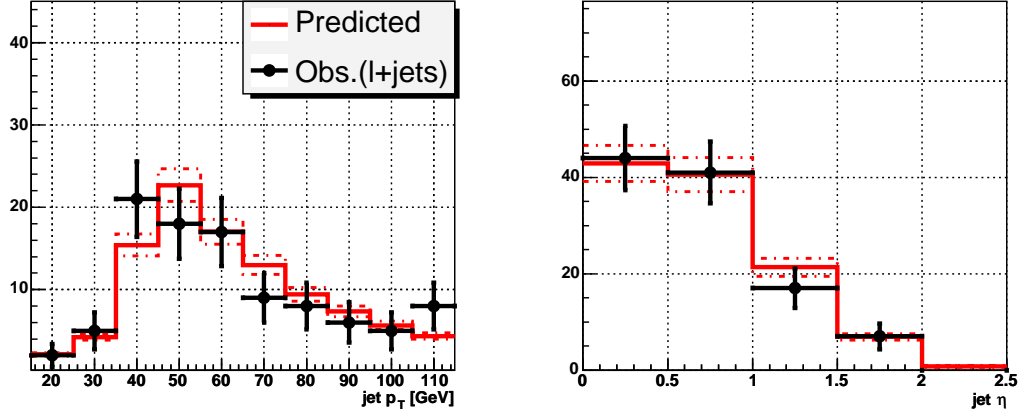


Figure 100. Inclusive  $p_T$  (left) and  $\eta$  (right) distributions of negatively tagged jets in the combined lepton+jets preselected compared with the distributions predicted by the negative tag rate parameterizations.

particles (ll).  $\varepsilon_{-}^{data}(p_T, \eta)$  is determined from the inclusive EMqcd data sample which consists predominantly of light jets, but also has a contribution from  $b$  and  $c$  jets (2% and 4%, respectively, as predicted by PYTHIA QCD-multijets MC simulation). Since the heavy flavor jets have a higher negative tagging efficiency than light jets, the heavy flavor contamination needs to be corrected for. The correction factor  $SF_{hf}$  is derived from PYTHIA QCD-multijets MC events as the ratio between the negative tagging rate observed for light jets and that corresponding to a sample with jets of all flavors

$$SF_{hf}(p_T, \eta) = \frac{\varepsilon_{-}^{light}(p_T, \eta)}{\varepsilon_{-}^{inclusive}(p_T, \eta)}, \quad (6.9)$$

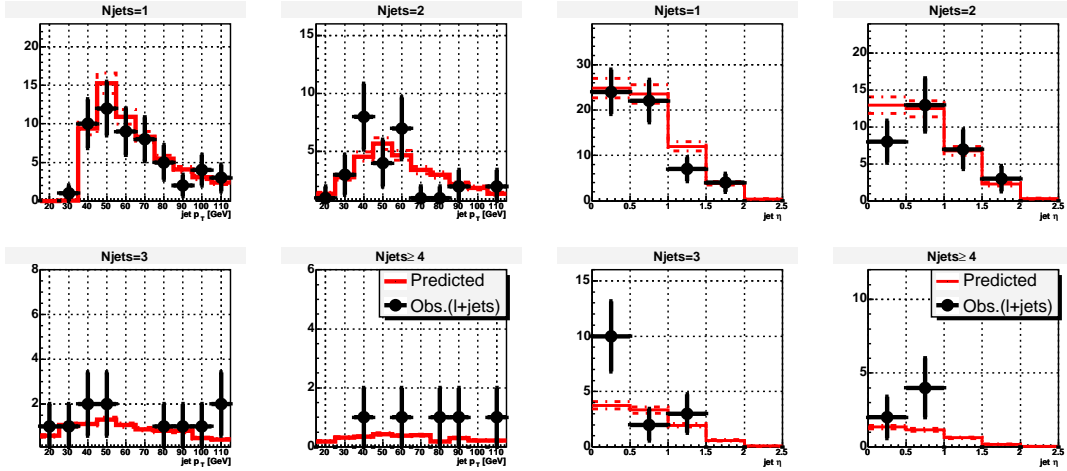


Figure 101.  $p_T$  (four left plots) and  $\eta$  (four right plots) distributions of negatively tagged jets in combined lepton+jets preselected compared with the distributions predicted by the negative tag rate parametrizations in each jet multiplicity bin.

and shown in Figure 102. The efficiency for light jets corrected for heavy flavor contamination is therefore computed as

$$\varepsilon_{-}^{light}(p_T, \eta) = \varepsilon_{-}^{data}(p_T, \eta) SF_{hf}(p_T, \eta) . \quad (6.10)$$

The long lived particles ( $K_s^0, \Lambda^0$ ) present in light jets lead to a larger positive than negative tagging efficiency since they have real lifetime. A correction factor  $SF_{ll}$  is derived from  $Wjjjj$  MC as the ratio between the positive and the negative tagging rates for light jets:

$$SF_{ll}(p_T, \eta) = \frac{\varepsilon_+^{light}(p_T, \eta)}{\varepsilon_-^{light}(p_T, \eta)} \quad (6.11)$$

and also shown in Figure 102. The mistagging efficiency for light jets corrected for long lived particles is finally computed as:

$$\varepsilon_+^{light}(p_T, \eta) = \varepsilon_-^{light}(p_T, \eta) SF_{ll}(p_T, \eta) \quad (6.12)$$

representing the positive mis-tagging efficiency.

Both the heavy flavor contamination and the presence of long lived particles correction are found to be independent of the jet  $\eta$ , so that the positive mis-tagging efficiency is given by

$$\varepsilon_+^{light}(p_T, \eta) = \varepsilon_-^{data}(p_T, \eta) SF_{hf}(p_T) SF_{ll}(p_T). \quad (6.13)$$

The systematic uncertainty associated to the mis-tagging efficiency involves the statistical uncertainties of the fits used to derive the parameterizations for  $\varepsilon_-^{data}(p_T, \eta)$ ,  $SF_{hf}(p_T)$  and  $SF_{ll}(p_T)$ .

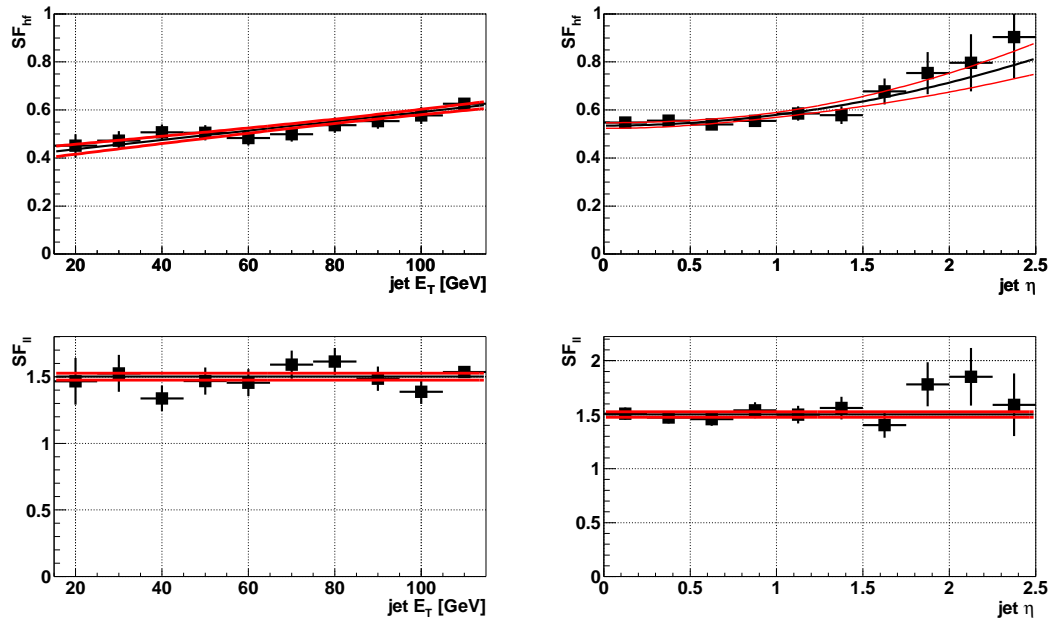


Figure 102. Correction factors for the contribution of heavy flavor in the negative tag rate ( $SF_{hf}$ , upper plots) and contribution to the mistag rate from long lived light particles ( $SF_{ll}$ , lower plots). The two right plots show the  $E_T$  dependence and the two left show the  $\eta$  dependence.

## CHAPTER 7

### THE $t\bar{t}$ PRODUCTION CROSS-SECTION MEASUREMENT

The  $t\bar{t}$  production cross-section at  $\sqrt{s} = 1.96$  TeV is measured using data recorded by the DØ detector at the Fermilab Tevatron, by applying a lifetime  $b$ -tagging algorithm that explicitly reconstructs secondary vertices. As a first step in the analysis, a sample is preselected based on the decay products of the  $W$  boson and the number of jets in the event. This preselection enhances the signal fraction and removes an important fraction of the instrumental background. Most of the non- $t\bar{t}$  processes found in the preselected sample do not contain heavy flavor quarks in the final state. Requiring that one or more of the jets in the event be tagged as defined in Section 4.7 removes approximately 95 % of the background while keeping more than half of the  $t\bar{t}$  events. The  $t\bar{t}$  signal is expected to dominate the preselected sample with three or more jets after the application of lifetime  $b$ -tagging. An excess of observed events over the expected background is assumed to be entirely due to  $t\bar{t}$  production. The  $t\bar{t}$  contribution is negligible in the tagged preselected sample with one or two jets, and the observed results for those jet multiplicities serve as a check of the background prediction.

The  $t\bar{t}$  production cross section is extracted by counting the number of tagged events,  $N_{observed}^{tag}$ , and subtracting the estimated number of tagged background events,  $N_{background}^{tag}$ , according to:

$$\sigma = \frac{N_{observed}^{tag} - N_{background}^{tag}}{BR \cdot L \cdot \varepsilon_{presel} \cdot \bar{P}^{tag}} , \quad (7.1)$$

where  $BR$  is the branching ratio of the considered final state,  $L$  is the integrated luminosity,  $\varepsilon_{\text{presel}}$  is the  $t\bar{t}$  preselection efficiency and  $\bar{P}^{\text{tag}}$  is the probability for a  $t\bar{t}$  event to have one or more jets identified as  $b$  jets, also called *event tagging probability*.

Section 7.1 discusses the individual preselection cuts and their efficiencies, and presents the composition of the preselected sample. The details on the determination and parameterization of the  $b$ -tagging efficiencies are given in Chapter 6. The application of  $b$ -tagging in the analysis and the contributions to the tagged preselected sample are specified in Section 7.2. The systematic uncertainties are discussed in Section 7.3. The cross-section extraction procedure is explained in Section 7.4. Finally, the result of the  $t\bar{t}$  production cross-section measurement is presented in Section 7.6.

## 7.1 $t\bar{t}$ Event Preselection

The signature of  $t\bar{t}$  events is discussed in Section 2.4 and can be summarized as a leptonically decaying  $W$  boson,  $W \rightarrow \ell\nu$ , produced in association with jets. The preselection aims to select the individual objects in the final state with high efficiency and purity while minimizing the instrumental background.

The samples for the electron-plus-jets and  $\mu$ -plus-jets channels are preselected requiring, respectively, a high  $p_T$  isolated electron or muon coming from the primary vertex, and high missing transverse energy signaling the presence of a neutrino. To further reject background from QCD, the missing energy has to be separated from the lepton in the plane transverse to the beam axis. Events with a second lepton with high transverse momentum are analyzed in (52) and are explicitly vetoed in this analysis.

All cuts used to define the preselected sample and the corresponding efficiencies are listed in Table XXIII for the  $\mu$ -plus-jets channel and in Table XXIV for the electron-plus-jets channel. The acceptance, reconstruction efficiencies and the survival efficiencies for the preselection cuts for  $t\bar{t}$  events ( $\varepsilon_{presel}$ ) are measured in a combination of data and Monte Carlo.  $\varepsilon_{presel}$  is measured in the  $t\bar{t}$  simulation with respect to  $t\bar{t} \rightarrow W + jets$ , where the following  $W$  boson decays are allowed:  $W \rightarrow \ell\nu_\ell$  or  $W \rightarrow \tau\nu_\tau$  with  $\tau \rightarrow \ell\nu_\ell\nu_\tau$  ( $\ell$  represents either a muon or an electron). Possible inaccuracies in the MC description of individual object identification or selection efficiencies are corrected by MC-to-data scale factors which are derived on a control sample where the respective efficiency can be extracted both on MC and data. The MC-to-data scale factor is defined as the efficiency measured in data divided by the efficiency measured in MC, and is determined as a function of the relevant quantities. These MC-to-data correction factors are referenced as  $\kappa$  with a descriptive subscript.

A detailed explanation of the preselection criteria can be found in (111) and (141) for the muon and electron channels, respectively.

### **7.1.1 Muon Channel Preselection**

The requirements imposed to select the sample in the  $\mu$ -plus-jets channel are summarized next.

- Events are accepted if they have at least one reconstructed jet passing the identification criteria described in Section 4.5. Jets are required to have  $p_T > 20$  GeV and  $|\eta| < 2.5$ . For the leading jet, the jet with highest transverse momentum in the event, the  $p_T$  cut is increased to 40 GeV. This rise in the acceptance threshold for the leading jet results

in a loss of less than 0.5% in signal efficiency but at the same time reduces the  $W+\text{jets}$  background, which dominates the preselected sample, by roughly 13%. Figure 103 shows the leading jet  $p_T$  distributions for  $t\bar{t}$  signal and  $W+\text{jets}$  background events.

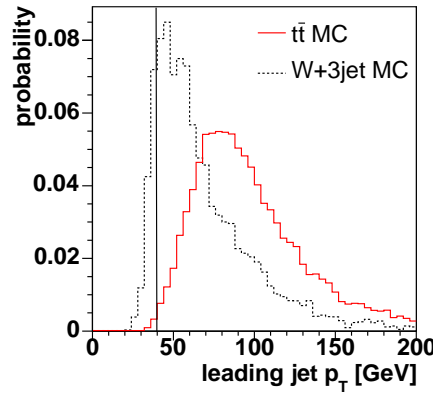


Figure 103. Leading jet  $p_T$  threshold. The simulation includes the corresponding trigger efficiencies (111).

- Muons are required to fulfill the standard Muon ID requirements as defined in Section 4.3.1:
  - *medium* quality,
  - $nseg = \pm 3$ , and
  - $|t_A| < 10 \text{ ns}$  and  $|t_{BC}| < 10 \text{ ns}$ .

- Muons are required to have a matching track.
- A cut is placed on the muon's pseudorapidity forcing it to be reconstructed in the fiducial region of the muon detector and preventing boundary effects from possible marginal differences between data and simulation.
- Muons are required to have  $p_T > 20 \text{ GeV}$ .
- In order to reject muons from semileptonic  $B$  meson decays, the selected muon is required to be isolated from any good jet in the event by  $\Delta R(\mu, \text{jet}) > 0.5$ . This cut is also referred to as the *loose muon isolation* cut.
- The track associated to the muon is required to be of good quality in order to reject mismeasured tracks. The cut is applied on the track fit  $\chi^2$  and required to be  $\chi^2 < 4$ .
- The cut on the  $dca$  significance of the track matched to the muon,  $|dca|/\sigma_{dca} < 3$ , is used to reject muons from semileptonic  $b$ -decays, while keeping most of the muons from  $W$  decays.
- The offline muon is required to match a muon trigger object.
- The tight muon isolation cuts are applied as defined in Section 4.3.4
  - $\text{rat11} < 0.08$ ,
  - $\text{rattrk} < 0.06$ .
- A cut on the missing transverse energy and on the relative angle between the  $\cancel{E}_T$  and the muon is applied in order to reject QCD background. QCD is found to have the missing

transverse energy mainly back-to-back with the leading jet for events where the missing transverse energy originates from the mismeasurement of the leading jet energy. QCD is also found to have the missing transverse energy either in the direction of the muon or back-to-back to it. This can be explained by  $b\bar{b}$  production where one or both of the b-hadrons decay semileptonically, and one of the jets is not reconstructed in the calorimeter, or the muon transverse momentum is mismeasured, giving rise to the  $\cancel{E}_T$ . The cut giving the highest  $t\bar{t}$  efficiency  $\times$  purity corresponds to (111):

- $\cancel{E}_T > 15 \text{ GeV}$ ,
- $\Delta\phi(\mu, \cancel{E}_T) > 0.7\pi - 0.7\pi \cdot \cancel{E}_T/(30 \text{ GeV})$ .

- Events with a second lepton with high transverse momentum are analyzed in (52) and are explicitly vetoed here. Events are rejected if a second muon is found which satisfies:

- $p_T > 15 \text{ GeV}$ ,
- *medium* quality,
- $nseg = \pm 3$ ,
- track-match,
- $rat11 < 0.12$ ,
- $rattrk < 0.12$ .

Events are also rejected if an electron is found which satisfies:

- $p_T > 15 \text{ GeV}$ ,

- EMF > 0.9,
  - isolation < 0.15,
  - H-matrix7 < 50.0,
  - track-match  $\chi^2 \neq -1.0$ ,
  - electron likelihood > 0.85,
  - $|\eta_{det}| < 1.1$  or  $1.5 < |\eta_{det}| < 2.5$ .
- The second muon veto ensures the orthogonality of samples for the various  $t\bar{t}$  final states.

However, it is not sufficient to exclude  $Z \rightarrow \mu\mu$ -plus-jet events where the second muon is of low quality. These events appear to have large  $\cancel{E}_T$  due to the finite  $\cancel{E}_T$  resolution in events with three or more jets, or due to the fact that muons not fulfilling the medium  $|nseg| = 3$  requirement are not used for the  $\cancel{E}_T$  correction. Events with invariant dimuon mass between  $70 \text{ GeV} < m_{\mu\mu} < 110 \text{ GeV}$ , are rejected.  $m_{\mu\mu}$  is calculated from the leading tight muon used in the analysis, and a second high  $p_T$  muon in the event satisfying the following criteria:

- *loose* quality,
  - central track match,
  - isolated from a jet:  $\Delta R(\mu, \text{jet}) > 0.5$ .
- The primary vertex is required to fulfill:
- $|z_{PV}| \leq 60 \text{ cm}$ .
  - At least three tracks fitted into the PV:  $Ntrks_{PV} > 2$ .

- The DØreco PV and the DØroot PV are required to have a  $z$ -separation of less than 5 cm.
- Finally, the cut  $|\Delta z(\mu, \text{PV})| < 1 \text{ cm}$  is used to reject both muons from semileptonic decays and cosmic muons, while most of the muons from  $W$  decays are kept.
- The determination of the jet and muon trigger efficiencies are described in Sections 5.1.1 and 5.1.3, respectively. The event trigger efficiency is evaluated in the simulation by folding in the trigger parametrizations per muon and per jet given by Equation 5.5.

A summary of the preselection efficiency in the  $\mu$ -plus-jets channel is given in Table XXIII.

### **7.1.2 Electron Channel Preselection**

The requirements imposed to select the sample in the electron-plus-jets channel are described below.

- As for the  $\mu$ -plus-jets channel, events are accepted if they have at least one good jet with  $p_T > 20 \text{ GeV}$  and  $|\eta| < 2.5$ . The leading jet is required to have a transverse momentum of at least 40 GeV.
- Electrons are required to be of *medium* quality (113) as part of the identification criteria described in 4.4.1:
  - $p_T > 15 \text{ GeV}$ ,
  - $EM_f > 0.9$ ,

	exclusive efficiency		cumulative efficiency	
	3 jets	$\geq 4$ jets	3 jets	$\geq 4$ jets
$N_{jet}$	41.17 $\pm$ 0.18	40.68 $\pm$ 0.18	41.17 $\pm$ 0.18	40.68 $\pm$ 0.18
Muon selection	74.99 $\pm$ 0.25	76.09 $\pm$ 0.24	30.88 $\pm$ 0.17	30.95 $\pm$ 0.17
Muon Track Match	96.85 $\pm$ 0.11	97.04 $\pm$ 0.11	29.90 $\pm$ 0.17	30.04 $\pm$ 0.17
$ \eta_{det}  < 2.0$	99.85 $\pm$ 0.03	99.89 $\pm$ 0.02	29.86 $\pm$ 0.17	30.00 $\pm$ 0.17
Muon $p_T$ cut	72.43 $\pm$ 0.30	73.36 $\pm$ 0.29	21.63 $\pm$ 0.15	22.01 $\pm$ 0.15
Muon $\Delta r$ cut	86.73 $\pm$ 0.27	78.38 $\pm$ 0.32	18.76 $\pm$ 0.14	17.25 $\pm$ 0.14
Track $\chi^2$ cut	99.88 $\pm$ 0.03	99.90 $\pm$ 0.03	18.74 $\pm$ 0.14	17.24 $\pm$ 0.14
Muon DCA Significance	93.49 $\pm$ 0.21	93.83 $\pm$ 0.21	17.52 $\pm$ 0.14	16.17 $\pm$ 0.13
Muon-trigger match	100.00 $\pm$ 0.00	100.00 $\pm$ 0.00	17.52 $\pm$ 0.14	16.17 $\pm$ 0.13
$E_T$ cut	93.11 $\pm$ 0.22	92.81 $\pm$ 0.23	16.31 $\pm$ 0.13	15.01 $\pm$ 0.13
Muon Isolation	87.30 $\pm$ 0.30	87.20 $\pm$ 0.31	14.24 $\pm$ 0.13	13.09 $\pm$ 0.12
Second Muon veto	99.95 $\pm$ 0.02	99.97 $\pm$ 0.02	14.23 $\pm$ 0.13	13.09 $\pm$ 0.12
Electron Veto	99.91 $\pm$ 0.03	99.95 $\pm$ 0.02	14.22 $\pm$ 0.13	13.08 $\pm$ 0.12
Z mass veto	99.56 $\pm$ 0.06	99.86 $\pm$ 0.04	14.15 $\pm$ 0.13	13.06 $\pm$ 0.12
$ PV_z  < 60.0$ cm	98.77 $\pm$ 0.11	98.99 $\pm$ 0.10	13.98 $\pm$ 0.13	12.93 $\pm$ 0.12
$PV$ $n_{tracks}$ cut	99.79 $\pm$ 0.04	99.90 $\pm$ 0.03	13.95 $\pm$ 0.13	12.91 $\pm$ 0.12
$\Delta z(reco, d\mathcal{O}root)$ cut	99.77 $\pm$ 0.05	99.78 $\pm$ 0.05	13.92 $\pm$ 0.13	12.89 $\pm$ 0.12
$\Delta z(\mu, PV)$ cut	99.99 $\pm$ 0.01	99.98 $\pm$ 0.01	13.92 $\pm$ 0.13	12.88 $\pm$ 0.12
Trigger Efficiency	90.36 $\pm$ 0.07	90.63 $\pm$ 0.07	12.58 $\pm$ 0.11	11.68 $\pm$ 0.11
$\kappa_{MUID}$	1.000	1.000	12.58 $\pm$ 0.11	11.68 $\pm$ 0.11
$\kappa_{track}$	0.988		12.42 $\pm$ 0.11	11.54 $\pm$ 0.11
$\kappa_{DCA}$	0.997		12.39 $\pm$ 0.11	11.50 $\pm$ 0.11
$\kappa_{\chi^2}$	0.983		12.18 $\pm$ 0.11	11.31 $\pm$ 0.11
$\kappa_{iso}$	0.985		11.99 $\pm$ 0.11	11.14 $\pm$ 0.11
$\kappa_{PV}$	0.991		11.89 $\pm$ 0.11	11.04 $\pm$ 0.10
$\kappa_{\Delta(\mu, PV)}$	0.998		11.86 $\pm$ 0.11	11.01 $\pm$ 0.10
$\epsilon_{total}$	—		11.86 $\pm$ 0.11	11.01 $\pm$ 0.10

TABLE XXIII

SUMMARY OF  $t\bar{t} \rightarrow \text{LEPTON+JETS}$  PRESELECTION EFFICIENCIES IN THE MUON+JETS CHANNEL. THE QUOTED UNCERTAINTIES RESULT ONLY FROM LIMITED MC STATISTICS.

–  $EM_{iso} < 0.15$ ,

–  $\chi^2_{hmx7} < 50$ .

- Electrons are required to have a track within  $0.05 \times 0.05$  in an  $\eta \times \phi$  road around the EM cluster.
- Electrons are required to have  $p_T > 20 \text{ GeV}$  to reduce the trigger bias and the electron fake rate.
- The track associated to the electron is required to have a transverse momentum greater than  $10 \text{ GeV}$ .
- The tight criteria is applied for the electrons to be accepted:
  - $EM_{likelihood} > 0.85$ .
- The offline electron is required to match an electron trigger object in the event.
- The main background source for  $t\bar{t}$  apart from  $W+\text{jets}$  production are QCD multijet events, with a jet misidentified as an electron or an electron produced inside a jet. Thus, QCD events contain both real and fake electrons. At the same time, an energy imbalance in QCD events occurs predominately due to jet energy mis-measurements, which causes the direction of the missing transverse energy to point along (or opposite) to the electron in the event. In order to suppress the QCD background more efficiently than just cutting on missing transverse energy ( $\cancel{E}_T$ ) alone, the different angular distributions between the  $\cancel{E}_T$  and the electron can be exploited. The cuts applied on the  $\cancel{E}_T$  and the  $\Delta\phi$  between the  $\cancel{E}_T$  and the electron are (141):

- $\cancel{E}_T > 25 \text{ GeV}$ ,
- $\Delta\phi(e, \cancel{E}_T) > 2.3 * \left(1 - \frac{\cancel{E}_T}{50}\right)$ .

- Events with a second lepton with high transverse momentum are analyzed in (52) and are explicitly vetoed here. Events are rejected if an isolated muon is found which satisfies:

- $p_T > 15 \text{ GeV}$ ,
- ‘medium’ quality,
- $nseg = \pm 3$ ,
- track-match,
- $Rat11 < 0.12$ ,
- $Rattrk < 0.12$ .

Events are also rejected if a second electron is found which satisfies:

- $p_T > 15 \text{ GeV}$ ,
- $\text{EMF} > 0.9$ ,
- isolation  $< 0.15$ ,
- H-matrix7  $< 50.0$ ,
- track-match  $\chi^2 \neq -1.0$ ,
- electron likelihood  $> 0.85$ ,
- $|\eta_{det}| < 1.1$  or  $1.5 < |\eta_{det}| < 2.5$ .

Contamination from  $Z \rightarrow ee + \text{jets}$  events after this cut is found to be negligible.

- The primary vertex reconstruction and the quality cuts are applied as described in Section 4.2:
  - $|z_{PV}| \leq 60$  cm,
  - At least three tracks fitted into the PV:  $Ntrks_{PV} > 2$ ,
  - The DØreco PV and the DØroot PV are required to have a  $z$ -separation of less than 5 cm.
- The cut  $|\Delta z(e, \text{PV})| < 1$  cm is used to confirm that the electron comes from the primary vertex.
- The determination of the jet and electron trigger efficiencies are described in Sections 5.1.3 and 5.1.2, respectively. The event trigger efficiency is evaluated in the simulation by folding in the trigger parametrizations per electron and per jet given by Equation 5.6.

A summary of the preselection efficiency in the electron-plus-jets channel is given in Table XXIV.

### **7.1.3 Composition of the Preselected Samples - Matrix Method**

The preselection, as described in Sections 7.1.1 and 7.1.2, serves to enhance the signal fraction in the selected data sample. However, not only  $t\bar{t}$  events survive the preselection. The backgrounds that are present in the preselected samples can be subdivided into two components:

- **Physics background:** Physics processes with the same objects in the final state: an isolated high  $p_T$  lepton,  $\cancel{E}_T$ , and jets. The dominant contribution comes from the elec-

	exclusive efficiency		cumulative efficiency	
	3 jets	$\geq 4$ jets	3 jets	$\geq 4$ jets
$N_{jet}$	40.63 $\pm$ 0.18	39.30 $\pm$ 0.18	40.63 $\pm$ 0.18	39.30 $\pm$ 0.18
Loose EM Criteria	70.65 $\pm$ 0.26	58.87 $\pm$ 0.29	28.70 $\pm$ 0.17	23.14 $\pm$ 0.15
EM Cluster within $\eta < 1.1$	84.64 $\pm$ 0.25	82.23 $\pm$ 0.29	24.29 $\pm$ 0.16	19.02 $\pm$ 0.14
EM Track Match	91.58 $\pm$ 0.21	93.14 $\pm$ 0.21	22.25 $\pm$ 0.15	17.72 $\pm$ 0.14
EM $E_T$ cut	93.61 $\pm$ 0.19	93.95 $\pm$ 0.21	20.83 $\pm$ 0.15	16.65 $\pm$ 0.14
Track $p_T$ cut	99.88 $\pm$ 0.03	99.94 $\pm$ 0.02	20.80 $\pm$ 0.15	16.64 $\pm$ 0.14
EM Likelihood	88.11 $\pm$ 0.26	89.75 $\pm$ 0.27	18.33 $\pm$ 0.14	14.93 $\pm$ 0.13
Electron-trigger match	100.00 $\pm$ 0.00	100.00 $\pm$ 0.00	18.33 $\pm$ 0.14	14.93 $\pm$ 0.13
$\not{E}_T$ cut	84.45 $\pm$ 0.31	83.58 $\pm$ 0.35	15.48 $\pm$ 0.13	12.48 $\pm$ 0.12
$\Delta\phi(e, \not{E}_T)$ cut	94.83 $\pm$ 0.21	94.62 $\pm$ 0.23	14.68 $\pm$ 0.13	11.81 $\pm$ 0.12
Second Electron Veto	99.96 $\pm$ 0.02	100.00 $\pm$ 0.00	14.67 $\pm$ 0.13	11.81 $\pm$ 0.12
Isolated Muon Veto	99.99 $\pm$ 0.01	99.97 $\pm$ 0.02	14.67 $\pm$ 0.13	11.80 $\pm$ 0.12
$ PV_z  < 60.0$ cm	99.32 $\pm$ 0.08	99.40 $\pm$ 0.08	14.57 $\pm$ 0.13	11.73 $\pm$ 0.12
$PV$ $n_{tracks}$ cut	99.75 $\pm$ 0.05	99.78 $\pm$ 0.05	14.54 $\pm$ 0.13	11.71 $\pm$ 0.12
$\Delta z(reco, d\Omega root)$ cut	99.81 $\pm$ 0.04	99.86 $\pm$ 0.04	14.51 $\pm$ 0.13	11.69 $\pm$ 0.12
$\Delta z(e, PV)$ cut	100.00 $\pm$ 0.00	99.98 $\pm$ 0.02	14.51 $\pm$ 0.13	11.69 $\pm$ 0.12
Trigger Efficiency	92.82 $\pm$ 0.02	92.87 $\pm$ 0.02	13.47 $\pm$ 0.12	10.86 $\pm$ 0.11
$\kappa_{EMID}$		0.984	13.25 $\pm$ 0.12	10.68 $\pm$ 0.11
$\kappa_{track}$		0.983	13.03 $\pm$ 0.12	10.50 $\pm$ 0.11
$\kappa_{Lhood}$		0.912	11.88 $\pm$ 0.11	9.58 $\pm$ 0.10
$\kappa_{PV}$		1.004	11.93 $\pm$ 0.11	9.62 $\pm$ 0.10
$\kappa_{\Delta z(e, PV)}$		0.997	11.89 $\pm$ 0.11	9.59 $\pm$ 0.10
$\epsilon^{total}$		—	11.89 $\pm$ 0.11	9.59 $\pm$ 0.10

TABLE XXIV

SUMMARY OF  $t\bar{t} \rightarrow \text{LEPTON+JETS}$  PRESELECTION EFFICIENCIES IN THE ELECTRON+JETS CHANNEL. THE QUOTED UNCERTAINTIES RESULT ONLY FROM LIMITED MC STATISTICS.

troweak  $W$  production accompanied by jets, as described in 2.5. Minor contributions arise from single top,  $Z+jets$ , and diboson production, discussed in Section 2.7.

- **Instrumental background:** This corresponds to the QCD-multijets background, a strong production of four or more jets, with fake  $\cancel{E}_T$  and a fake lepton, as described in 2.6.

The expected number of QCD background events is entirely derived from data through the *Matrix Method*. This method consist of defining two samples of events, a loose and a tight set, the latter being a subset of the first. The tight sample consists of  $N_t$  events and corresponds to the preselection sample. The loose sample consists of  $N_\ell$  events that pass the preselection but have the tight lepton requirement removed, i.e. the likelihood cut for electrons and the tight isolation for muons are dropped. The number of events with leptons originating from a  $W$  decay is denoted by  $N^{sig}$ . The number of events originating from QCD multijet production is denoted by  $N^{QCD}$ . Then  $N_\ell$  and  $N_t$  can be written as:

$$\begin{aligned} N_\ell &= N_\ell^{sig} + N_\ell^{QCD} \\ N_t &= \varepsilon_{sig} N_\ell^{sig} + \varepsilon_{QCD} N_\ell^{QCD} \end{aligned} \tag{7.2}$$

where  $\varepsilon_{sig}$  is the efficiency for a loose lepton from a  $W$  decay to pass tight criteria,  $\varepsilon_{QCD}$  is the (fake) rate at which a loose lepton in QCD events appears to be tight. Solving the linear system in Equation 7.2 for  $N_\ell^{QCD}$  and  $N_\ell^{sig}$  yields:

$$N_\ell^{sig} = \frac{N_t - \varepsilon_{QCD} N_\ell}{\varepsilon_{sig} - \varepsilon_{QCD}} \quad \text{and} \quad N_\ell^{QCD} = \frac{\varepsilon_{sig} N_\ell - N_t}{\varepsilon_{sig} - \varepsilon_{QCD}}, \quad (7.3)$$

and

$$N_t^{sig} = \varepsilon_{sig} N_\ell^{sig} \quad \text{and} \quad N_t^{QCD} = \varepsilon_{QCD} N_\ell^{QCD}. \quad (7.4)$$

In the  $\mu$ -plus-jets channel, the rate at which a muon in QCD-multijets events appears isolated,  $\varepsilon_{QCD}$ , is measured in a low  $\cancel{E}_T$  data sample selected with the same requirements as the preselection, but without applying the  $\cancel{E}_T$ -related set of cuts listed in Section 7.1.1. Instead, the following two cuts are applied:

- $\cancel{E}_T < 10 \text{ GeV}$  and
- $\cancel{E}_{TCAL}$  ( $=\cancel{E}_T$  without muon correction)  $< 30 \text{ GeV}$ .

$\varepsilon_{QCD}$  is found to be constant as a function of  $\cancel{E}_T$  for  $\cancel{E}_T < 10 \text{ GeV}$ , confirming the assumption that these low- $\cancel{E}_T$  events are dominated by QCD events.  $\varepsilon_{QCD}$  as a function of jet multiplicity is shown in Table XXV.

$\varepsilon_{sig}$  is the fraction of truly isolated muons originating from  $W$  boson decays surviving the tight isolation requirements. It is measured in  $W$ +jets MC, and corrected by a data to MC scale

factor derived from  $Z \rightarrow \mu\mu$  events.  $\varepsilon_{\text{sig}}$  as a function of jet multiplicity is shown in Table XXV.

	$\varepsilon_{\text{QCD}}$	$\varepsilon_{\text{sig}}$
$N_{\text{jet}} = 1$	$0.039 \pm 0.004$	$0.901 \pm 0.005$
$N_{\text{jet}} = 2$	$0.107 \pm 0.009$	$0.876 \pm 0.008$
$N_{\text{jet}} \geq 3$	$0.107 \pm 0.009$	$0.848 \pm 0.005$

TABLE XXV

$\varepsilon_{\text{QCD}}$  AND  $\varepsilon_{\text{SIG}}$  AS A FUNCTION OF JET MULTIPLICITY IN THE MUON+JETS CHANNEL.

In the electron-plus-jets channel,  $\varepsilon_{\text{sig}}$  and  $\varepsilon_{\text{QCD}}$  are derived separately for trigger lists v8-v11, v12 and v13, due to the change of the shower shape cut on EM objects at L3. The efficiency for an electron originating from a  $W$  decay to pass the likelihood cut,  $\varepsilon_{\text{sig}}$ , is not sensitive to this change in trigger condition, and therefore inclusive values for the full data set are obtained.  $\varepsilon_{\text{QCD}}$  is measured from data using a sample that passed the preselection, but inverting the  $\cancel{E}_T$  cut ( $\cancel{E}_T < 10$  GeV). This method assumes that the low  $\cancel{E}_T$  region is dominated by background, and the fake rate is calculated as the ratio of tight to loose events in this  $\cancel{E}_T < 10$  GeV range.  $\varepsilon_{\text{sig}}$  and  $\varepsilon_{\text{QCD}}$  in the electron-plus-jets channel are summarized in Table XXVI as a function of the number of jets and trigger list version. As no variation is observed in  $\varepsilon_{\text{QCD}}$  versus the

$N_{\text{jets}}$	$\varepsilon_{\text{sig}}$	$\varepsilon_{QCD}$ v8-v11	$\varepsilon_{QCD}$ v12	$\varepsilon_{QCD}$ v13
= 1 jet	$0.853 \pm 0.010$	$0.124 \pm 0.005$	$0.171 \pm 0.006$	$0.167 \pm 0.011$
= 2 jets	$0.816 \pm 0.018$	$0.132 \pm 0.009$	$0.187 \pm 0.010$	$0.157 \pm 0.019$
$\geq 2$ jets	-	$0.129 \pm 0.009$	$0.189 \pm 0.009$	$0.172 \pm 0.018$
= 3 jets	$0.830 \pm 0.007$	$0.114 \pm 0.021$	$0.186 \pm 0.025$	$0.195 \pm 0.058$
$\geq 3$ jets	$0.829 \pm 0.006$	$0.108 \pm 0.019$	$0.197 \pm 0.024$	$0.194 \pm 0.050$
$\geq 4$ jets	$0.816 \pm 0.006$	$0.116 \pm 0.078$	$0.205 \pm 0.062$	$0.163 \pm 0.150$

TABLE XXVI

$\varepsilon_{\text{SIG}}$  PER JET MULTIPLICITY IN THE ELECTRON+JETS CHANNEL, AND  $\varepsilon_{QCD}$  AS A FUNCTION OF THE NUMBER OF JETS AND TRIGGER LIST VERSION.

number of jets, the second inclusive jet multiplicity bin is used.  $\varepsilon_{\text{sig}}$  is measured in  $W+\text{jets}$  MC and corrected by a data to MC scale factor derived from  $Z \rightarrow ee$  events.

The estimated number of preselected QCD and  $W$ -like events in the  $\mu$ -plus-jets and electron-plus-jets channels are given in Table XXVII and Table XXVIII, respectively.

	1 jet	2 jets	3 jets	$\geq 4$ jets
$N_{l+jets}^{\text{presel}}$	13532	4549	897	215
$N_{(W \rightarrow l)+jets}^{\text{presel}}$	$13186.0 \pm 120.9$	$4227.0 \pm 70.1$	$814.3 \pm 31.1$	$190.7 \pm 15.3$
$N_{QCD \rightarrow l+jets}^{\text{presel}}$	$346.0 \pm 22.6$	$322.0 \pm 12.2$	$82.7 \pm 4.6$	$24.3 \pm 2.2$

TABLE XXVII

NUMBER OF PRESELECTED EVENTS IN THE MUON+JETS CHANNEL AND EXPECTED CONTRIBUTION FROM QCD AND  $W$ -LIKE VERSUS EXCLUSIVE JET MULTIPLICITY.

	1 jet	2 jets	3 jets	$\geq 4$ jets
$N_{e+jets}^{presel}$	5557	1924	401	106
$N_{(W \rightarrow e) + jets}^{presel}$	$5362.4 \pm 79.7$	$1789.4 \pm 46.7$	$357.5 \pm 21.2$	$92.4 \pm 10.9$
$N_{QCD \rightarrow e+jets}^{presel}$	$194.6 \pm 19.9$	$134.6 \pm 10.8$	$43.5 \pm 4.1$	$13.6 \pm 2.0$

TABLE XXVIII

NUMBER OF PRESELECTED EVENTS IN THE ELECTRON+JETS CHANNEL AND EXPECTED CONTRIBUTION FROM QCD AND  $W$ -LIKE EVENTS VERSUS EXCLUSIVE JET MULTIPLICITY.

## 7.2 Composition of the Tagged Sample

The data sample before tagging is given by events passing the preselection described in Section 7.1.3. The Matrix Method provides the number of  $W$ -like and QCD events per exclusive jet multiplicity (except for the fourth jet bin which is treated inclusively). In order to measure the  $t\bar{t}$  production cross section using lifetime tagging, the probability to identify one or more jets in an event as  $b$ -jets, referred to as  $\bar{P}^{tag}$  in Equation 7.1, is needed. The probability  $\bar{P}_{background}^{tag}$  is also required for the background prediction, implicitly contained in  $N_{background}^{tag}$  in Equation 7.1. The event tagging probability depends on the flavor content and topology of the events, and is evaluated on MC, applying to each jet the appropriate tagging rates as measured in data.

The following method is used to evaluate the expected number of tagged signal and background events:

- According to (142), the probability for a jet of a given flavor  $\alpha$  ( $b$ ,  $c$  or light jet) to be tagged is the product of the taggability and the calibrated tagging efficiency defined in Section 6.2.2:

$$\mathcal{P}_\alpha(p_T, \eta) = P^{tagg,data}(p_T, \eta) \epsilon_\alpha(p_T, \eta) \quad (7.5)$$

- The event tagging probabilities  $P_{event}$  are derived by weighting each reconstructed jet in the MC event by the per jet tagging probability  $\mathcal{P}_\alpha(p_T, \eta)$  according to its flavor  $\alpha$ , its  $p_T$  and its  $\eta$ . The probability to have at least one tag in a given event is given by the complement of the probability that none of the jets is tagged:

$$P_{event}^{tag}(\geq 1 \text{ tag}) = 1 - P_{event}^{tag}(0 \text{ tag}) = 1 - \prod_{j=1}^{N_{jets}} (1 - \mathcal{P}_{\alpha_j}(p_{T_j}, \eta_j)). \quad (7.6)$$

The probabilities to have exactly one and to have two or more tags are:

$$P_{event}^{tag}(1 \text{ tag}) = \sum_{j=1}^{N_{jets}} \mathcal{P}_{\alpha_j}(p_{T_j}, \eta_j) \prod_{i \neq j} (1 - \mathcal{P}_{\alpha_i}(p_{T_i}, \eta_i)), \quad (7.7)$$

and

$$P_{event}^{tag}(\geq 2 \text{ tag}) = P_{event}^{tag}(\geq 1 \text{ tag}) - P_{event}^{tag}(1 \text{ tag}), \quad (7.8)$$

respectively. The average event tagging probability can be obtained by averaging over all preselected Monte Carlo events for signal and background samples.

- The trigger can significantly distort the jet  $p_T$  and also the  $\eta$  spectrum, particularly for the low jet multiplicity bins, and therefore needs to be taken into account when calculating the average event tagging probability. The probability for an event to satisfy the  $\mu$ +jets trigger is given by Equation 5.5, and by Equation 5.6 for the  $e$ +jets trigger. The event tagging probability is corrected for this trigger bias by weighting each event with the trigger probability  $P_{event}^{trigg}$ . The average event tagging probability, taking into account the trigger bias, is then computed as:

$$\bar{P}_{event}^{tag} = \frac{\langle P_{event}^{tag} P_{event}^{trigg} \rangle}{\langle P_{event}^{trigg} \rangle}. \quad (7.9)$$

- The expected number of tagged events in the preselected sample for each jet multiplicity is obtained by multiplying the expected number of preselected events with the average event tagging probability:

$$N_{event}^{tag} = N_{event}^{presel} \bar{P}_{event}^{tag}. \quad (7.10)$$

### 7.2.1 Evaluation of the QCD Background

The QCD-multijets background in the tagged sample can be evaluated in two ways, either by applying the matrix method after  $b$ -tagging (used in this analysis), or by applying the matrix

method before  $b$ -tagging and correcting for the QCD-multijets event tagging probability. Both methods and their results are presented next.

**1. Applying the matrix method on the tagged data sample:** The loose and the tight samples, originally defined on the preselected sample in Section 7.1.3, can be defined in the same way for the tagged samples (1 tag and  $\geq 2$  tags). Solving the linear system of equations for the tagged samples

$$\begin{aligned} N_\ell^{\text{tag}} &= N_\ell^{\text{tag},\text{sig}} + N_\ell^{\text{tag},\text{QCD}} \\ N_t^{\text{tag}} &= \varepsilon_{\text{sig}}^{\text{tag}} N_\ell^{\text{tag},\text{sig}} + \varepsilon_{\text{QCD}}^{\text{tag}} N_\ell^{\text{tag},\text{QCD}} \end{aligned} \quad (7.11)$$

allows to directly extract  $N_t^{\text{tag},\text{QCD}}$ . Both  $\varepsilon_{\text{sig}}^{\text{tag}}$  and  $\varepsilon_{\text{QCD}}^{\text{tag}}$  are measured in the same way as described in Section 7.1.3. In contrast to  $\varepsilon_{\text{sig}}^{\text{tag}}$ ,  $\varepsilon_{\text{QCD}}^{\text{tag}}$  could possibly be different for the untagged  $\varepsilon_{\text{QCD}}$ , i.e.  $\varepsilon_{\text{QCD}}$  might depend on the heavy flavor composition of the sample, since the jets are the source of both the fake electron and the muons with fake isolation. However, given the limited statistics in the tagged samples, no statistically significant discrepancies could be found (143), and the untagged values are used for the tagged samples, both for  $\varepsilon_{\text{sig}}^{\text{tag}} = \varepsilon_{\text{sig}}$  and for  $\varepsilon_{\text{QCD}}^{\text{tag}} = \varepsilon_{\text{QCD}}$ .

**2. Applying the QCD tagging probability on the untagged data sample:** The number of preselected (untagged) QCD-multijets events is determined according to Equation 7.4 by solving the matrix method as given in Equation 7.2. In order to extract the number of tagged QCD-multijets events, according to Equation 7.10, the average event tagging

probability for a QCD-multijets event,  $\bar{P}_{QCD \rightarrow l+nj}^{tag}$  is needed. This probability is defined as the fraction of (positively) tagged events over the total

$$\bar{P}_{QCD \rightarrow l+nj}^{tag} = \frac{\# \text{ tagged } (l+nj) \text{ events}}{\# (l+nj) \text{ events}}, \quad (7.12)$$

and is measured on the *loose-minus-tight* preselected data sample. This sample consists of events passing the loose but not the tight selection requirement, and is dominated by QCD-multijets events. The estimated number of tagged events is then given by

$$\bar{N}_{QCD \rightarrow l+nj}^{tag} = \bar{N}_{QCD \rightarrow l+nj}^{presel} \bar{P}_{QCD \rightarrow l+nj}^{tag}, \quad (7.13)$$

where  $\bar{N}_{QCD \rightarrow l+nj}^{presel}$  is the estimated number of preselected QCD events in the  $n$ -jets bin.

The second method assumes that the heavy flavor composition in the loose-minus-tight data sample, where the event tagging probability is derived, is identical to the heavy flavor composition in the tight preselected sample. In the  $e+jets$  channel this assumption applies, since the instrumental background mainly originates from electromagnetically fluctuating jets misreconstructed as electrons. Thus, the heavy flavor fraction of the remaining jets in the event is not expected to depend on the quality requirements on this jet (i.e. applying the electron likelihood cut or inverting it). This hypothesis is demonstrated by studying the variation of the tagging probability with the maximum allowed value of the electron likelihood, as shown in Figure 104. An electron likelihood requirement of  $\leq 0.5$  was used to derive the average tagging probability for the multijet QCD background, since no significant dependence is observed.

In the  $\mu$ -plus-jets channel, the instrumental background originates mainly from semimuonically decaying  $b$  quarks. The heavy flavor fraction is enriched when the isolation criteria is inverted, leading to a higher event tagging probability. Thus, the second method can not be applied to the  $\mu$ -plus-jets channel.

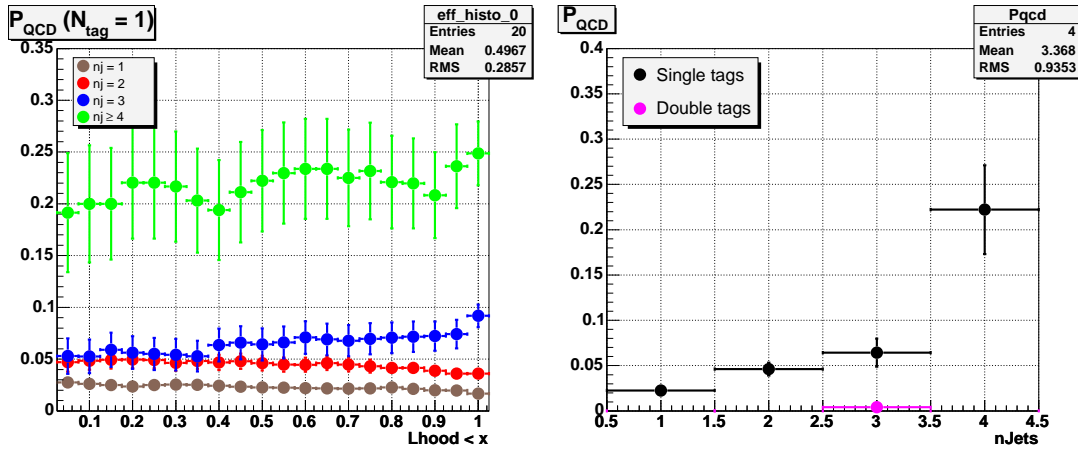


Figure 104. The average single tag probability for QCD events as a function of the maximum allowed value of the electron likelihood is shown in the left plot. In the right plot the average tagging probability per jet multiplicity bin for a likelihood requirement of  $\leq 0.5$  is shown for single and double tagged events respectively.

The prediction for the number of tagged QCD events in the  $\mu$ +jets channel obtained with the first method is shown in Table XXIX for single tagged events and in Table XXX for double tagged events. The predictions from both methods in the  $e$ +jets channel are presented in Ta-

ble XXXI for single tagged events and in Table XXXII for double tagged events, and are in a good agreement with each other.

	1 jet	2 jet	3 jet	$\geq 4$ jet
$N^{loose}$	248	170	77	44
$N^{tight}$	125	82	46	23
$N_{QCD}^{tagged}$	$4.45 \pm 1.04$	$9.3 \pm 0.9$	$2.79 \pm 0.53$	$2.07 \pm 0.43$

TABLE XXIX

NUMBER OF SINGLE TAGGED QCD EVENTS IN THE MUON+JETS CHANNEL OBTAINED BY APPLYING THE MATRIX METHOD ON THE TAGGED SAMPLE.

### 7.2.2 $t\bar{t}$ Signal

According to Equation 7.10, the expected number of  $t\bar{t}$  signal events in the tagged preselected sample is given by

$$N^{tag,expected} = \sigma_{t\bar{t}} \cdot \varepsilon \cdot BR \cdot \mathcal{L} \cdot P^{tag}, \quad (7.14)$$

where the branching ratios are given in Table V, the integrated luminosities  $\mathcal{L}$  are given in Table XX, the expected  $t\bar{t}$  cross section is assumed to be 7 pb, and the preselection efficiencies are summarized in Table XXXIII as a function of the jet multiplicity.

	2 jet	3 jet	$\geq 4$ jet
$N^{loose}$	9	5	10
$N^{tight}$	7	4	9
$N_{QCD}^{tagged}$	$0.12 \pm 0.14$	$0.03 \pm 0.10$	$< 0.01$

TABLE XXX

NUMBER OF DOUBLE TAGGED QCD EVENTS IN THE MUON+JETS CHANNEL OBTAINED BY APPLYING THE MATRIX METHOD ON THE DOUBLE TAGGED SAMPLE.

	1 jet	2 jet	3 jet	$\geq 4$ jet
<b>Matrix Method in V8-V11</b>				
$N^{loose}$	59	39	23	20
$N^{tight}$	34	19	13	14
$N_{QCD}^{tagged}$	$2.57 \pm 0.73$	$2.26 \pm 0.64$	$1.02 \pm 0.45$	$0.38 \pm 0.36$
<b>Matrix Method in V12-V13</b>				
$N^{loose}$	68	70	42	29
$N^{tight}$	49	46	30	15
$N_{QCD}^{tagged}$	$2.18 \pm 1.03$	$3.38 \pm 1.14$	$1.34 \pm 0.82$	$2.33 \pm 0.86$
<b>Matrix Method V8-V13</b>				
$N_{QCD}^{tagged}$	$5.0 \pm 1.3$	$5.7 \pm 1.3$	$2.52 \pm 0.94$	$2.99 \pm 0.94$
<b>QCD Tagging Probabilities</b>				
$P_{QCD}$	$2.26 \pm 0.38$	$4.61 \pm 0.71$	$6.4 \pm 1.6$	$22.2 \pm 4.9$
$N_{QCD}^{untagged}$	$194.6 \pm 19.9$	$134.6 \pm 10.8$	$43.5 \pm 4.1$	$13.6 \pm 2.0$
$N_{QCD}^{tagged}$	$4.41 \pm 0.86$	$6.2 \pm 1.1$	$2.80 \pm 0.73$	$3.03 \pm 0.80$

TABLE XXXI

NUMBER OF EXPECTED SINGLE TAGGED QCD EVENTS IN THE ELECTRON+JETS CHANNEL OBTAINED BY TWO METHODS, USING THE MATRIX METHOD ON THE TAGGED SAMPLE AND USING EVENT TAGGING PROBABILITIES.

	2 jet	3 jet	$\geq 4$ jet
<b>Matrix Method in V8-V11</b>			
$N^{loose}$	5	1	1
$N^{tight}$	5	1	1
$N_{QCD}^{tagged}$	$< 0.01$	$< 0.01$	$< 0.01$
<b>Matrix Method in V12-V13</b>			
$N^{loose}$	7	2	9
$N^{tight}$	7	1	9
$N_{QCD}^{tagged}$	$< 0.01$	$0.18 \pm 0.22$	$< 0.01$
<b>Matrix Method V8-V13</b>			
$N_{QCD}^{tagged}$	$< 0.01$	$0.16 \pm 0.23$	$< 0.01$
<b>QCD Tagging Probabilities</b>			
$P_{QCD}$	$< 0.01$	$0.40 \pm 0.40$	$< 0.01$
$N_{QCD}^{untagged}$	$134.6 \pm 10.8$	$43.5 \pm 4.1$	$13.6 \pm 2.0$
$N_{QCD}^{tagged}$	$< 0.01$	$0.17 \pm 0.18$	$< 0.01$

TABLE XXXII

NUMBER OF EXPECTED DOUBLE TAGGED QCD EVENTS IN THE ELECTRON+JETS CHANNEL OBTAINED BY TWO METHODS, USING THE MATRIX METHOD ON THE TAGGED SAMPLE AND USING EVENT TAGGING PROBABILITIES.

	= 1 jet	= 2 jets	= 3 jets	$\geq 4$ jets
$t\bar{t} \rightarrow \mu + \text{jets}$	$0.524 \pm 0.024$	$4.67 \pm 0.07$	$11.86 \pm 0.11$	$11.01 \pm 0.10$
$t\bar{t} \rightarrow e + \text{jets}$	$0.770 \pm 0.029$	$5.29 \pm 0.07$	$11.89 \pm 0.11$	$9.59 \pm 0.10$
$t\bar{t} \rightarrow \ell\ell \rightarrow \mu + \text{jets}$	$3.30 \pm 0.06$	$10.58 \pm 0.11$	$4.29 \pm 0.07$	$0.660 \pm 0.030$
$t\bar{t} \rightarrow \ell\ell \rightarrow e + \text{jets}$	$4.04 \pm 0.07$	$11.55 \pm 0.11$	$4.21 \pm 0.07$	$0.667 \pm 0.029$

TABLE XXXIII

SUMMARY OF  $t\bar{t}$  PRESELECTION EFFICIENCIES IN THE MUON+JETS AND ELECTRON+JETS CHANNELS (%).

The  $t\bar{t}$  event tagging probabilities,  $\bar{P}^{tag}$ , are given in Table XXXIV for exactly one tag and in Table XXXV for  $\geq 2$  tags.

	$e+$ jets				$\mu+$ jets			
	1 jet	2 jets	3 jets	$\geq 4$ jets	1 jet	2 jets	3 jets	$\geq 4$ jets
$t\bar{t} \rightarrow l+jets$	$26.7 \pm 0.8$	$38.7 \pm 0.2$	$43.2 \pm 0.1$	$44.7 \pm 0.1$	$25.7 \pm 1.0$	$38.1 \pm 0.2$	$42.6 \pm 0.1$	$44.2 \pm 0.1$
$t\bar{t} \rightarrow ll$	$39.2 \pm 0.2$	$44.5 \pm 0.1$	$45.0 \pm 0.2$	$44.9 \pm 0.4$	$38.3 \pm 0.3$	$44.0 \pm 0.1$	$44.5 \pm 0.2$	$44.1 \pm 0.5$

TABLE XXXIV

SINGLE TAG PROBABILITIES (%) FOR  $t\bar{t}$  EVENTS AFTER PRESELECTION.  
ERRORS ARE STATISTICAL ONLY.

	$e+$ jets			$\mu+$ jets		
	2 jets	3 jets	$\geq 4$ jets	2 jets	3 jets	$\geq 4$ jets
$t\bar{t} \rightarrow l+jets$	$4.88 \pm 0.11$	$11.3 \pm 0.1$	$15.3 \pm 0.1$	$5.0 \pm 0.1$	$11.3 \pm 0.1$	$15.2 \pm 0.1$
$t\bar{t} \rightarrow ll$	$12.3 \pm 0.1$	$13.6 \pm 0.1$	$14.2 \pm 0.3$	$12.2 \pm 0.1$	$13.5 \pm 0.1$	$13.6 \pm 0.4$

TABLE XXXV

DOUBLE TAG PROBABILITIES (%) FOR  $t\bar{t}$  EVENTS AFTER PRESELECTION.  
ERRORS ARE STATISTICAL ONLY.

### 7.2.3 $W$ -plus-jets Background

The  $W$ -plus-jets is the dominant physics background in the tagged preselected sample. The expected number of preselected  $W$ -plus-jets events can be obtained from the matrix method,

which is used to evaluate the expected number of non-QCD events, referred to as  $N_t^{sig}$ .  $N_t^{sig}$  contains contribution from the  $t\bar{t}$  signal, the  $W$ -plus-jets background and the small backgrounds listed in Section 7.2.4. Thus, the  $W$ -plus-jets contribution is determined by:

$$N_{(W \rightarrow l\nu) + nj}^{presel} = N_t^{sig} - N_{t\bar{t} \rightarrow l+jets}^{presel} - N_{t\bar{t} \rightarrow ll}^{presel} - \sum_{bkg\ i} N_{bkg\ i}^{presel}, \quad (7.15)$$

where  $i$  loops over the above mentioned small backgrounds. For the cross section determination (see Section 7.6) the  $t\bar{t}$  cross section is allowed to float both in Equation 7.15 and Equation 7.14.

The number of tagged  $W$ -plus-jets events is estimated as

$$\bar{N}_{(W \rightarrow l) + nj}^{tag} = \bar{N}_{(W \rightarrow l) + nj}^{presel} \bar{P}_{(W \rightarrow l) + nj}^{tag}, \quad (7.16)$$

where  $\bar{P}_{(W \rightarrow l) + nj}^{tag}$  is the average event tagging probability for  $W$ -plus-jets events. This probability is determined from MC. It is crucial for the evaluation of the event tagging probability to properly describe the flavor composition of the  $W$ -plus-jets events in the preselected sample. The event tagging probability for inclusive  $W$ +jets events is obtained by adding the tagging probabilities for the different flavor configurations considered, weighted by their fractions within a given jet multiplicity bin:

$$\bar{P}_{(W \rightarrow l) + nj}^{tag} = \sum_{\Phi_n} F_{\Phi_n} \cdot \bar{P}_{\Phi_n}^{tag} \quad (7.17)$$

where  $F_{\Phi,n}$  stands for the fraction of events with flavor configuration  $\Phi$  in the  $n$ -jets bin, determined from the ALPGEN Monte Carlo as described in Section 2.8.2.1.  $\bar{P}_{\Phi,n}^{tag}$  stands for the average tagging probability for such an event. The exclusive  $W$ -plus-jets MC samples which are used are discussed in Section 2.8.2, and their cross sections are summarized in Table VIII. The necessity for a parton-jet matching prescription and its implementation is detailed in Section 2.8.2.1. The fraction  $F$  of each flavor configuration  $\Phi$  per jet multiplicity bin  $n$ , for events that pass the preselection, is determined by:

$$F_{\Phi,n} = \frac{\sigma_{\Phi,n}^{\text{eff}}}{\sum_{\Phi} \sigma_{\Phi,n}^{\text{eff}}}, \quad (7.18)$$

where  $\sigma_{\Phi,n}^{\text{eff}} = \sigma_{\Phi,n} \varepsilon_{\Phi,n}^{\text{presel,match}}$  is the effective cross-section and  $\varepsilon_{\Phi,n}^{\text{presel,match}}$  is the preselection and matching efficiency. The flavor configurations shown in Table XXXVI are identified according to the ad-hoc prescription discussed in Section 2.8.2.1.

The  $W$ +jets fractions were also derived from MLM-matched MC samples using different matching schemes (143). The difference between the fractions obtained from the ad-hoc matching method described in Section 2.8.2.1 and the MLM matching method is less than 20% for the region of interest (three or more jets), and does not depend on the scheme of MLM matching. The ratios of the fractions obtained by the two methods are shown in Figure 105.

The fractions calculated with both ad-hoc and MLM matching procedures are obtained on MC samples based on LO calculations, which have large theoretical uncertainties. There has been significant progress in the calculation of  $W+2$  jets processes at NLO (144). Special studies

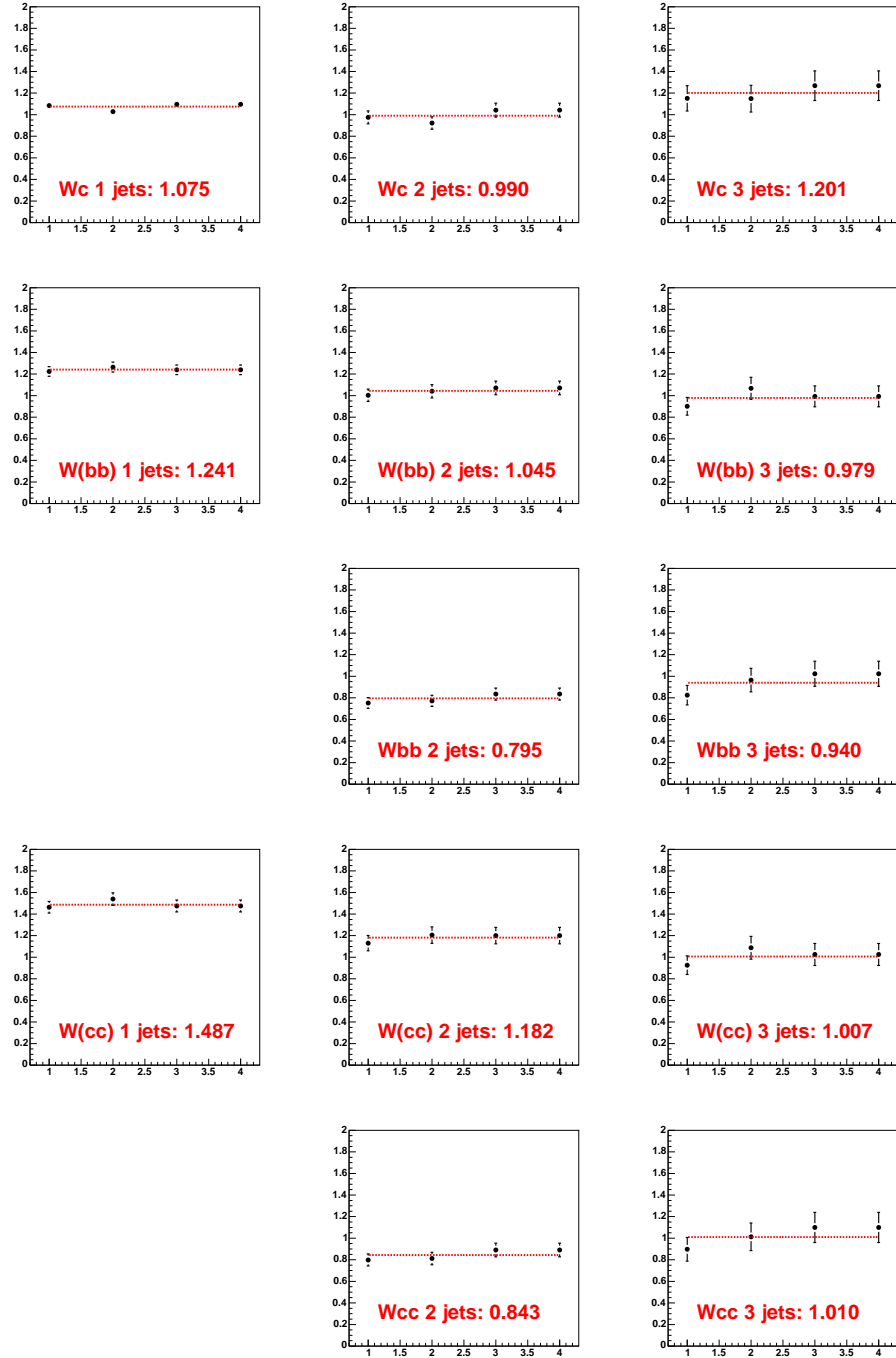


Figure 105. Ratios of *ad-hoc* to MLM fractions. Left, center and right columns correspond to  $N_{jets} = 1, 2, 3$ , respectively. In each plot, each of the four points shown corresponds to one choice for MLM matching:  $(p_T, R) = (5, 0.5), (5, 0.7), (10, 0.5), (10, 0.7)$  (143).

Contribution	W + 1jet	W + 2jets	W + 3jets	W + $\geq$ 4jets
Wbb		(1.23 $\pm$ 0.08)%	(2.05 $\pm$ 0.21)%	(2.84 $\pm$ 0.16)%
Wc $\bar{c}$		(1.69 $\pm$ 0.12)%	(2.94 $\pm$ 0.37)%	(4.44 $\pm$ 0.29)%
W(b $\bar{b}$ )	(0.86 $\pm$ 0.03)%	(1.46 $\pm$ 0.09)%	(2.03 $\pm$ 0.15)%	(2.99 $\pm$ 0.24)%
W(c $\bar{c}$ )	(1.23 $\pm$ 0.05)%	(2.26 $\pm$ 0.15)%	(3.08 $\pm$ 0.24)%	(5.06 $\pm$ 0.54)%
Wc	(4.41 $\pm$ 0.18)%	(6.25 $\pm$ 0.43)%	(4.93 $\pm$ 0.48)%	(4.30 $\pm$ 0.23)%
W + jets(mistags)	(93.50 $\pm$ 0.20)%	(87.10 $\pm$ 0.70)%	(84.96 $\pm$ 1.12)%	(80.36 $\pm$ 0.64)%

TABLE XXXVI

FRACTION OF THE DIFFERENT  $W$ +JETS FLAVOR SUBPROCESSES CONTRIBUTING TO EACH EXCLUSIVE JET MULTIPLICITY BIN. PARTON-JET MATCHING AND PRESELECTION ARE REQUIRED. THE QUOTED UNCERTAINTIES RESULT ONLY FROM LIMITED MC STATISTICS.

for the Tevatron (145) have been done to compare the  $Wb\bar{b}$  and  $Wjj$  cross sections at LO and NLO. It has been found that the ratio of  $Wb\bar{b}$  to  $Wjj$  cross sections at NLO is higher by a factor of 1.05 compared to the LO prediction. This factor is applied to correct the ad-hoc fractions of  $Wb\bar{b}$ ,  $W(b\bar{b})$ ,  $Wc\bar{c}$ ,  $W(c\bar{c})$ , while for the  $Wc$  fraction the LO prediction is assumed. The fraction of  $W$ +light jets process is adjusted to cover the corrections in fractions of the  $Wb\bar{b}$ ,  $W(b\bar{b})$ ,  $Wc\bar{c}$ ,  $W(c\bar{c})$ , so that the final sum of all fractions equals 1.

The average event tagging probability is obtained by combining the  $W$ +jets flavor fractions with the event tagging probability for each flavor. The event tagging probabilities for each flavor are shown in Table XXXVII for single tagged events and in Table XXXVIII for double tagged events.

An alternative way of obtaining the event tagging probability for  $W$ +light jets is to apply the light tagging efficiency parametrization directly to the preselected signal sample. Under

	e+jets				$\mu$ +jets			
	W+1 jet	W+2 jets	W+3 jets	W+ $\geq$ 4 jets	W+1 jet	W+2 jets	W+3 jets	W+ $\geq$ 4 jets
W+light	0.38 $\pm$ 0.01	0.59 $\pm$ 0.03	0.92 $\pm$ 0.06	1.18 $\pm$ 0.05	0.38 $\pm$ 0.01	0.68 $\pm$ 0.03	0.90 $\pm$ 0.07	1.17 $\pm$ 0.04
W( $c\bar{c}$ )	9.3 $\pm$ 0.1	8.9 $\pm$ 0.2	8.7 $\pm$ 0.2	9.9 $\pm$ 0.9	9.4 $\pm$ 0.1	8.9 $\pm$ 0.2	8.4 $\pm$ 0.1	10.0 $\pm$ 0.6
W( $b\bar{b}$ )	39.1 $\pm$ 0.4	35.7 $\pm$ 0.6	34.2 $\pm$ 0.4	34.2 $\pm$ 1.6	38.6 $\pm$ 0.4	35.6 $\pm$ 0.5	33.2 $\pm$ 0.3	34.8 $\pm$ 1.5
W $c$	9.6 $\pm$ 0.1	9.3 $\pm$ 0.2	9.6 $\pm$ 0.3	9.8 $\pm$ 0.2	9.5 $\pm$ 0.1	9.3 $\pm$ 0.2	9.7 $\pm$ 0.3	9.2 $\pm$ 0.2
W $c\bar{c}$		15.4 $\pm$ 0.4	15.0 $\pm$ 0.9	15.6 $\pm$ 0.6		15.2 $\pm$ 0.3	15.3 $\pm$ 0.6	15.8 $\pm$ 0.4
W $b\bar{b}$		43.9 $\pm$ 0.7	44.8 $\pm$ 0.8	45.0 $\pm$ 0.5		43.3 $\pm$ 0.7	43.9 $\pm$ 0.8	43.4 $\pm$ 0.7
W+jets	1.23 $\pm$ 0.01	2.62 $\pm$ 0.03	3.58 $\pm$ 0.06	4.87 $\pm$ 0.08	1.22 $\pm$ 0.01	2.68 $\pm$ 0.03	3.53 $\pm$ 0.06	4.82 $\pm$ 0.07

TABLE XXXVII. SINGLE TAG PROBABILITIES (%) FOR PRESELECTED W+JETS EVENTS. ERRORS ARE STATISTICAL ONLY.

	$e+$ jets			$\mu+$ jets		
	$W+2$ jets	$W+3$ jets	$W+\geq 4$ jets	$W+2$ jets	$W+3$ jets	$W+\geq 4$ jets
$W+$ light	< 0.01	< 0.01	< 0.01	< 0.01	< 0.01	< 0.01
$W(c\bar{c})$	0.03±0.01	0.08±0.01	0.15±0.06	0.05±0.01	0.08±0.01	0.17±0.04
$W(b\bar{b})$	0.60±0.11	0.98±0.08	0.67±0.16	0.76±0.12	0.79±0.06	1.42±0.39
$Wc$	0.023±0.002	0.046±0.004	0.074±0.004	0.027±0.002	0.052±0.003	0.066±0.003
$Wc\bar{c}$	0.76±0.04	0.75±0.08	0.90±0.07	0.73±0.03	0.77±0.08	0.89±0.06
$Wb\bar{b}$	12.0±0.4	12.4±0.7	13.4±0.5	12.7±0.4	12.4±0.6	12.2±0.5
$W+$ jets	0.17±0.01	0.30±0.01	0.46±0.02	0.184±0.005	0.30±0.01	0.45±0.02

TABLE XXXVIII

DOUBLE TAG PROBABILITIES (%) FOR PRESELECTED  $W+$ JETS EVENTS. ERRORS ARE STATISTICAL ONLY.

the assumption that the preselected sample is dominated by  $W+$ light jets events, this method has the advantage of taking the kinematic information directly from the data. The obtained event tagging probabilities are shown in Table XXXIX, and are in good agreement with the ones obtained from Monte Carlo (see Table XXXVII).

	$e+$ jets				$\mu+$ jets			
	1 jet	2 jets	3 jets	$\geq 4$ jets	1 jet	2 jets	3 jets	$\geq 4$ jets
$W+$ light	0.39±0.01	0.63±0.02	0.89±0.05	1.28±0.14	0.37±0.01	0.58±0.01	0.83±0.04	1.17±0.13

TABLE XXXIX

SINGLE TAG PROBABILITIES (%) OBTAINED FROM APPLYING THE LIGHT TAGGING EFFICIENCY PARAMETRIZATION TO THE PRESELECTED SIGNAL SAMPLE.

### 7.2.4 Other Physics Backgrounds

Contributions from other low rate electroweak physics backgrounds to the preselected tagged sample are estimated from MC. The following processes are considered:

- diboson production:  $WW \rightarrow l + jets$ ,  $WZ \rightarrow l + jets$ ,  $WZ \rightarrow jjl\bar{l}$ ,  $ZZ \rightarrow l\bar{l}jj$ ,
- single top production in the  $s$ - and  $t$ -channel,
- $Z \rightarrow \tau\tau \rightarrow l + jets$

For a given process  $i$ , the number of events before tagging is determined as

$$N_i^{presel} = \sigma_i \epsilon_i^{presel,tot} BR_i \mathcal{L} \quad (7.19)$$

where  $\sigma_i$ ,  $BR_i$  and  $\mathcal{L}$  stand, respectively, for the cross section (see Table IX), branching ratio and integrated luminosity for the process under consideration. The accuracy with which the cross sections are known does not affect the final result significantly due to the very small contribution from these processes. The total preselection efficiency  $\epsilon_i^{presel,tot}$  for the process  $i$  is defined as

$$\epsilon_i^{presel,tot} = \epsilon_i^{trig} \epsilon_i^{presel} \quad (7.20)$$

where  $\epsilon_i^{trig}$  and  $\epsilon_i^{presel}$  are the trigger and preselection efficiencies, respectively. The trigger efficiency is the marginal efficiency only for events that pass the preselection, and is obtained by folding into the Monte Carlo the per-lepton and per-jet trigger efficiencies measured in data.

The preselection efficiency is entirely determined from Monte Carlo with the appropriate scale factors applied (Section 7.1).

The tagging probabilities are determined by Equation 7.9, so that the estimated number of tagged events is given by

$$N_i^{tag} = N_i^{presel} \bar{P}_i^{tag}, \quad (7.21)$$

where  $\bar{P}_i^{tag}$  is the average event tagging probability.

Table XL and Table XLI summarize the preselection efficiencies for different jet multiplicities for the  $\mu$ -plus-jets and electron-plus-jets channels, respectively.

	1 jet	2 jets	3 jets	$\geq 4$ jets
$t b$	$5.69 \pm 0.12$	$13.97 \pm 0.18$	$2.43 \pm 0.08$	$0.272 \pm 0.027$
$t q b$	$5.41 \pm 0.12$	$11.13 \pm 0.16$	$4.09 \pm 0.10$	$0.823 \pm 0.047$
$WW \rightarrow l\nu jj$	$7.67 \pm 0.25$	$9.89 \pm 0.29$	$0.613 \pm 0.075$	$0.009 \pm 0.009$
$WZ \rightarrow l\nu jj$	$6.66 \pm 0.24$	$11.36 \pm 0.31$	$1.01 \pm 0.10$	$0.045 \pm 0.020$
$WZ \rightarrow jj ll$	$3.39 \pm 0.16$	$5.28 \pm 0.20$	$0.604 \pm 0.068$	$0.031 \pm 0.016$
$ZZ \rightarrow jj ll$	$3.63 \pm 0.18$	$5.58 \pm 0.23$	$0.689 \pm 0.083$	$0.062 \pm 0.025$
$Z \rightarrow \tau^+ \tau^-$	$0.076 \pm 0.004$	$0.029 \pm 0.003$	$0.004 \pm 0.001$	$0.000 \pm 0.000$

TABLE XL

SUMMARY OF PRESELECTION EFFICIENCIES IN THE MUON+JETS CHANNEL (%).  
THE QUOTED UNCERTAINTIES RESULT ONLY FROM LIMITED MC STATISTICS.

The average event tagging probabilities are listed in Table XLII for single tagged events in the  $\mu$ -plus-jets and electron-plus-jets channels and in Table XLIII for double tagged events.

	1 jet	2 jets	3 jets	$\geq 4$ jets
$t\bar{t} \rightarrow l + \text{jets}$	0.770 $\pm 0.029$	5.29 $\pm 0.07$	11.89 $\pm 0.11$	9.59 $\pm 0.10$
$t\bar{t} \rightarrow ll$	4.04 $\pm 0.07$	11.55 $\pm 0.11$	4.21 $\pm 0.07$	0.667 $\pm 0.029$
$tb$	5.96 $\pm 0.12$	13.21 $\pm 0.17$	2.27 $\pm 0.07$	0.212 $\pm 0.023$
$tqb$	5.38 $\pm 0.11$	10.82 $\pm 0.15$	3.76 $\pm 0.09$	0.775 $\pm 0.044$
$WW \rightarrow l\nu jj$	6.37 $\pm 0.23$	7.06 $\pm 0.24$	0.461 $\pm 0.064$	0.000 $\pm 0.000$
$WZ \rightarrow l\nu jj$	5.64 $\pm 0.21$	7.92 $\pm 0.25$	0.565 $\pm 0.071$	0.061 $\pm 0.023$
$WZ \rightarrow jjll$	0.601 $\pm 0.065$	0.840 $\pm 0.078$	0.308 $\pm 0.047$	0.006 $\pm 0.006$
$ZZ \rightarrow jjll$	0.850 $\pm 0.071$	1.09 $\pm 0.08$	0.296 $\pm 0.043$	0.037 $\pm 0.015$
$Z \rightarrow \tau^+\tau^-$	0.025 $\pm 0.002$	0.012 $\pm 0.002$	0.003 $\pm 0.001$	0.001 $\pm 0.000$

TABLE XLI

SUMMARY OF PRESELECTION EFFICIENCIES IN THE ELECTRON+JETS CHANNEL (%). THE QUOTED UNCERTAINTIES RESULT ONLY FROM LIMITED MC STATISTICS.

### 7.3 Systematic Uncertainties

A complete list of systematic uncertainties is given in Table XLIV, where a cross indicates which channels and what quantity (background normalization and/or  $t\bar{t}$  efficiency) are affected within a given channel. The systematic uncertainties have been classified as uncorrelated (usually of statistical origin in either Monte Carlo or data) and correlated. The correlation can be between analysis channels (i.e. electron-plus-jets and  $\mu$ -plus-jets) and/or between jet multiplicity bins ( $N_{jet} = 3$  and  $N_{jet} \geq 4$ ) within a particular channel. All systematic uncertainties are fully correlated between single tagged and double tagged samples. A brief description of each source of systematic uncertainty is given below.

The systematic uncertainties on the selection efficiency that are common to all processes are shown in Table LVI in Appendix C. Table LVII and Table LVIII show the systematic uncer-

	$e+$ jets				$\mu+$ jets			
	1 jet	2 jets	3 jets	$\geq 4$ jets	1 jet	2 jets	3 jets	$\geq 4$ jets
$t b$	$38.8 \pm 0.3$	$45.1 \pm 0.1$	$45.6 \pm 0.3$	$43.5 \pm 1.2$	$38.2 \pm 0.3$	$44.6 \pm 0.1$	$44.1 \pm 0.4$	$45.1 \pm 0.9$
$tqb$	$31.5 \pm 0.4$	$36.9 \pm 0.2$	$40.6 \pm 0.3$	$42.7 \pm 0.6$	$31.0 \pm 0.4$	$36.2 \pm 0.2$	$40.4 \pm 0.3$	$41.9 \pm 0.6$
$WW \rightarrow l\nu jj$	$3.32 \pm 0.17$	$4.68 \pm 0.19$	$5.6 \pm 0.7$	$< 0.01$	$3.27 \pm 0.17$	$4.29 \pm 0.14$	$5.6 \pm 0.6$	$1.31 \pm 1.31$
$WZ \rightarrow l\nu jj$	$13.1 \pm 0.8$	$13.2 \pm 0.7$	$10.0 \pm 2.2$	$3.42 \pm 2.29$	$11.7 \pm 0.7$	$10.8 \pm 0.5$	$10.5 \pm 1.8$	$8.6 \pm 7.3$
$WZ \rightarrow jj ll$	$3.43 \pm 0.50$	$5.2 \pm 0.5$	$5.6 \pm 0.7$	$12.9 \pm 12.9$	$2.44 \pm 0.20$	$4.17 \pm 0.18$	$3.95 \pm 0.49$	$4.46 \pm 1.82$
$ZZ \rightarrow jj ll$	$20.2 \pm 1.9$	$16.9 \pm 1.6$	$12.6 \pm 2.8$	$1.48 \pm 0.16$	$12.4 \pm 1.0$	$11.6 \pm 0.8$	$14.4 \pm 2.4$	$15.2 \pm 8.5$
$Z \rightarrow \tau^+ \tau^-$	$1.13 \pm 0.39$	$2.60 \pm 1.17$	$3.43 \pm 2.10$	$1.15 \pm 0.25$	$0.90 \pm 0.23$	$1.96 \pm 0.51$	$4.70 \pm 2.85$	$1.48 \pm 0.06$

TABLE XLII. SINGLE TAG PROBABILITIES (%) AFTER FULL PRESELECTION FOR PHYSICS BACKGROUNDS OTHER THAN  $W+jets$ . ERRORS ARE STATISTICAL ONLY.

	$e$ +jets			$\mu$ +jets		
	2 jets	3 jets	$\geq 4$ jets	2 jets	3 jets	$\geq 4$ jets
$tb$	13.2±0.1	14.2±0.2	12.6±0.8	12.9±0.1	13.3±0.3	13.9±0.8
$tqb$	1.71±0.07	7.2±0.2	10.6±0.4	1.55±0.07	7.2±0.2	9.9±0.5
$WW \rightarrow l\nu jj$	0.018±0.004	0.018±0.002	< 0.01	0.011±0.001	0.04±0.02	< 0.01
$WZ \rightarrow l\nu jj$	3.18±0.20	2.69±0.75	< 0.01	2.54±0.16	2.25±0.49	1.38±1.25
$WZ \rightarrow jj ll$	0.03±0.01	0.04±0.01	0.037±0.000	0.011±0.001	0.017±0.003	0.01±0.01
$ZZ \rightarrow jj ll$	3.21±0.48	2.52±0.76	< 0.01	2.53±0.24	3.31±0.74	3.68±2.25
$Z \rightarrow \tau^+ \tau^-$	0.16±0.15	0.10±0.09	< 0.01	< 0.01	1.29±1.25	< 0.01

TABLE XLIII. DOUBLE TAG PROBABILITIES (%) AFTER FULL PRESELECTION FOR PHYSICS BACKGROUNDS OTHER THAN  $W$ +JETS. ERRORS ARE STATISTICAL ONLY.

		e+jets		$\mu+$ jets	
		$\Delta b$	$\Delta \varepsilon$	$\Delta b$	$\Delta \varepsilon$
Uncorrelated	Preselection efficiency (stat)		x		x
	Tagging probability (stat)	x	x	x	x
	W fractions (stat)	x		x	
	$\epsilon_{qcd}$ and $\epsilon_{sig}$	x		x	
	primary vertex	x	x	x	x
	$\mu$ tracking			x	x
	$\mu$ ID			x	x
	$\mu$ isolation			x	x
	$\mu$ $\sigma_{dca}$			x	x
	$\mu$ track $\chi^2$			x	x
	$\mu$ $\Delta z$			x	x
	L1 $\mu$ trigger			x	x
	L2 $\mu$ trigger			x	x
	EM reconstruction	x	x		
	EM ID	x	x		
	EM tracking	x	x		
	EM likelihood	x	x		
	EM $\Delta z$	x	x		
Correlated	L1 EM trigger	x	x		
	L2 EM trigger	x	x		
	L3 EM trigger	x	x		
	Jet Energy Scale	x	x	x	x
	Jet Energy Resolution	x	x	x	x
	Jet Reco and ID	x	x	x	x
	L1 jet trigger	x	x	x	x
	L2 jet trigger	x	x	x	x
	L3 jet trigger	x	x	x	x
	Taggability in data	x	x	x	x
	Flavor dependence of taggability	x	x	x	x
	Inclusive $b$ -tagging eff in MC	x	x	x	x
	Inclusive $c$ -tagging eff in MC	x	x	x	x
	Semilept $b$ -tagging eff in MC	x	x	x	x
	Semilept $b$ -tagging eff in data	x	x	x	x
	Negative tagging eff in data	x	x	x	x
	Light flavor SF in MC	x	x	x	x
	W fractions (syst)	x		x	

TABLE XLIV

SUMMARY OF SYSTEMATIC UNCERTAINTIES AFFECTING THE SIGNAL EFFICIENCY AND/OR BACKGROUND PREDICTION. *CORRELATED* AND *UNCORRELATED* REFER TO THE MUON-PLUS-JETS AND ELECTRON-PLUS-JETS CHANNELS.

tainties related to the preselection of the signal samples, and similar tables for the backgrounds are also shown in Appendix C.

A detailed description of the systematic uncertainties contributing to the preselection efficiency uncertainty and methods used to evaluate them is given in (111; 141).

### **Jet Energy Scale**

As described in Section 4.5.5, Jet Energy Scale (JES) corrections are applied to jets in both data and Monte Carlo, bringing them on an equal footing. Statistical and systematic uncertainties on the JES corrections result in systematic uncertainties on the preselection efficiencies and tagging probabilities for  $t\bar{t}$  and backgrounds. The effect of the jet energy scale uncertainty on the preselection efficiency and tagging probabilities uncertainty is obtained by varying the JES by  $\pm 1\sigma$  as defined in Equation 4.12.

These systematic uncertainties, i.e. on preselection efficiency and tagging probabilities, are fully correlated. They are also fully correlated between channels and between jet multiplicity bins. Table LXVI and Table LXVII in Appendix D show relative systematic errors from Jet Energy Scale for single and double tagged events, respectively.

### **Jet Energy Resolution**

Jets in Monte Carlo are smeared to match the jet resolution observed in data. The parameters of the jet energy smearing are varied by the size of the uncertainty on the jet energy resolution parameters in Monte Carlo. Preselection efficiencies and tagging probabilities are recalculated for these variations. Table LXVIII and Table LXIX in Appendix D show relative systematic errors from Jet Energy Resolution for single and double tagged events, respectively.

## Jet Reconstruction and Identification Efficiency

The study of the jet reconstruction and identification efficiency in data and Monte Carlo shows that the efficiency in Monte Carlo is higher than in data (see Section 4.5.6). A  $p_T$ -dependent data to MC scale factor has been determined, and is used to randomly remove MC jets to reproduce the jet reconstruction and identification efficiency present in data. The systematic uncertainty arises from the accuracy with which this scale factor is known. The scale factor is varied by  $\pm 1\sigma$  and the impact on the preselection efficiencies and tagging probabilities are evaluated. Table LXX and Table LXXI in Appendix D show relative systematic errors from Jet Reconstruction and Identification for single and double tagged events, respectively.

## Trigger Efficiency

The trigger efficiency is determined by folding into preselected MC events the per-lepton and per-jet trigger turn-on curves measured in data as described in Section 5.1. The systematic uncertainty on the trigger efficiency results in systematic uncertainties on the preselection efficiency and tagging probabilities for  $t\bar{t}$  and backgrounds. It is obtained by varying the trigger efficiency parameterization by  $\pm 1\sigma$ . Table LXXII and Table LXXIII in Appendix D show relative systematic errors from the Trigger Efficiency for single and double tagged events, respectively.

## Tagging Probability

The calibrated event tagging probabilities are evaluated in Monte Carlo following the procedure described in Section 7.2. Limited Monte Carlo statistics results in an uncertainty on the determination of these probabilities, and thus in a systematic uncertainty on the signal and

background predictions. All these systematic uncertainties are of statistical origin, and taken to be fully uncorrelated among signal and backgrounds, jet multiplicity bins and channels.

- **Taggability in Data.** The taggability is parameterized as a function of jet  $E_T$  and  $\eta$  in six regions of  $PV_Z \times \eta$  in the combined lepton+jets signal samples, as described in Section 6.1. These parameterizations are then applied to Monte Carlo jets for both signal and backgrounds, in order to predict the tagging probabilities. Systematic uncertainties on the parameterizations arise from the limited statistics in the signal samples. Table LXXIV and Table LXXV in Appendix D show relative systematic errors from the Taggability in Data for single and double tagged events, respectively.
- **Flavor Dependence of Taggability.** The systematic uncertainty on the flavor dependence of the taggability is obtained by substituting the parameterization derived on QCD Monte Carlo by the one determined from  $Wb\bar{b}$  and  $Wjj$  samples for  $b$ -jets and  $c$ -jets, respectively, and QCD Monte Carlo for light jets in the flavor dependence correction to the Taggability, as described in Section 6.1.1 (see Figure 106 and compare to Figure 91). Half of the observed difference with respect to the default parameterization is assigned as a systematic uncertainty. Table LXXVI and Table LXXVII in Appendix D show relative systematic errors from Taggability flavor dependence for single and double tagged events, respectively.
- **Tagging Efficiencies in Monte Carlo.** The tagging efficiency for inclusive  $b$ -decays in Monte Carlo is parameterized as a function of jet  $p_T$  and  $\eta$  as described in Section 6.2.2. The limited available statistics leads to a statistical uncertainty on this parameterization,

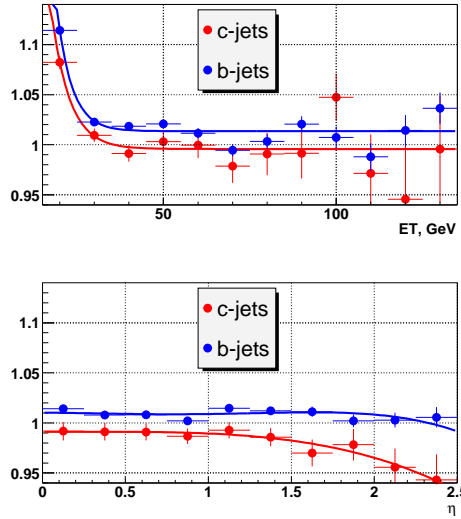


Figure 106. Alternative ratios of the  $b$ - to light and  $c$ - to light jet taggabilities used for the systematics uncertainty calculations (136).

which results in a systematic uncertainty on the predicted tagging probabilities for signal and background. This systematic uncertainty is derived by varying by  $\pm 1\sigma$  the parameterization and computing the resulting change on the different tagging probabilities. It is taken to be fully correlated between signal and backgrounds, among jet multiplicity bins and between channels. Table LXXVIII and Table LXXIX in Appendix D show relative systematic errors from the inclusive  $b$ -tagging efficiency in Monte Carlo for single and double tagged events, respectively.

The same procedure is used in the case of the tagging efficiencies for semileptonic  $b$ -decays and inclusive  $c$ -decays. Table LXXX and Table LXXXI in Appendix D show relative sys-

tematic errors from the semileptonic  $b$ -tagging efficiency in Monte Carlo for single and double tagged events, respectively. Table LXXXII and Table LXXXIII show relative systematic errors from the inclusive  $c$ -tagging efficiency in Monte Carlo for single and double tagged events, respectively.

- **Semileptonic  $b$ -Tagging Efficiency in Data.** The uncertainty on the  $b$ -tagging efficiency on data (see Section 6.2) is derived from the systematic error obtained for the method used to parameterize the  $b$ -tagging efficiency in data. The major contribution comes from the uncertainties due to the assumption of decorrelation between a lifetime tagging algorithm and the soft lepton tagging (SLT) algorithm ( $\kappa_b$ ), and decorrelation between tagging probabilities for two  $b$ -jets ( $\beta$ ). Both factors have been evaluated on  $Z \rightarrow b\bar{b} \rightarrow \mu$  Monte Carlo and propagated to the event tagging probabilities. Table LXXXIV and Table LXXXV in Appendix D show relative systematic errors from the semileptonic  $b$ -tagging efficiency in data for single and double tagged events, respectively.
- **Negative Tagging Efficiency in Data.** The negative tagging efficiency is parameterized as a function of jet  $p_T$  and  $\eta$  in the EMqcd data sample (see Section 6.4), which has limited statistics. The uncertainty on the mistagging rate is varied by  $\pm 1\sigma$  and the impact on the tagging efficiency es estimated. Table LXXXVI and Table LXXXVII in Appendix D show relative systematic errors from the negative tagging rate in data for single and double tagged events, respectively.
- **Light Flavor Scale Factor in Monte Carlo.** In order to compute the positive tagging efficiency for light flavor jets, the negative tagging efficiency (measured in data) is cor-

rected by scale factors,  $SF_{ll}$  and  $SF_{hf}$ , derived from Monte Carlo (see Section 6.4). The statistical error due to finite Monte Carlo statistics gives rise to a systematic uncertainty for these scale factors. In addition, the scale factor  $SF_{hf}$  depends on the heavy flavor content of QCD, and a systematic uncertainty on the modeling of the heavy flavor fractions needs to be included. Table LXXXVIII and Table LXXXIX in Appendix D show relative systematic errors from the  $SF_{ll}$  for single and double tagged events, respectively. Table XC and Table XCI show relative systematic errors from the  $SF_{hf}$  for single and double tagged events, respectively.

### **$W + \text{jets}$ fractions**

The fractions for the different flavor configurations in  $W + \text{jets}$  events are estimated following the procedure described in Section 7.2. Several sources of systematic uncertainties are associated with this approach. In addition to the limited MC statistics, jet energy scale and jet energy resolution and ID, systematic uncertainties arise from the matching procedure and from the theoretical modeling. These uncertainties are described below.

The systematics associated to the matching procedure arise from the following sources:

- The choice of cone size used for ad-hoc matching of the ALPGEN parton to the reconstructed jet introduces a systematic uncertainty calculated as half the difference between the fractions obtained with the default cone size of  $R = 0.5$  and a cone size of  $R = 0.7$ . The relative error due to the different cone size is found to be 2% for the  $Wc$  fractions and 5% for the  $Wb\bar{b}$ ,  $W(b\bar{b})$ ,  $Wc\bar{c}$  and  $W(c\bar{c})$  in all jet multiplicity bins;

- The  $W$  fractions obtained from the ad-hoc matching and used in this analysis were compared with MLM fractions obtained with 4 different schemes: parton  $p_T > 5$  GeV and cone sizes of  $R = 0.5, 0.7$  and parton  $p_T > 10$  GeV and cone sizes of  $R = 0.5, 0.7$ . Ratios of heavy flavor fractions obtained with ad-hoc procedure to those obtained with MLM matching are shown in Figure 105 for the different heavy flavor configurations of  $W$ +jets events in the first three jet multiplicity bins (there is lack of statistics in the fourth jet multiplicity bin in the MLM matched samples). The third jet multiplicity bin is used to derive the systematic uncertainty due to the choice of matching procedure used to compute the  $t\bar{t}$  cross section that has enough statistics to get reliable results. A conservative 20% systematic error to heavy flavor fractions due to the matching procedure is assigned based on this consideration.

The systematics associated to the  $W$  boson modelling arise from the following contributions:

- Parton distribution functions: the relative change in the ALPGEN cross sections when considering the 20 eigenvector pairs from CTEQ6M is propagated as a systematic uncertainty on all  $W$ +jets fractions properly taking into account correlations;
- Choice of factorization scale: the relative change in the ALPGEN cross sections when varying by a factor of 2 up and down the factorization scale with respect to the default choice (shown in Table VII) is propagated as a systematic uncertainty on all  $W$ +jets fractions properly taking into account correlations;

- Heavy quark mass: the relative change in the ALPGEN cross sections when varying by  $\pm 0.3$  GeV the heavy quark masses with respect to their default values ( $m_b = 4.75$  GeV and  $m_c = 1.55$  GeV), is propagated as a systematic uncertainty on all  $W+\text{jets}$  fractions;
- NLO K-factor: as discussed in Section 7.2, the fractions for  $W+\text{jets}$  processes involving gluon splitting into heavy quarks ( $W + Q\bar{Q} + X$  and  $W + (Q\bar{Q}) + X$ ,  $Q = b, c$ ) are scaled to account for the difference between the NLO and LO theoretical prediction (145). The scale factor used is  $K = 1.05 \pm 0.07$ , where the assigned systematic uncertainty arises from the residual dependence on the factorization scale (0.05) and from the uncertainty on the PDFs obtained considering the 20 eigenvector pairs from CTEQ6M (0.05).

$\varepsilon_{sig}$  and  $\varepsilon_{QCD}$

The uncertainty on the number of  $W+\text{jets}$  and QCD events per exclusive jet multiplicity after preselection obtained from the Matrix method is obtained by varying  $\varepsilon_{sig}$  and  $\varepsilon_{bkg}$  by one standard deviation. The results of the two variations are added in quadrature.

### Top Mass

The top quark mass is not considered as a source of systematic uncertainty. Instead, the  $t\bar{t}$  production cross-section is calculated as a function of the top mass. For this purpose, both preselection efficiencies and  $t\bar{t}$  event tagging probabilities are measured from the Monte Carlo samples generated for top masses of  $m_t = 150, 160, 165, 170, 175, 180, 185, 190$  and 200 GeV. Figure 107 and Figure 108 show the mass dependance of the preselection and tagging efficiencies, respectively.

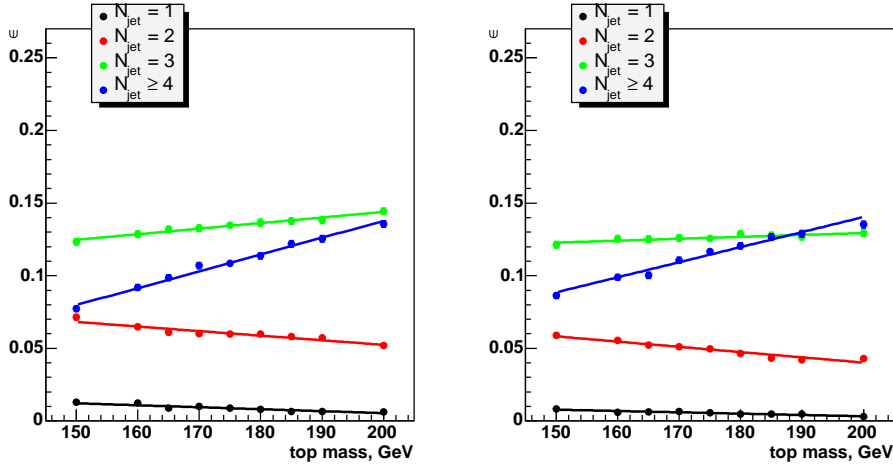


Figure 107. Mass dependence of the  $t\bar{t}$  preselection efficiencies in the  $e+\text{jets}$  (left plot) and  $\mu+\text{jets}$  (right plot) channels.

## Luminosity Uncertainty

The determination of the luminosity is described in Section 2.9. The DØ luminosity uncertainty arises from relative uncertainty on the effective  $p\bar{p}$  inelastic cross section, and is currently set to 6.5% as described in (83).

### 7.4 Cross-Section Extraction Procedure

The  $t\bar{t}$  production cross section is calculated by performing a maximum likelihood fit to the observed number of events. The analysis is split into eight different channels. The resulting cross sections are given for the electron and the muon channels separately and combined. If the index  $\gamma$  refers to one of the eight channels ( $e+3$  jets single tag,  $e+3$  jets double tag,  $e+4$

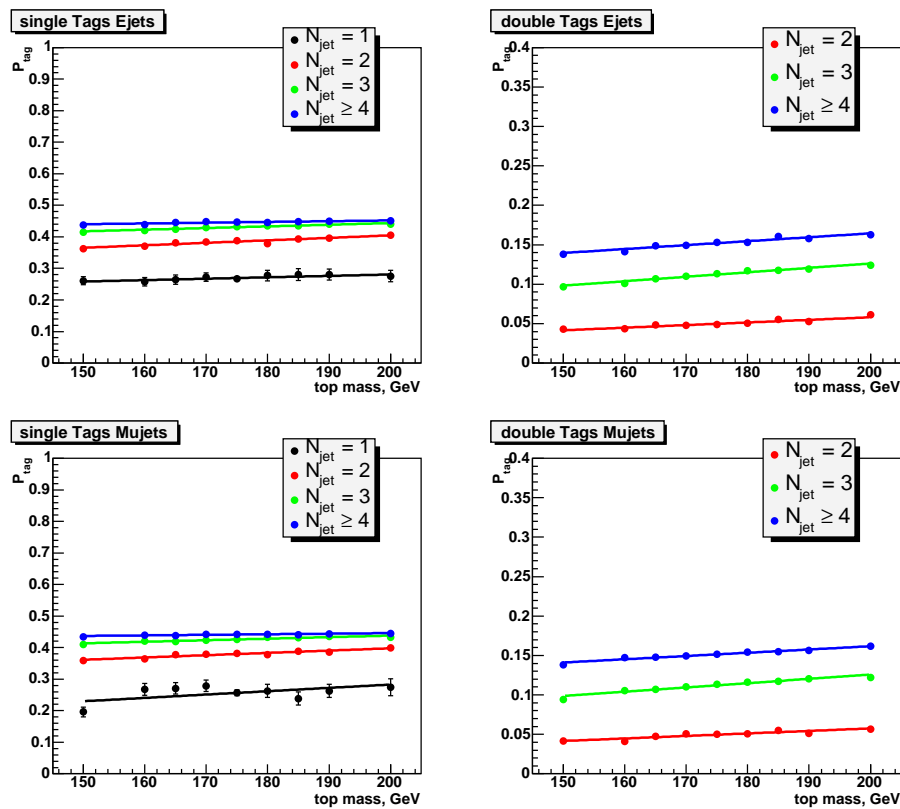


Figure 108. Mass dependence of the  $t\bar{t}$  tagging efficiencies in the  $e + jets$  (top plots) and  $\mu + jets$  (bottom plots) channels.

jets single tag,  $e+4$  jets double tag,  $\mu+3$  jets single tag,  $\mu+3$  jets double tag,  $\mu+4$  jets single tag or  $\mu+4$  jets double tag) then the likelihood  $\mathcal{L}_1$  to observe  $N_\gamma^{\text{obs}}$  for a cross section  $\sigma_{t\bar{t}}$  is proportional to

$$\mathcal{L}_1 = \prod_\gamma \mathcal{P}(N_\gamma^{\text{obs}}, N_\gamma^{\text{pred}}(\sigma_{t\bar{t}})), \quad (7.22)$$

where  $\gamma$  runs over all 8 channels when the total combined cross section is computed. Here  $P(n, \mu) = \frac{\mu^n e^{-\mu}}{n!}$  generically denotes the Poisson probability density function for  $n$  observed events, given an expectation of  $\mu$ .

The predicted number of events in each channel is the sum of the predicted number of background events ( $W+\text{jets}$ , QCD, single top, diboson processes,  $Z \rightarrow \tau\tau$ ) and the number of expected  $t\bar{t}$  events, which is a function of the  $t\bar{t}$  cross section that is being determined.

The number of predicted background events also depends on the  $t\bar{t}$  cross section. The matrix method gives the number of events with a real lepton originating from a  $W$  decay. The number of  $W+\text{jets}$  events before tagging is then obtained by subtracting from the number of events with a real lepton, the predicted number of single top, diboson and  $Z \rightarrow \tau\tau$  events predicted from Monte Carlo, as well as the number of  $t\bar{t}$  events. This can be expressed in the following way:

$$N_{(W \rightarrow \ell) + \text{jets}}^{\text{presel}} = N_{(W \rightarrow \ell) + \text{jets}}^{\text{presel}} - \sum_i N_i^{\text{presel}} - N_{t\bar{t}}^{\text{presel}}. \quad (7.23)$$

For each iteration of the maximization procedure of the likelihood, the number of  $t\bar{t}$  events in the untagged sample is calculated and the number of  $W+\text{jets}$  is rederived.  $N_i^{\text{presel}}$  is the number of predicted events in the preselected sample for the process  $i$  (single top, diboson processes,  $Z \rightarrow \tau\tau$ ), while  $N_{(W \rightarrow \ell)+nj}^{\text{presel}}$  is the number of events with a real lepton as predicted by the matrix method and  $\bar{N}_{(W \rightarrow \ell)+nj}^{\text{presel}}$  is the number of  $W+\text{jets}$  events.

A detailed explanation regarding the treatment of the event statistics in the cross section calculation can be found in Appendix B.

#### **7.4.1 Treatment of systematic uncertainties**

The final cross section is determined using a nuisance parameter likelihood method that incorporates all systematic uncertainties in the fit. In addition, a second *standard method* is used as a cross check. Both procedures give consistent results and are briefly described below.

In the standard method the systematic uncertainty on the cross section is obtained for each independent source by varying the central value by one standard deviation up and down and propagating the variation into both background estimates and signal efficiencies. A new likelihood function is derived for each such variation to give a new optimal cross section. These variations in the central value of the cross section are then summed quadratically to obtain the total systematic uncertainty.

The nuisance parameter method incorporates the systematic errors in such a way that allows them to affect the central value of the cross section. In this approach, each independent source of systematic error is modeled by a free parameter, floating freely during the optimization. We choose to model each nuisance parameter with a Gaussian centered on zero and with a standard

deviation of one. The nuisance parameters are allowed to change the central values of all efficiencies, tagging probabilities and flavor fractions. It means that the preselection efficiencies, tagging probabilities and flavor fractions are recomputed at each step of the maximization procedure before a prediction of number of events can be made. For example, the preselection efficiency in the  $t\bar{t} \rightarrow e+3\text{jets}$  channel can be written as

$$\begin{aligned}\hat{\epsilon}_{t\bar{t} \rightarrow \ell j}^{e+3j} = & \hat{\epsilon}_{t\bar{t} \rightarrow \ell j}^{e+3j} + \sigma_{PV}\nu_1 + \sigma_{\Delta z}\nu_2 + \sigma_{EMreco*ID}\nu_3 + \sigma_{EMtrk}\nu_4 + \sigma_{EMlhood}\nu_5 \\ & + \sigma_{EM L1}\nu_6 + \sigma_{EM L3}\nu_7 + \sigma_{Jet L1}\nu_8 + \sigma_{Jet L2}\nu_9 + \sigma_{Jet L3}\nu_{10} + \sigma_{MCstat}\nu_{11} \\ & + \sigma_{JES}\nu_{12} + \sigma_{JER}\nu_{13} + \sigma_{JetID}\nu_{14}\end{aligned}$$

where  $\hat{\epsilon}_{t\bar{t} \rightarrow \ell j}^{e+3j}$  is the central value of the preselection efficiency, and  $\nu_1, \nu_2, \dots, \nu_{14}$  are the nuisance parameters associated to the systematic uncertainties on the primary vertex, lepton promptness, electron reconstruction, track match, electron likelihood, level 1 EM trigger, level 3 EM trigger, jet triggers, Monte Carlo statistics, jet energy scale, jet energy resolution and jet identification. The  $\sigma_{syst}$  are the one standard deviation errors on the preselection efficiency from the various systematic sources. They are a measure of how much the preselection efficiency varies when the nuisance parameter varies by one sigma.

The same procedure is applied to all tagging probabilities which are recomputed at each step of the maximization procedure as a function of the central value of the tagging probabilities, the systematic errors and the nuisance parameters. Equal treatment is applied to efficiencies entering the Matrix Method, as well as the flavor fractions of  $Wj$ ,  $Wbb$ ,  $W(bb)$ ,  $Wcc$ ,  $W(cc)$

and  $Wc$ . With this procedure the preselection efficiencies, tagging probabilities, efficiencies and flavor fractions are floating in the maximization, and can vary within their errors. The correlations are taken into account in a natural way, by letting the same nuisance parameter affect different efficiencies or tagging probabilities. The total likelihood function that is maximized is the product of  $\mathcal{L}_1$  and  $\mathcal{L}_2$ , with

$$\mathcal{L}_2 = \prod_i \mathcal{G}(\nu_i; 0, 1), \quad (7.24)$$

where  $\mathcal{G}(\nu_i; 0, 1)$  is the normal probability of the nuisance parameter  $i$  to take the value  $\nu_i$ .

The nuisance parameter likelihood provides the total error on the cross section including all systematics along with the statistical error. To estimate the contribution of each systematic uncertainty, all but the corresponding nuisance parameters are fixed in the fit, and the maximization is redone. The statistical error is then deconvoluted from the obtained error to extract the uncertainty for that particular systematic. The systematic errors can shift the central value of the cross section; a different cross section is fitted for each systematic or group of systematics that is allowed to float. The differences between the refitted cross section obtained by the nuisance parameter likelihood for each source of systematic, and the cross section obtained in the standard method are referred to as *offsets*, and are shown in Table XLI, Table L and Table LI for the  $\mu$ +jets,  $e$ +jets and combined  $\ell$ +jets channels, respectively.

## 7.5 Observed and Predicted Number of Tagged Events

This section summarizes the observed number of tagged events presented together with the expected signal and background contributions. The results for single tagged events are summarized in Table XLV for the  $\mu$ -plus-jets and the electron-plus-jets channels, separately, and

in Table XLVI for the combined lepton-plus-jets channel. The corresponding results for double tagged events are summarized in Table XLVII and in Table XLVIII. Figure 109, Figure 111 and Figure 113 show the observed number of tagged events in data compared to the total signal and background predictions assuming a  $t\bar{t}$  production cross section of 7 pb.

The largest background in the first jet multiplicity bin comes from  $W$ +light and  $Wc$ . Contribution from heavy flavors (especially from  $Wb\bar{b}$ ) dominates starting from the second jet multiplicity bin. The signal ( $t\bar{t}$ ) contributes primarily to the third and fourth bins. The composition of the predicted background is shown in Figure 110, Figure 112 and Figure 114 for the  $\mu$ -plus-jets, electron-plus-jets and combined lepton-plus-jets channels, respectively, together with the expected signal contribution assuming a  $t\bar{t}$  production cross section of 7 pb.

	$e+$ jets				$\mu+$ jets			
	1jet	2jets	3jets	$\geq 4$ jets	1jet	2jets	3jets	$\geq 4$ jets
$W+\text{light}$	$18.9 \pm 0.6$	$8.7 \pm 0.5$	$2.28 \pm 0.22$	$0.46 \pm 0.11$	$27.7 \pm 0.8$	$13.7 \pm 0.7$	$2.98 \pm 0.28$	$0.46 \pm 0.10$
$W(c\bar{c})$	$6.1 \pm 0.1$	$3.43 \pm 0.13$	$0.78 \pm 0.06$	$0.24 \pm 0.06$	$9.0 \pm 0.2$	$4.69 \pm 0.15$	$1.01 \pm 0.06$	$0.25 \pm 0.06$
$W(b\bar{b})$	$17.8 \pm 0.3$	$8.8 \pm 0.3$	$2.03 \pm 0.15$	$0.49 \pm 0.11$	$25.6 \pm 0.4$	$12.1 \pm 0.3$	$2.63 \pm 0.16$	$0.50 \pm 0.11$
$Wc$	$22.4 \pm 0.5$	$9.9 \pm 0.4$	$1.38 \pm 0.11$	$0.20 \pm 0.05$	$32.4 \pm 0.5$	$13.4 \pm 0.4$	$1.86 \pm 0.12$	$0.19 \pm 0.04$
$Wc\bar{c}$		$4.44 \pm 0.17$	$1.29 \pm 0.12$	$0.33 \pm 0.08$		$6.0 \pm 0.2$	$1.75 \pm 0.12$	$0.34 \pm 0.08$
$Wb\bar{b}$		$9.2 \pm 0.3$	$2.68 \pm 0.20$	$0.62 \pm 0.14$		$12.4 \pm 0.3$	$3.51 \pm 0.21$	$0.60 \pm 0.13$
$W+\text{jets}$	$65.1 \pm 0.9$	$44.4 \pm 0.8$	$10.5 \pm 0.4$	$2.35 \pm 0.24$	$94.8 \pm 1.0$	$62.4 \pm 1.0$	$13.8 \pm 0.4$	$2.34 \pm 0.23$
QCD	$5.0 \pm 1.3$	$5.7 \pm 1.3$	$2.52 \pm 0.94$	$2.99 \pm 0.94$	$4.45 \pm 1.04$	$9.3 \pm 0.9$	$2.79 \pm 0.53$	$2.07 \pm 0.43$
$tb$	$2.49 \pm 0.04$	$6.1 \pm 0.1$	$1.81 \pm 0.04$	$0.34 \pm 0.02$	$2.38 \pm 0.04$	$6.1 \pm 0.1$	$1.92 \pm 0.04$	$0.36 \pm 0.02$
$t\bar{t} \rightarrow ll$	$1.94 \pm 0.04$	$6.3 \pm 0.1$	$2.32 \pm 0.04$	$0.37 \pm 0.02$	$1.53 \pm 0.03$	$5.7 \pm 0.1$	$2.32 \pm 0.04$	$0.35 \pm 0.02$
$VV$	$1.75 \pm 0.08$	$2.59 \pm 0.10$	$0.18 \pm 0.03$	$< 0.01$	$2.04 \pm 0.09$	$3.34 \pm 0.11$	$0.29 \pm 0.03$	$< 0.01$
$Z \rightarrow \tau^+ \tau^-$	$0.10 \pm 0.03$	$0.10 \pm 0.05$	$0.03 \pm 0.02$	$< 0.01$	$0.22 \pm 0.06$	$0.18 \pm 0.05$	$0.06 \pm 0.04$	$< 0.01$
background	$76.4 \pm 1.5$	$65.2 \pm 1.5$	$17.3 \pm 1.0$	$6.1 \pm 1.0$	$105.4 \pm 1.5$	$87.0 \pm 1.3$	$21.1 \pm 0.7$	$5.1 \pm 0.5$
syst.	$+9.79-17.75$	$+7.61-10.58$	$+1.79-2.36$	$+0.41-0.54$	$+14.16-19.73$	$+10.26-13.33$	$+2.35-2.76$	$+0.39-0.52$
$t\bar{t} \rightarrow l+jets$	$0.90 \pm 0.04$	$9.0 \pm 0.1$	$22.6 \pm 0.2$	$18.8 \pm 0.2$	$0.58 \pm 0.03$	$7.7 \pm 0.1$	$22.0 \pm 0.2$	$21.2 \pm 0.2$
total	$77.3 \pm 1.5$	$74.2 \pm 1.5$	$39.9 \pm 1.0$	$24.9 \pm 1.0$	$106.0 \pm 1.5$	$94.7 \pm 1.3$	$43.1 \pm 0.7$	$26.3 \pm 0.5$
syst.	$+9.81-17.90$	$+7.68-11.12$	$+1.96-2.44$	$+2.00-2.63$	$+14.16-19.84$	$+10.34-13.92$	$+2.46-2.73$	$+2.22-2.68$
tags	83	65	43	29	125	82	46	23

TABLE XLV. SUMMARY OF OBSERVED AND PREDICTED NUMBER OF SINGLE TAGGED EVENTS IN THE ELECTRON+JETS AND THE MUON+JETS CHANNELS. ERRORS ARE STATISTICAL ONLY UNLESS STATED OTHERWISE.

	$l+jets$			
	1jet	2jets	3jets	$\geq 4$ jets
$W+light$	$46.6 \pm 1.0$	$22.4 \pm 0.9$	$5.3 \pm 0.4$	$0.91 \pm 0.15$
$W(c\bar{c})$	$15.1 \pm 0.2$	$8.1 \pm 0.2$	$1.79 \pm 0.08$	$0.49 \pm 0.08$
$W(b\bar{b})$	$43.4 \pm 0.5$	$20.9 \pm 0.4$	$4.67 \pm 0.22$	$1.00 \pm 0.16$
$Wc$	$54.9 \pm 0.7$	$23.3 \pm 0.5$	$3.25 \pm 0.16$	$0.40 \pm 0.06$
$Wc\bar{c}$		$10.4 \pm 0.3$	$3.04 \pm 0.17$	$0.67 \pm 0.11$
$Wb\bar{b}$		$21.6 \pm 0.5$	$6.2 \pm 0.3$	$1.22 \pm 0.19$
$W+jets$	$159.9 \pm 1.3$	$106.8 \pm 1.3$	$24.2 \pm 0.6$	$4.69 \pm 0.33$
QCD	$9.5 \pm 1.6$	$15.0 \pm 1.6$	$5.3 \pm 1.1$	$5.1 \pm 1.0$
$tb$	$4.87 \pm 0.06$	$12.2 \pm 0.1$	$3.73 \pm 0.06$	$0.70 \pm 0.03$
$t\bar{t} \rightarrow ll$	$3.48 \pm 0.05$	$12.0 \pm 0.1$	$4.64 \pm 0.06$	$0.72 \pm 0.02$
$VV$	$3.80 \pm 0.12$	$5.9 \pm 0.1$	$0.48 \pm 0.04$	$0.01 \pm 0.01$
$Z \rightarrow \tau^+\tau^-$	$0.31 \pm 0.07$	$0.28 \pm 0.07$	$0.09 \pm 0.04$	$< 0.01$
background	$181.8 \pm 2.1$	$152.2 \pm 2.0$	$38.5 \pm 1.3$	$11.2 \pm 1.1$
syst.	$+23.95-37.17$	$+17.88-23.86$	$+4.12-5.11$	$+0.80-1.06$
$t\bar{t} \rightarrow l+jets$	$1.49 \pm 0.05$	$16.7 \pm 0.2$	$44.6 \pm 0.3$	$40.0 \pm 0.3$
total	$183.3 \pm 2.1$	$168.9 \pm 2.0$	$83.0 \pm 1.3$	$51.2 \pm 1.1$
syst.	$+23.96-37.42$	$+18.00-24.99$	$+4.37-5.13$	$+4.22-5.30$
tags	208	147	89	52

TABLE XLVI

SUMMARY OF OBSERVED AND PREDICTED NUMBER OF SINGLE TAGGED EVENTS IN THE COMBINED LEPTON+JETS CHANNEL. ERRORS ARE STATISTICAL ONLY UNLESS STATED OTHERWISE.

	e+jets			$\mu$ +jets		
	2jets	3jets	$\geq$ 4jets	2jets	3jets	$\geq$ 4jets
$W$ +light	0.013 $\pm$ 0.002	< 0.01	< 0.01	0.025 $\pm$ 0.003	0.010 $\pm$ 0.002	< 0.01
$W(c\bar{c})$	0.012 $\pm$ 0.002	< 0.01	< 0.01	0.024 $\pm$ 0.004	< 0.01	< 0.01
$W(b\bar{b})$	0.15 $\pm$ 0.03	0.06 $\pm$ 0.01	< 0.01	0.26 $\pm$ 0.04	0.06 $\pm$ 0.01	0.02 $\pm$ 0.01
$Wc$	0.025 $\pm$ 0.002	< 0.01	< 0.01	0.039 $\pm$ 0.002	< 0.01	< 0.01
$Wc\bar{c}$	0.22 $\pm$ 0.01	0.06 $\pm$ 0.01	0.019 $\pm$ 0.005	0.29 $\pm$ 0.01	0.09 $\pm$ 0.01	0.019 $\pm$ 0.004
$Wb\bar{b}$	2.52 $\pm$ 0.11	0.74 $\pm$ 0.07	0.18 $\pm$ 0.04	3.64 $\pm$ 0.13	0.99 $\pm$ 0.07	0.17 $\pm$ 0.04
$W$ +jets	2.93 $\pm$ 0.11	0.89 $\pm$ 0.07	0.22 $\pm$ 0.04	4.27 $\pm$ 0.14	1.17 $\pm$ 0.07	0.22 $\pm$ 0.04
QCD	< 0.01	0.16 $\pm$ 0.23	< 0.01	0.12 $\pm$ 0.14	0.03 $\pm$ 0.10	< 0.01
$tb$	0.88 $\pm$ 0.01	0.38 $\pm$ 0.01	0.09 $\pm$ 0.01	0.88 $\pm$ 0.01	0.40 $\pm$ 0.01	0.09 $\pm$ 0.01
$t\bar{t} \rightarrow ll$	1.74 $\pm$ 0.02	0.70 $\pm$ 0.01	0.12 $\pm$ 0.01	1.58 $\pm$ 0.02	0.70 $\pm$ 0.01	0.11 $\pm$ 0.01
$VV$	0.31 $\pm$ 0.02	0.02 $\pm$ 0.01	< 0.01	0.39 $\pm$ 0.02	0.04 $\pm$ 0.01	< 0.01
$Z \rightarrow \tau^+\tau^-$	< 0.01	< 0.01	< 0.01	< 0.01	0.02 $\pm$ 0.02	< 0.01
background	5.3 $\pm$ 0.2	2.15 $\pm$ 0.25	< 0.01	7.2 $\pm$ 0.2	2.36 $\pm$ 0.14	0.34 $\pm$ 0.14
syst.	+0.88-0.97	+0.29-0.37	+0.07-0.08	+1.16-1.23	+0.38-0.41	+0.07-0.07
$t\bar{t} \rightarrow l+$ jets	1.14 $\pm$ 0.03	5.9 $\pm$ 0.1	6.5 $\pm$ 0.1	1.02 $\pm$ 0.03	5.8 $\pm$ 0.1	7.3 $\pm$ 0.1
total	6.5 $\pm$ 0.2	8.1 $\pm$ 0.2	6.4 $\pm$ 0.2	8.3 $\pm$ 0.2	8.2 $\pm$ 0.1	7.6 $\pm$ 0.1
syst.	+0.95-1.08	+0.80-0.84	+1.01-1.16	+1.22-1.32	+0.83-0.83	+1.13-1.21
tags	12	2	10	7	4	9

TABLE XLVII. SUMMARY OF OBSERVED AND PREDICTED NUMBER OF DOUBLE TAGGED EVENTS IN THE ELECTRON+JETS AND THE MUON+JETS CHANNELS. ERRORS ARE STATISTICAL ONLY UNLESS STATED OTHERWISE.

	$l+$ jets		
	2jets	3jets	$\geq 4$ jets
$W + \text{light}$	$0.038 \pm 0.003$	$0.018 \pm 0.002$	$< 0.01$
$W(c\bar{c})$	$0.037 \pm 0.004$	$0.016 \pm 0.001$	$< 0.01$
$W(b\bar{b})$	$0.40 \pm 0.05$	$0.12 \pm 0.01$	$0.03 \pm 0.01$
$Wc$	$0.063 \pm 0.003$	$0.017 \pm 0.001$	$< 0.01$
$Wc\bar{c}$	$0.51 \pm 0.02$	$0.15 \pm 0.01$	$0.04 \pm 0.01$
$Wb\bar{b}$	$6.2 \pm 0.2$	$1.74 \pm 0.10$	$0.35 \pm 0.06$
$W+\text{jets}$	$7.2 \pm 0.2$	$2.06 \pm 0.10$	$0.44 \pm 0.06$
QCD	$< 0.01$	$0.19 \pm 0.25$	$< 0.01$
$tb$	$1.76 \pm 0.02$	$0.78 \pm 0.02$	$0.17 \pm 0.01$
$t\bar{t} \rightarrow ll$	$3.32 \pm 0.03$	$1.41 \pm 0.02$	$0.22 \pm 0.01$
$VV$	$0.70 \pm 0.03$	$0.06 \pm 0.01$	$< 0.01$
$Z \rightarrow \tau^+ \tau^-$	$< 0.01$	$0.02 \pm 0.02$	$< 0.01$
background	$12.6 \pm 0.3$	$4.51 \pm 0.29$	$0.24 \pm 0.22$
syst.	$+2.04-2.19$	$+0.68-0.77$	$+0.13-0.16$
$tt \rightarrow l+\text{jets}$	$2.16 \pm 0.04$	$11.8 \pm 0.1$	$13.7 \pm 0.1$
total	$14.7 \pm 0.3$	$16.3 \pm 0.3$	$14.0 \pm 0.2$
syst.	$+2.17-2.39$	$+1.65-1.63$	$+2.14-2.37$
tags	19	6	19

TABLE XLVIII

SUMMARY OF OBSERVED AND PREDICTED NUMBER OF DOUBLE TAGGED EVENTS IN THE COMBINED LEPTON+JETS CHANNEL. ERRORS ARE STATISTICAL ONLY UNLESS STATED OTHERWISE.

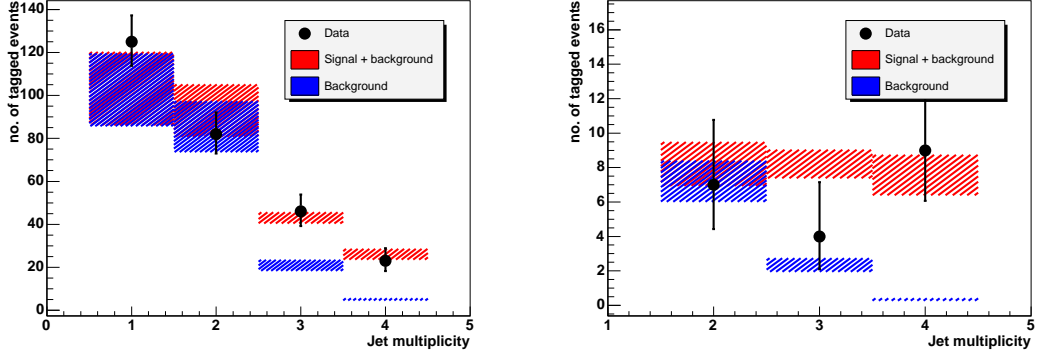


Figure 109. Observed and predicted number of tagged events in the  $\mu + \text{jets}$  channel. The left plot shows single tagged events and the right plot shows double tagged events. The total error on the background prediction is represented by the dashed blue band and the total error on the sum of the signal and background prediction is represented by the dashed red band.

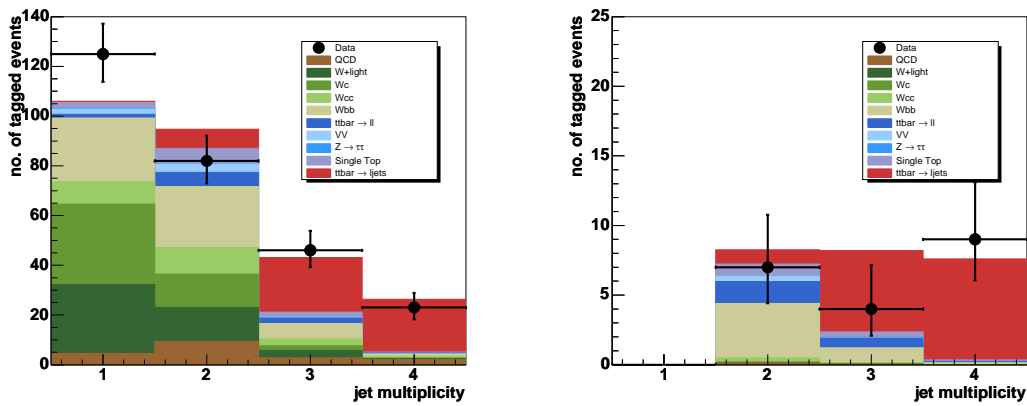


Figure 110. The predicted background composition in the  $\mu + \text{jets}$  channel for single tagged events (left) and double tagged events (right).

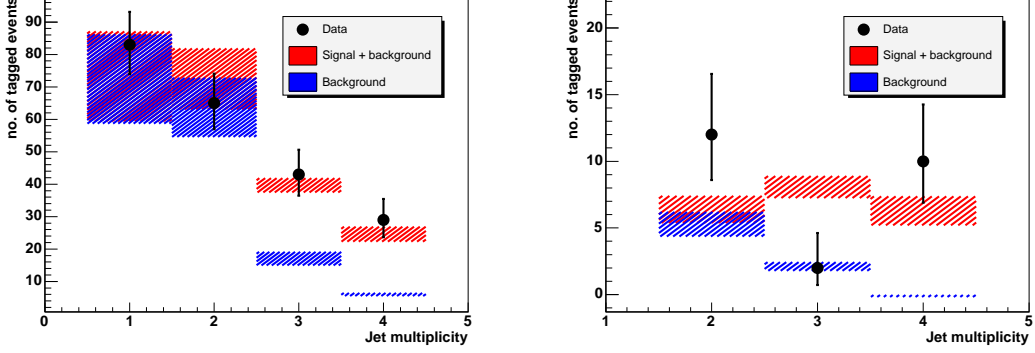


Figure 111. Observed and predicted number of tagged events in the  $e+jets$  channel. The left plot shows single tagged events and the right plot shows double tagged events. The total error on the background prediction is represented by the dashed blue band and the total error on the sum of the signal and background prediction is represented by the dashed red band.

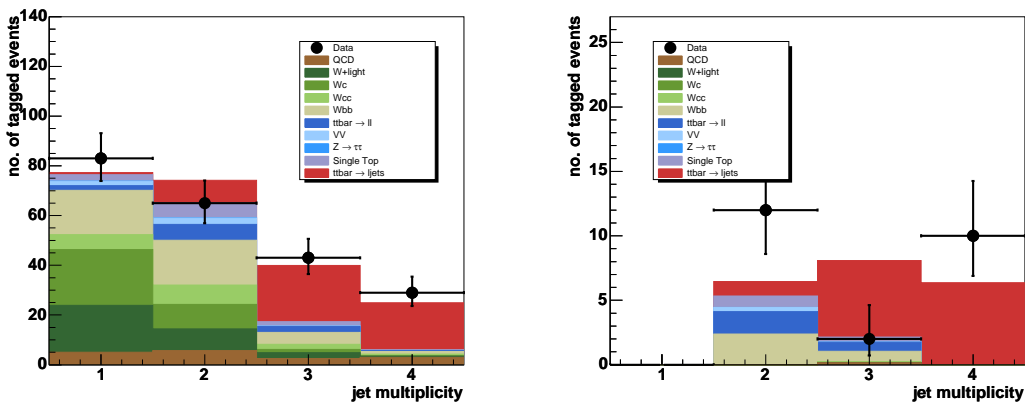


Figure 112. The predicted background composition in the  $e+jets$  channel for single tagged events (left) and double tagged events (right).

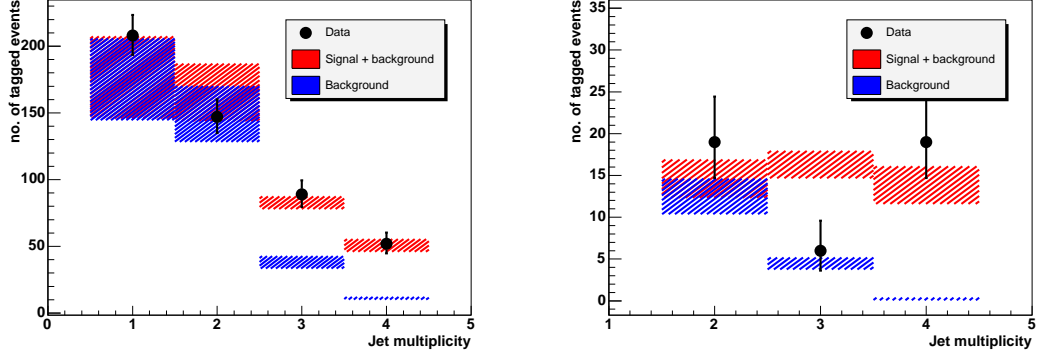


Figure 113. Observed and predicted number of tagged events in the combined  $l+jets$  channel. The left plot shows single tagged events and the right plot shows double tagged events. The total error on the background prediction is represented by the dashed blue band and the total error on the sum of the signal and background prediction is represented by the dashed red band.

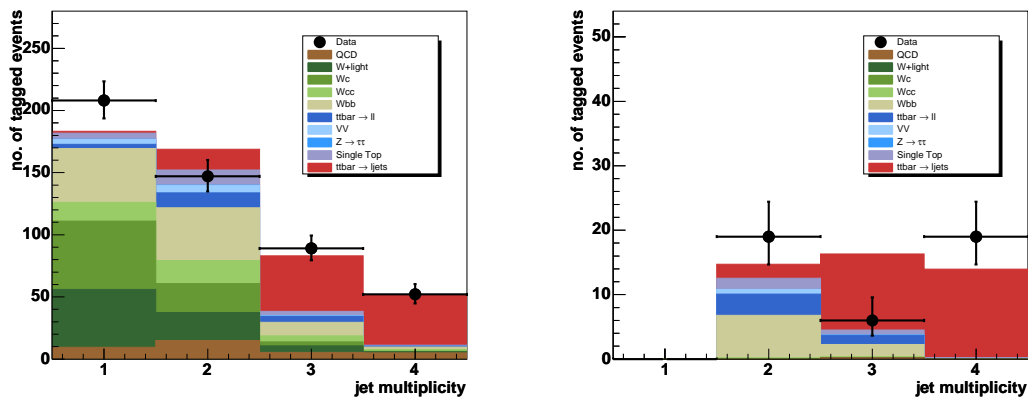


Figure 114. The predicted background composition in the combined  $l+jets$  channel for single tagged events (left) and double tagged events (right).

## 7.6 The $t\bar{t}$ Production Cross-Section

The nuisance parameter likelihood method used to calculate the  $t\bar{t}$  production cross section measurement is described in Section 7.4. The result of the  $t\bar{t}$  production cross section in the  $e+jets$  and  $\mu+jets$  channel at  $\sqrt{s}=1.96$  TeV yields:

$$\mu + \text{jets} : \quad \sigma_{t\bar{t}} = 6.39^{+1.36}_{-1.22}(\text{stat+syst}) \pm 0.42(\text{lumi}) \text{ pb}$$

$$e + \text{jets} : \quad \sigma_{t\bar{t}} = 7.57^{+1.46}_{-1.31}(\text{stat+syst}) \pm 0.49(\text{lumi}) \text{ pb}$$

and for the combination:

$$\text{lepton} + \text{jets} : \quad \sigma_{t\bar{t}} = 6.96^{+1.07}_{-0.98}(\text{stat+syst}) \pm 0.45(\text{lumi}) \text{ pb.}$$

Table XLIX, Table L and Table LI summarize the shifts from different sources of systematic uncertainties to the central value of the cross section and the total error on the cross section in  $\mu+jets$ ,  $e+jets$  and combined  $\ell+jets$  channels, respectively.

As a cross check, the cross section is calculated using the standard likelihood method which does not allow to change the central value due to variations of the systematic errors. The results obtained by this method are quoted below and are in a good agreement with the results obtained with the nuisance parameter likelihood method:

$$\mu + \text{jets} : \quad \sigma_{t\bar{t}} = 6.41^{+1.14}_{-1.05}(\text{stat})^{+0.87}_{-0.66}(\text{syst}) \pm 0.42(\text{lumi}) \text{ pb}$$

$$e + \text{jets} : \quad \sigma_{t\bar{t}} = 7.61^{+1.24}_{-1.15}(\text{stat})^{+0.99}_{-0.71}(\text{syst}) \pm 0.49(\text{lumi}) \text{ pb}$$

Source	Offset	$\sigma^+$	$\sigma^-$
Muon preselections	-0.00	+0.30	-0.22
Electron preselections	-0.00	+0.01	+0.00
EM triggers	-0.00	+0.01	+0.00
Muon triggers	-0.00	+0.07	-0.05
Jet triggers	-0.00	+0.01	+0.00
Jet energy scale	-0.00	+0.34	-0.23
Jet energy resolution	-0.00	+0.05	-0.04
Jet reco and jet ID	+0.00	+0.33	+0.00
Taggability in data	-0.00	+0.01	-0.01
Flavor dependence of taggability	+0.00	+0.00	-0.02
b-tag efficiency in MC	+0.01	+0.20	-0.16
c-tag efficiency in MC	-0.00	+0.01	-0.02
SML b-tag eff in MC	+0.00	+0.12	-0.11
Semileptonic b-tagging efficiency in data	+0.02	+0.33	-0.26
NTRF parametrisation	+0.00	+0.00	-0.03
Light tag scale factors	-0.00	+0.02	-0.03
QCD tagging probability	-0.00	+0.01	+0.00
Matrix method $\epsilon_{QCD}$ in e+jet channel	-0.00	+0.01	+0.00
Matrix method $\epsilon_{sig}$ in e+jet channel	-0.00	+0.01	+0.00
Matrix method $\epsilon_{QCD}$ in $\mu$ +jet channel	-0.00	+0.00	-0.03
Matrix method $\epsilon_{sig}$ in $\mu$ +jet channel	-0.00	+0.01	-0.01
Monte Carlo statistics on W fractions	-0.00	+0.07	-0.08
Monte Carlo statistics	-0.00	+0.06	-0.05
Factorization scale on W fractions	-0.00	+0.05	-0.05
Heavy quark mass on W fractions	-0.01	+0.13	-0.13
W fractions matching + higher order effects	-0.03	+0.33	-0.33
PDF on W fractions	-0.00	+0.02	-0.03
Event statistics for matrix method	-0.01	+0.15	-0.16
Total systematics (quad sum of the above)	-0.02	+0.81	+0.62
All systematics (nuisance parameter lhood)	6.39	+1.36	-1.22

TABLE XLIX

SYSTEMATIC UNCERTAINTIES IN THE MUON+JET CHANNEL ONLY,  
DETERMINED WITH THE NUISANCE PARAMETER LIKELIHOOD. FOR EACH  
SOURCE OF SYSTEMATIC THE LIKELIHOOD MAXIMIZATION IS REDONE GIVING  
A NEW CENTRAL VALUE OF THE CROSS SECTION. THE COLUMN LABELED  
OFFSET GIVES THE DIFFERENCE BETWEEN THE REFITTED CROSS SECTION  
AND THE CROSS SECTION OBTAINED IN THE STANDARD METHOD.

Source	Offset	$\sigma^+$	$\sigma^-$
Muon preselections	-0.00	+0.00	+0.00
Electron preselections	+0.00	+0.37	-0.28
EM triggers	-0.00	+0.14	+0.00
Muon triggers	-0.00	+0.00	+0.00
Jet triggers	+0.00	+0.00	-0.01
Jet energy scale	-0.14	+0.36	-0.27
Jet energy resolution	-0.00	+0.03	-0.02
Jet reco and jet ID	+0.00	+0.00	+0.00
Taggability in data	+0.00	+0.00	-0.02
Flavor dependence of taggability	+0.00	+0.01	-0.01
b-tag efficiency in MC	+0.03	+0.23	-0.18
c-tag efficiency in MC	+0.00	+0.03	-0.01
SML b-tag eff in MC	+0.01	+0.14	-0.10
Semileptonic b-tagging efficiency in data	+0.07	+0.36	-0.29
NTRF parametrisation	+0.00	+0.00	-0.05
Light tag scale factors	+0.00	+0.00	-0.04
QCD tagging probability	-0.00	+0.00	+0.00
Matrix method $\epsilon_{QCD}$ in e+jet channel	+0.00	+0.00	-0.09
Matrix method $\epsilon_{sig}$ in e+jet channel	-0.00	+0.04	+0.00
Matrix method $\epsilon_{QCD}$ in $\mu$ +jet channel	-0.00	+0.00	+0.00
Matrix method $\epsilon_{sig}$ in $\mu$ +jet channel	-0.00	+0.00	+0.00
Monte Carlo statistics on W fractions	+0.00	+0.04	-0.05
Monte Carlo statistics	+0.00	+0.06	-0.05
Factorization scale on W fractions	-0.00	+0.04	-0.04
Heavy quark mass on W fractions	+0.00	+0.09	-0.10
W fractions matching + higher order effects	+0.02	+0.22	-0.24
PDF on W fractions	-0.00	+0.05	+0.00
Event statistics for matrix method	-0.02	+0.22	-0.23
Total systematics (quad sum of the above)	-0.03	+0.78	+0.65
All systematics (nuisance parameter lhood)	7.57	+1.46	-1.31

TABLE L

SYSTEMATIC UNCERTAINTIES IN THE ELECTRON+JET CHANNEL ONLY,  
DETERMINED WITH THE NUISANCE PARAMETER LIKELIHOOD. FOR EACH  
SOURCE OF SYSTEMATIC THE LIKELIHOOD MAXIMIZATION IS REDONE GIVING  
A NEW CENTRAL VALUE OF THE CROSS SECTION. THE COLUMN LABELED  
OFFSET GIVES THE DIFFERENCE BETWEEN THE REFITTED CROSS SECTION  
AND THE CROSS SECTION OBTAINED IN THE STANDARD METHOD.

Source	Offset	$\sigma^+$	$\sigma^-$
Muon preselections	+0.02	+0.16	-0.13
Electron preselections	-0.02	+0.15	-0.13
EM triggers	+0.00	+0.00	-0.07
Muon triggers	+0.00	+0.04	-0.03
Jet triggers	+0.00	+0.00	-0.01
Jet energy scale	-0.12	+0.31	-0.26
Jet energy resolution	-0.00	+0.03	-0.04
Jet reco and jet ID	-0.00	+0.00	+0.00
Taggability in data	-0.00	+0.00	+0.00
Flavor dependence of taggability	+0.00	+0.01	-0.01
b-tag efficiency in MC	+0.04	+0.21	-0.18
c-tag efficiency in MC	-0.00	+0.02	-0.02
SML b-tag eff in MC	+0.01	+0.12	-0.11
Semileptonic b-tagging efficiency in data	+0.08	+0.33	-0.28
NTRF parametrisation	-0.00	+0.01	-0.02
Light tag scale factors	-0.00	+0.02	-0.03
QCD tagging probability	-0.00	+0.00	+0.00
Matrix method $\epsilon_{QCD}$ in e+jet channel	+0.01	+0.00	-0.09
Matrix method $\epsilon_{sig}$ in e+jet channel	-0.00	+0.00	-0.01
Matrix method $\epsilon_{QCD}$ in $\mu$ +jet channel	-0.00	+0.00	-0.01
Matrix method $\epsilon_{sig}$ in $\mu$ +jet channel	-0.00	+0.00	-0.00
Monte Carlo statistics on W fractions	+0.00	+0.04	-0.04
Monte Carlo statistics	+0.00	+0.04	-0.04
Factorization scale on W fractions	-0.00	+0.04	-0.05
Heavy quark mass on W fractions	-0.00	+0.11	-0.11
W fractions matching + higher order effects	+0.00	+0.27	-0.28
PDF on W fractions	-0.00	+0.03	+0.00
Event statistics for matrix method	-0.02	+0.14	-0.14
Total systematics (quad sum of the above)	+0.00	+0.65	+0.60
All systematics (nuisance parameter lhood)	6.96	+1.07	-0.98

TABLE LI

SYSTEMATIC UNCERTAINTIES IN THE ELECTRON+JET AND MUON+JET CHANNELS COMBINED, DETERMINED WITH THE NUISANCE PARAMETER LIKELIHOOD. FOR EACH SOURCE OF SYSTEMATIC THE LIKELIHOOD MAXIMIZATION IS REDONE GIVING A NEW CENTRAL VALUE OF THE CROSS SECTION. THE COLUMN LABELED OFFSET GIVES THE DIFFERENCE BETWEEN THE REFITTED CROSS SECTION AND THE CROSS SECTION OBTAINED IN THE STANDARD METHOD.

and for the combination:

$$\text{lepton + jets} : \quad \sigma_{t\bar{t}} = 6.99^{+0.83}_{-0.79}(\text{stat})^{+0.70}_{-0.64}(\text{syst}) \pm 0.45(\text{lumi}) \text{ pb.}$$

Table LII, Table LIII and Table LIV summarize the contributions from different sources of systematics into the total error on the cross section in  $\mu$ +jets,  $e$ +jets and combined  $\ell$ +jets channel, respectively.

The dependence of the estimated combined cross section with the top quark mass in the  $\ell$ +jets channel is shown in Figure 115.

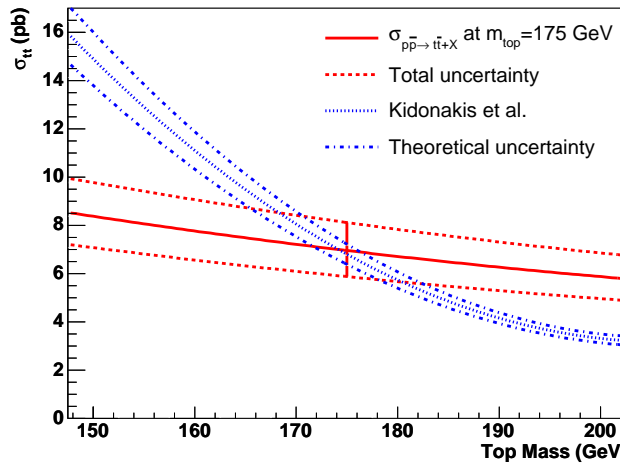


Figure 115. Top quark mass dependence of the measured cross section compared to the theoretical prediction (39).

Source	$\sigma^+$	$\sigma^-$
Muon preselections	0.27	-0.25
Electron preselections	0.00	-0.00
EM triggers	0.00	-0.00
Muon triggers	0.06	-0.06
Jet triggers	0.00	-0.00
Jet energy scale	0.37	-0.30
Jet energy resolution	0.02	-0.04
Jet reco and jet ID	0.49	-0.03
Taggability in data	0.00	-0.03
Flavor dependence of taggability	0.01	-0.01
b-tag efficiency in MC	0.19	-0.18
c-tag efficiency in MC	0.02	-0.02
SML b-tag eff in MC	0.11	-0.12
Semileptonic b-tagging efficiency in data	0.31	-0.29
NTRF parametrisation	0.02	-0.02
Light tag scale factors	0.03	-0.03
QCD tagging probability	0.00	-0.00
Matrix method $\epsilon_{QCD}$ in e+jet channel	0.00	-0.00
Matrix method $\epsilon_{sig}$ in e+jet channel	0.00	-0.00
Matrix method $\epsilon_{QCD}$ in $\mu$ +jet channel	0.00	-0.02
Matrix method $\epsilon_{sig}$ in $\mu$ +jet channel	0.00	-0.00
Monte Carlo statistics on W fractions	0.07	-0.07
Monte Carlo statistics	0.05	-0.05
Factorization scale on W fractions	0.02	-0.03
Heavy quark mass on W fractions	0.13	-0.12
W fractions matching + higher order effects	0.33	-0.32
PDF on W fractions	0.02	-0.03
Event statistics for matrix method	0.15	-0.15
Total systematic	0.87	-0.66

TABLE LII

BREAKDOWN OF SYSTEMATIC UNCERTAINTIES IN THE MUON+JET CHANNEL ONLY. THESE SYSTEMATIC UNCERTAINTIES ARE DERIVED WITH THE STANDARD METHOD.

Source	$\sigma^+$	$\sigma^-$
Muon preselections	0.00	-0.00
Electron preselections	0.33	-0.31
EM triggers	0.10	-0.05
Muon triggers	0.00	-0.00
Jet triggers	0.00	-0.00
Jet energy scale	0.45	-0.34
Jet energy resolution	0.00	-0.03
Jet reco and jet ID	0.60	-0.00
Taggability in data	0.00	-0.03
Flavor dependence of taggability	0.01	-0.01
b-tag efficiency in MC	0.22	-0.21
c-tag efficiency in MC	0.02	-0.02
SML b-tag eff in MC	0.12	-0.13
Semileptonic b-tagging efficiency in data	0.34	-0.32
NTRF parametrisation	0.01	-0.01
Light tag scale factors	0.02	-0.02
QCD tagging probability	0.00	-0.00
Matrix method $\epsilon_{QCD}$ in e+jet channel	0.00	-0.02
Matrix method $\epsilon_{sig}$ in e+jet channel	0.00	-0.01
Matrix method $\epsilon_{QCD}$ in $\mu$ +jet channel	0.00	-0.00
Matrix method $\epsilon_{sig}$ in $\mu$ +jet channel	0.00	-0.00
Monte Carlo statistics on W fractions	0.05	-0.06
Monte Carlo statistics	0.06	-0.06
Factorization scale on W fractions	0.02	-0.02
Heavy quark mass on W fractions	0.10	-0.10
W fractions matching + higher order effects	0.26	-0.25
PDF on W fractions	0.01	-0.02
Event statistics for matrix method	0.21	-0.21
Total systematic	0.99	-0.71

TABLE LIII

BREAKDOWN OF SYSTEMATIC UNCERTAINTIES IN THE ELECTRON+JET CHANNEL ONLY. THESE SYSTEMATIC UNCERTAINTIES ARE DERIVED WITH THE STANDARD METHOD.

Source	$\sigma^+$	$\sigma^-$
Muon preselections	0.15	-0.15
Electron preselections	0.14	-0.14
EM triggers	0.04	-0.02
Muon triggers	0.04	-0.04
Jet triggers	0.00	-0.00
Jet energy scale	0.41	-0.31
Jet energy resolution	0.01	-0.04
Jet reco and jet ID	0.00	-0.00
Taggability in data	0.00	-0.03
Flavor dependence of taggability	0.01	-0.01
b-tag efficiency in MC	0.20	-0.19
c-tag efficiency in MC	0.02	-0.02
SML b-tag eff in MC	0.12	-0.12
Semileptonic b-tagging efficiency in data	0.33	-0.30
NTRF parametrisation	0.02	-0.02
Light tag scale factors	0.02	-0.02
QCD tagging probability	0.00	-0.00
Matrix method $\epsilon_{QCD}$ in e+jet channel	0.00	-0.01
Matrix method $\epsilon_{sig}$ in e+jet channel	0.00	-0.00
Matrix method $\epsilon_{QCD}$ in $\mu$ +jet channel	0.00	-0.01
Matrix method $\epsilon_{sig}$ in $\mu$ +jet channel	0.00	-0.00
Monte Carlo statistics on W fractions	0.04	-0.05
Monte Carlo statistics	0.04	-0.04
Factorization scale on W fractions	0.02	-0.03
Heavy quark mass on W fractions	0.11	-0.11
W fractions matching + higher order effects	0.29	-0.28
PDF on W fractions	0.02	-0.03
Event statistics for matrix method	0.13	-0.13
Total systematic	0.70	-0.64

TABLE LIV

BREAKDOWN OF SYSTEMATIC UNCERTAINTIES IN THE ELECTRON+JET AND MUON+JET COMBINED. THESE SYSTEMATIC UNCERTAINTIES ARE DERIVED WITH THE STANDARD METHOD.

## CHAPTER 8

### SUMMARY AND CONCLUSIONS

A measurement of the  $t\bar{t}$  production cross section in  $p\bar{p}$  collisions at a center of mass energy of 1.96 TeV is presented in events with a lepton, a neutrino and  $\geq 3$  jets. After a preselection of the objects in the final state, a lifetime  $b$ -tagging algorithm which explicitly reconstructs secondary vertices is applied, removing approximately 95 % of the background while keeping 60 % of the  $t\bar{t}$  signal. The measurement combines the muon+jets and the electron+jets channel, using  $363 \text{ pb}^{-1}$  and  $366 \text{ pb}^{-1}$  of data, respectively, yielding a  $t\bar{t}$  production cross section of

$$\sigma_{p\bar{p} \rightarrow t\bar{t}+X} = 6.96^{+1.07}_{-0.98} (\text{stat+syst}) \pm 0.45 \text{ (lumi) pb}.$$

Figure 116 summarizes all current  $t\bar{t}$  production cross-section measurements from DØ, showing that the measurement in the lepton-plus-jets channel using vertex tagging, presented in this thesis, is the most precise.

With increasing statistics, the current analysis will be limited by the systematic uncertainty. However, most of the systematic uncertainties will be reduced with increasing statistics. The dominant source of systematic uncertainty is the one corresponding to the jet energy scale. The statistical component will be reduced by collecting more data, the systematic component is at present slightly overestimated, since the systematic effects in data and in MC are treated as uncorrelated. However, many of the systematics are correlated between data and MC and do

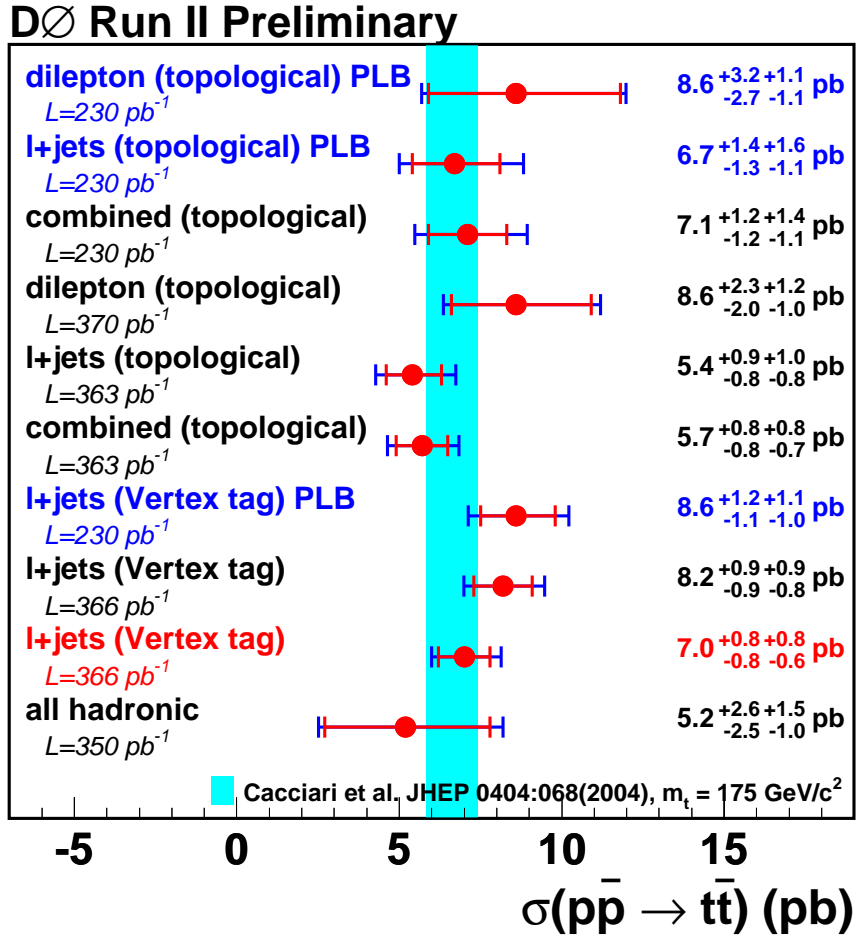


Figure 116. Comparison of all current  $t\bar{t}$  production cross-section measurements from DØ with the theoretical expectation (39; 40). The figure shows the integrated luminosities used and the measured  $t\bar{t}$  cross-section. From top to bottom: combined dilepton ( $ee$ ,  $\mu\mu$  and  $e\mu$ ) topological (146), lepton-plus-jets topological (147), combined dilepton-lepton-plus-jets topological (148), combined dilepton ( $ee$ ,  $\mu\mu$  and  $e\mu$ ) topological (52), lepton-plus-jets topological, combined dilepton-lepton-plus-jets topological, lepton-plus-jets using (SVT and CSIP) lifetime  $b$ -tagging (149), lepton-plus-jets using (SVT) lifetime  $b$ -tagging preliminary result for the summer of 2005 (150), measurement presented in this thesis and the all-jets channel (151).

not affect the cross section measurement. The evaluation of the correlations will decrease the jet energy scale uncertainty dramatically. The other dominant systematic uncertainty corresponds to the tagging probabilities determined both in data and in Monte Carlo, that will decrease with more statistics.

The top quark production studies at the Tevatron lay the ground for the future physics analyses at the Large Hadron Collider (LHC). The LHC is considered a top factory, where the  $t\bar{t}$  production will be the process of choice to calibrate and understand the detectors. Moreover, the top quark pair production will be the dominant background for the Higgs boson production, and new physics searches beyond the Standard Model. Understanding the  $t\bar{t}$  production cross section in detail is therefore of uttermost importance to future studies at the Tevatron and the LHC.

## **APPENDICES**

## Appendix A

### SANITY CHECKS

As a sanity check of the analysis, the kinematic distributions of the tagged events in data are compared with the expected kinematic distributions for the sum of the signal and background. Typical kinematic and topological distributions are shown in Figure 117- Figure 129 for the tagged data events overlaid with the predicted signal ( $\sigma_{t\bar{t}} = 7 \text{ pb}$ ) and backgrounds. For the calculation of these variables the four-vectors of the final state objects and their correlations are used. Some of these are event shape variables that are defined based on the normalized momentum tensor  $\mathcal{M}$ :

$$\mathcal{M}_{ij} = \frac{\Sigma_o p_i^o p_j^o}{\Sigma_o |\vec{p}^o|^2}, \quad (\text{A.1})$$

where  $\vec{p}^o$  is the momentum-vector of a reconstructed object  $o$ ,  $i$  and  $j$  are Cartesian coordinates. By standard diagonalization of  $\mathcal{M}_{ij}$  three eigenvalues  $\lambda_1 \geq \lambda_2 \geq \lambda_3$  are found, with  $\lambda_1 + \lambda_2 + \lambda_3 = 1$ .

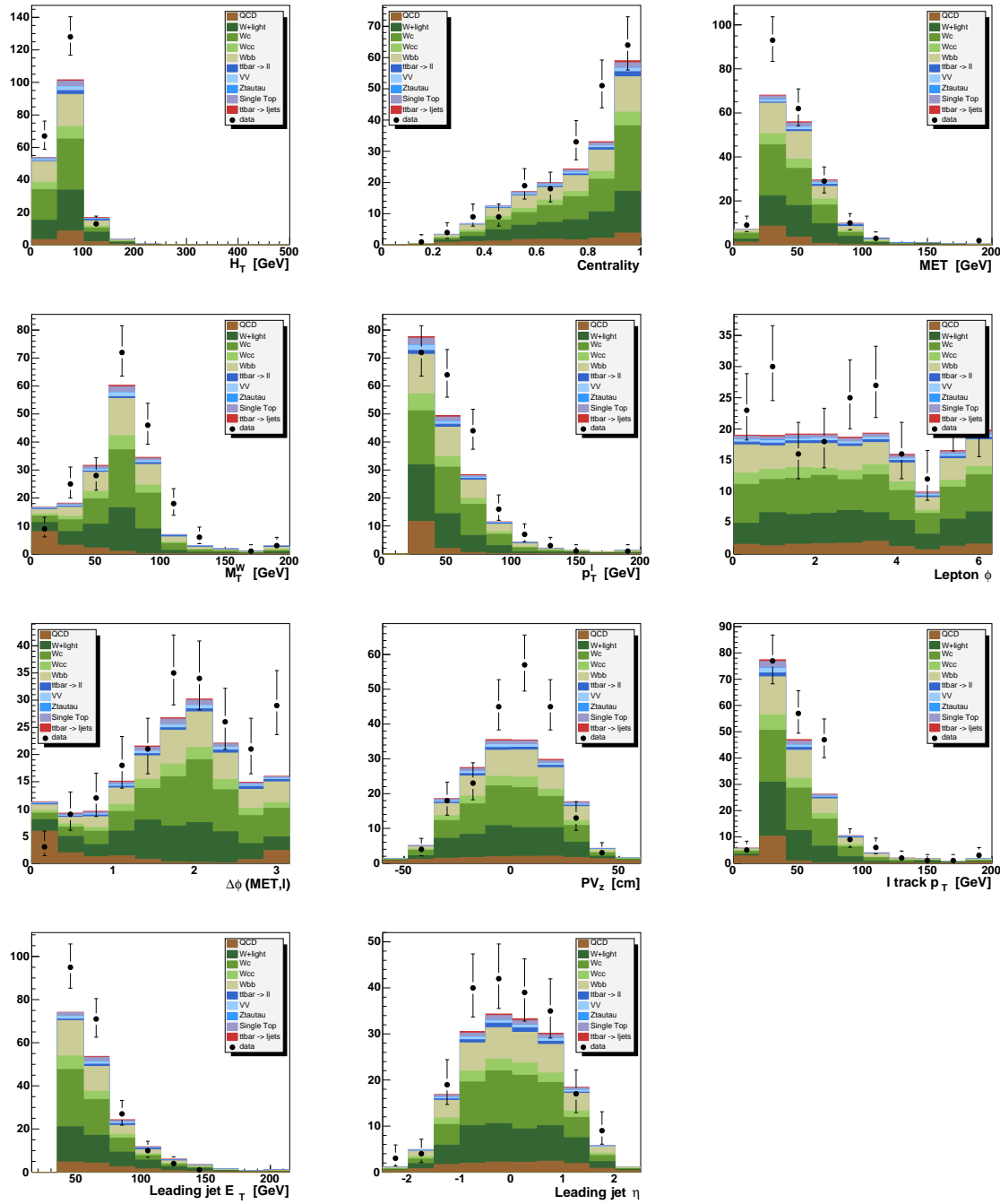
Table LV summarizes the variables used for the sanity check. The shapes of all distributions in data are reasonably well described by the background and signal contributions.

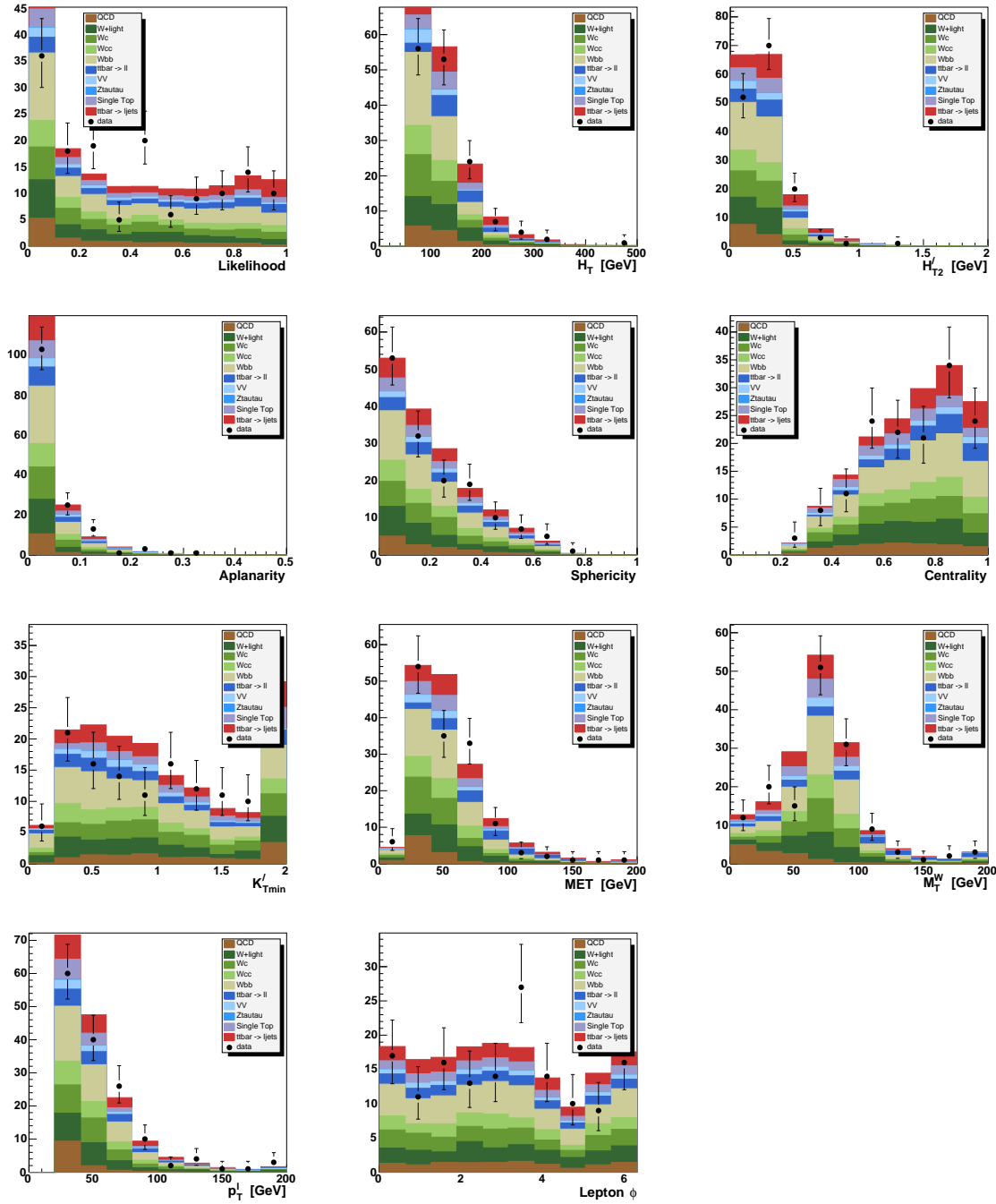
Variable	Definition
$H_T$	Scalar sum of transverse energies of the four leading jets.
Leading jet $p_T$	$p_T$ of the jet with highest $p_T$ .
Second jet $p_T$	$p_T$ of the jet with the next highest $p_T$ .
Third jet $p_T$	$p_T$ of the jet with the third highest $p_T$ .
Forth jet $p_T$	$p_T$ of the jet with the forth highest $p_T$ .
$M_T^W$	$W$ transverse mass.
$\cancel{E}_T$	Missing transverse energy.
$p_T^\ell$	$p_T$ of the lepton.
$\phi^\ell$	$\phi$ of the lepton.
$\ell$ track $p_T$	$p_T$ of the track matched to the lepton.
Aplanarity $\mathcal{A}$	$3/2\lambda_3$ .
Sphericity $\mathcal{S}$	$3/2(\lambda_2 + \lambda_3)$ .
Centrality $\mathcal{C}$	$H_T/H$ , the scalar sum of transverse energies divided by the scalar sum of energies of the four leading jets.
$H_T^{2'}$	$H_T^2/H_z$ , the scalar sum of transverse energies of the four leading jets, except the first one, divided by the scalar sum of the longitudinal energies of the four leading jets, the muon and an hypothesis for the neutrino.
$K_T^{min'}$	$\Delta R_{jj}^{min} E_T^4/E_T^W$ , product of minimum di-jet separation in $R$ and $E_T$ of the less energetic jet of that pair, divided by the scalar sum of the transverse energies of the muon and the $\cancel{E}_T$ .
$\Delta\phi(\ell, \cancel{E}_T)$	Azimuthal opening angle between the lepton and the $\cancel{E}_T$ .
Likelihood	Topological Likelihood discriminant.

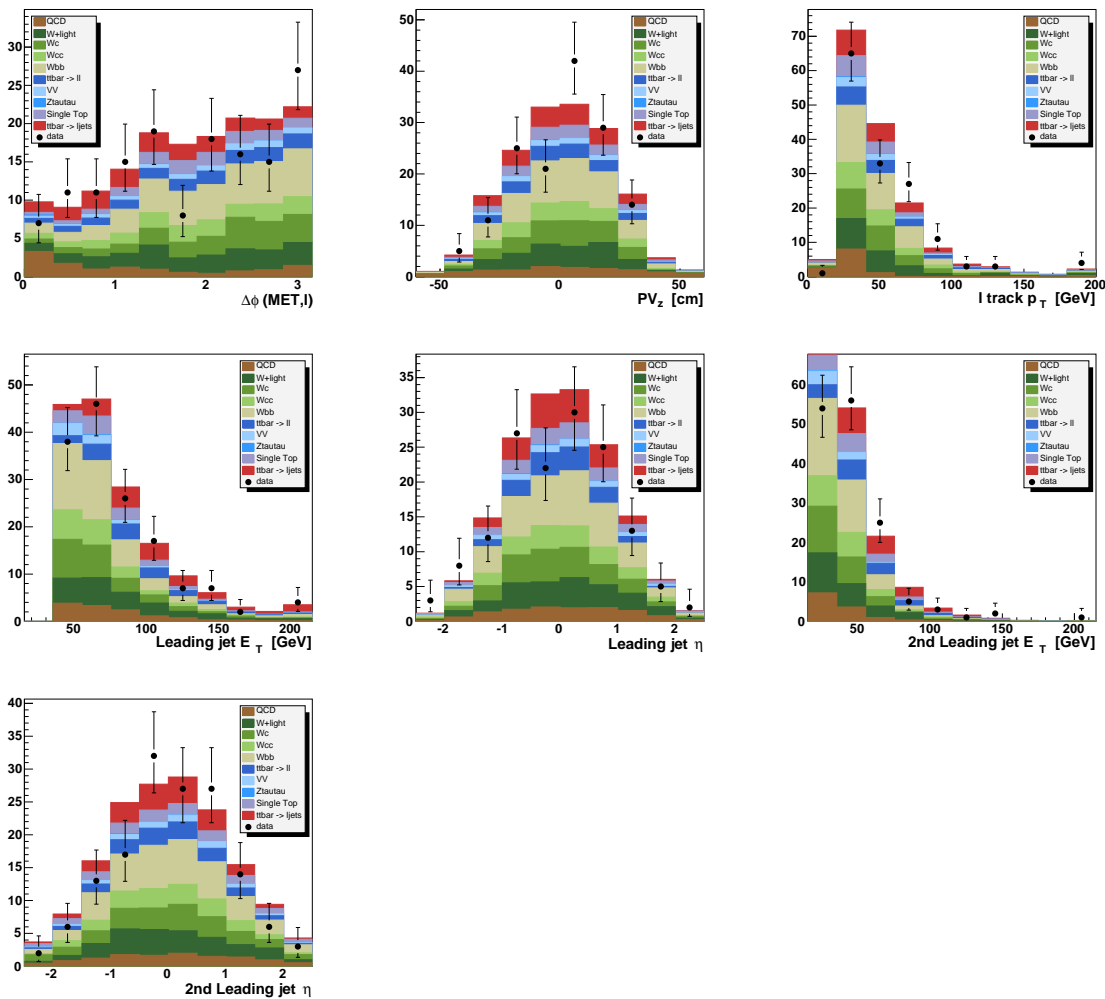
TABLE LV

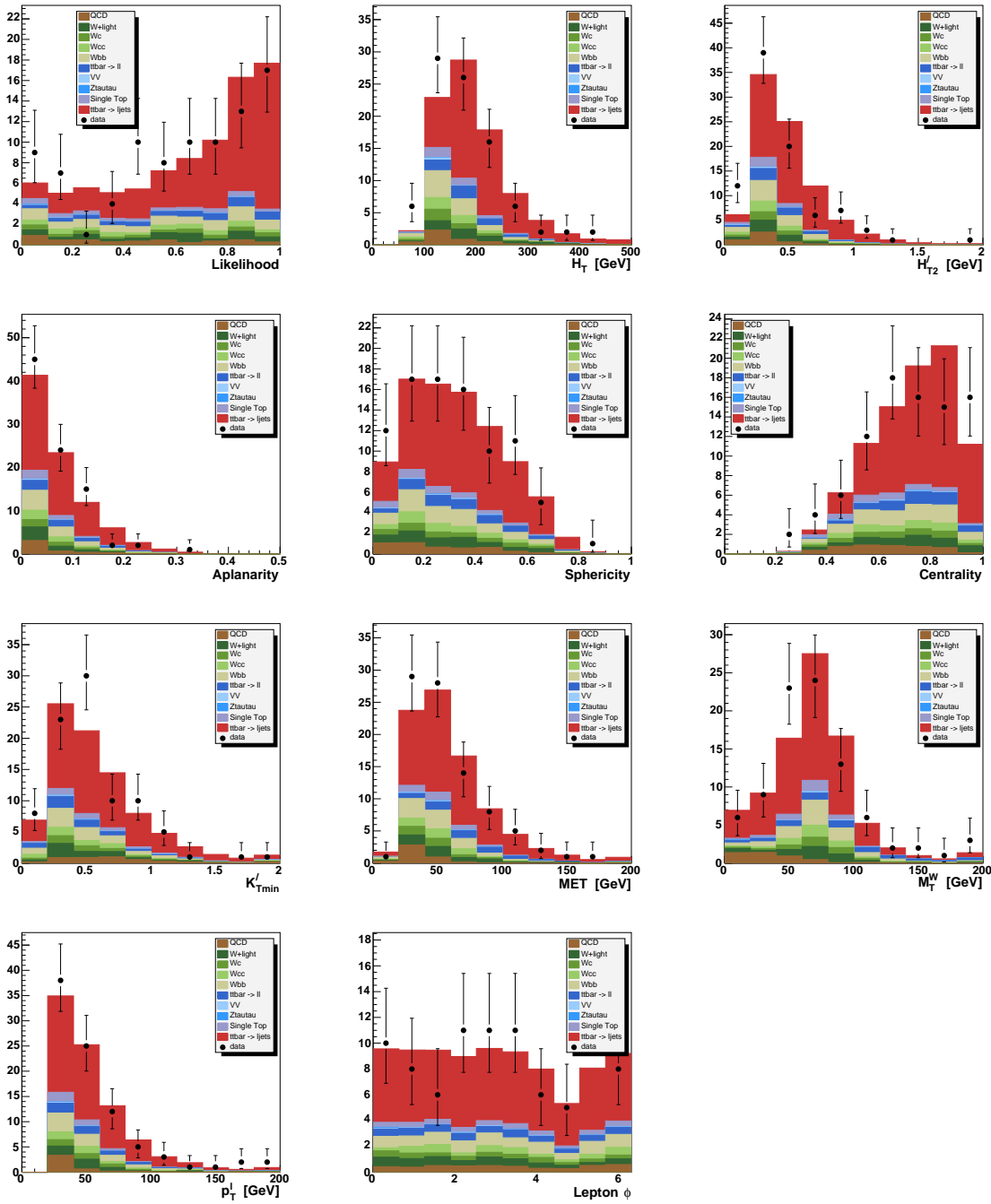
DEFINITION OF TOPOLOGICAL VARIABLES CONSIDERED. THE NORMALIZED MOMENTUM TENSOR IS DEFINED IN EQUATION D.1 AND THE THREE EIGENVALUES ARE ORDERED SUCH THAT  $\lambda_1 \geq \lambda_2 \geq \lambda_3$ , WITH  $\lambda_1 + \lambda_2 + \lambda_3 = 1$ . THE SETS OF VARIABLES CORRESPOND TO VARIABLES PROPORTIONAL TO THE ENERGY PRESENT IN THE EVENT, LEPTON KINEMATIC VARIABLES, EVENT SHAPE VARIABLES, RATIOS OF ENERGY DEPENDENT VARIABLES, ANGULAR VARIABLES AND A TOPOLOGICAL DISCRIMINANT.

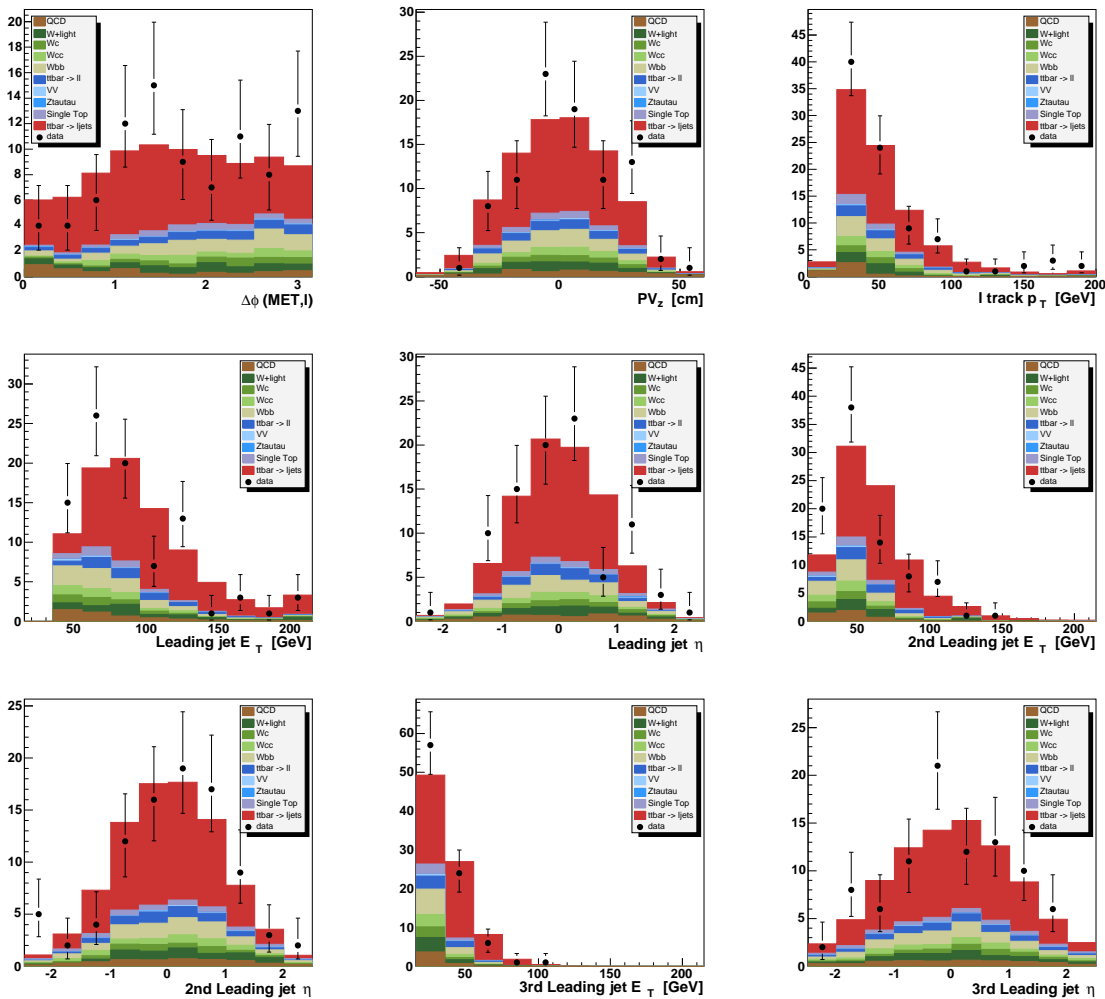
(111)

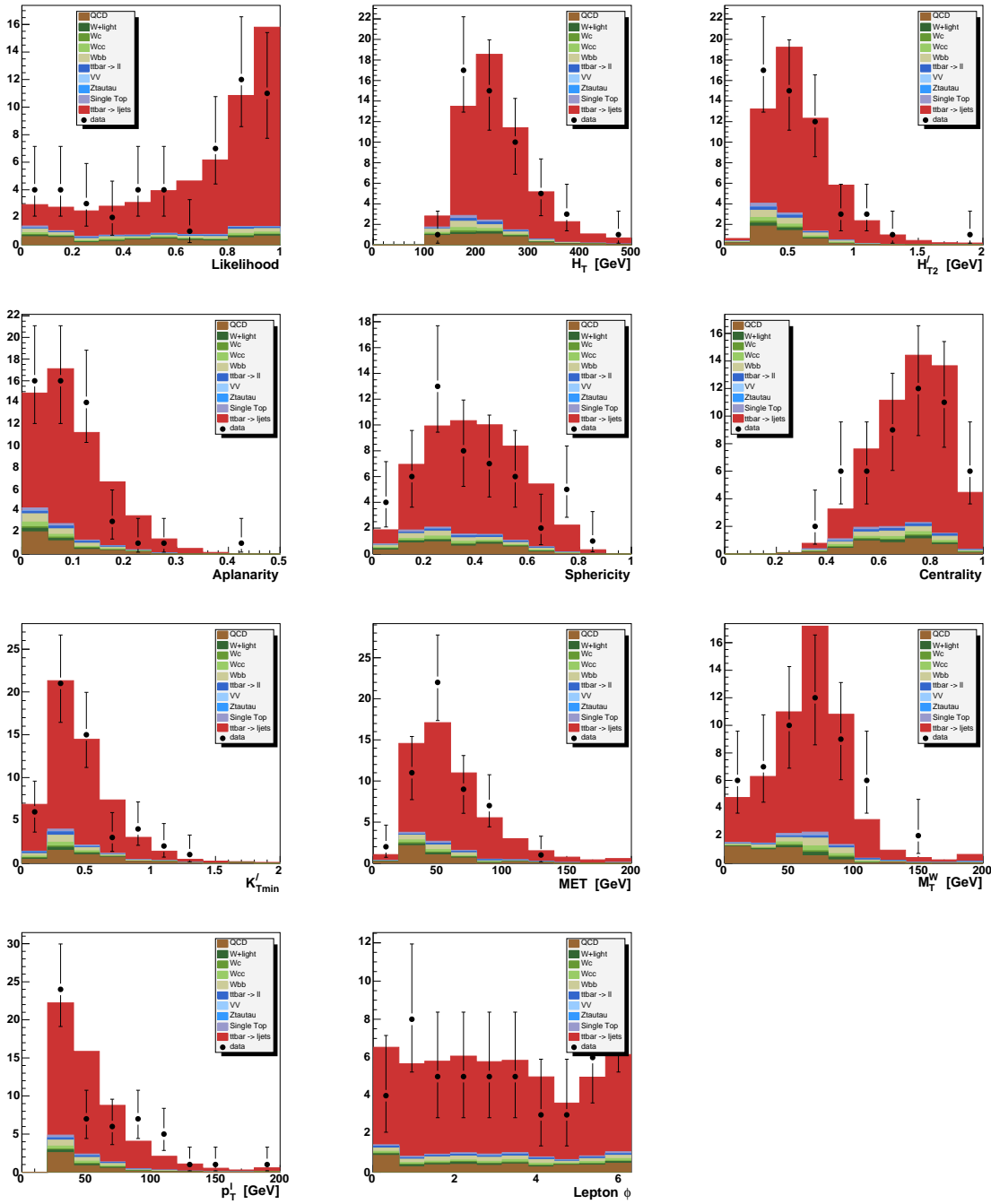
Figure 117. Sanity checks for single tagged events in the  $l+1$  jet bin.

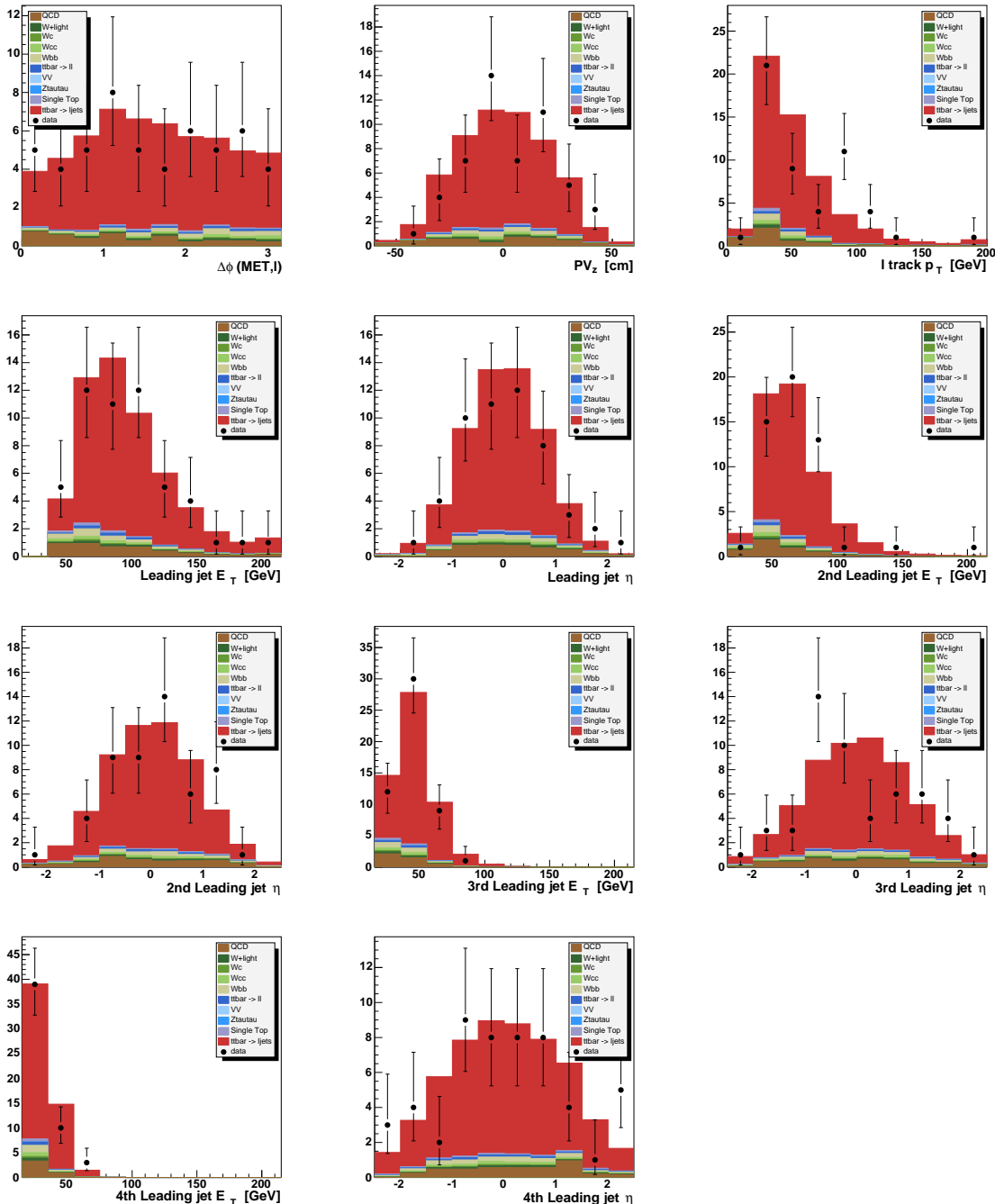
Figure 118. Sanity checks for single tagged events in the  $l+2$  jets bin.

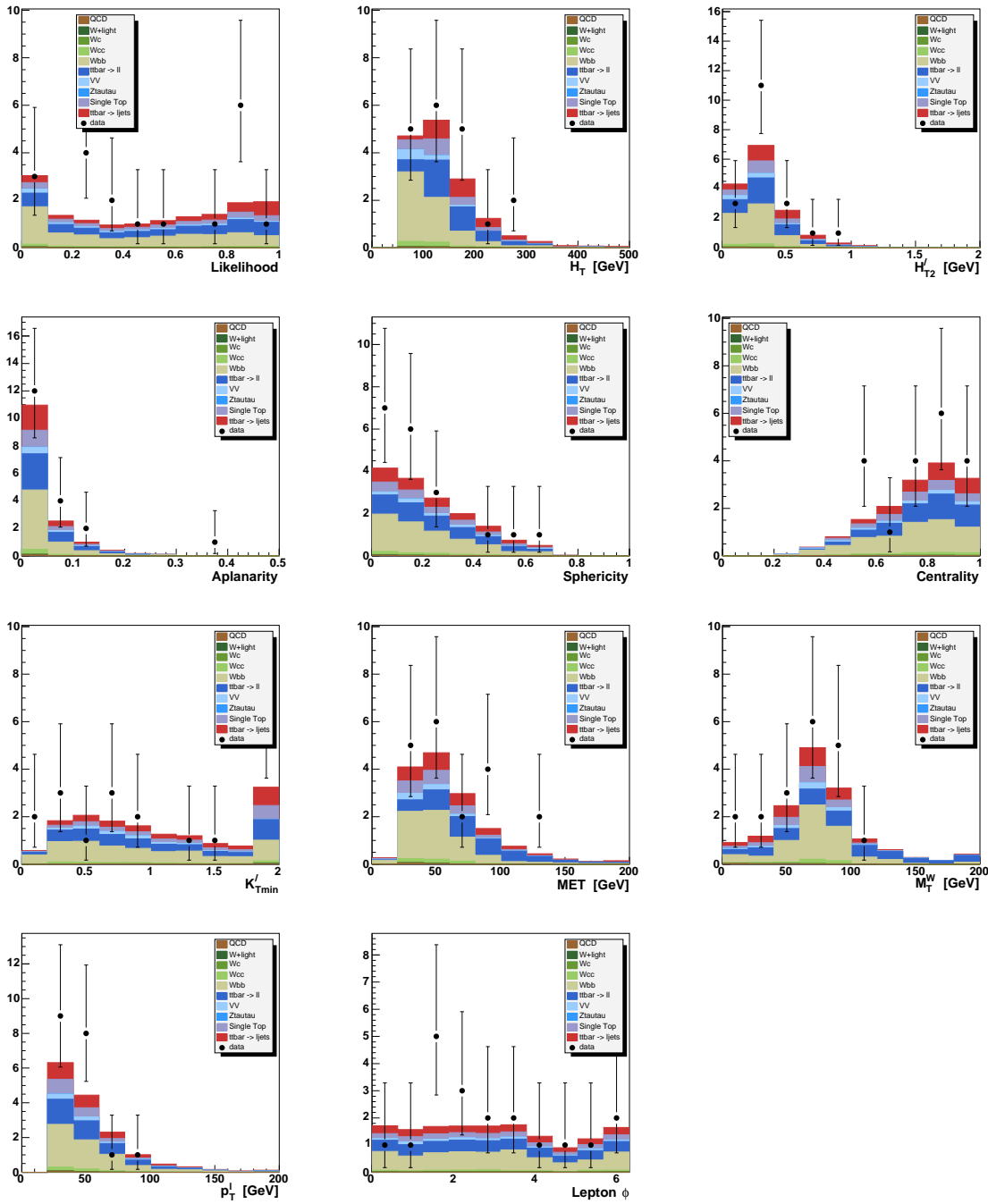
Figure 119. Sanity checks for single tagged events in the  $l+2$  jets bin.

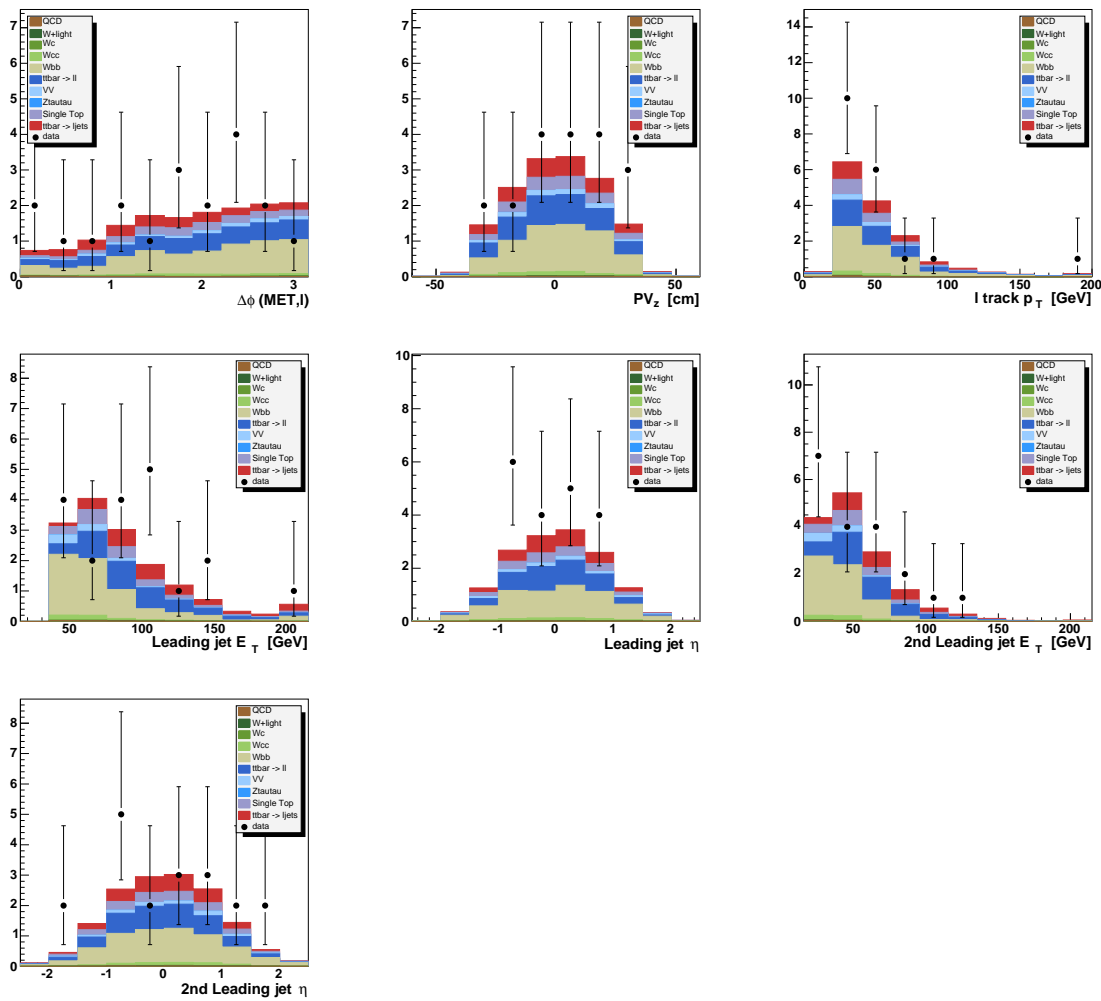
Figure 120. Sanity checks for single tagged events in the  $l+3$  jets bin.

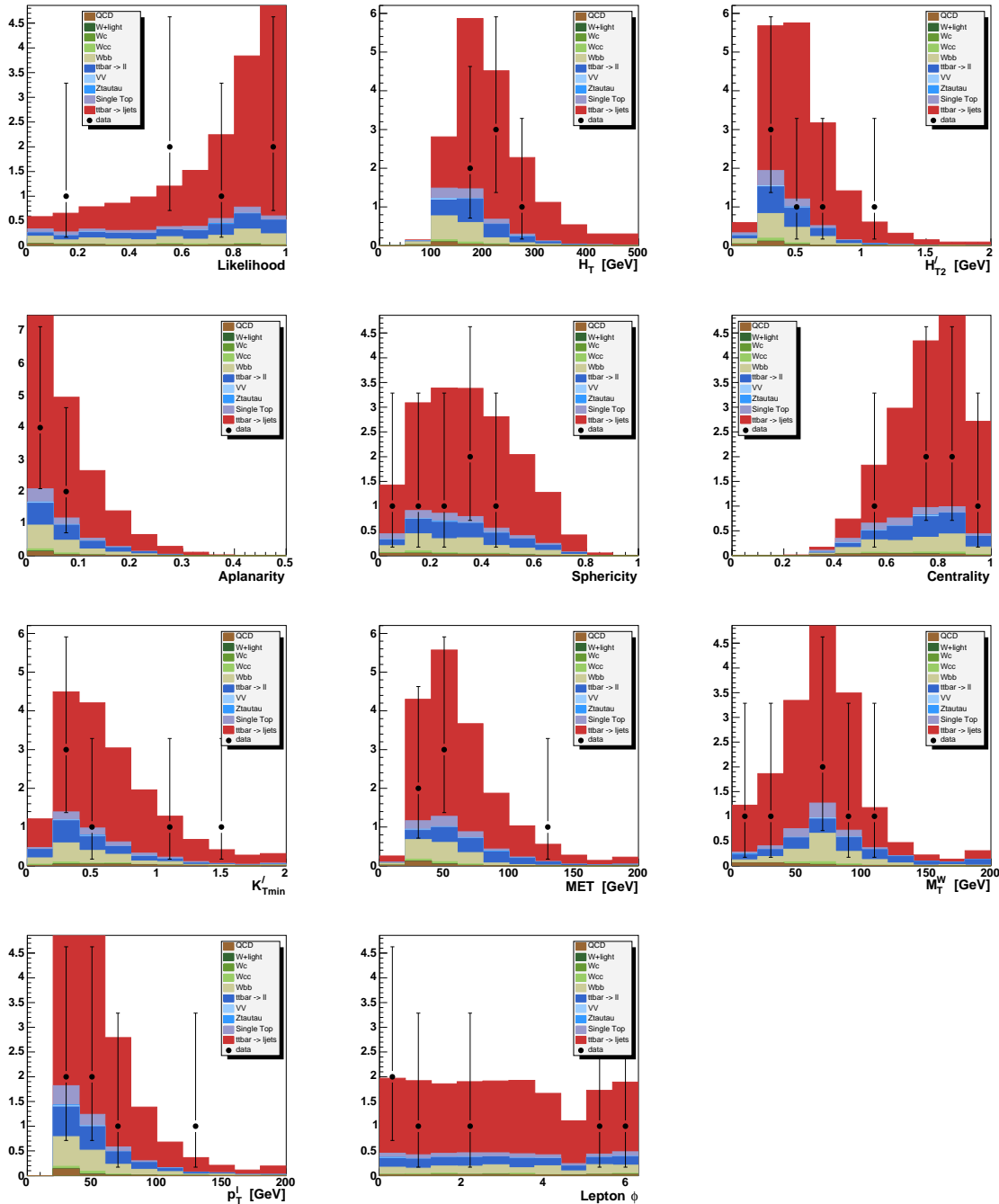
Figure 121. Sanity checks for single tagged events in the  $l+3$  jets bin.

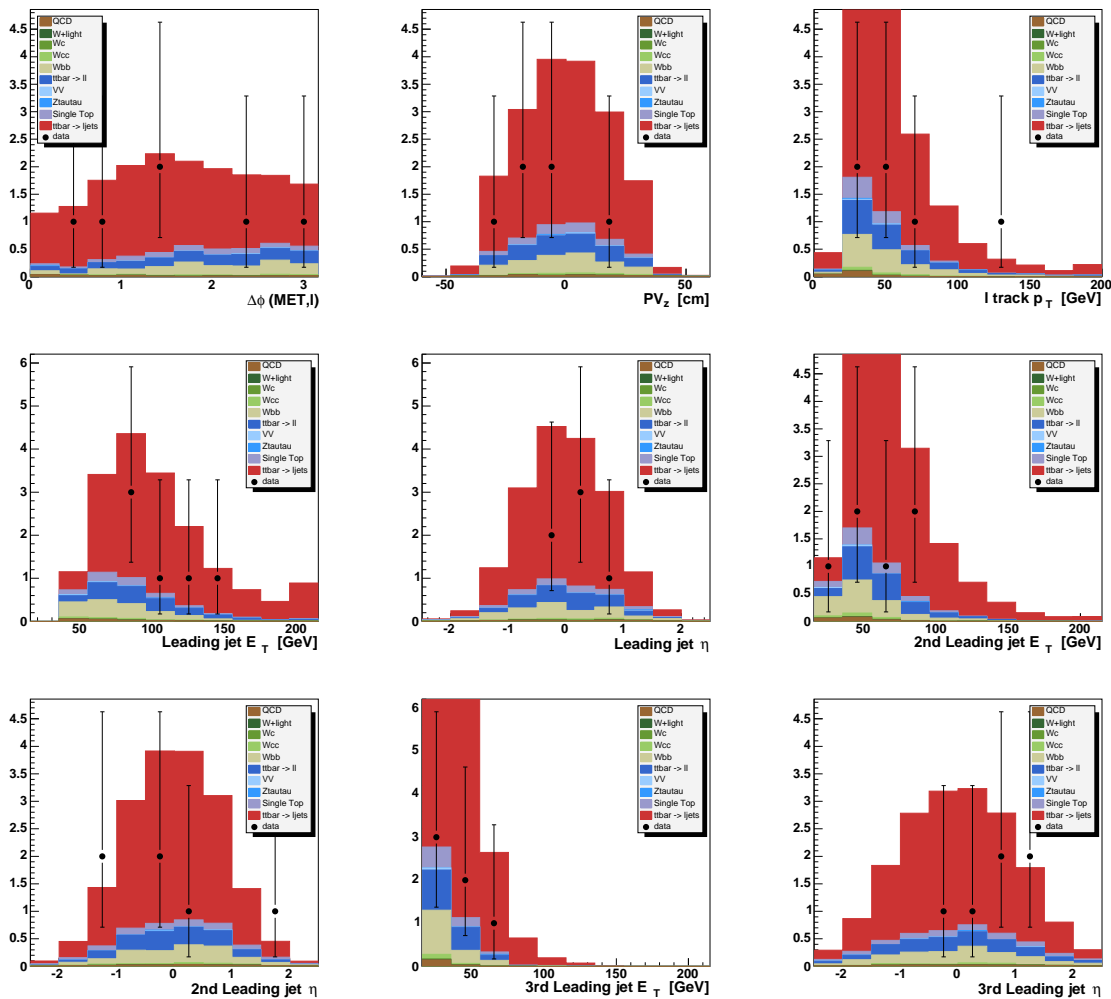
Figure 122. Sanity checks for single tagged events in the  $l+\geq 4$  jets bin.

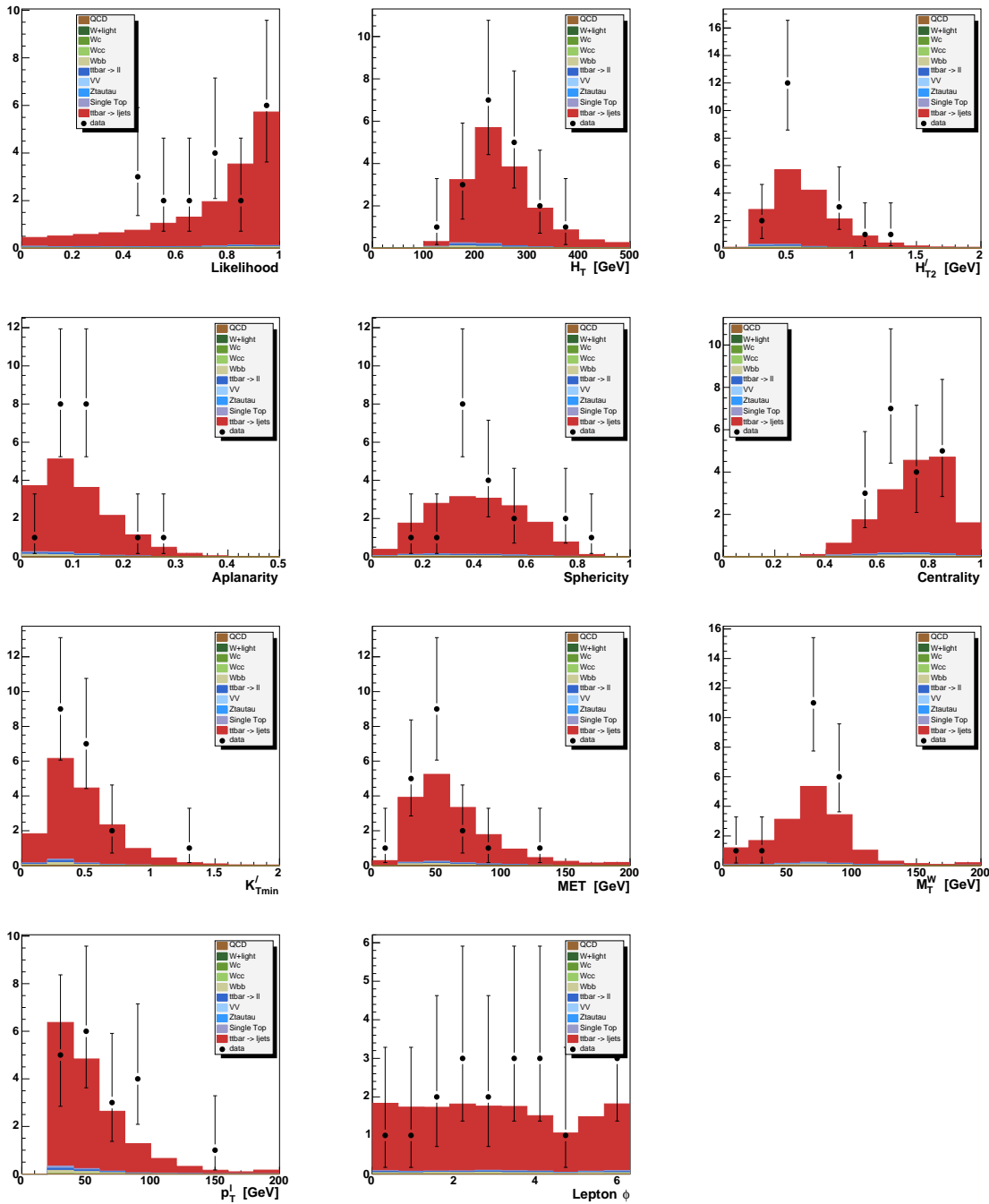
Figure 123. Sanity checks for single tagged events in the  $l+\geq 4$  jets bin.

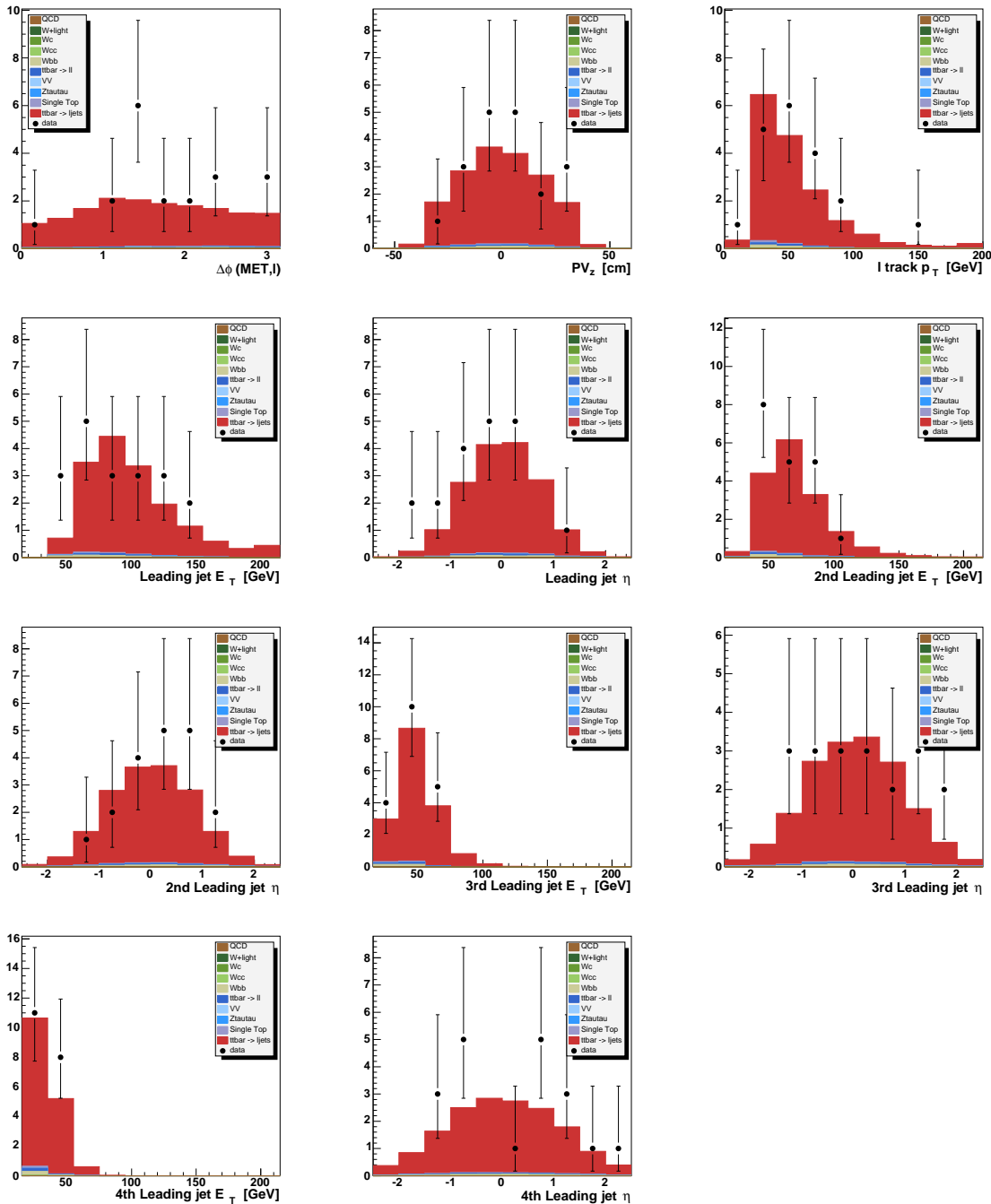
Figure 124. Sanity checks for double tagged events in the  $l+2$  jets bin.

Figure 125. Sanity checks for double tagged events in the  $l+2$  jets bin.

Figure 126. Sanity checks for double tagged events in the  $l+3$  jets bin.

Figure 127. Sanity checks for double tagged events in the  $l+3$  jets bin.

Figure 128. Sanity checks for double tagged events in the  $l+ \geq 4$  jets bin.

Figure 129. Sanity checks for double tagged events in the  $l+>4$  jets bin.

## Appendix B

### HANDLING OF THE MATRIX METHODS AND EVENT STATISTICS

The matrix method is applied three times in this analysis:

1. Before tagging (untagged sample) to derive the number of events with a real isolated lepton and the QCD contribution of fake isolated leptons. This matrix method is based on the observed numbers of loose and tight events in the untagged sample:  $N_{\text{loose}}^{\text{untagged}}$  and  $N_{\text{tight}}^{\text{untagged}}$  or in short  $N_{\text{loose}}$  and  $N_{\text{tight}}$ ,
2. In the sample made of events with exactly one tag. It is used to derive the number of “QCD” events (ie with fake isolated leptons) in the single tag sample and is based on the observed numbers of loose and tight events in the single tag samples:  $N_{\text{loose}}^{\text{1tag}}$  and  $N_{\text{tight}}^{\text{1tag}}$ ,
3. In the sample made of double tagged events, in order to derive the number of QCD events in the double tag sample. It is based on the observed number of loose and tight events in the double tag sample:  $N_{\text{loose}}^{\text{2tags}}$  and  $N_{\text{tight}}^{\text{2tags}}$ .

In the same way as the number of observed tagged events translates into the statistical error on the cross section, the number of observed events used for the matrix methods also contribute to the total error since they are subject to random fluctuations according to Poisson statistics.

Each number of events entering the matrix method is considered as a free parameter constrained to its observed value. We start by giving the equations of the matrix method in the case where it is applied only in the untagged sample. The equations are further refined later in this section

to include the matrix methods in the single and double tag samples. If  $\tilde{N}_{loose}$  and  $\tilde{N}_{tight}$  are the observed numbers of events in the loose and tight samples then the composition of the tight sample is given by

$$\begin{aligned} N_{W+t\bar{t}} &= \epsilon_{sig} \frac{\tilde{N}_{tight} - \epsilon_{QCD} \tilde{N}_{loose}}{\epsilon_{sig} - \epsilon_{QCD}}, \\ N_{QCD} &= \epsilon_{QCD} \frac{\epsilon_{sig} \tilde{N}_{loose} - \tilde{N}_{tight}}{\epsilon_{sig} - \epsilon_{QCD}}, \end{aligned} \quad (\text{B.1})$$

where  $N_{W+t\bar{t}}$  and  $N_{QCD}$  are the number of events with true and fake isolated leptons in the tight sample.  $\tilde{N}_{loose}$  and  $\tilde{N}_{tight}$  are the observed number of events in the loose and the tight samples. The tilde denotes observed numbers. The true values  $N_{loose}$  and  $N_{tight}$  are not known, what is known is their observed values. For this reason  $N_{loose}$  and  $N_{tight}$  are let floating in the cross section calculation but constrained to their measured values  $\tilde{N}_{tight}$  and  $\tilde{N}_{loose}$  using Poisson statistics.

It is now necessary to take into account the fact that  $\tilde{N}_{loose}$  and  $\tilde{N}_{tight}$  are not independent variables. To solve this problem the matrix method equations are expressed in terms of  $\tilde{N}_{loose-tight}$  and  $\tilde{N}_{tight}$  (number of events that are loose but not tight and number of tight events) instead of  $\tilde{N}_{loose}$  and  $\tilde{N}_{tight}$ . The equations for the matrix method in the untagged sample become

$$\begin{aligned} N_{W+t\bar{t}} &= \epsilon_{sig} \frac{N_{tight} - \epsilon_{QCD}(N_{tight} + N_{loose-tight})}{\epsilon_{sig} - \epsilon_{QCD}}, \\ N_{QCD} &= \epsilon_{QCD} \frac{\epsilon_{sig}(N_{tight} + N_{loose-tight}) - N_{tight}}{\epsilon_{sig} - \epsilon_{QCD}}. \end{aligned} \quad (\text{B.2})$$

The tilde on the number of loose and loose-tight events have been removed to indicate that the predictions on the number of true and fake isolated leptons are computed from the floating parameters  $N_{\text{tight}}$  and  $N_{\text{loose-tight}}$  at each step of the maximization procedure. In addition the floating parameters  $N_{\text{tight}}$  and  $N_{\text{loose-tight}}$  are constrained to the observed number of loose but non tight and the number of tight events by adding the following factor to the likelihood function

$$\mathcal{P}(\tilde{N}_{\text{tight}}; N_{\text{tight}}) \times \mathcal{P}(\tilde{N}_{\text{loose-tight}}; N_{\text{loose-tight}}),$$

which is simply the probability to observe  $\tilde{N}_{\text{tight}}$  and  $\tilde{N}_{\text{loose-tight}}$  given their true values  $N_{\text{tight}}$  and  $N_{\text{loose-tight}}$ .

So far only the matrix method in the untagged sample has been considered. It is necessary to take into account the matrix method in the single tag and double tag samples. The matrix method in the single and double tag samples is used only to predict the number of events with fake leptons. The number of events with fake leptons in the 1 and 2 tags samples ( $N_{QCD}^{1\text{tag}}$  and  $N_{QCD}^{2\text{tag}}$ ) are given by

$$\begin{aligned} N_{QCD}^{1\text{tag}} &= \epsilon_{QCD} \frac{\epsilon_{\text{sig}} \tilde{N}_{\text{loose}}^{1\text{tag}} - \tilde{N}_{\text{tight}}^{1\text{tag}}}{\epsilon_{\text{sig}} - \epsilon_{QCD}} \\ N_{QCD}^{2\text{tag}} &= \epsilon_{QCD} \frac{\epsilon_{\text{sig}} \tilde{N}_{\text{loose}}^{2\text{tag}} - \tilde{N}_{\text{tight}}^{2\text{tag}}}{\epsilon_{\text{sig}} - \epsilon_{QCD}}, \end{aligned} \quad (\text{B.3})$$

where  $\tilde{N}_{\text{loose}}^{1\text{tag}}$  and  $\tilde{N}_{\text{tight}}^{1\text{tag}}$  are the number of observed events with 1 tag in the loose and tight samples.  $\tilde{N}_{\text{loose}}^{2\text{tag}}$  and  $\tilde{N}_{\text{tight}}^{2\text{tag}}$  are the number of observed events with 2 tags in the loose and

tight samples. As it was done in the untagged sample we need to take into account correlations between the loose and tight samples. Therefore, Equation B.3 can be expressed in terms of the number of loose but non tight events in the 1 and 2 tag samples ( $N_{\text{loose-tight}}^{\text{1tag}}$  and  $N_{\text{loose-tight}}^{\text{2tag}}$ ):

$$\begin{aligned} N_{QCD}^{\text{1tag}} &= \epsilon_{QCD} \frac{\epsilon_{\text{sig}}(N_{\text{loose-tight}}^{\text{1tag}} + N_{\text{tight}}^{\text{1tag}}) - N_{\text{tight}}^{\text{1tag}}}{\epsilon_{\text{sig}} - \epsilon_{QCD}} \\ N_{QCD}^{\text{2tag}} &= \epsilon_{QCD} \frac{\epsilon_{\text{sig}}(N_{\text{loose-tight}}^{\text{2tag}} + N_{\text{tight}}^{\text{2tag}}) - N_{\text{tight}}^{\text{2tag}}}{\epsilon_{\text{sig}} - \epsilon_{QCD}}. \end{aligned} \quad (\text{B.4})$$

Again the tildes are dropped to indicate that the floating parameters  $N_{\text{loose-tight}}^{\text{1tag}}$ ,  $N_{\text{loose-tight}}^{\text{2tag}}$ ,  $N_{\text{tight}}^{\text{1tag}}$  and  $N_{\text{tight}}^{\text{2tag}}$  are used instead of the number of observed events. These floating parameters need to be constrained to their observed values by including additional Poisson factors into the likelihood.

Before expressing these factors one should observe that the number of tight events with 1 tag is just the number of single tag events used to constrain the cross section, i.e. one of the  $N_{\gamma}^{\text{obs}}$  in Equation 7.22. Similarly the number of tight events with 2 tags is simply the number of double tag events used in the analysis to constrain the cross section, again one of the  $N_{\gamma}^{\text{obs}}$  in Equation 7.22. Therefore  $N_{\text{tight}}^{\text{1tag}}$  and  $N_{\text{tight}}^{\text{2tag}}$  are already constrained to their observed values. Only additional constraints for the number of events in the loose-tight sample with 1 and 2 tags need to be introduced:

$$\mathcal{P}(\tilde{N}_{\text{loose-tight}}^{\text{1tag}}; N_{\text{loose-tight}}^{\text{1tag}}) \times \mathcal{P}(\tilde{N}_{\text{loose-tight}}^{\text{2tag}}; N_{\text{loose-tight}}^{\text{2tag}})$$

which simply expresses the probability to observe  $\tilde{N}_{\text{loose-tight}}^{1\text{tag}}$  from a Poisson distribution with parameter  $N_{\text{loose-tight}}^{1\text{tag}}$  and  $\tilde{N}_{\text{loose-tight}}^{2\text{tag}}$  from a Poisson distribution with parameter  $N_{\text{loose-tight}}^{2\text{tag}}$ . The parameters  $N_{\text{loose-tight}}^{1\text{tag}}$  and  $N_{\text{loose-tight}}^{2\text{tag}}$  are left floating in the maximization.

Equation B.3 constrains the number of loose-tight events while Equation B.5 constrains the number of loose-tight events with 1 and 2 tags. The loose-tight samples with one and two tags are subsets of the loose-tight sample. This correlation needs to be taken into account too in Equation B.3. This is solved by splitting the loose-tight sample into events with 0, 1 and 2 tags. For this purpose, the number of observed events with 0 tags in the loose-tight sample,  $\tilde{N}_{\text{loose-tight}}^{0\text{tag}}$ , is introduced.

Another correlation that needs to be taken into account arises from the fact that the events in the tight sample (Equation B.2) contain events with one and two tags that are used to extract the cross section and which are already constrained in Equation 7.22. For this reason the observed number of tight events in the 0 tag sample,  $\tilde{N}_{\text{tight}}^{0\text{tag}}$ , is introduced.

$N_{\text{tight}}^{0\text{tag}}$  and  $N_{\text{loose-tight}}^{0\text{tag}}$  are two free parameters that are constrained to their observed values with Poisson probabilities

$$\mathcal{P}(\tilde{N}_{\text{loose-tight}}^{0\text{tag}}; N_{\text{loose-tight}}^{0\text{tag}}) \times \mathcal{P}(\tilde{N}_{\text{tight}}^{0\text{tag}}; N_{\text{tight}}^{0\text{tag}}).$$

Equation B.5 replaces the constraint of Equation B.3.  $N_{W+t\bar{t}}$  and  $N_{QCD}$  are predicted numbers of true and fake isolated leptons. The number of predicted single and double tag events can be expressed by

$$\begin{aligned} N_{tight}^{1tag} &= P_{t\bar{t}}^{1tag} N_{t\bar{t}} + N_{QCD}^{1tag} + P_W^{1tag} N_W + P_{MC \ bkg}^{1tag} N_{MC \ bkg}, \\ N_{tight}^{2tag} &= P_{t\bar{t}}^{2tag} N_{t\bar{t}} + N_{QCD}^{2tag} + P_W^{2tag} N_W + P_{MC \ bkg}^{2tag} N_{MC \ bkg}. \end{aligned} \quad (\text{B.5})$$

These equations simply express that the number of single tag events is equal to the sum of the number of single tag events from  $t\bar{t}$ , QCD multijet,  $W+jets$  and other backgrounds with real leptons (diboson, single top and  $Z \rightarrow \tau\tau$  referred to as “MC backgrounds” since their normalization before tagging is obtained from Monte Carlo). The same applies to the double tagged sample.

The matrix method in the untagged sample provides the number of events with real leptons

$$N_W = N_{W+t\bar{t}} - N_{t\bar{t}} - N_{MC \ bkg}. \quad (\text{B.6})$$

If this is inserted into Equation B.5, then

$$\begin{aligned} N_{tight}^{1tag} &= P_{t\bar{t}}^{1tag} N_{t\bar{t}} + N_{QCD}^{1tag} + P_W^{1tag} N_{W+t\bar{t}} - P_W^{1tag} N_{MC \ bkg} \\ &\quad - P_W^{1tag} N_{t\bar{t}} + P_{MC \ bkg}^{1tag} N_{MC \ bkg}, \\ N_{tight}^{2tag} &= P_{t\bar{t}}^{2tag} N_{t\bar{t}} + N_{QCD}^{2tag} + P_W^{2tag} N_{W+t\bar{t}} - P_W^{2tag} N_{MC \ bkg} \\ &\quad - P_W^{2tag} N_{t\bar{t}} + P_{MC \ bkg}^{2tag} N_{MC \ bkg}. \end{aligned} \quad (\text{B.7})$$

Now  $N_{tight}^{1tag}$  and  $N_{tight}^{2tag}$  are present on both sides of these equations since they also enter into the expressions of  $N_{W+t\bar{t}}$  and  $N_{QCD}$ . Equation B.7 makes up a system of 2 equations with 2 unknowns namely  $N_{tight}^{1tag}$  and  $N_{tight}^{2tag}$ . Writting  $N_{W+t\bar{t}}$ ,  $N_{QCD}^{1tag}$  and  $N_{QCD}^{2tag}$  explicitly as functions of  $N_{tight}^{0tag}$ ,  $N_{tight}^{1tag}$ ,  $N_{tight}^{2tag}$ ,  $N_{loose-tight}^{0tag}$ ,  $N_{loose-tight}^{1tag}$ ,  $N_{loose-tight}^{2tag}$ :

$$\begin{aligned} N_{tight}^{1tag} &= k_1 + a_1 N_{tight}^{0tag} + b_1 N_{tight}^{1tag} + c_1 N_{tight}^{2tag} + d_1 N_{loose-tight}^{0tag} \\ &\quad + e_1 N_{loose-tight}^{1tag} + f_1 N_{loose-tight}^{2tag}, \\ N_{tight}^{2tag} &= k_2 + a_2 N_{tight}^{0tag} + b_2 N_{tight}^{1tag} + c_2 N_{tight}^{2tag} + d_2 N_{loose-tight}^{0tag} \\ &\quad + e_2 N_{loose-tight}^{1tag} + f_2 N_{loose-tight}^{2tag}. \end{aligned} \quad (\text{B.8})$$

where  $k_1$  and  $k_2$  are defined by:

$$\begin{aligned} k_1 &= P_{t\bar{t}}^{1tag} N_{t\bar{t}} - P_W^{1tag} N_{MC\ bkg} - P_W^{1tag} N_{t\bar{t}} + P_{MC\ bkg}^{1tag} N_{MC\ bkg}, \\ k_2 &= P_{t\bar{t}}^{2tag} N_{t\bar{t}} - P_W^{2tag} N_{MC\ bkg} - P_W^{2tag} N_{t\bar{t}} + P_{MC\ bkg}^{2tag} N_{MC\ bkg}, \end{aligned} \quad (\text{B.9})$$

and  $a_1, b_1, c_1, d_1, e_1, f_1$  are given by

$$a_1 = \frac{P_W^{1tag} \epsilon_{sig} (1 - \epsilon_{QCD})}{\epsilon_{sig} - \epsilon_{QCD}} \quad (\text{B.10})$$

$$b_1 = \frac{\epsilon_{sig} \epsilon_{QCD} - \epsilon_{QCD} + P_W^{1tag} \epsilon_{sig} - P_W^{1tag} \epsilon_{sig} \epsilon_{QCD}}{\epsilon_{sig} - \epsilon_{QCD}} \quad (\text{B.11})$$

$$c_1 = a_1 \quad (\text{B.12})$$

$$d_1 = \frac{-P_W^{1tag} \epsilon_{sig} \epsilon_{QCD}}{\epsilon_{sig} - \epsilon_{QCD}} \quad (\text{B.13})$$

$$e_1 = \frac{\epsilon_{sig}\epsilon_{QCD} - P_W^{1tag}\epsilon_{sig}\epsilon_{QCD}}{\epsilon_{sig} - \epsilon_{QCD}} \quad (B.14)$$

$$f_1 = d_1$$

while  $a_2, b_2, c_2, d_2, e_2, f_2$  are given by:

$$a_2 = \frac{P_W^{2tag}\epsilon_{sig}(1 - \epsilon_{QCD})}{\epsilon_{sig} - \epsilon_{QCD}} \quad (B.15)$$

$$b_2 = a_2 \quad (B.16)$$

$$c_2 = \frac{\epsilon_{sig}\epsilon_{QCD} - \epsilon_{QCD} + P_W^{2tag}\epsilon_{sig} - P_W^{2tag}\epsilon_{sig}\epsilon_{QCD}}{\epsilon_{sig} - \epsilon_{QCD}} \quad (B.17)$$

$$d_2 = \frac{-P_W^{2tag}\epsilon_{sig}\epsilon_{QCD}}{\epsilon_{sig} - \epsilon_{QCD}} \quad (B.18)$$

$$e_2 = d_2 \quad (B.19)$$

$$f_2 = \frac{\epsilon_{sig}\epsilon_{QCD} - P_W^{2tag}\epsilon_{sig}\epsilon_{QCD}}{\epsilon_{sig} - \epsilon_{QCD}}$$

This system is solved in order to express  $N_{tight}^{1tag}$  and  $N_{tight}^{2tag}$  as a functions of the tagging probabilities, efficiencies for the matrix method, prediction for the processes such as single top, diboson,  $Z \rightarrow \tau\tau$  and the floating parameters  $N_{tight}^{0tag}$ ,  $N_{loose-tight}^{0tag}$ ,  $N_{loose-tight}^{1tag}$  and  $N_{loose-tight}^{2tag}$ . The final expressions for the predicted number of events in the single and double tagged samples are:

$$\begin{aligned} N_{tight}^{1tag} &= \frac{1}{(c_2 - 1)(b_1 - 1) - c_1 b_2} \times \\ &\quad ( - k_2 c_1 - k_1 c_2 + k_1 \\ &\quad + N_{tight}^{0tag} (c_1 a_2 - (c_2 - 1) a_1) \end{aligned} \quad (B.20)$$

$$\begin{aligned}
 & + N_{\text{loose-tight}}^{\text{0tag}}(c_1 d_2 - (c_2 - 1) d_1) \\
 & + N_{\text{loose-tight}}^{\text{1tag}}(c_1 e_2 - (c_2 - 1) e_1) \\
 & + N_{\text{loose-tight}}^{\text{2tag}}(c_1 f_2 - (c_2 - 1) f_1)) \\
 N_{\text{tight}}^{\text{2tag}} & = \frac{1}{(c_2 - 1)(b_1 - 1) - c_1 b_2} \times \\
 & (k_1 b_2 - k_2 b_1 + k_2 \\
 & + N_{\text{tight}}^{\text{0tag}}(b_2 a_1 - (b_1 - 1) a_2) \\
 & + N_{\text{loose-tight}}^{\text{0tag}}(b_2 d_1 - (b_1 - 1) d_2) \\
 & + N_{\text{loose-tight}}^{\text{1tag}}(b_2 e_1 - (b_1 - 1) e_2) \\
 & + N_{\text{loose-tight}}^{\text{2tag}}(b_2 f_1 - (b_1 - 1) f_2))
 \end{aligned} \tag{B.21}$$

To summarize, the parameters  $N_{\text{tight}}^{\text{0tag}}$ ,  $N_{\text{loose-tight}}^{\text{0tag}}$ ,  $N_{\text{loose-tight}}^{\text{1tag}}$  and  $N_{\text{loose-tight}}^{\text{2tag}}$  are floating during the optimization. They are all constrained to their observed values using the Poisson constraints given in Equation B.5 and Equation B.5.

The predicted numbers of events with one and two tags  $N_{\text{tight}}^{\text{1tag}}$  and  $N_{\text{tight}}^{\text{2tag}}$  are computed from the floating parameters above and tagging probabilities and efficiencies for the matrix method using the Equation B.7 and Equation B.8.  $N_{\text{tight}}^{\text{1tag}}$  and  $N_{\text{tight}}^{\text{2tag}}$  are constrained to their observed values using Poisson statistics by:

$$\mathcal{P}(\tilde{N}_{\text{tight}}^{\text{1tag}}; N_{\text{tight}}^{\text{1tag}}) \times \mathcal{P}(\tilde{N}_{\text{tight}}^{\text{2tag}}; N_{\text{tight}}^{\text{2tag}})$$

Finally this procedure is applied in the electron + 3 jets, electron + 4 jets, muon + 3 jets and muon + 4 jets channels, giving the following product of Poisson constrains:

$$\begin{aligned}\mathcal{L}_1 = & \prod_i \mathcal{P}(\tilde{N}_{\text{tight}}^{0\text{tag}}; N_{\text{tight}}^{0\text{tag}}) \times \mathcal{P}(\tilde{N}_{\text{tight}}^{1\text{tag}}; N_{\text{tight}}^{1\text{tag}}) \times \mathcal{P}(\tilde{N}_{\text{tight}}^{2\text{tag}}; N_{\text{tight}}^{2\text{tag}}) \\ & \times \mathcal{P}(\tilde{N}_{\text{loose-tight}}^{0\text{tag}}; N_{\text{loose-tight}}^{0\text{tag}}) \times \mathcal{P}(\tilde{N}_{\text{loose-tight}}^{1\text{tag}}; N_{\text{loose-tight}}^{1\text{tag}}) \times \mathcal{P}(\tilde{N}_{\text{loose-tight}}^{2\text{tag}}; N_{\text{loose-tight}}^{2\text{tag}})\end{aligned}\quad (\text{B.22})$$

$\mathcal{L}_1$  summarizes all Poisson constrains used in the cross section calculations to take into account the number of observed events in the tight and loose-tight samples for events with 0, 1, 2 tags. In Equation B.22 the index  $i$  in the product runs over the electron + 3 jets, electron + 4 jets, muon + 3 jets and muon + 4 jets channels.

## Appendix C

### UNCERTAINTIES ON PRESELECTION EFFICIENCIES

	$e+\text{jets}$	$\mu+\text{jets}$
primary vertex	$\pm 1.8$	$\pm 2.8$
$\Delta z(l, PV)$	$\pm 0.4$	$\pm 0.02$
EM reconstruction $\times$ EM ID	$\pm 2.7$	
EM tracking	$\pm 0.7$	
EM likelihood	$\pm 1.6$	
muon ID		$\pm 4$
muon tracking		$\pm 3$
muon isolation		$\pm 0.7$
muon $\sigma_{dca}$		$\pm 0.2$
muon track $\chi^2$		$\pm 0.3$

TABLE LVI

RELATIVE SYSTEMATIC UNCERTAINTIES ON THE SELECTION EFFICIENCY (%)  
COMMON TO ALL PROCESSES.

	$e+\text{jets}$		$\mu+\text{jets}$	
	$N_{jet}=3$	$N_{jet} \geq 4$	$N_{jet}=3$	$N_{jet} \geq 4$
EM trigger (L1)			+0.19-1.26	+0.17-1.10
EM trigger (L3)			$\pm 0.60$	$\pm 0.60$
muon trigger (L1)	$\pm 0.93$	$\pm 0.92$		
muon trigger (L2)	$< 0.01$	$< 0.01$		
jet trigger (L1)	$< 0.01$	$< 0.01$	$\pm 0.03$	$\pm 0.03$
jet trigger (L2)	$< 0.01$	$< 0.01$	$< 0.01$	$< 0.01$
jet trigger (L3)	$\pm 0.07$	$\pm 0.03$	$\pm 0.02$	$< 0.01$
jet energy scale	-2.25+2.06	+8.79-8.97	-0.98+0.22	+9.36-9.29
jet energy resolution	+0.67+0.19	+1.04-0.73	-0.33+0.89	+1.48-0.98
jet ID	-0.24+2.52	+6.72-8.48	-0.32+1.01	+6.36-9.29
MC statistics	$\pm 0.91$	$\pm 0.95$	$\pm 0.89$	$\pm 1.00$

TABLE LVII

RELATIVE SYSTEMATIC UNCERTAINTIES ON THE  $t\bar{t} \rightarrow \text{LEPTON}+\text{JETS}$  SELECTION EFFICIENCY (%).

	$e+\text{jets}$		$\mu+\text{jets}$	
	$N_{jet}=3$	$N_{jet} \geq 4$	$N_{jet}=3$	$N_{jet} \geq 4$
EM trigger (L1)			+0.24-1.63	+0.22-1.55
EM trigger (L3)			$\pm 0.59$	$\pm 0.61$
muon trigger (L1)	$\pm 0.91$	$\pm 0.98$		
muon trigger (L2)	$< 0.01$	$< 0.01$		
jet trigger (L1)	$< 0.01$	$< 0.01$	$\pm 0.03$	$\pm 0.03$
jet trigger (L2)	$< 0.01$	$< 0.01$	$< 0.01$	$< 0.01$
jet trigger (L3)	$\pm 0.14$	$\pm 0.11$	$\pm 0.05$	$\pm 0.03$
jet energy scale	+8.43-6.64	+20.20-18.15	+9.12-8.83	+18.57-16.35
jet energy resolution	$< 0.01$	$< 0.01$	$< 0.01$	$< 0.01$
jet ID	+4.04-6.37	+17.09-8.16	+5.21-7.08	+13.27-12.61
MC statistics	$\pm 1.73$	$\pm 4.49$	$\pm 1.70$	$\pm 4.36$

TABLE LVIII

RELATIVE SYSTEMATIC UNCERTAINTIES ON THE  $t\bar{t} \rightarrow \text{DILEPTON}$  SELECTION EFFICIENCY (%).

	$e+\text{jets}$		$\mu+\text{jets}$	
	$N_{\text{jet}}=3$	$N_{\text{jet}} \geq 4$	$N_{\text{jet}}=3$	$N_{\text{jet}} \geq 4$
EM trigger (L1)			+0.33-2.73	+0.27-1.78
EM trigger (L3)			$\pm 0.71$	$\pm 0.58$
muon trigger (L1)	$\pm 0.89$	$\pm 0.93$		
muon trigger (L2)	$< 0.01$	$< 0.01$		
jet trigger (L1)	$< 0.01$	$< 0.01$	$\pm 0.03$	$\pm 0.03$
jet trigger (L2)	$< 0.01$	$< 0.01$	$< 0.01$	$< 0.01$
jet trigger (L3)	$\pm 0.22$	$\pm 0.20$	$\pm 0.07$	$\pm 0.03$
jet energy scale	+15.10-12.87	+29.20-33.74	+18.03-16.26	+29.60-27.25
jet energy resolution	$< 0.01$	$< 0.01$	$< 0.01$	$< 0.01$
jet ID	+6.86-7.40	+18.09-22.44	+7.81-12.71	-1.27-21.48
MC statistics	$\pm 3.32$	$\pm 10.06$	$\pm 3.28$	$\pm 10.90$

TABLE LIX

RELATIVE SYSTEMATIC UNCERTAINTIES ON THE SINGLE TOP S-CHANNEL  
SELECTION EFFICIENCY (%).

	$e+\text{jets}$		$\mu+\text{jets}$	
	$N_{\text{jet}}=3$	$N_{\text{jet}} \geq 4$	$N_{\text{jet}}=3$	$N_{\text{jet}} \geq 4$
EM trigger (L1)			+0.35-2.91	+0.30-2.25
EM trigger (L3)			$\pm 0.73$	$\pm 0.68$
muon trigger (L1)	$\pm 0.92$	$\pm 0.92$		
muon trigger (L2)	$< 0.01$	$< 0.01$		
jet trigger (L1)	$< 0.01$	$< 0.01$	$\pm 0.04$	$\pm 0.03$
jet trigger (L2)	$< 0.01$	$< 0.01$	$< 0.01$	$< 0.01$
jet trigger (L3)	$\pm 0.19$	$\pm 0.13$	$\pm 0.06$	$\pm 0.02$
jet energy scale	+8.87-10.17	+23.78-14.36	+10.12-9.42	+20.17-18.56
jet energy resolution	$< 0.01$	$< 0.01$	$< 0.01$	$< 0.01$
jet ID	+3.05-10.43	-0.04-14.51	+4.41-8.61	+8.67-17.87
MC statistics	$\pm 2.51$	$\pm 5.71$	$\pm 2.50$	$\pm 5.63$

TABLE LX

RELATIVE SYSTEMATIC UNCERTAINTIES ON THE SINGLE TOP T-CHANNEL  
SELECTION EFFICIENCY (%).

	$e+\text{jets}$		$\mu+\text{jets}$	
	$N_{\text{jet}}=3$	$N_{\text{jet}} \geq 4$	$N_{\text{jet}}=3$	$N_{\text{jet}} \geq 4$
EM trigger (L1)			+0.53-4.34	< 0.01
EM trigger (L3)			$\pm 0.68$	< 0.01
muon trigger (L1)	$\pm 0.98$	$\pm 0.82$		
muon trigger (L2)	$< 0.01$	$< 0.01$		
jet trigger (L1)	$\pm 0.01$	$< 0.01$	$\pm 0.03$	< 0.01
jet trigger (L2)	$< 0.01$	$< 0.01$	$< 0.01$	< 0.01
jet trigger (L3)	+0.39-0.41	+0.76-0.79	$\pm 0.15$	< 0.01
jet energy scale	+28.14-32.21	+192.63+0.00	+23.19-15.73	< 0.01
jet energy resolution	$< 0.01$	$< 0.01$	$< 0.01$	< 0.01
jet ID	+26.84-10.88	+272.35+95.54	+18.04-14.69	< 0.01
MC statistics	$\pm 12.32$	$\pm 99.99$	$\pm 13.97$	< 0.01

TABLE LXI

RELATIVE SYSTEMATIC UNCERTAINTIES ON THE  $WW \rightarrow L\nu JJ$  SELECTION EFFICIENCY (%).

	$e+\text{jets}$		$\mu+\text{jets}$	
	$N_{\text{jet}}=3$	$N_{\text{jet}} \geq 4$	$N_{\text{jet}}=3$	$N_{\text{jet}} \geq 4$
EM trigger (L1)			+0.44-3.28	+0.80-10.65
EM trigger (L3)			$\pm 0.61$	$\pm 1.22$
muon trigger (L1)	$\pm 0.84$	$\pm 1.07$		
muon trigger (L2)	$< 0.01$	$< 0.01$		
jet trigger (L1)	$\pm 0.01$	$\pm 0.02$	$\pm 0.03$	$\pm 0.05$
jet trigger (L2)	$< 0.01$	$< 0.01$	$< 0.01$	$< 0.01$
jet trigger (L3)	$\pm 0.38$	$\pm 0.23$	$\pm 0.10$	$\pm 0.10$
jet energy scale	+29.07-22.37	+67.62-20.76	+25.35-34.93	+29.61-55.36
jet energy resolution	$< 0.01$	$< 0.01$	$< 0.01$	$< 0.01$
jet ID	+9.93-12.67	+16.57+3.56	+18.27-20.97	-11.94-28.64
MC statistics	$\pm 9.65$	$\pm 44.75$	$\pm 12.56$	$\pm 37.86$

TABLE LXII

RELATIVE SYSTEMATIC UNCERTAINTIES ON THE  $WZ \rightarrow L\nu JJ$  SELECTION EFFICIENCY (%).

	$e+\text{jets}$		$\mu+\text{jets}$	
	$N_{jet}=3$	$N_{jet} \geq 4$	$N_{jet}=3$	$N_{jet} \geq 4$
EM trigger (L1)			+0.33-2.22	+1.22-17.48
EM trigger (L3)			$\pm 0.54$	$\pm 5.48$
muon trigger (L1)	$\pm 0.98$	$\pm 0.58$		
muon trigger (L2)	$< 0.01$	$< 0.01$		
jet trigger (L1)	$\pm 0.02$	$\pm 0.01$	$\pm 0.03$	$\pm 0.38$
jet trigger (L2)	$< 0.01$	$< 0.01$	$< 0.01$	$< 0.01$
jet trigger (L3)	$+0.40-0.43$	$\pm 0.48$	$\pm 0.02$	$+0.21-0.23$
jet energy scale	$+21.68-25.12$	$+0.00-24.87$	$+19.00-18.80$	$+228.48+0.00$
jet energy resolution	$< 0.01$	$< 0.01$	$< 0.01$	$< 0.01$
jet ID	$+26.26-18.07$	$+26.53-25.98$	$-9.09-21.94$	$+471.18+184.24$
MC statistics	$\pm 11.25$	$\pm 49.99$	$\pm 15.40$	$\pm 100.00$

TABLE LXIII

RELATIVE SYSTEMATIC UNCERTAINTIES ON THE  $WZ \rightarrow LLJJ$  SELECTION EFFICIENCY (%).

	$e+\text{jets}$		$\mu+\text{jets}$	
	$N_{jet}=3$	$N_{jet} \geq 4$	$N_{jet}=3$	$N_{jet} \geq 4$
EM trigger (L1)			+0.28-1.96	+0.32-3.97
EM trigger (L3)			$\pm 0.62$	$\pm 1.06$
muon trigger (L1)	$\pm 0.93$	$\pm 0.58$		
muon trigger (L2)	$< 0.01$	$< 0.01$		
jet trigger (L1)	$\pm 0.01$	$< 0.01$	$\pm 0.03$	$\pm 0.03$
jet trigger (L2)	$< 0.01$	$< 0.01$	$< 0.01$	$< 0.01$
jet trigger (L3)	$\pm 0.39$	$\pm 0.31$	$\pm 0.02$	$\pm 0.03$
jet energy scale	$+26.69-10.93$	$+46.29-32.17$	$+8.32-20.93$	$+0.00-15.96$
jet energy resolution	$< 0.01$	$< 0.01$	$< 0.01$	$< 0.01$
jet ID	$+49.17+23.41$	$+48.93-2.76$	$+15.51-12.72$	$+55.50+7.31$
MC statistics	$\pm 11.99$	$\pm 40.86$	$\pm 14.41$	$\pm 40.83$

TABLE LXIV

RELATIVE SYSTEMATIC UNCERTAINTIES ON THE  $ZZ \rightarrow LLJJ$  SELECTION EFFICIENCY (%).

	$e + \text{jets}$		$\mu + \text{jets}$	
	$N_{jet}=3$	$N_{jet} \geq 4$	$N_{jet}=3$	$N_{jet} \geq 4$
EM trigger (L1)			+0.64-6.88	+0.31-2.95
EM trigger (L3)			$\pm 1.22$	$\pm 0.76$
muon trigger (L1)	$\pm 0.73$	$\pm 0.52$		
muon trigger (L2)	$< 0.01$	$< 0.01$		
jet trigger (L1)	$< 0.01$	$< 0.01$	$\pm 0.05$	$\pm 0.03$
jet trigger (L2)	$< 0.01$	$< 0.01$	$< 0.01$	$< 0.01$
jet trigger (L3)	$\pm 0.32$	$< 0.01$	$\pm 0.10$	$< 0.01$
jet energy scale	-1.19-27.26	+94.81+0.00	+26.76-29.03	+33.55+0.00
jet energy resolution	$< 0.01$	$< 0.01$	$< 0.01$	$< 0.01$
jet ID	-28.77+22.73	+125.63+49.85	+167.45+115.13	+12.48-100.00
MC statistics	$\pm 23.64$	$\pm 70.75$	$\pm 26.75$	$\pm 57.74$

TABLE LXV

RELATIVE SYSTEMATIC UNCERTAINTIES ON THE  $Z \rightarrow \tau^+\tau^-$  SELECTION  
EFFICIENCY (%).

## Appendix D

### SYSTEMATIC UNCERTAINTIES ON THE TAGGING PROBABILITIES

Tables with systematic uncertainties on the event tagging probabilities are presented in this Appendix.

Appendix D (Continued)

	$e + \text{jets}$				$\mu + \text{jets}$			
	1 jet	2 jets	3 jets	$\geq 4$ jets	1 jet	2 jets	3 jets	$\geq 4$ jets
$W + \text{light}$	+0.26-1.14	-2.81+0.47	+1.14-4.65	+3.13+0.19	+0.21-0.68	-2.20+1.73	+1.14+1.08	-0.16-3.12
$W(c\bar{c})$	-1.32+0.00	-0.97-1.99	-0.65-2.15	-1.14-4.26	-0.20-0.36	-1.29-0.49	+0.66+0.39	+2.03-1.15
$W(b\bar{b})$	-0.71-0.41	+0.10-1.90	+0.34-1.29	-1.43+1.19	-0.67-0.35	-0.68-0.71	-0.07-0.60	-0.96+0.05
$W_c$	+0.20-0.36	+1.41-1.11	-1.88+0.32	-1.46+1.27	-0.12-0.36	-0.83-0.20	-0.65-1.75	+1.11+1.28
$W_{c\bar{c}}$		+0.66-0.93	+2.56+2.21	-0.07+0.25		-1.32-0.73	+2.12-2.57	+0.42-0.93
$W_{b\bar{b}}$		-0.25+0.05	-3.02-1.14	-1.10-0.59		+0.02+1.01	+0.77-0.63	+0.55-1.42
$W + \text{jets}$	-0.17-0.57	-0.28-0.77	-0.44-1.40	-0.23-0.16	-0.18-0.45	-1.02+0.30	+0.66-0.58	+0.27-1.11
$t\bar{t} \rightarrow l + \text{jets}$	+0.22-0.78	+0.09-0.31	+0.22-0.25	+0.17-0.12	-0.68-1.79	+0.27-0.22	$\pm 0.30$	+0.18-0.23
$t\bar{t} \rightarrow ll$	-0.21-0.18	+0.19-0.16	+0.34-0.36	-0.66-0.57	+0.51-0.38	+0.09-0.34	+0.45-0.29	-0.54-0.73
$tb$	+0.52-0.25	+0.01-0.17	+0.00+0.49	+0.84-2.54	+0.06-0.63	+0.02-0.16	+1.09-0.23	-1.03-0.43
$tqb$	+0.48-1.32	+0.37-0.49	+0.61-0.31	$\mp 1.12$	+0.83-1.97	+0.65-0.25	-0.07+0.20	+0.42-0.09
$WW \rightarrow l\nu jj$	-1.36+0.43	-0.07-4.02	+3.82+1.30	< 0.01	+1.47-1.45	+0.70-0.92	+3.69+11.04	-17.11-6.67
$WZ \rightarrow l\nu jj$	+4.06-0.13	+1.45-4.42	+3.55+18.75	-14.94-65.31	+1.23-0.70	+2.75-3.34	+7.24-4.05	+46.03+22.92
$WZ \rightarrow jjll$	-13.56+4.16	-9.21+10.72	+18.53-2.42	-62.99-0.19	+1.94+2.84	+0.49-0.88	+11.18+0.86	+3.61-40.63
$ZZ \rightarrow jjll$	-12.08-3.91	-1.65+1.15	+6.14-13.04	+4.87+0.90	-2.14-4.74	+3.14-1.77	+9.49-0.10	+0.56-21.85
$Z \rightarrow \tau^+\tau^-$	-6.69+5.39	-15.06+12.47	-13.02-58.12	+4.19-5.76	+1.96+20.63	-9.72+0.35	+1.76+16.37	-21.46-4.28

TABLE LXVI. RELATIVE SYSTEMATIC UNCERTAINTY FROM THE JET ENERGY SCALE (%) FOR SINGLE TAGGED EVENTS.

Appendix D (Continued)

	$e+$ jets			$\mu+$ jets		
	2 jets	3 jets	$\geq 4$ jets	2 jets	3 jets	$\geq 4$ jets
$W+light$	-11.65+2.61	-2.71-8.55	+4.24+1.31	-4.71+3.89	+0.86-1.63	+0.46-5.04
$W(c\bar{c})$	+2.93-4.16	-0.32+0.49	-3.45-3.80	-1.97-6.57	-0.39-3.19	+0.81-0.30
$W(b\bar{b})$	+2.72-4.11	-0.51-1.31	+33.74+0.36	-2.55+5.93	-2.32-0.08	-4.51-6.57
$Wc$	-0.43+1.96	-0.31+2.78	-0.32+2.17	-3.05-3.74	-4.94-3.63	+1.99+0.62
$Wc\bar{c}$	+0.32-1.73	+2.39+2.72	-2.00-0.11	-1.15-0.80	+5.68-6.14	+0.67+0.80
$Wb\bar{b}$	+0.24-0.87	-2.79-4.09	-1.75-1.56	+0.74+0.80	+4.28-2.32	+1.38-2.86
$W+jets$	+0.33-1.07	-2.22-3.36	-0.18-1.33	+0.33+0.94	+3.88-2.50	+0.74-2.84
$t\bar{t} \rightarrow l+jets$	+0.47-0.77	+0.67-0.62	$\pm 1.14$	+2.01-1.78	+0.30-0.53	+1.40-1.37
$t\bar{t} \rightarrow ll$	+0.53-0.77	+1.01-1.51	-0.25-0.58	+0.82-1.03	+1.08-1.69	+1.14-1.35
$tb$	+0.03-0.47	-0.80+0.24	+4.58-6.50	+0.24-0.64	+2.71-1.17	-0.56+0.66
$tgb$	-0.45-0.38	+0.33+1.46	-2.22-0.93	+0.30-1.22	-1.77+1.06	+1.66-1.02
$WW \rightarrow l\nu jj$	-9.36-26.99	+136.51-3.23	< 0.01	+6.37-3.61	-3.72+22.97	-13.19-15.11
$WZ \rightarrow l\nu jj$	+2.32-3.38	+0.08+11.36	+3.39+42.25	+4.65-3.72	+14.46-13.09	+46.36+19.49
$WZ \rightarrow jj ll$	-35.65+16.43	+17.33-4.36	-57.63-11.21	+5.09-2.06	+5.54+5.45	+13.92-36.58
$ZZ \rightarrow jj ll$	-1.11+5.83	-5.37-11.49	+10.65+0.45	+3.13-1.25	+5.61-3.96	+1.07-12.26
$Z \rightarrow \tau^+\tau^-$	-22.35+12.65	-11.40-96.66	+5.11-10.45	-9.14+6.27	+1.82+36.28	-29.32-9.98

TABLE LXVII. RELATIVE SYSTEMATIC UNCERTAINTY FROM THE JET ENERGY SCALE (%) FOR DOUBLE TAGGED EVENTS.

	$e+$ jets				$\mu+$ jets			
	1 jet	2 jets	3 jets	$\geq 4$ jets	1 jet	2 jets	3 jets	$\geq 4$ jets
$t\bar{t} \rightarrow l+jets$	-0.88-2.34	+0.42+0.54	+0.11+0.03	-0.26+0.08	-0.76-1.45	+0.63+0.62	-0.05+0.01	-0.15-0.08

TABLE LXVIII. RELATIVE SYSTEMATIC UNCERTAINTY FROM THE JET ENERGY RESOLUTION (%) FOR SINGLE TAGGED EVENTS.

	$e+$ jets			$\mu+$ jets		
	2 jets	3 jets	$\geq 4$ jets	2 jets	3 jets	$\geq 4$ jets
$t\bar{t} \rightarrow l+jets$	+1.87+0.60	-0.09-0.09	-0.74+0.14	+2.11-0.51	-0.33-0.26	-0.10+0.23

TABLE LXIX. RELATIVE SYSTEMATIC UNCERTAINTY FROM THE JET ENERGY RESOLUTION (%) FOR DOUBLE TAGGED EVENTS.

**Appendix D (Continued)**

	$e+$ jets				$\mu+$ jets			
	1 jet	2 jets	3 jets	$\geq 4$ jets	1 jet	2 jets	3 jets	$\geq 4$ jets
$W+\text{light}$	-40.21-31.68	-38.13-27.19	-27.54-23.29	-21.57-14.39	-30.29-17.03	-34.88-14.12	-18.77-13.30	-18.03-7.84
$W(c\bar{c})$	-14.16-12.36	-15.17-15.16	-15.71-10.34	-16.73-17.00	-6.64-5.89	-11.97-8.17	-8.81-5.13	-13.56-11.18
$W(b\bar{b})$	-11.68-10.47	-10.08-10.56	-7.05-4.94	-7.84-3.14	-4.45-3.58	-6.10-5.35	-3.02-2.34	-8.40-6.49
$Wc$	-14.27-13.13	-13.34-12.59	-13.46-10.99	-12.08-12.37	-5.86-5.08	-8.88-7.08	-7.28-5.79	-1.77-0.55
$Wc\bar{c}$		-14.50-10.66	-10.57-2.46	-8.38-10.04		-5.66-4.72	-9.74-8.25	-7.78-3.87
$Wb\bar{b}$		-1.89-0.71	-7.53-5.66	-6.79-4.81		+0.10+0.74	-0.94-2.82	-3.08-0.88
$W+\text{jets}$	-21.06-17.70	-15.42-12.59	-13.57-10.03	-11.60-8.98	-12.71-8.25	-12.20-6.59	-7.76-6.26	-8.82-4.94
$t\bar{t} \rightarrow l+l$ -jets	+0.12+0.56	+0.23+0.01	+0.23-0.04	-0.19-0.22	-4.02+0.09	+1.03+0.19	+0.16-0.20	-0.25+0.12
$t\bar{t} \rightarrow ll$	+0.00-1.25	+0.29+0.27	-0.10+0.17	-0.51-0.08	-0.15-0.04	-0.02-0.14	+0.01+0.35	-0.50+0.82
$tb$	+0.76+0.56	-0.39-0.03	-0.87-0.42	+2.92-0.24	-0.21+0.50	+0.15-0.01	+0.96+0.05	-4.09-2.76
$tqb$	-0.53-2.89	+0.18+0.33	+0.58+1.10	-1.40-0.32	+0.29-1.57	+0.59+0.47	-1.31-0.11	-0.48-1.54
$WW \rightarrow l\nu jj$	-1.19-5.92	+0.73+2.54	-20.33-18.25	< 0.01	+0.95-2.10	-0.38+0.45	-6.68-13.68	+152.53+80.81
$WZ \rightarrow l\nu jj$	+1.90+2.52	-1.02+2.55	+37.73+17.27	+140.80+312.66	+3.73+1.15	+4.03+4.05	-20.82-13.66	+74.55-2.05
$WZ \rightarrow jjll$	-3.24-2.36	+2.10-3.74	-2.10+0.93	-80.95-94.64	+1.82+0.61	-5.52-5.98	+11.39+27.85	-29.29+36.05
$ZZ \rightarrow jjll$	-17.08-17.86	+2.94+5.45	+22.82+29.65	+282.80+450.46	+0.10+1.11	+5.34+1.96	+16.39+15.88	-39.36-38.87
$Z \rightarrow \tau^+\tau^-$	+3.27-6.82	-9.61-2.72	-48.33-44.92	-43.94-100.00	+60.29+36.45	-57.85-63.05	-41.50-84.84	-70.97-75.88

TABLE LXX. RELATIVE SYSTEMATIC UNCERTAINTY FROM THE JET RECONSTRUCTION AND IDENTIFICATION EFFICIENCY (%) FOR SINGLE TAGGED EVENTS.

Appendix D (Continued)

	e+jets			$\mu$ +jets		
	2 jets	3 jets	$\geq 4$ jets	2 jets	3 jets	$\geq 4$ jets
$W + \text{light}$	-59.41-43.98	-45.44-38.87	-39.27-30.72	-59.52-26.67	-38.76-29.72	-33.67-16.38
$W(c\bar{c})$	-2.67-18.30	-36.85-17.76	-42.04-29.37	-41.17-21.23	-26.34-12.51	-45.28-45.24
$W(b\bar{b})$	-18.17-8.09	-27.15-11.60	-11.74-7.50	-13.34-23.97	-19.43-14.03	-35.17-26.21
$W c$	-39.68-31.32	-33.34-25.31	-34.39-32.61	-27.81-15.05	-34.10-24.73	-12.78-6.45
$W c\bar{c}$	-27.69-20.74	-23.02-8.12	-18.93-22.55	-12.97-10.58	-20.65-17.88	-14.42-2.47
$W b\bar{b}$	-13.52-8.59	-20.48-13.98	-20.80-13.36	-9.75-6.56	-6.89-2.97	-15.62-5.08
$W + \text{jets}$	-15.18-9.86	-21.54-13.72	-20.88-14.49	-10.82-8.15	-9.27-5.18	-18.10-7.75
$t\bar{t} \rightarrow l + \text{jets}$	+3.78+1.54	+0.70-0.61	-0.80-0.26	+2.11-1.40	+1.17-0.04	-0.40+0.64
$t\bar{t} \rightarrow ll$	+0.42+0.18	-0.24-0.07	-3.04+1.44	+0.29-0.64	-0.77+0.17	-1.94+0.92
$tb$	-1.54-0.88	-2.76-2.14	+2.16-7.22	-1.01-0.55	+0.78+0.76	-8.37-10.04
$tqb$	-5.50+0.19	+0.49+2.84	-2.51+0.67	-1.08+4.42	-1.97+0.67	-1.04-0.80
$WW \rightarrow l\nu jj$	-19.35-1.19	-21.56-15.19	< 0.01	-4.84+2.63	-19.28-29.89	+1771.36+174.67
$WZ \rightarrow l\nu jj$	-0.42+2.57	+34.08+2.91	+41740.84+88448.09	+4.06+2.43	-18.50-14.41	+167.56-5.19
$WZ \rightarrow jjll$	-36.37-36.90	-11.33+40.85	-43.15-95.13	+7.84+1.92	+12.54+117.37	-6.47+137.25
$ZZ \rightarrow jjll$	+2.95+1.03	+51.01+39.69	+13357.63+12851.82	+3.86-0.07	+19.23+33.90	-60.07-44.49
$Z \rightarrow \tau^+\tau^-$	-89.78-76.73	-95.11-95.72	-69.60-100.00	-85.37-85.46	-99.28-99.91	-91.51-95.50

TABLE LXXI. RELATIVE SYSTEMATIC UNCERTAINTY FROM THE JET RECONSTRUCTION AND IDENTIFICATION EFFICIENCY (%) FOR DOUBLE TAGGED EVENTS.

Appendix D (Continued)

	e+jets				$\mu$ +jets			
	1 jet	2 jets	3 jets	$\geq 4$ jets	1 jet	2 jets	3 jets	$\geq 4$ jets
$W + \text{light}$	$\pm 0.01$	$\mp 0.03$	$\mp 0.03$	$\mp 0.02$	$< 0.01$	$\mp 0.08$	$\mp 0.07$	$\mp 0.04$
$W(c\bar{c})$	$\pm 0.04$	$\mp 0.02$	$< 0.01$	$< 0.01$	$\pm 0.01$	$\mp 0.04$	$\mp 0.03$	$\mp 0.03$
$W(b\bar{b})$	$< 0.01$	$\mp 0.02$	$\mp 0.01$	$< 0.01$	$< 0.01$	$\mp 0.03$	$\mp 0.03$	$\mp 0.03$
$Wc$	$\pm 0.03$	$< 0.01$	$\mp 0.01$	$< 0.01$	$< 0.01$	$\mp 0.03$	$\mp 0.02$	$\mp 0.02$
$Wc\bar{c}$		$\mp 0.01$	$< 0.01$	$< 0.01$		$\mp 0.03$	$\mp 0.03$	$\mp 0.02$
$Wb\bar{b}$		$< 0.01$	$< 0.01$	$< 0.01$		$\mp 0.02$	$< 0.01$	$\mp 0.01$
$W + \text{jets}$	$\pm 0.02$	$\mp 0.02$	$\mp 0.01$	$< 0.01$	$< 0.01$	$\mp 0.04$	$\mp 0.03$	$\mp 0.02$
$t\bar{t} \rightarrow l+\text{jets}$	$< 0.01$	$\mp 0.01$	$< 0.01$	$< 0.01$	$\mp 0.01$	$\mp 0.03$	$< 0.01$	$< 0.01$
$t\bar{t} \rightarrow ll$	$< 0.01$	$< 0.01$	$< 0.01$	$< 0.01$	$< 0.01$	$\mp 0.01$	$< 0.01$	$< 0.01$
$tb$	$< 0.01$	$< 0.01$	$< 0.01$	$< 0.01$	$< 0.01$	$\mp 0.01$	$\mp 0.01$	$\mp 0.01$
$tqb$	$\pm 0.04$	$< 0.01$	$< 0.01$	$< 0.01$	$\pm 0.03$	$\mp 0.02$	$\mp 0.02$	$< 0.01$
$WW \rightarrow l\nu jj$	$< 0.01$	$< 0.01$	$\pm 0.01$	$< 0.01$	$< 0.01$	$\mp 0.02$	$\mp 0.08$	$< 0.01$
$WZ \rightarrow l\nu jj$	$\pm 0.07$	$\pm 0.03$	$< 0.01$	$\pm 0.07$	$\pm 0.05$	$\pm 0.08$	$\pm 0.16$	$\mp 0.09$
$WZ \rightarrow jjll$	$\mp 0.01$	$\mp 0.02$	$< 0.01$	$< 0.01$	$< 0.01$	$\mp 0.02$	$\mp 0.14$	$\pm 0.34$
$ZZ \rightarrow jjll$	$\pm 0.03$	$\pm 0.07$	$\pm 0.02$	$< 0.01$	$\pm 0.04$	$\pm 0.08$	$\pm 0.18$	$\pm 0.49$
$Z \rightarrow \tau^+\tau^-$	$\mp 0.13$	$< 0.01$	$\mp 0.01$	$< 0.01$	$\mp 0.07$	$\pm 0.05$	$\mp 0.22$	$< 0.01$

TABLE LXXII. RELATIVE SYSTEMATIC UNCERTAINTY FROM THE JET TRIGGER (L3) (%) FOR SINGLE TAGGED EVENTS.

Appendix D (Continued)

	$e+$ jets			$\mu+$ jets		
	2 jets	3 jets	$\geq 4$ jets	2 jets	3 jets	$\geq 4$ jets
$W + \text{light}$	$\pm 0.10$	$\pm 0.04$	$\pm 0.03$	$\pm 0.22$	$\pm 0.12$	$\pm 0.07$
$W(c\bar{c})$	$\pm 0.08$	$\pm 0.01$	$\pm 0.01$	$\pm 0.06$	$\pm 0.06$	$\pm 0.08$
$W(b\bar{b})$	$\pm 0.06$	$\pm 0.04$	$\pm 0.03$	$\pm 0.10$	$\pm 0.09$	$\pm 0.08$
$Wc$	$\pm 0.10$	$\pm 0.05$	$\pm 0.02$	$\pm 0.18$	$\pm 0.10$	$\pm 0.07$
$Wc\bar{c}$	$\pm 0.04$	$\pm 0.01$	$\pm 0.02$	$\pm 0.08$	$\pm 0.04$	$\pm 0.05$
$Wb\bar{b}$	$\pm 0.05$	$\pm 0.03$	$< 0.01$	$\pm 0.10$	$\pm 0.05$	$\pm 0.04$
$W+\text{jets}$	$\pm 0.05$	$\pm 0.03$	$\pm 0.01$	$\pm 0.10$	$\pm 0.06$	$\pm 0.04$
$t\bar{t} \rightarrow l+\text{jets}$	$\pm 0.05$	$\pm 0.01$	$< 0.01$	$\pm 0.09$	$\pm 0.03$	$\pm 0.01$
$t\bar{t} \rightarrow ll$	$\pm 0.05$	$\pm 0.02$	$\pm 0.01$	$\pm 0.09$	$\pm 0.04$	$\pm 0.03$
$tb$	$\pm 0.06$	$\pm 0.02$	$< 0.01$	$\pm 0.09$	$\pm 0.08$	$\pm 0.07$
$tqb$	$\pm 0.02$	$\pm 0.02$	$\pm 0.01$	$\pm 0.03$	$\pm 0.06$	$\pm 0.04$
$WW \rightarrow l\nu jj$	$\pm 0.06$	$\pm 0.03$	$< 0.01$	$\pm 0.08$	$\pm 0.17$	$< 0.01$
$WZ \rightarrow l\nu jj$	$< 0.01$	$\pm 0.03$	$\pm 0.07$	$\pm 0.01$	$\pm 0.18$	$\pm 0.10$
$WZ \rightarrow jjll$	$\pm 0.10$	$< 0.01$	$< 0.01$	$\pm 0.15$	$\pm 0.17$	$\pm 0.22$
$ZZ \rightarrow jjll$	$\pm 0.01$	$< 0.01$	$\pm 0.02$	$\pm 0.01$	$\pm 0.16$	$\pm 0.36$
$Z \rightarrow \tau^+\tau^-$	$\pm 0.32$	$\pm 0.04$	$< 0.01$	$\pm 0.27$	$\pm 0.32$	$< 0.01$

TABLE LXXIII. RELATIVE SYSTEMATIC UNCERTAINTY FROM THE JET TRIGGER (L3) (%) FOR DOUBLE TAGGED EVENTS.

Appendix D (Continued)

	e+jets				$\mu$ +jets			
	1 jet	2 jets	3 jets	$\geq 4$ jets	1 jet	2 jets	3 jets	$\geq 4$ jets
$W + \text{light}$	$\pm 0.34$	$\pm 0.32$	$\pm 0.30$	$\pm 0.36$	$\pm 0.33$	$\pm 0.33$	$\pm 0.35$	$\pm 0.35$
$W(c\bar{c})$	$\pm 0.37$	$\pm 0.33$	$\pm 0.36$	$\pm 0.32$	$\pm 0.37$	$\pm 0.34$	$\pm 0.37$	$\pm 0.27$
$W(b\bar{b})$	$\pm 0.32$	$\pm 0.35$	$\pm 0.35$	$\pm 0.32$	$\pm 0.34$	$\pm 0.36$	$\pm 0.36$	$\pm 0.36$
$Wc$	$\pm 0.35$	$\pm 0.34$	$\pm 0.32$	$\pm 0.31$	$\pm 0.36$	$\pm 0.33$	$\pm 0.32$	$\pm 0.40$
$Wc\bar{c}$		$\pm 0.35$	$\pm 0.35$	$\pm 0.36$		$\pm 0.33$	$\pm 0.32$	$\pm 0.32$
$Wb\bar{b}$		$\pm 0.23$	$\pm 0.18$	$\pm 0.16$		$\pm 0.21$	$\pm 0.20$	$\pm 0.22$
$W + \text{jets}$	$\pm 0.34$	$\pm 0.32$	$\pm 0.29$	$\pm 0.29$	$\pm 0.35$	$\pm 0.31$	$\pm 0.31$	$\pm 0.31$
$t\bar{t} \rightarrow l + \text{jets}$	$\pm 0.29$	$\pm 0.26$	$\pm 0.20$	$\pm 0.16$	$\pm 0.32$	$\pm 0.27$	$\pm 0.22$	$\pm 0.18$
$t\bar{t} \rightarrow ll$	$\pm 0.32$	$\pm 0.20$	$\pm 0.18$	$\pm 0.18$	$\pm 0.34$	$\pm 0.22$	$\pm 0.20$	$\pm 0.21$
$tb$	$\pm 0.32$	$\pm 0.18$	$\pm 0.16$	$\pm 0.22$	$\pm 0.34$	$\pm 0.20$	$\pm 0.21$	$\pm 0.15$
$tqb$	$\pm 0.32$	$\pm 0.31$	$\pm 0.25$	$\pm 0.21$	$\pm 0.33$	$\pm 0.32$	$\pm 0.25$	$\pm 0.22$
$WW \rightarrow l\nu jj$	$\pm 0.34$	$\pm 0.36$	$\pm 0.33$	$< 0.01$	$\pm 0.34$	$\pm 0.36$	$\pm 0.29$	$\pm 0.22$
$WZ \rightarrow l\nu jj$	$\pm 0.32$	$\pm 0.20$	$\pm 0.15$	$\pm 0.08$	$\pm 0.34$	$\pm 0.22$	$\pm 0.28$	$\pm 0.18$
$WZ \rightarrow jjll$	$\pm 0.41$	$\pm 0.31$	$\pm 0.30$	$\pm 0.01$	$\pm 0.36$	$\pm 0.38$	$\pm 0.34$	$\pm 0.49$
$ZZ \rightarrow jjll$	$\pm 0.30$	$\pm 0.25$	$\pm 0.37$	$\pm 0.22$	$\pm 0.44$	$\pm 0.29$	$\pm 0.29$	$\pm 0.15$
$Z \rightarrow \tau^+\tau^-$	$\pm 0.31$	$\pm 0.33$	$\pm 0.59$	$\pm 0.29$	$\pm 0.32$	$\pm 0.40$	$\pm 0.12$	$\pm 0.27$

TABLE LXXIV. RELATIVE SYSTEMATIC UNCERTAINTY FROM THE TAGGABILITY IN DATA (%) FOR SINGLE TAGGED EVENTS.

Appendix D (Continued)

	e+jets			$\mu$ +jets		
	2 jets	3 jets	$\geq 4$ jets	2 jets	3 jets	$\geq 4$ jets
$W + \text{light}$	$\pm 0.61$	$\pm 0.58$	$\pm 0.58$	$\pm 0.56$	$\pm 0.54$	$\pm 0.57$
$W(c\bar{c})$	$\pm 0.65$	$\pm 0.63$	$\pm 0.55$	$\pm 0.71$	$\pm 0.65$	$\pm 0.51$
$W(b\bar{b})$	$\pm 0.70$	$\pm 0.60$	$\pm 0.79$	$\pm 0.59$	$\pm 0.59$	$\pm 0.59$
$Wc$	$\pm 0.62$	$\pm 0.60$	$\pm 0.57$	$\pm 0.60$	$\pm 0.60$	$\pm 0.67$
$Wc\bar{c}$	$\pm 0.68$	$\pm 0.69$	$\pm 0.67$	$\pm 0.61$	$\pm 0.66$	$\pm 0.61$
$Wb\bar{b}$	$\pm 0.64$	$\pm 0.60$	$\pm 0.59$	$\pm 0.59$	$\pm 0.65$	$\pm 0.61$
$W + \text{jets}$	$\pm 0.65$	$\pm 0.61$	$\pm 0.60$	$\pm 0.59$	$\pm 0.65$	$\pm 0.61$
$t\bar{t} \rightarrow l + \text{jets}$	$\pm 0.54$	$\pm 0.53$	$\pm 0.54$	$\pm 0.53$	$\pm 0.54$	$\pm 0.56$
$t\bar{t} \rightarrow ll$	$\pm 0.55$	$\pm 0.54$	$\pm 0.56$	$\pm 0.56$	$\pm 0.57$	$\pm 0.58$
$tb$	$\pm 0.57$	$\pm 0.55$	$\pm 0.61$	$\pm 0.59$	$\pm 0.58$	$\pm 0.56$
$tqb$	$\pm 0.59$	$\pm 0.62$	$\pm 0.62$	$\pm 0.62$	$\pm 0.62$	$\pm 0.64$
$WW \rightarrow l\nu jj$	$\pm 0.98$	$\pm 0.71$	$< 0.01$	$\pm 0.63$	$\pm 0.57$	$\pm 0.43$
$WZ \rightarrow l\nu jj$	$\pm 0.62$	$\pm 0.54$	$\pm 1.44$	$\pm 0.66$	$\pm 0.71$	$\pm 0.67$
$WZ \rightarrow jjll$	$\pm 0.53$	$\pm 0.54$	$\pm 0.67$	$\pm 0.75$	$\pm 0.57$	$\pm 0.86$
$ZZ \rightarrow jjll$	$\pm 0.50$	$\pm 0.69$	$\pm 0.44$	$\pm 0.65$	$\pm 0.66$	$\pm 0.66$
$Z \rightarrow \tau^+\tau^-$	$\pm 0.58$	$\pm 3.95$	$\pm 0.57$	$\pm 0.81$	$\pm 0.44$	$\pm 0.58$

TABLE LXXV. RELATIVE SYSTEMATIC UNCERTAINTY FROM THE TAGGABILITY IN DATA (%) FOR DOUBLE TAGGED EVENTS.

Appendix D (Continued)

	e+jets				$\mu$ +jets			
	1 jet	2 jets	3 jets	$\geq 4$ jets	1 jet	2 jets	3 jets	$\geq 4$ jets
$W + \text{light}$	< 0.01	< 0.01	< 0.01	< 0.01	< 0.01	< 0.01	< 0.01	< 0.01
$W(c\bar{c})$	$\mp 0.02$	$\mp 0.04$	$\mp 0.05$	< 0.01	< 0.01	$\mp 0.05$	$\mp 0.05$	$\mp 0.08$
$W(b\bar{b})$	$\pm 0.13$	$\pm 0.11$	$\pm 0.09$	$\pm 0.16$	$\pm 0.14$	$\pm 0.10$	$\pm 0.08$	$\pm 0.05$
$W_c$	$\pm 0.02$	$\mp 0.01$	< 0.01	< 0.01	$\pm 0.02$	< 0.01	$\mp 0.02$	< 0.01
$W c\bar{c}$		$\mp 0.02$	$\mp 0.07$	$\mp 0.08$		$\mp 0.05$	$\mp 0.07$	$\mp 0.02$
$W b\bar{b}$		$\pm 0.05$	$\pm 0.04$	$\pm 0.03$		$\pm 0.05$	$\pm 0.08$	$\pm 0.03$
$W + \text{jets}$	$\pm 0.04$	$\pm 0.02$	$\pm 0.01$	$\pm 0.03$	$\pm 0.05$	$\pm 0.02$	$\pm 0.02$	< 0.01
$t\bar{t} \rightarrow l + \text{jets}$	$\pm 0.14$	$\pm 0.10$	$\pm 0.06$	$\pm 0.04$	$\pm 0.14$	$\pm 0.10$	$\pm 0.06$	$\pm 0.04$
$t\bar{t} \rightarrow ll$	$\pm 0.15$	$\pm 0.06$	$\pm 0.05$	$\pm 0.05$	$\pm 0.15$	$\pm 0.06$	$\pm 0.05$	$\pm 0.05$
$tb$	$\pm 0.15$	$\pm 0.05$	$\pm 0.04$	$\pm 0.05$	$\pm 0.15$	$\pm 0.05$	$\pm 0.05$	$\pm 0.05$
$tqb$	$\pm 0.15$	$\pm 0.11$	$\pm 0.06$	$\pm 0.06$	$\pm 0.15$	$\pm 0.11$	$\pm 0.07$	$\pm 0.05$
$WW \rightarrow l\nu jj$	$\mp 0.04$	$\mp 0.06$	$\mp 0.10$	< 0.01	< 0.01	$\mp 0.08$	$\mp 0.04$	< 0.01
$WZ \rightarrow l\nu jj$	$\pm 0.11$	$\pm 0.04$	< 0.01	< 0.01	$\pm 0.14$	$\pm 0.05$	$\pm 0.06$	$\pm 0.08$
$WZ \rightarrow jj ll$	$\pm 0.07$	$\pm 0.01$	< 0.01	< 0.01	$\mp 0.10$	$\mp 0.10$	$\mp 0.04$	$\mp 0.40$
$ZZ \rightarrow jj ll$	$\pm 0.14$	$\pm 0.08$	$\pm 0.04$	< 0.01	$\pm 0.15$	$\pm 0.08$	$\pm 0.04$	$\pm 0.08$
$Z \rightarrow \tau^+ \tau^-$	$\mp 0.03$	$\pm 0.14$	$\mp 0.34$	< 0.01	$\pm 0.08$	$\mp 0.03$	$\mp 0.04$	< 0.01

TABLE LXXVI. RELATIVE SYSTEMATIC UNCERTAINTY FROM THE TAGGABILITY FLAVOR DEPENDENCE (%) FOR SINGLE TAGGED EVENTS.

Appendix D (Continued)

	e+jets			$\mu$ +jets		
	2 jets	3 jets	$\geq 4$ jets	2 jets	3 jets	$\geq 4$ jets
$W + \text{light}$	< 0.01	< 0.01	< 0.01	< 0.01	< 0.01	< 0.01
$W(c\bar{c})$	$\mp 0.05$	$\mp 0.08$	$\pm 0.01$	$\mp 0.10$	$\mp 0.05$	$\mp 0.09$
$W(b\bar{b})$	$\pm 0.15$	$\pm 0.04$	$\pm 0.05$	$\pm 0.12$	$\pm 0.11$	$\pm 0.18$
$Wc$	$\mp 0.03$	$\pm 0.03$	< 0.01	< 0.01	$\mp 0.02$	< 0.01
$Wc\bar{c}$	$\mp 0.01$	$\mp 0.14$	$\mp 0.16$	$\mp 0.11$	$\mp 0.08$	$\mp 0.08$
$Wb\bar{b}$	$\pm 0.23$	$\pm 0.16$	$\pm 0.13$	$\pm 0.18$	$\pm 0.23$	$\pm 0.13$
$W + \text{jets}$	$\pm 0.21$	$\pm 0.13$	$\pm 0.10$	$\pm 0.16$	$\pm 0.19$	$\pm 0.11$
$t\bar{t} \rightarrow l + \text{jets}$	$\pm 0.25$	$\pm 0.22$	$\pm 0.20$	$\pm 0.24$	$\pm 0.22$	$\pm 0.20$
$t\bar{t} \rightarrow ll$	$\pm 0.25$	$\pm 0.23$	$\pm 0.23$	$\pm 0.25$	$\pm 0.24$	$\pm 0.22$
$tb$	$\pm 0.24$	$\pm 0.22$	$\pm 0.19$	$\pm 0.24$	$\pm 0.22$	$\pm 0.23$
$tqb$	$\pm 0.17$	$\pm 0.17$	$\pm 0.16$	$\pm 0.21$	$\pm 0.21$	$\pm 0.19$
$WW \rightarrow l\nu jj$	$\pm 0.05$	$\mp 0.16$	< 0.01	$\mp 0.08$	$\mp 0.01$	< 0.01
$WZ \rightarrow l\nu jj$	$\pm 0.15$	$\pm 0.11$	< 0.01	$\pm 0.15$	$\pm 0.12$	$\mp 0.38$
$WZ \rightarrow jjll$	$\pm 0.13$	$\pm 0.02$	< 0.01	$\mp 0.14$	$\mp 0.03$	$\mp 0.47$
$ZZ \rightarrow jjll$	$\pm 0.23$	$\pm 0.30$	< 0.01	$\pm 0.21$	$\pm 0.17$	$\pm 0.25$
$Z \rightarrow \tau^+\tau^-$	$\mp 0.34$	$\mp 1.02$	< 0.01	$\mp 0.49$	$\pm 0.19$	< 0.01

TABLE LXXVII. RELATIVE SYSTEMATIC UNCERTAINTY FROM THE TAGGABILITY FLAVOR DEPENDENCE (%) FOR DOUBLE TAGGED EVENTS.

Appendix D (Continued)

	$e+$ jets				$\mu+$ jets			
	1 jet	2 jets	3 jets	$\geq 4$ jets	1 jet	2 jets	3 jets	$\geq 4$ jets
$W+light$	< 0.01	< 0.01	< 0.01	< 0.01	< 0.01	< 0.01	< 0.01	< 0.01
$W(c\bar{c})$	< 0.01	< 0.01	< 0.01	< 0.01	< 0.01	< 0.01	< 0.01	< 0.01
$W(b\bar{b})$	$\pm 1.78$	$\pm 2.81$	$\pm 3.16$	$\pm 3.09$	$\pm 1.71$	$\pm 2.65$	$\pm 3.20$	$\pm 3.06$
$W_c$	$< 0.01$	< 0.01	< 0.01	< 0.01	< 0.01	< 0.01	< 0.01	< 0.01
$W c\bar{c}$		< 0.01	< 0.01	< 0.01		< 0.01	< 0.01	< 0.01
$W b\bar{b}$		+1.04-1.12	+1.31-1.42	+1.33-1.45		+0.98-1.05	+1.47-1.60	+1.43-1.55
$W+jets$	$\pm 0.49$	$\pm 0.78$	$+0.95-0.98$	$+1.00-1.03$	$\pm 0.46$	$\pm 0.72$	$+0.99-1.02$	$+1.02-1.06$
$t\bar{t} \rightarrow l+jets$	$\pm 2.49$	+1.91-1.94	+1.25-1.31	+0.89-0.97	$\pm 2.33$	+1.87-1.90	+1.22-1.28	+0.87-0.95
$t\bar{t} \rightarrow ll$	$\pm 2.40$	+1.07-1.15	+0.98-1.07	+0.99-1.08	$\pm 2.32$	+1.04-1.11	+0.97-1.05	+1.03-1.12
$tb$	$\pm 1.88$	+0.94-1.02	+0.93-1.01	+1.13-1.22	$\pm 1.69$	+0.93-1.00	+0.97-1.06	+1.02-1.11
$tqb$	$\pm 1.52$	$\pm 1.99$	+1.66-1.71	+1.35-1.43	$\pm 1.47$	$\pm 2.00$	+1.62-1.67	+1.48-1.56
$WW \rightarrow l\nu jj$	$< 0.01$	$\pm 0.29$	< 0.01	< 0.01	$\pm 0.05$	< 0.01	< 0.01	< 0.01
$WZ \rightarrow l\nu jj$	$\pm 1.81$	+1.19-1.26	+0.75-0.82	$\pm 6.62$	$\pm 1.68$	+1.16-1.23	+1.13-1.20	$\pm 0.72$
$WZ \rightarrow jj ll$	$< 0.01$	< 0.01	< 0.01	< 0.01	$< 0.01$	$\pm 0.06$	< 0.01	< 0.01
$ZZ \rightarrow jj ll$	$\pm 2.16$	+1.25-1.30	+1.38-1.42	< 0.01	$\pm 1.80$	+1.24-1.30	+1.24-1.32	+1.34-1.43
$Z \rightarrow \tau^+\tau^-$	$\pm 1.19$	$\pm 1.47$	+3.50-3.54	< 0.01	$\pm 0.38$	$\pm 0.69$	+0.24-0.27	< 0.01

TABLE LXXVIII. RELATIVE SYSTEMATIC UNCERTAINTY FROM THE INCLUSIVE  $B$ -TAGGING EFFICIENCY IN MONTE CARLO (%) FOR SINGLE TAGGED EVENTS.

Appendix D (Continued)

	$e+$ jets			$\mu+$ jets		
	2 jets	3 jets	$\geq 4$ jets	2 jets	3 jets	$\geq 4$ jets
$W+\text{light}$	< 0.01	< 0.01	< 0.01	< 0.01	< 0.01	< 0.01
$W(c\bar{c})$	< 0.01	< 0.01	< 0.01	< 0.01	< 0.01	< 0.01
$W(b\bar{b})$	+4.66-4.59	+4.97-4.88	+5.18-5.10	+4.73-4.65	+4.71-4.61	+4.35-4.25
$Wc$	< 0.01	< 0.01	< 0.01	< 0.01	< 0.01	< 0.01
$Wc\bar{c}$	< 0.01	< 0.01	< 0.01	< 0.01	< 0.01	< 0.01
$Wb\bar{b}$	+6.17-6.01	+6.48-6.28	+6.46-6.26	+5.71-5.58	+6.75-6.53	+6.56-6.36
$W+\text{jets}$	+5.53-5.39	+5.75-5.58	+5.62-5.45	+5.15-5.04	+5.96-5.77	+5.54-5.36
$t\bar{t} \rightarrow l+\text{jets}$	+5.05-4.93	+4.91-4.79	+4.82-4.71	+4.98-4.86	+4.85-4.74	+4.73-4.62
$t\bar{t} \rightarrow ll$	+5.30-5.16	+5.35-5.21	+5.48-5.33	+5.17-5.04	+5.29-5.15	+5.52-5.37
$tb$	+5.32-5.18	+5.40-5.26	+5.48-5.34	+5.25-5.12	+5.42-5.28	+5.67-5.52
$tqb$	+5.36-5.24	+5.88-5.72	+5.94-5.79	+5.19-5.08	+5.73-5.59	+5.85-5.70
$WW \rightarrow l\nu jj$	+3.04-3.00	< 0.01	< 0.01	< 0.01	< 0.01	< 0.01
$WZ \rightarrow l\nu jj$	+6.15-6.00	+5.27-5.15	$\pm 0.24$	+6.09-5.95	+6.72-6.56	+6.89-6.84
$WZ \rightarrow jjll$	< 0.01	< 0.01	< 0.01	$\pm 0.07$	< 0.01	< 0.01
$ZZ \rightarrow jjll$	+5.70-5.54	+6.14-6.02	< 0.01	+5.94-5.80	+6.30-6.12	+7.86-7.68
$Z \rightarrow \tau^+\tau^-$	+6.55-6.40	+12.36-11.62	< 0.01	$\pm 0.23$	+4.64-4.57	< 0.01

TABLE LXXIX. RELATIVE SYSTEMATIC UNCERTAINTY FROM THE INCLUSIVE  $B$ -TAGGING EFFICIENCY IN MONTE CARLO (%) FOR DOUBLE TAGGED EVENTS.

Appendix D (Continued)

	$e+$ jets				$\mu+$ jets			
	1 jet	2 jets	3 jets	$\geq 4$ jets	1 jet	2 jets	3 jets	$\geq 4$ jets
$W + \text{light}$	< 0.01	< 0.01	< 0.01	< 0.01	< 0.01	< 0.01	< 0.01	< 0.01
$W(c\bar{c})$	-1.61+1.73	-1.49+1.58	-1.47+1.57	-1.18+1.24	-1.49+1.59	-1.51+1.61	-1.48+1.59	-1.46+1.57
$W(b\bar{b})$	-1.52+1.63	-1.65+1.79	-1.62+1.75	-1.90+2.15	-1.54+1.65	-1.60+1.73	-1.69+1.85	-1.69+1.87
$Wc$	-1.30+1.37	-1.32+1.38	-1.37+1.45	-1.30+1.37	-1.31+1.38	-1.26+1.32	-1.27+1.32	-1.27+1.34
$Wc\bar{c}$		-1.38+1.47	-1.38+1.45	-1.31+1.38		-1.43+1.53	-1.44+1.56	-1.37+1.45
$Wb\bar{b}$		$\mp 0.75$	-0.78+0.80	-0.77+0.81		-0.67+0.69	-0.81+0.85	-0.75+0.77
$W + \text{jets}$	-1.01+1.08	-1.03+1.09	-0.98+1.03	-1.02+1.11	-1.01+1.07	-0.97+1.03	-0.99+1.06	-1.01+1.09
$t\bar{t} \rightarrow l + \text{jets}$	-1.30+1.35	-1.02+1.06	$\mp 0.69$	$\mp 0.51$	-1.28+1.34	-0.99+1.03	$\mp 0.69$	$\mp 0.51$
$t\bar{t} \rightarrow ll$	-1.25+1.30	$\mp 0.63$	$\mp 0.56$	$\mp 0.54$	-1.25+1.29	$\mp 0.62$	$\mp 0.56$	$\mp 0.55$
$tb$	-1.40+1.48	$\mp 0.63$	$\mp 0.61$	-0.77+0.81	-1.42+1.50	$\mp 0.63$	$\mp 0.60$	$\mp 0.63$
$tqb$	-1.29+1.35	-1.30+1.37	-0.97+1.02	-0.82+0.85	-1.28+1.34	-1.30+1.38	-1.00+1.06	-0.87+0.92
$WW \rightarrow l\nu jj$	-1.63+1.77	-1.58+1.73	-1.35+1.41	< 0.01	-1.45+1.57	-1.46+1.58	-1.21+1.26	< 0.01
$WZ \rightarrow l\nu jj$	-1.81+2.01	-0.93+0.99	-0.74+0.77	-4.49+5.10	-1.73+1.91	-0.99+1.05	-1.10+1.14	-1.15+1.24
$WZ \rightarrow jjll$	-1.72+1.85	-1.48+1.62	-1.48+1.62	-1.14+1.17	-1.43+1.53	-1.47+1.58	-1.37+1.47	-2.26+2.49
$ZZ \rightarrow jjll$	-1.27+1.31	$\mp 0.74$	-0.98+1.02	< 0.01	-1.33+1.39	-0.95+1.00	-0.90+0.95	$\mp 0.66$
$Z \rightarrow \tau^+\tau^-$	-1.20+1.30	-0.86+0.89	-1.65+1.82	< 0.01	-0.78+0.80	-0.99+1.10	$\mp 0.50$	< 0.01

TABLE LXXX. RELATIVE SYSTEMATIC UNCERTAINTY FROM THE SEMILEPTONIC  $B$ -TAGGING EFFICIENCY IN MONTE CARLO (%) FOR SINGLE TAGGED EVENTS.

Appendix D (Continued)

	e+jets			$\mu$ +jets		
	2 jets	3 jets	$\geq 4$ jets	2 jets	3 jets	$\geq 4$ jets
$W + \text{light}$	< 0.01	< 0.01	< 0.01	< 0.01	< 0.01	< 0.01
$W(c\bar{c})$	-1.91+2.07	-2.05+2.19	-1.49+1.55	-1.90+1.99	-2.00+2.14	-2.52+2.73
$W(b\bar{b})$	-3.30+3.66	-2.83+3.09	-2.73+2.95	-3.06+3.40	-2.73+2.95	-2.14+2.24
$Wc$	-1.37+1.44	-1.40+1.48	-1.36+1.43	-1.33+1.40	-1.27+1.32	-1.36+1.44
$Wc\bar{c}$	-2.88+3.11	-2.87+3.08	-2.75+2.96	-3.04+3.29	-3.08+3.42	-2.99+3.23
$Wb\bar{b}$	-3.25+3.56	-3.32+3.66	-3.06+3.37	-3.16+3.47	-3.20+3.50	-3.04+3.29
$W + \text{jets}$	-3.19+3.49	-3.20+3.52	-2.95+3.24	-3.10+3.41	-3.11+3.40	-2.90+3.13
$t\bar{t} \rightarrow l + \text{jets}$	-2.67+2.84	-2.64+2.82	-2.67+2.86	-2.55+2.69	-2.64+2.82	-2.65+2.84
$t\bar{t} \rightarrow ll$	-2.76+2.95	-2.72+2.91	-2.66+2.83	-2.74+2.93	-2.73+2.91	-2.73+2.92
$tb$	-2.91+3.14	-2.94+3.17	-3.32+3.68	-2.94+3.18	-2.92+3.15	-3.02+3.30
$tqb$	-3.07+3.34	-3.20+3.52	-3.26+3.63	-3.15+3.45	-3.12+3.41	-3.21+3.52
$WW \rightarrow l\nu jj$	-3.31+3.79	-1.62+1.71	< 0.01	-1.79+1.95	-2.08+2.18	< 0.01
$WZ \rightarrow l\nu jj$	-3.32+3.69	-3.05+3.23	-0.14+0.18	-3.69+4.17	-3.88+4.37	-9.11+10.99
$WZ \rightarrow jjll$	-1.59+1.68	-1.51+1.63	-1.14+1.20	-1.61+1.71	-1.31+1.40	-2.59+2.86
$ZZ \rightarrow jjll$	-2.70+2.84	-4.19+4.74	< 0.01	-3.20+3.50	-2.83+3.02	-2.51+2.62
$Z \rightarrow \tau^+\tau^-$	-8.98+10.78	-11.64+15.05	< 0.01	-2.49+2.68	-2.56+2.67	< 0.01

TABLE LXXXI. RELATIVE SYSTEMATIC UNCERTAINTY FROM THE SEMILEPTONIC  $B$ -TAGGING EFFICIENCY IN MONTE CARLO (%) FOR DOUBLE TAGGED EVENTS.

Appendix D (Continued)

	e+jets				$\mu$ +jets			
	1 jet	2 jets	3 jets	$\geq 4$ jets	1 jet	2 jets	3 jets	$\geq 4$ jets
$W + \text{light}$	< 0.01	< 0.01	< 0.01	< 0.01	< 0.01	< 0.01	< 0.01	< 0.01
$W(c\bar{c})$	$\pm 2.26$	$\pm 2.17$	$\pm 2.18$	$\pm 1.90$	$\pm 2.12$	$\pm 2.19$	$\pm 2.17$	$\pm 2.15$
$W(b\bar{b})$	< 0.01	$\pm 0.01$	$\pm 0.02$	$\pm 0.02$	< 0.01	< 0.01	$\pm 0.02$	$\pm 0.02$
$Wc$	$\pm 1.95$	$\pm 1.99$	$\pm 2.04$	$\pm 1.99$	$\pm 1.93$	$\pm 1.96$	$\pm 1.92$	$\pm 1.93$
$Wc\bar{c}$		$\pm 2.04$	$\pm 2.07$	$\pm 1.96$		$\pm 2.06$	$\pm 2.09$	$\pm 2.05$
$Wb\bar{b}$		< 0.01	< 0.01	< 0.01		< 0.01	< 0.01	< 0.01
$W + \text{jets}$	$\pm 0.88$	$\pm 0.81$	$\pm 0.69$	$\pm 0.65$	$\pm 0.86$	$\pm 0.79$	$\pm 0.69$	$\pm 0.69$
$t\bar{t} \rightarrow l + \text{jets}$	$\pm 0.10$	$\pm 0.04$	< 0.01	$\mp 0.01$	$\pm 0.11$	$\pm 0.04$	< 0.01	$\mp 0.01$
$t\bar{t} \rightarrow ll$	< 0.01	< 0.01	< 0.01	< 0.01	< 0.01	< 0.01	< 0.01	< 0.01
$tb$	< 0.01	< 0.01	< 0.01	< 0.01	< 0.01	< 0.01	< 0.01	< 0.01
$tqb$	< 0.01	< 0.01	< 0.01	< 0.01	< 0.01	< 0.01	< 0.01	< 0.01
$WW \rightarrow l\nu jj$	$\pm 2.20$	$\pm 2.06$	$\pm 1.91$	< 0.01	$\pm 2.00$	$\pm 2.09$	$\pm 1.85$	< 0.01
$WZ \rightarrow l\nu jj$	< 0.01	$\pm 0.01$	$\pm 0.24$	< 0.01	< 0.01	< 0.01	$\pm 0.06$	< 0.01
$WZ \rightarrow jj ll$	$\pm 2.28$	$\pm 2.19$	$\pm 2.10$	$\pm 2.12$	$\pm 2.07$	$\pm 2.10$	$\pm 2.00$	$\pm 2.77$
$ZZ \rightarrow jj ll$	< 0.01	$\pm 0.02$	< 0.01	< 0.01	$\pm 0.02$	$\pm 0.02$	< 0.01	< 0.01
$Z \rightarrow \tau^+ \tau^-$	$\pm 0.80$	$\pm 0.20$	$\pm 0.51$	< 0.01	$\pm 0.31$	$\pm 0.98$	$\pm 0.47$	< 0.01

TABLE LXXXII. RELATIVE SYSTEMATIC UNCERTAINTY FROM THE INCLUSIVE C-TAGGING EFFICIENCY IN MONTE CARLO (%) FOR SINGLE TAGGED EVENTS.

Appendix D (Continued)

	$e+$ jets			$\mu+$ jets		
	2 jets	3 jets	$\geq 4$ jets	2 jets	3 jets	$\geq 4$ jets
$W + \text{light}$	< 0.01	< 0.01	< 0.01	< 0.01	< 0.01	< 0.01
$W(c\bar{c})$	+2.83-2.81	+3.08-3.04	$\pm 2.38$	+2.87-2.85	+3.06-3.02	+3.64-3.58
$W(b\bar{b})$	$\pm 0.57$	$\pm 0.61$	$\pm 0.85$	$\pm 0.49$	$\pm 0.79$	$\pm 0.91$
$Wc$	$\pm 2.09$	$\pm 2.13$	$\pm 2.12$	$\pm 2.09$	$\pm 1.97$	$\pm 2.08$
$Wc\bar{c}$	+4.45-4.35	+4.42-4.32	+4.27-4.18	+4.53-4.43	+4.69-4.59	+4.54-4.44
$Wb\bar{b}$	< 0.01	$\pm 0.02$	$\pm 0.05$	< 0.01	$\pm 0.04$	$\pm 0.03$
$W + \text{jets}$	$\pm 0.38$	$\pm 0.41$	$\pm 0.51$	$\pm 0.37$	$\pm 0.47$	$\pm 0.59$
$t\bar{t} \rightarrow l+\text{jets}$	$\pm 0.34$	$\pm 0.26$	$\pm 0.26$	$\pm 0.32$	$\pm 0.25$	$\pm 0.26$
$t\bar{t} \rightarrow ll$	< 0.01	$\pm 0.01$	$\pm 0.04$	< 0.01	< 0.01	$\pm 0.03$
$tb$	< 0.01	$\pm 0.02$	$\pm 0.08$	< 0.01	$\pm 0.02$	$\pm 0.06$
$tgb$	$\pm 0.06$	$\pm 0.05$	$\pm 0.06$	$\pm 0.09$	$\pm 0.05$	$\pm 0.06$
$WW \rightarrow l\nu jj$	$\pm 2.24$	$\pm 2.21$	< 0.01	$\pm 2.52$	+3.18-3.14	< 0.01
$WZ \rightarrow l\nu jj$	< 0.01	$\pm 0.12$	< 0.01	< 0.01	< 0.01	< 0.01
$WZ \rightarrow jjll$	$\pm 2.57$	$\pm 2.24$	$\pm 2.15$	$\pm 2.32$	$\pm 2.04$	+3.05-3.07
$ZZ \rightarrow jjll$	$\pm 0.03$	< 0.01	< 0.01	$\pm 0.02$	$\pm 0.04$	< 0.01
$Z \rightarrow \tau^+\tau^-$	< 0.01	$\pm 0.03$	< 0.01	+3.52-3.47	< 0.01	< 0.01

TABLE LXXXIII. RELATIVE SYSTEMATIC UNCERTAINTY FROM THE INCLUSIVE  $C$ -TAGGING EFFICIENCY IN MONTE CARLO (%) FOR DOUBLE TAGGED EVENTS.

Appendix D (Continued)

	$e+$ jets				$\mu+$ jets			
	1 jet	2 jets	3 jets	$\geq 4$ jets	1 jet	2 jets	3 jets	$\geq 4$ jets
$W+\text{light}$	< 0.01	< 0.01	< 0.01	< 0.01	< 0.01	< 0.01	< 0.01	< 0.01
$W(c\bar{c})$	$\pm 4.01$	$\pm 3.57$	$\pm 3.34$	$\pm 3.25$	$\pm 3.89$	$\pm 3.52$	$\pm 3.26$	$\pm 3.16$
$W(b\bar{b})$	$\pm 3.90$	$\pm 3.59$	$\pm 3.35$	$\pm 3.51$	$\pm 3.90$	$\pm 3.53$	$\pm 3.40$	$\pm 3.52$
$Wc$	$\pm 3.82$	$\pm 3.57$	$\pm 3.57$	$\pm 3.49$	$\pm 3.81$	$\pm 3.61$	$\pm 3.52$	$\pm 3.45$
$Wc\bar{c}$		+3.35-3.37	+3.18-3.20	+3.07-3.10		+3.32-3.34	+3.10-3.12	+3.04-3.06
$Wb\bar{b}$		+1.63-1.78	+1.57-1.72	+1.43-1.57		+1.44-1.60	+1.51-1.64	+1.49-1.62
$W+\text{jets}$	$\pm 2.75$	+2.45-2.49	+2.17-2.21	+2.19-2.23	$\pm 2.73$	+2.33-2.37	+2.15-2.19	+2.20-2.24
$t\bar{t} \rightarrow l+\text{jets}$	$\pm 4.24$	+3.01-3.09	+1.86-2.02	+1.25-1.43	$\pm 4.23$	+2.94-3.03	+1.84-2.00	+1.25-1.43
$t\bar{t} \rightarrow ll$	$\pm 4.18$	+1.71-1.88	+1.47-1.65	+1.39-1.57	$\pm 4.17$	+1.70-1.87	+1.46-1.64	+1.45-1.63
$tb$	$\pm 4.04$	+1.54-1.72	+1.40-1.59	+1.65-1.83	$\pm 4.02$	+1.54-1.72	+1.46-1.64	+1.42-1.60
$tqb$	$\pm 3.87$	+3.48-3.50	+2.38-2.47	+1.87-2.01	$\pm 3.85$	+3.50-3.52	+2.39-2.48	+1.91-2.03
$WW \rightarrow l\nu jj$	$\pm 3.78$	$\pm 3.39$	$\pm 3.37$	< 0.01	$\pm 3.70$	$\pm 3.27$	$\pm 3.09$	< 0.01
$WZ \rightarrow l\nu jj$	$\pm 4.05$	+1.77-1.89	+1.47-1.59	$\pm 3.64$	$\pm 4.04$	+1.78-1.91	+1.93-2.03	+2.36-2.51
$WZ \rightarrow jjll$	$\pm 3.96$	$\pm 3.64$	$\pm 3.23$	$\pm 4.41$	$\pm 3.65$	$\pm 3.31$	$\pm 3.01$	$\pm 3.36$
$ZZ \rightarrow jjll$	$\pm 4.10$	+2.19-2.29	+2.03-2.14	< 0.01	$\pm 3.88$	+1.95-2.06	+1.82-1.92	+1.43-1.51
$Z \rightarrow \tau^+\tau^-$	$\pm 2.64$	+2.58-2.63	+2.22-2.25	< 0.01	$\pm 2.25$	$\pm 2.90$	+1.22-1.41	< 0.01

TABLE LXXXIV. RELATIVE SYSTEMATIC UNCERTAINTY FROM THE SEMILEPTONIC  $B$ -TAGGING EFFICIENCY IN DATA (%) FOR SINGLE TAGGED EVENTS.

Appendix D (Continued)

	e+jets			$\mu$ +jets		
	2 jets	3 jets	$\geq 4$ jets	2 jets	3 jets	$\geq 4$ jets
$W + \text{light}$	< 0.01	< 0.01	< 0.01	< 0.01	< 0.01	< 0.01
$W(c\bar{c})$	+4.11-4.08	+4.63-4.56	+4.94-4.84	+4.99-4.89	+4.79-4.70	+5.39-5.26
$W(b\bar{b})$	+7.03-6.79	+6.40-6.20	+5.11-5.01	+7.00-6.76	+6.28-6.10	+6.73-6.51
$Wc$	$\pm 3.66$	$\pm 3.75$	$\pm 3.70$	$\pm 3.76$	$\pm 3.68$	$\pm 3.68$
$Wc\bar{c}$	+7.55-7.28	+7.19-6.93	+6.89-6.66	+7.43-7.16	+6.80-6.58	+6.76-6.54
$Wb\bar{b}$	+7.44-7.18	+7.39-7.12	+7.04-6.81	+7.40-7.14	+7.09-6.85	+6.93-6.70
$W + \text{jets}$	+7.35-7.09	+7.20-6.95	+6.81-6.59	+7.29-7.03	+6.91-6.68	+6.77-6.55
$t\bar{t} \rightarrow l + \text{jets}$	+8.31-7.98	+7.83-7.55	+7.49-7.24	+8.28-7.95	+7.85-7.57	+7.49-7.25
$t\bar{t} \rightarrow ll$	+8.13-7.81	+7.90-7.60	+7.66-7.38	+8.14-7.82	+7.93-7.62	+7.67-7.39
$tb$	+8.05-7.74	+7.96-7.66	+7.98-7.67	+8.04-7.73	+7.92-7.62	+7.67-7.39
$tqb$	+7.40-7.14	+7.49-7.23	+7.50-7.23	+7.48-7.21	+7.43-7.17	+7.35-7.10
$WW \rightarrow l\nu jj$	+5.42-5.29	$\pm 3.44$	< 0.01	+3.62-3.60	+4.93-4.82	< 0.01
$WZ \rightarrow l\nu jj$	+7.18-6.93	+6.73-6.52	+0.15-0.11	+7.31-7.05	+7.15-6.91	+10.17-9.72
$WZ \rightarrow jjll$	+5.20-5.10	$\pm 3.52$	$\pm 4.49$	$\pm 3.56$	$\pm 3.19$	$\pm 3.57$
$ZZ \rightarrow jjll$	+7.25-7.00	+7.66-7.39	< 0.01	+7.23-6.98	+6.83-6.60	+5.84-5.68
$Z \rightarrow \tau^+\tau^-$	+9.67-9.27	+10.44-10.04	< 0.01	+6.18-6.00	+8.56-8.21	< 0.01

TABLE LXXXV. RELATIVE SYSTEMATIC UNCERTAINTY FROM THE SEMILEPTONIC  $B$ -TAGGING EFFICIENCY IN DATA (%) FOR DOUBLE TAGGED EVENTS.

Appendix D (Continued)

	e+jets				$\mu$ +jets			
	1 jet	2 jets	3 jets	$\geq 4$ jets	1 jet	2 jets	3 jets	$\geq 4$ jets
$W + \text{light}$	$\pm 3.55$	$\pm 3.60$	$\pm 3.67$	$\pm 3.76$	$\pm 3.61$	$\pm 3.75$	$\pm 3.83$	$\pm 3.75$
$W(c\bar{c})$	$< 0.01$	$\pm 0.11$	$\pm 0.22$	$\pm 0.28$	$< 0.01$	$\pm 0.10$	$\pm 0.22$	$\pm 0.26$
$W(b\bar{b})$	$< 0.01$	$< 0.01$	$\pm 0.02$	$\pm 0.03$	$< 0.01$	$< 0.01$	$\pm 0.02$	$\pm 0.02$
$Wc$	$< 0.01$	$\pm 0.08$	$\pm 0.16$	$\pm 0.23$	$< 0.01$	$\pm 0.09$	$\pm 0.17$	$\pm 0.23$
$Wc\bar{c}$		$< 0.01$	$\pm 0.06$	$\pm 0.09$		$< 0.01$	$\pm 0.06$	$\pm 0.09$
$Wb\bar{b}$		$< 0.01$	$< 0.01$	$< 0.01$		$< 0.01$	$< 0.01$	$< 0.01$
$W + \text{jets}$	$\pm 1.03$	$\pm 0.73$	$\pm 0.85$	$\pm 0.80$	$\pm 1.06$	$\pm 0.85$	$\pm 0.88$	$\pm 0.79$
$t\bar{t} \rightarrow l + \text{jets}$	$\pm 0.02$	$< 0.01$	$< 0.01$	$< 0.01$	$\pm 0.03$	$< 0.01$	$< 0.01$	$< 0.01$
$t\bar{t} \rightarrow ll$	$< 0.01$	$< 0.01$	$< 0.01$	$< 0.01$	$< 0.01$	$< 0.01$	$< 0.01$	$< 0.01$
$tb$	$< 0.01$	$< 0.01$	$< 0.01$	$< 0.01$	$< 0.01$	$< 0.01$	$< 0.01$	$< 0.01$
$tqb$	$\pm 0.01$	$\pm 0.01$	$< 0.01$	$< 0.01$	$\pm 0.01$	$\pm 0.01$	$< 0.01$	$< 0.01$
$WW \rightarrow l\nu jj$	$\pm 0.35$	$\pm 0.30$	$\pm 0.30$	$< 0.01$	$\pm 0.36$	$\pm 0.33$	$\pm 0.30$	$\pm 3.90$
$WZ \rightarrow l\nu jj$	$\pm 0.09$	$\pm 0.12$	$\pm 0.18$	$\pm 0.92$	$\pm 0.10$	$\pm 0.15$	$\pm 0.17$	$\pm 0.28$
$WZ \rightarrow jj ll$	$\pm 0.47$	$\pm 0.33$	$\pm 0.49$	$\pm 0.06$	$\pm 0.49$	$\pm 0.33$	$\pm 0.52$	$\pm 0.63$
$ZZ \rightarrow jj ll$	$\pm 0.06$	$\pm 0.10$	$\pm 0.19$	$\pm 3.75$	$\pm 0.09$	$\pm 0.13$	$\pm 0.14$	$\pm 0.14$
$Z \rightarrow \tau^+\tau^-$	$\pm 1.62$	$\pm 0.96$	$\pm 0.92$	$\pm 4.05$	$\pm 1.43$	$\pm 1.06$	$\pm 0.44$	$\pm 3.48$

TABLE LXXXVI. RELATIVE SYSTEMATIC UNCERTAINTY FROM THE NEGATIVE TAGGING RATE IN DATA (%) FOR SINGLE TAGGED EVENTS.

Appendix D (Continued)

	$e+$ jets			$\mu+$ jets		
	2 jets	3 jets	$\geq 4$ jets	2 jets	3 jets	$\geq 4$ jets
$W + \text{light}$	+7.37-7.14	+7.55-7.28	+7.67-7.39	+7.84-7.54	+7.72-7.43	+7.70-7.42
$W(c\bar{c})$	$\pm 3.00$	$\pm 2.59$	$\pm 2.31$	$\pm 2.04$	$\pm 2.35$	$\pm 1.93$
$W(b\bar{b})$	$\pm 0.66$	$\pm 0.79$	$\pm 1.74$	$\pm 0.49$	$\pm 0.94$	$\pm 0.83$
$Wc$	$\pm 3.90$	$\pm 3.89$	$\pm 3.83$	$\pm 3.82$	$\pm 3.93$	$\pm 3.84$
$Wc\bar{c}$	< 0.01	$\pm 0.25$	$\pm 0.36$	< 0.01	$\pm 0.21$	$\pm 0.35$
$Wb\bar{b}$	< 0.01	$\pm 0.04$	$\pm 0.08$	< 0.01	$\pm 0.04$	$\pm 0.08$
$W + \text{jets}$	$\pm 0.11$	$\pm 0.22$	$\pm 0.32$	$\pm 0.12$	$\pm 0.22$	$\pm 0.31$
$t\bar{t} \rightarrow l+\text{jets}$	$\pm 0.07$	$\pm 0.06$	$\pm 0.06$	$\pm 0.07$	$\pm 0.05$	$\pm 0.06$
$t\bar{t} \rightarrow ll$	< 0.01	$\pm 0.03$	$\pm 0.06$	< 0.01	$\pm 0.03$	$\pm 0.06$
$tb$	< 0.01	$\pm 0.02$	$\pm 0.05$	< 0.01	$\pm 0.02$	$\pm 0.05$
$tgb$	$\pm 0.28$	$\pm 0.10$	$\pm 0.09$	$\pm 0.30$	$\pm 0.09$	$\pm 0.09$
$WW \rightarrow l\nu jj$	$\pm 2.22$	$\pm 3.76$	< 0.01	$\pm 3.42$	$\pm 1.72$	+8.05-7.73
$WZ \rightarrow l\nu jj$	< 0.01	$\pm 0.02$	+7.35-7.18	< 0.01	$\pm 0.03$	$\pm 0.07$
$WZ \rightarrow jjll$	$\pm 2.27$	$\pm 3.65$	+3.69-3.67	$\pm 3.33$	+3.75-3.73	+5.34-5.32
$ZZ \rightarrow jjll$	$\pm 0.02$	$\pm 0.09$	+7.88-7.69	< 0.01	$\pm 0.03$	$\pm 0.06$
$Z \rightarrow \tau^+\tau^-$	$\pm 0.08$	$\pm 0.35$	+8.78-8.32	$\pm 1.44$	$\pm 0.07$	+6.90-6.67

TABLE LXXXVII. RELATIVE SYSTEMATIC UNCERTAINTY FROM THE NEGATIVE TAGGING RATE IN DATA (%) FOR DOUBLE TAGGED EVENTS.

Appendix D (Continued)

	e+jets				$\mu$ +jets			
	1 jet	2 jets	3 jets	$\geq 4$ jets	1 jet	2 jets	3 jets	$\geq 4$ jets
$W+\text{light}$	$\pm 2.48$	$\pm 2.47$	$\pm 2.47$	$\pm 2.46$	$\pm 2.48$	$\pm 2.47$	$\pm 2.47$	$\pm 2.46$
$W(c\bar{c})$	$< 0.01$	$\pm 0.07$	$\pm 0.14$	$\pm 0.19$	$< 0.01$	$\pm 0.07$	$\pm 0.15$	$\pm 0.17$
$W(b\bar{b})$	$< 0.01$	$< 0.01$	$\pm 0.01$	$\pm 0.02$	$< 0.01$	$< 0.01$	$\pm 0.01$	$\pm 0.01$
$Wc$	$< 0.01$	$\pm 0.05$	$\pm 0.10$	$\pm 0.15$	$< 0.01$	$\pm 0.06$	$\pm 0.11$	$\pm 0.16$
$Wc\bar{c}$		$< 0.01$	$\pm 0.04$	$\pm 0.06$		$< 0.01$	$\pm 0.04$	$\pm 0.06$
$Wb\bar{b}$		$< 0.01$	$< 0.01$	$< 0.01$		$< 0.01$	$< 0.01$	$< 0.01$
$W+\text{jets}$	$\pm 0.72$	$\pm 0.50$	$\pm 0.57$	$\pm 0.52$	$\pm 0.73$	$\pm 0.56$	$\pm 0.57$	$\pm 0.52$
$t\bar{t} \rightarrow l+\text{jets}$	$\pm 0.02$	$< 0.01$	$< 0.01$	$< 0.01$	$\pm 0.02$	$< 0.01$	$< 0.01$	$< 0.01$
$t\bar{t} \rightarrow ll$	$< 0.01$	$< 0.01$	$< 0.01$	$< 0.01$	$< 0.01$	$< 0.01$	$< 0.01$	$< 0.01$
$tb$	$< 0.01$	$< 0.01$	$< 0.01$	$< 0.01$	$< 0.01$	$< 0.01$	$< 0.01$	$< 0.01$
$tqb$	$< 0.01$	$< 0.01$	$< 0.01$	$< 0.01$	$< 0.01$	$< 0.01$	$< 0.01$	$< 0.01$
$WW \rightarrow l\nu jj$	$\pm 0.24$	$\pm 0.21$	$\pm 0.21$	$< 0.01$	$\pm 0.24$	$\pm 0.24$	$\pm 0.21$	$\pm 2.47$
$WZ \rightarrow l\nu jj$	$\pm 0.06$	$\pm 0.08$	$\pm 0.12$	$\pm 0.62$	$\pm 0.07$	$\pm 0.10$	$\pm 0.12$	$\pm 0.14$
$WZ \rightarrow jj ll$	$\pm 0.30$	$\pm 0.22$	$\pm 0.34$	$\pm 0.04$	$\pm 0.32$	$\pm 0.23$	$\pm 0.37$	$\pm 0.38$
$ZZ \rightarrow jj ll$	$\pm 0.04$	$\pm 0.07$	$\pm 0.13$	$\pm 2.46$	$\pm 0.06$	$\pm 0.09$	$\pm 0.10$	$\pm 0.09$
$Z \rightarrow \tau^+ \tau^-$	$\pm 1.07$	$\pm 0.63$	$\pm 0.58$	$\pm 2.46$	$\pm 1.00$	$\pm 0.73$	$\pm 0.30$	$\pm 2.46$

TABLE LXXXVIII. RELATIVE SYSTEMATIC UNCERTAINTY FROM THE  $SF_{ll}$  (%) FOR SINGLE TAGGED EVENTS.

Appendix D (Continued)

	e+jets			$\mu$ +jets		
	2 jets	3 jets	$\geq 4$ jets	2 jets	3 jets	$\geq 4$ jets
W+light	+5.03-4.85	+5.03-4.91	+5.01-4.90	+5.04-4.87	+5.02-4.90	+5.01-4.90
$W(c\bar{c})$	$\pm 2.06$	$\pm 1.71$	$\pm 1.59$	$\pm 1.43$	$\pm 1.57$	$\pm 1.24$
$W(b\bar{b})$	$\pm 0.44$	$\pm 0.52$	$\pm 1.10$	$\pm 0.33$	$\pm 0.63$	$\pm 0.56$
$Wc$	$\pm 2.48$	$\pm 2.51$	$\pm 2.53$	$\pm 2.48$	$\pm 2.51$	$\pm 2.54$
$Wc\bar{c}$	< 0.01	$\pm 0.13$	$\pm 0.24$	< 0.01	$\pm 0.15$	$\pm 0.23$
$Wb\bar{b}$	< 0.01	$\pm 0.03$	$\pm 0.05$	< 0.01	$\pm 0.03$	$\pm 0.05$
$W+$ jets	$\pm 0.07$	$\pm 0.14$	$\pm 0.21$	$\pm 0.08$	$\pm 0.15$	$\pm 0.21$
$t\bar{t} \rightarrow l+$ jets	$\pm 0.05$	$\pm 0.04$	$\pm 0.04$	$\pm 0.04$	$\pm 0.04$	$\pm 0.04$
$t\bar{t} \rightarrow ll$	< 0.01	$\pm 0.02$	$\pm 0.04$	< 0.01	$\pm 0.02$	$\pm 0.04$
$tb$	< 0.01	$\pm 0.02$	$\pm 0.03$	< 0.01	$\pm 0.02$	$\pm 0.03$
$tqb$	$\pm 0.16$	$\pm 0.05$	$\pm 0.05$	$\pm 0.17$	$\pm 0.05$	$\pm 0.05$
$WW \rightarrow l\nu jj$	$\pm 1.63$	$\pm 2.58$	< 0.01	$\pm 2.47$	$\pm 1.25$	+4.96-5.02
$WZ \rightarrow l\nu jj$	< 0.01	$\pm 0.01$	+4.89-4.86	< 0.01	$\pm 0.02$	$\pm 0.06$
$WZ \rightarrow jjll$	$\pm 1.56$	$\pm 2.62$	+2.50-2.48	$\pm 2.40$	$\pm 2.67$	+2.87-2.90
$ZZ \rightarrow jjll$	$\pm 0.01$	$\pm 0.06$	+4.98-4.91	< 0.01	$\pm 0.02$	$\pm 0.04$
$Z \rightarrow \tau^+\tau^-$	$\pm 0.06$	$\pm 0.23$	+5.02-4.86	$\pm 1.08$	$\pm 0.05$	+5.06-4.95

TABLE LXXXIX. RELATIVE SYSTEMATIC UNCERTAINTY FROM THE  $SF_{ll}$  (%) FOR DOUBLE TAGGED EVENTS.

## Appendix D (Continued)

	e+jets				$\mu$ +jets			
	1 jet	2 jets	3 jets	$\geq 4$ jets	1 jet	2 jets	3 jets	$\geq 4$ jets
$W+\text{light}$	$\pm 3.15$	$\pm 3.43$	$\pm 3.38$	$\pm 3.32$	$\pm 3.18$	$\pm 3.30$	$\pm 3.33$	$\pm 3.32$
$W(c\bar{c})$	$< 0.01$	$\pm 0.10$	$\pm 0.19$	$\pm 0.25$	$< 0.01$	$\pm 0.09$	$\pm 0.20$	$\pm 0.24$
$W(b\bar{b})$	$< 0.01$	$< 0.01$	$\pm 0.02$	$\pm 0.03$	$< 0.01$	$< 0.01$	$\pm 0.02$	$\pm 0.02$
$Wc$	$< 0.01$	$\pm 0.08$	$\pm 0.15$	$\pm 0.22$	$< 0.01$	$\pm 0.08$	$\pm 0.16$	$\pm 0.22$
$Wc\bar{c}$			$< 0.01$	$\pm 0.05$	$\pm 0.08$		$< 0.01$	$\pm 0.05$
$Wb\bar{b}$			$< 0.01$	$< 0.01$	$< 0.01$		$< 0.01$	$< 0.01$
$W+\text{jets}$	$\pm 0.91$	$\pm 0.70$	$\pm 0.78$	$\pm 0.71$	$\pm 0.93$	$\pm 0.75$	$\pm 0.77$	$\pm 0.71$
$t\bar{t} \rightarrow l+\text{jets}$	$\pm 0.02$	$< 0.01$	$< 0.01$	$< 0.01$	$\pm 0.02$	$< 0.01$	$< 0.01$	$< 0.01$
$t\bar{t} \rightarrow ll$	$< 0.01$	$< 0.01$	$< 0.01$	$< 0.01$	$< 0.01$	$< 0.01$	$< 0.01$	$< 0.01$
$tb$	$< 0.01$	$< 0.01$	$< 0.01$	$< 0.01$	$< 0.01$	$< 0.01$	$< 0.01$	$< 0.01$
$tqb$	$< 0.01$	$< 0.01$	$< 0.01$	$< 0.01$	$< 0.01$	$< 0.01$	$< 0.01$	$< 0.01$
$WW \rightarrow l\nu jj$	$\pm 0.29$	$\pm 0.29$	$\pm 0.31$	$< 0.01$	$\pm 0.29$	$\pm 0.32$	$\pm 0.31$	$\pm 3.18$
$WZ \rightarrow l\nu jj$	$\pm 0.07$	$\pm 0.11$	$\pm 0.18$	$\pm 0.93$	$\pm 0.08$	$\pm 0.14$	$\pm 0.17$	$\pm 0.26$
$WZ \rightarrow jj ll$	$\pm 0.35$	$\pm 0.29$	$\pm 0.45$	$\pm 0.08$	$\pm 0.41$	$\pm 0.32$	$\pm 0.51$	$\pm 0.59$
$ZZ \rightarrow jj ll$	$\pm 0.05$	$\pm 0.09$	$\pm 0.17$	$\pm 3.16$	$\pm 0.07$	$\pm 0.13$	$\pm 0.13$	$\pm 0.12$
$Z \rightarrow \tau^+ \tau^-$	$\pm 1.29$	$\pm 0.83$	$\pm 0.77$	$\pm 3.50$	$\pm 1.27$	$\pm 0.97$	$\pm 0.44$	$\pm 3.20$

TABLE XC. RELATIVE SYSTEMATIC UNCERTAINTY FROM THE  $SF_{hf}$  (%) FOR SINGLE TAGGED EVENTS.

Appendix D (Continued)

	e+jets			$\mu$ +jets		
	2 jets	3 jets	$\geq 4$ jets	2 jets	3 jets	$\geq 4$ jets
W+light	+6.97-6.76	+6.97-6.76	+6.66-6.44	+6.67-6.49	+6.69-6.50	+6.75-6.53
$W(c\bar{c})$	$\pm 2.83$	$\pm 2.29$	$\pm 2.08$	$\pm 1.89$	$\pm 2.10$	$\pm 1.74$
$W(b\bar{b})$	$\pm 0.59$	$\pm 0.70$	$\pm 1.56$	$\pm 0.45$	$\pm 0.84$	$\pm 0.73$
$Wc$	$\pm 3.58$	$\pm 3.66$	$\pm 3.64$	$\pm 3.43$	$\pm 3.59$	$\pm 3.65$
$Wc\bar{c}$	< 0.01	$\pm 0.19$	$\pm 0.32$	< 0.01	$\pm 0.19$	$\pm 0.32$
$Wb\bar{b}$	< 0.01	$\pm 0.04$	$\pm 0.07$	< 0.01	$\pm 0.04$	$\pm 0.07$
$W+$ jets	$\pm 0.10$	$\pm 0.19$	$\pm 0.28$	$\pm 0.11$	$\pm 0.20$	$\pm 0.28$
$t\bar{t} \rightarrow l+$ jets	$\pm 0.06$	$\pm 0.05$	$\pm 0.06$	$\pm 0.05$	$\pm 0.05$	$\pm 0.05$
$t\bar{t} \rightarrow ll$	< 0.01	$\pm 0.03$	$\pm 0.05$	< 0.01	$\pm 0.03$	$\pm 0.06$
$tb$	< 0.01	$\pm 0.02$	$\pm 0.05$	< 0.01	$\pm 0.03$	$\pm 0.05$
$tqb$	$\pm 0.22$	$\pm 0.08$	$\pm 0.08$	$\pm 0.23$	$\pm 0.08$	$\pm 0.08$
$WW \rightarrow l\nu jj$	$\pm 2.32$	$\pm 4.28$	< 0.01	$\pm 3.48$	$\pm 1.87$	+7.85-7.62
$WZ \rightarrow l\nu jj$	< 0.01	$\pm 0.02$	+7.85-7.59	< 0.01	$\pm 0.03$	$\pm 0.09$
$WZ \rightarrow jj ll$	$\pm 2.05$	$\pm 3.41$	$\pm 4.95$	$\pm 3.34$	+3.78-3.76	$\pm 5.13$
$ZZ \rightarrow jj ll$	$\pm 0.02$	$\pm 0.08$	+6.62-6.53	< 0.01	$\pm 0.04$	$\pm 0.06$
$Z \rightarrow \tau^+\tau^-$	$\pm 0.09$	$\pm 0.36$	+7.39-7.09	$\pm 1.57$	$\pm 0.06$	+6.78-6.56

TABLE XCI. RELATIVE SYSTEMATIC UNCERTAINTY FROM THE  $SF_{hf}$  (%) FOR DOUBLE TAGGED EVENTS.

## CITED LITERATURE

1. M. J. G. Veltman: Physica 29 186, 1963);  
G. 't Hooft: Gauge Field Theory, in Proceedings of the Adriatic Meeting, Rovinj (1973), ed. M. Martinis et al., North Holland / Am. Elsevier, p.321.
2. D. Griffiths: Introduction to Elementary Particles, Wiley, 1987.
3. S. Weinberg: Phys. Rev. Lett. 19 1264, 1967  
S. L. Glashow: Nucl. Phys. 22 579, 1961.
4. D. J. Gross and F. Wilczek: Phys. Rev. D 8 3633, 1973.
5. CDF Collaboration: Observation of the Top Quark in  $p\bar{p}$  Collisions with the Collider Detector at Fermilab Phys. Rev. Lett. 74 2626. 1995.
6. D0 Collaboration: Observation of the Top Quark Phys. Rev. Lett. 74 2632, 1995.
7. CDF Collaboration: Study of  $t\bar{t}$  Production in  $p\bar{p}$  Collisions Using Total Transverse Energy Phys. Rev. Lett. 75, 3997, 1995.
8. M. K. Gaillard, P. Grannis and F. J. Sciulli: The Standard Model of Particle Physics Rev. Mod. Phys. 71 96-111, 1999.
9. K. Kodama et al. : Observation of tau neutrino interactions Physics Letters B 504 218-224, 2001.
10. P. W. Higgs: Phys. Lett. 12 132, 1964;
11. P. W. Higgs: Phys. Rev. Lett. 145 1156, 1966;
12. F. Englert and R. Brout: Phys. Rev. Lett. 13 321, 1964;
13. G. S. Guralnik, C. R. Hagen and T. W. B. Kibble: Phys. Rev. Lett. 13 585, 1964.
14. LEP Collaborations: Phys. Lett. B 276 247, 1992.

15. LEP Collaboration: [arXiv:hep-ex/0509008](https://arxiv.org/abs/hep-ex/0509008), 2005.
16. CDF Collaboration and DØ Collaboration and Tevatron Electroweak Working Group: [arXiv:hep-ex/0404010](https://arxiv.org/abs/hep-ex/0404010), 2004.
17. CDF Collaboration and DØ Collaboration and Tevatron Electroweak Working Group: Combination of CDF and DØ Results on the Top Quark Mass, [arXiv:hep-ex/0507091](https://arxiv.org/abs/hep-ex/0507091), 2005.
18. CDF and DØ Collaborations: [FERMILAB-CONF-01-095-E](https://cds.cern.ch/record/320000), 2001.
19. ATLAS Collaboration: “ATLAS: Detector and physics performance technical design report.” [CERN-LHCC-99-14](https://cds.cern.ch/record/290000), 1999.
20. D. Chakraborty, J. Konigsberg, D. Rainwater: Review of Top Quark Physics [arXiv:hep-ph/0303092](https://arxiv.org/abs/hep-ph/0303092), 2003.
21. DØ Collaboration: Spin Correlation in  $t\bar{t}$  Production from  $p\bar{p}$  Collisions at  $\sqrt{s} = 1.8$  TeV [Phys. Rev. Lett. 85 256](https://doi.org/10.1103/PhysRevLett.85.256), 2000.
22. DØ Collaboration Measurement of the  $W$  helicity in  $t\bar{t}$  decays at  $\sqrt{s} = 1.96$  TeV in the Lepton+jets Final States using a lifetime tag [Conference DØ-Note 4545](https://cds.cern.ch/record/320000), 2005.
23. DØ Collaboration Measurement of the charge of the Top quark with the DØ detector. [Conference DØ-Note 4876](https://cds.cern.ch/record/320000), 2005.
24. DØ Collaboration Search for a  $t\bar{t}$  resonance in  $p\bar{p}$  Collisions at  $\sqrt{s} = 1.96$  TeV in the Lepton+jets Final State. [Conference DØ-Note 4880](https://cds.cern.ch/record/320000), 2005.
25. LEP Collaboration: “A combination of preliminary electroweak measurements and constraints on the standard model,” [arXiv:hep-ex/0312023](https://arxiv.org/abs/hep-ex/0312023), 2004.
26. T. van Ritbergen and R. G. Stuart: [Phys. Rev. Lett. 82 488](https://doi.org/10.1103/PhysRevLett.82.488), 1999.
27. LEP Collaboration:  
<http://lepewwwg.web.cern.ch/LEPEWWG/plots/summer2005/>.
28. J .C. Collins and D. E. Soper: [Ann. Rev. Nucl. Part. Sci. 37 383](https://doi.org/10.1146/annurev.ns.37.120887.001533), 1987.

29. J. Huston et al: [JHEP 0207 012](#), 2002.
30. A. D. Martin, R. G. Roberts, W. J. Stirling and R. S. Thorne: [Phys. Lett. B 604](#) 61, 2004.
31. H. L. Lai et al: [Eur. Phys. J. C 12](#) 375, 2000.
32. A. M. Cooper-Sarkar, R. C. E. Devenish, A. De Roeck: [Int. J. Mod. Phys. A 13](#) 3385-3586, 1998.
33. P. Nason, S. Dawson and R. K. Ellis: [Nucl. Phys. B 303](#) 607, 1988.
34. W. Beenakker, H. Kuijf, W. L. van Neerven and J. Smith: [Phys. Rev. D 40](#) 54, 1989.
35. S. Catani, M. L. Mangano, P. Nason and L. Trentadue: [Nucl.Phys. B 478](#) 273-310, 1996.  
S. Catani, M. L. Mangano, P. Nason and L. Trentadue: [Phys. Lett. B 378](#) 329, 1996.
36. R. Bonciani, S. Catani, M. L. Mangano and P. Nason: [Nucl.Phys. B 529](#) 424-450, 1998.
37. R. K. Ellis, W. J. Sterling and B. R. Webber: [QCD and Collider Physics](#), Cambridge University Press, 1996.
38. A. D. Martin et al: [arXiv:hep-ph/0211080](#), 2002.
39. N. Kidonakis and R. Vogt: [Phys. Rev. D 68](#) 114014, 2003. [Eur. Phys. J. C 33](#), 2004.
40. Cacciari et al: [arXiv:hep-ph/0303085](#), 2003.
41. B. W. Harris, E. Laenen, L. Phaf, Z. Sullivan and S. Weinzierl: [Phys. Rev. D 66](#) 054024, 2002.
42. S. Catani: [arXiv:hep-ph/0005233](#), 1999.
43. DØ Collaboration: [Phys. Lett. B 517](#) 282, 2001.
44. CDF Collaboration: [Phys. Rev. D 65](#) 091102, 2002.
45. DØ Collaboration: [Phys. Let. B 622](#) 265, 2005.

46. CDF Collaboration: [arXiv:hep-ex/0410058](#), 2004.
47. A. Czarnecki and K. Melnikov: [Nucl. Phys. B 544](#) 520, 1999.
48. CDF Collaboration: [Phys. Rev. Lett. 86](#) 3233, 2001.
49. DØ Collaboration: Measurement of  $BR(t \rightarrow Wb)/BR(t \rightarrow Wq)$  at DØ [Conference DØ-Note 4833](#), (2005).
50. CDF Collaboration: [Phys. Rev. Lett. 80](#) 2525, 1998.
51. DØ Collaboration: Direct Search for Charged Higgs Bosons in Decays of Top Quarks [Phys. Rev. Lett. 88](#), 151803, 2002.
52. DØ Collaboration Measurement of the  $t\bar{t}$  Production Cross Section at  $\sqrt{s} = 1.96$  TeV in Dilepton Final States at DØ. [Conference DØ-Note 4850](#), 2005.
53. DØ Collaboration Measurement of the  $t\bar{t}$  Production Cross Section at  $\sqrt{s} = 1.96$  TeV in the all-Hadronic Final State. [Conference DØ-Note 4879](#), 2005.
54. J. M. Campbell and R. K. Ellis: “An update on vector boson pair production at hadron colliders”, [Phys. Rev. D 60](#), 113006, 1999.
55. DØ Collaboration: “Measurement of the  $W W$  production cross section in p anti-p collisions at  $s^{**}(1/2) = 1.96$ -TeV,” [arXiv:hep-ex/0410066](#), 2005.
56. F. A. Berends, W. T. Giele, H. Kuif, R. Kleiss and W. J. Stirling: [Phys. Lett. B 224](#), 237, 1989.
57. M. L. Mangano et al: ALPGEN, a Generator for Hard Multiparton Processes in Hadronic Collisions [hep-ph/0206293](#), 2003.
58. CDF Collaboration: [Phys. Rev. D 65](#) 092002, 2002.
59. T. Sjöstrand, L. Lönnblad and S. Mrenna: PYTHIA 6.2: PHYSICS AND MANUAL [hep-ph/0108264](#), 2001.
60. G. Marchesini et al: HERWIG: A Monte Carlo event generator for simulating hadron emission reactions with interfering gluons. [Comp. Phys. Comm. 67](#), 1992.

61. R. Brun et al: GEANT: user guide and reference manual [CERN DD 78-2](#), 1978.
62. M. Klute, L. Phaf, D. Whiteson: TopAnalyze - A Framework Analyze Package for Top Group Analyses [DØ-Note 4122](#), 2003.
63. ROOT: an Object-Oriented Data Analysis Framework  
<http://root.cern.ch>
64. T. Nunnemann: NNLO Cross Sections for Drell-Yan,  $Z$  and  $W$  Production using Modern Parton Distribution Functions, [DØ Note 4476](#), 2004.
65. D. J. Lange: [Nucl. Instrum. Meth. A 462](#) 152, 2001.
66. Z. Was and P. Golonka: [arXiv:hep-ph/0411377](#), 2004.
67. S. Catani, F. Krauss, R. Kuhn and B. R. Webber: [JHEP 0111](#), 063, 2001. [arXiv:hep-ph/0109231].
68. M. Mangano: Talk given at the Matrix Element and Monte Carlo Tuning Workshop, Fermilab, Nov 16 2002.  
<http://cepa.fnal.gov/personal/mrenna/tuning/nov2002/mlm.pdf>
69. S. Willenbrock: “Hadron Colliders, the Standard Model and Beyond”, [hep-ph/0212032](#), 2002.
70. S. Klimenko, J. Konigsberg, T. M. Liss: [FERMILAB-FN-0741](#), 2003.
71. W. T. Giele and S. A. Keller: Hard scattering based luminosity measurement at hadron colliders [arXiv:hep-ph/0104053](#), 2001.
72. S. I. Alekhin: The NNLO predictions for the rates of the  $W / Z$  production in (anti)-p p collisions [arXiv:hep-ph/0307219](#), 2003.
73. D0 Collaboration: Measurement of  $Z \rightarrow ee$  and  $W \rightarrow e\nu$  Production Cross Sections with  $|\eta| < 2.3$  [Conference DØ-Note 4403](#), 2004.
74. D0 Collaboration: Measurement of the Cross section for Inclusive  $Z$  Production in Di-muon Final States at  $\sqrt{s} = 1.96$  TeV [Conference DØ-Note 4573](#), 2004.

75. Thompson, J.: Introduction to Colliding Beams at Fermilab. FERMILAB-TM-1909, 1994.
76. General Reference Documents for Accelerators. 2002.  
[http://www-numi.fnal.gov/workgrps/protonwg/accel\\_reference.html](http://www-numi.fnal.gov/workgrps/protonwg/accel_reference.html).
77. Accelerator Concepts Rookie Books. 2003.  
[http://www-bdnew.fnal.gov/operations/rookie\\_books/rbooks.html](http://www-bdnew.fnal.gov/operations/rookie_books/rbooks.html).
78. Edmunds, D.: RunII a Tevatron Beam Structure.  
[http://www.pa.msu.edu/hep/d0/ftp/l1/framework/drawings/run\\_ia\\_beam\\_structure.ps](http://www.pa.msu.edu/hep/d0/ftp/l1/framework/drawings/run_ia_beam_structure.ps).
79. Particle Data Group Collaboration: Phys. Lett. 1B, 592, 2004.
80. Ferbel, T.: A Brief Description of the D0 Detector in Run II. 2004.  
<http://www-d0.fnal.gov/Run2Physics/WWW/templates/detector.tex>.
81. D0 Collaboration: The Upgraded D0 Detector. hep-ph/0507191, 2005.
82. C-C.Miao: FERMILAB-CONF-98-395-E, 1998.
83. T. Edwards et al.: FERMILAB-TM-2278-EB, 2004.
84. E. Kajfasz: DØ Silicon Microstrip Tracker for RunIIa. hep-ex/0112014, 2001.
85. T. Zimmermann et al.: The SVXII Readout chip IEEE Trans. Nucl. Sci. NS42 803, 1995.
86. D0 Collaboration: The DØ Upgrade FERMILAB-PUB-96/357-E, 1996.
87. D0 Collaboration: The D0 Upgrade: Central Tracker Technical Design Report. 1999.  
[http://d0server1.fnal.gov/users/stefan/www/CFT\\_TDR/CFT\\_TDR.ps](http://d0server1.fnal.gov/users/stefan/www/CFT_TDR/CFT_TDR.ps).
88. J. Brzenziak et al: FERMILAB-TM-1886, 1994.
89. Adams, M. et al.: Design Report of the Central Preshower Detector for the D0 Upgrade. 1996.  
<http://d0server1.fnal.gov/users/qianj/CPS/doc/dn3104.pdf>.
90. Gordeev, A. et al.: Technical Design Report of the Forward Preshower Detector for the D0 Upgrade. D0 Note 3445, 1998.

91. L. Groers: DØ Calorimeter Upgrades for Tevatron Run II DØ-Note 4240 Proceedings for the IXth International Conference on Calorimetry in Particle Physics, Annecy, France, Oct 9-14, 2000.
92. D0 Collaboration: Nucl. Instrum. Meth. A, 324/53, 1993.
93. D0 Collaboration: Phys. Rev. D 58/092003, 1998.
94. J. Stark: Internal Communication.
95. T. Diehl et al.: Technical Design of the Central Muon System DØ-Note 3365, March 1998.
96. T. Diehl et al.: Technical Design for the DØ Forward Muon Tracking Detector Based on Mini-Drift Tubes DØ-Note 3366, December 1997.
97. T. Diehl et al.: Technical Design Report for the DØ forward trigger scintillator counters DØ-Note 3237, November 1987.
98. J. Buttler: Local Muon Momentum Resolution DØ-Note 4002, July 2002.
99. D0 Collaboration: Reconstruction of B Hadron Signals at DØ Conference DØ-Note 4481, 2004.
100. A. Brandt et al: Fermilab-Pub-97-377, 1997.
101. D0 Collaboration: d0reco. 2004.  
<http://wwwd0.fnal.gov/Run2Physics/WWW/algorithm.htm>.
102. R. E. Kalman: J. Bas. Eng. 82 D, 35, 1960;  
 R. E. Kalman and R. S. Brucy: J. Bas. Eng. 83 D, 95, 1961;  
 P. Billoir: Nucl. Instrum. Meth. A 225, 352, 1984.
103. A. Garcia-Bellido et al: Primary Vertex certification in p14 DØ-Note 4320, January 2004.
104. A. Schwartzman and M. Narain: Probabilistic Primary Vertex Selection DØ-Note 4042, November 2002.
105. T. Golling et al: p14 Muon-ID certification note DØ-Note 4350, February 2004.

106. Emily Nurse and Paul Telford: Measurement of cross section times branching ratio for  $Z \rightarrow \mu\mu$  in ppbar collisions at 1.96 TeV, DØ-Note 4231, August 2003.
107. Top Physics Working Group: DØ Top Analyses and Data Sample for the Winter Conferences 2004 DØ-Note 4419, April 2004.
108. Chakravarti, Laha, and Roy: Handbook of Methods of Applied Statistics Volume I, Wiley, 1967.
109. M. Klute: Measurement of the ttbar cross section at  $\sqrt{s} = 1.96$  TeV in the muon-plus-jets channel DØ-Note 4185, July 2003.
110. D. Whiteson and M. Kado: Muon Isolation Studies, DØ-Note 4070, December 2002.
111. N. Gollub and L. Shabalina: Measurement of the ttbar Production Cross Section at  $\sqrt{s} = 1.96$  TeV in the muon-plus-jets Final State using a Topological Method on  $363Pb^{-1}$  of PASS2 data DØ-Note 4954, December 2005.
112. J. Kozminski, R. Kehoe, H. Weerts, S. Park, A. Quadt, J. Gardner, S. Jabeen: Electron Likelihood in p14, DØ note 4449, April 2004.
113. C. Gerber, E. Shabalina, G. Otero y Garzón: Study of EM Efficiencies in p14 for Top Analyses, DØ note 4655, February 2005.
114. S. Jain: A study of the scale and over-smearing parameters for MC electrons. DØ note 4402, March 2004.
115. G. Blazey et al: Run II Jet Physics, DØ-Note 3750, April 2000.
116. U. Bassler and G. Bernardi: Towards a Coherent Treatment of Calorimetric Energies, DØ-Note 4124, March 2003.
117. J-R. Vlimant, U. Bassler, G. Bernardi and S. Trincaz-Duvold: Technical description of the T42 algorithm for the calorimeter noise suppression, DØ-Note 4146, May 2003.
118. G. Bernardi, E. Busato and J-R. Vlimant: Improvements from the T42 Algorithm on Calorimeter Objects Reconstruction, DØ-Note 4335, January 2004.
119. T. Golling: private communication.

120. S. Anderson et al: Measurement of the ttbar cross section at  $\sqrt{s} = 1.96$  TeV, DØ-Note 4116, July 2003.
121. DØ Jet Energy Scale study group: Jet Energy Scale at DØ RunII, DØ-Note 4720, February 2005.
122. DØ Jet Energy Scale study group:  
[http://www-d0.fnal.gov/phys\\_id/jes/d0\\_private/certified/v5.3/links.html](http://www-d0.fnal.gov/phys_id/jes/d0_private/certified/v5.3/links.html)
123. A. Kumar et al: Oversmearing of Missing Transverse Energy in  $Z \rightarrow ee + X$  Monte Carlo DØ-Note 4551, July 2004.
124. T. Christiansen: The DØ L2-Muon Trigger Performance for P11, DØ-Note 4053, November 2003.
125. C. Belanger-Champagne, Y. Coadou, D. O'Neil, S. Beale: TrigSimCert: A New Package to Certify and Analyze Triggers DØ-Note 4570, August 2004.
126. R. Schwienhorst: Top Trigger Selection and Application of Turn-On Curves to the Monte Carlo, DØ-Note 4508, July 2004.
127. M. Klute and A. Quadt: Measurements of Level 1 Trigger Efficiencies from DØ Data, DØ-Note 3949, March 2002.
128. M. Agelou et al: Top Trigger Efficiency Measurement adn the top\_trigger package, DØ-Note 4512, July 2004.
129. S. Anderson et al: Measurement of the ttbar cross section at  $\text{sqrt}(s) = 1.96$  TeV, DØ-Note 4116, March 2003.
130. T. Golling: Measurement of the  $t\bar{t}$  Production Cross-Section at  $\sqrt{s} = 1.96$  TeV in the Muon+Jets Final State using a Topological Method, DØ-Note 4667, December 2004.
131. The DØ Run Quality Database,  
<http://d0db-prd.fnal.gov/run/runQuery.html>.

132. Calgo group web page,  
<http://www-d0.fnal.gov/computing/algorithms/calgo/calgo.html>.
133. K. Ranjan et al.: Calorimeter Event Quality Using Level 1 Confirmation, DØ-Note 4554, July 2004.
134. U. Amaldi et al.: Phys. Lett. B 43/231, 1973.
135. R. J. Hooper and G. Landsberg: Search for Large Extra Spatial Dimensions in the Di-Muon Channel with  $100 \text{ pb}^{-1}$  of RunII data DØ-Note 4230, August 2003.
136. A. Khanov: private communication.
137. A. Schwartzman and M. Narain: Secondary Vertex Reconstruction using the Kalman Filter DØ-Note 3908, September 2001.
138. D0 Collaboration: Common Sample Group (CSG).  
<http://www-d0.fnal.gov/Run2Physics/cs/index.html>.
139. B. Clément et al.: SystemD or how to get signal, backgrounds and their efficiencies with real data DØ-Note 4159, March 2003.
140. R. Demina et al.: Measurement of the  $t\bar{t}$  production cross-section at  $\sqrt{s} = 1.96 \text{ TeV}$  using lifetime tagging DØ-Note 4141, April 2003.
141. J.R. Vlimant et al: Measurement of the ttbar Production Cross-Section at  $\text{sqrt}(s)=1.96 \text{ TeV}$  in the Electron+Jets Final State using a Topological Method DØ-Note 4662, December 2004.
142. R. Demina: Single and double b-tag event probability calculation. DØ-Note 4359, February 2004.
143. C. Clement et al: Measurement of the ttbar production cross section at  $\text{sqrt}(1.96) \text{ TeV}$  using Lifetime tagging, DØ-Note 4682, January 2005.
144. J. M. Campbell and R.K. Ellis: Phys. Rev. D 65 113007, 2002.
145. J. M. Campbell and J. Houston: arXiv:hep-ph/0405276, 2004.

146. DØ Collaboration: Physics Letters B **626** 55, 2005.
147. DØ Collaboration: Physics Letters B **626** 45, 2005.
148. DØ Collaboration: Combined ttbar production cross section at  $\text{sqrt}(1.96)$  TeV in the Lepton+Jets and Dilepton Final States using Event Topology. DØ-Note 4906, August 2005.
149. DØ Collaboration: Physics Letters B **626** 35, 2005.
150. G. Otero y Garzón et al: Measurement of the ttbar Production Cross Section in ppbar Collisions at  $\text{sqrt}(s)=1.96$  TeV Using b-tagged Lepton+Jets Events DØ-Note 4888, July 2005.
151. F. Blekman: A ttbar cross section measurement in the all-jets channel DØ-Note 4830, June 2005.